GSI-2016-2
REPORT
June 2016

News and Reports from

High Energy Density generated by Heavy IOn and Laser Beams

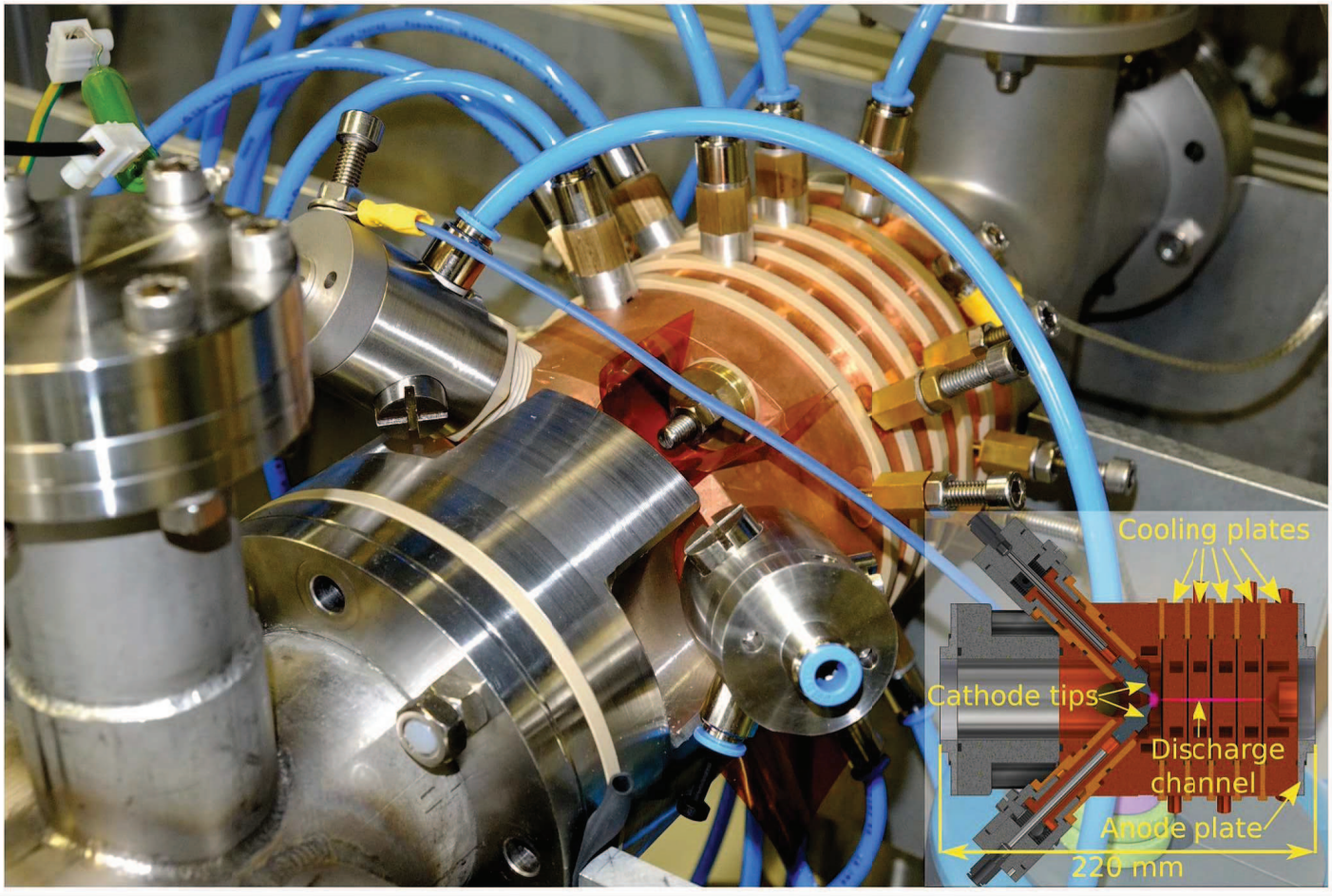

HEDgeHOB Collaboration at FAIR - Report 2015

The cover picture shows the set-up of a plasma window for FAIR built at the Goethe University in Frankfurt, while its scheme is depicted in the small picture in the right lower corner.

The plasma window is a membraneless vacuum-atmosphere-interface. One possible application is to use it between the accelerator vacuum and the gas stripper system. It is supposed to work more effective and is less space-consuming than a conventional differential pumping system. In addition it can be used at various experimental areas where a metal membrane is used to separate the beam line from the high pressure part of the experiments, especially for the high beam intensities in the SIS-100 where conventional metal foils as interface may be destroyed.

A closer description of the plasma window and its detailed working principle are found in the contribution on page 5 in this report.

(Pictures by B. Bohlender, J. Wiechula; Text: M. Iberler, J. Wiechula, K. Weyrich)

News and Reports from

High Energy Density generated by Heavy Ion and Laser Beams

2015

June 2016

Editor: K. Weyrich

Co-editor: D.H.H. Hoffmann

Editorial

Dear Colleagues,

this report is aimed to be available for the July 11-13, 2016 EMMI workshop on High Energy Density Plasma Physics at FAIR/GSI. During this workshop many scientists interested in High Energy Density Plasma Physics will convene to discuss the possibilities of intense heavy ion beams for this field.

This report starts with an overview on facilities worldwide that are engaged in High Energy Density Physics and where at the same time there is interest to collaborate in this field with FAIR/GSI. These facilities include LLNL (Livermore), LMJ/Petal (Bordeaux), NICA (Dubna), NDCXII (Berkeley), KUMGANG Laser and Large scale accelerator facilities (Korea) and the planned high intensity accelerator facility (HIAF) in China, just to name a few. The report continues with the traditional topic of Beam-Plasma Interaction Physics and diagnostic methods for High Energy Density Matter. Accelerator issues and theoretical issues complete this report. It may be interesting to have a look at the list of contributing institutes. Most of them are already member of a plasma physics collaboration at FAIR.

Scientific committees of FAIR and GSI have monitored the scientific program of the FAIR collaborations for many years. Most of the collaborations have adapted their scientific program towards the FAIR modified start version. In addition, the plasma physics collaborations have continuously adapted their programs towards the modifications of the FAIR project. However, we still have a long way to go. The proposal of a FAIR phase 0, which is aimed to prepare for the start of the FAIR facility during the years 2018-2022, is a new challenge for our collaboration. The task ahead of us, namely to secure the necessary resources and to formulate an excellent scientific program for plasma physics at FAIR, requires the consistent and unified action of the whole plasma physics community. During this workshop we also have to discuss our priority for experiments during the coming years as well as for the day one experiments. The envisioned procedure is that collaborations submit a priority list of experimental programs. A scientific committee of FAIR/GSI will then evaluate this suggestion and the available beam time will be distributed with respect to the assigned scientific priority. We therefore have to act as a unified collaboration and we call upon you to start the founding procedures for a “Plasma Physics Collaboration at FAIR” during the EMMI workshop at FAIR/GSI in July. Finalizing this procedure may take some time, but we have to give a strong signal to the FAIR/GSI management as well as to the respective funding agencies.

With kind regards,

Dieter H. H. Hoffmann

June 2016

Contents

2 Interaction Experiments with Ion – and Laser Beams

3 New Diagnostic Methods, Particle - and Plasma Sources and Target Design

1 New Facilities for HED/WDM Research and special FAIR related Issues

First Experiments at FAIR: HIHEX - Heavy Ion Heating and EXpansion

V.B. Mintsev[1], *V.V. Kim*[1], *I.V. Lomonosov*[1], *D.N. Nikolaev*[1], *A.V. Ostrik*[1], *N.S. Shilkin*[1], *A.V. Shutov*[1], *V.Ya. Ternovoi*[1], *D.S. Yuriev*[1], *V.E. Fortov*[1], *A.A. Golubev*[2], *A.V. Kantsyrev*[2], *D.V. Varentsov*[3], *and D.H.H. Hoffmann*[4]

[1]IPCP RAS, Chernogolovka, Russia; [2]ITEP, Moscow, Russia; [3]GSI, Darmstadt, Germany; [4]TUD, Darmstadt, Germany

Early experiments at FAIR in 2018–2022 suggested by the HEDgeHOB collaboration in the field of non-ideal plasma physics are discussed. Specific energies of 5–10 kJ/g, pressures of 1–2 GPa and temperatures of 1–2 eV are expected to be reached in the substance at the first experiments with a U^{28+} beam with the energy of 0.2 AGeV and maximal intensity $3{\cdot}10^{10}$ per impulse. It will provide the possibility to investigate the two phase region including the critical point of several metals in HIHEX (Heavy Ion Heating and EXpansion) experiments with the plane and cylindrical geometry, realizing regimes of quasi-isochoric heating, isentropic expansion and compression when the flow strikes the target. Analysis of thermal radiation transfer will give information on the vaporization dynamics. Measurements of electrical conductivity and optical properties on the supercritical adiabat will disclose information on the insulator to metal transition under these conditions.

We propose to use the HIHEX experimental setup to study thermophysical and transport properties of matter heated by intense beams of heavy ions and expanded adiabatically. Our goals are the determination of critical points (CP) for a number of elements, investigation of material properties and the metal-nonmetal transition in the near-CP region, including hot liquids and nonideal plasmas and the domain of high-pressure high-temperature vaporization along with kinetic effects in the two-phase liquid-gas region.

Comprehensive numerical modeling of HIHEX setups corresponding to ion-beam parameters for FAIR 1st-day experiments has been carried out employing a novel 3d gas-dynamic code [1] accounting for realistic properties of matter and energy deposition by intense beam of ions. The setup corresponds to heating of the cylindrical metallic wire with a diameter of 0.6 mm along the axe.

According to the evaluations of the critical point parameters based on the multi-phase equation of state for metals [2], in a HED experiment with the highest energy deposition for super-critical states for Pb with complete vaporization in the expansion isentrope will be accessed on the phase diagram. In the case of Cu and Ni, sub-critical states of liquid will be accessed while the expansion isentrope corresponds to the partial vaporization and is close to the critical point. These results are illustrated in Figure 1 for lead. The earlier evaluations [3] are also plotted in this figure. We may conclude that the project's goals can be successfully achieved because with the use of beam parameters from the table we will have high values of energy and entropy in the target.

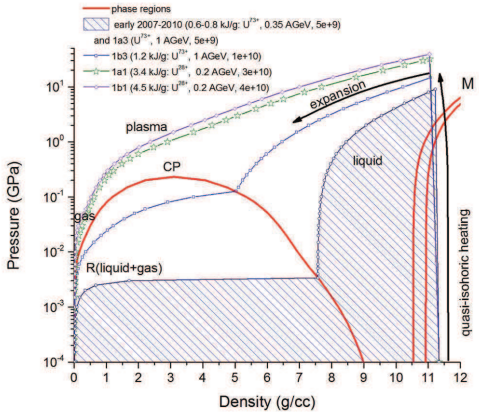

Figure 1: Pressure–density diagram for lead.

In future HIHEX experiments we propose to use the previously developed setups, diagnostic tools and intense beams of uranium ions providing for the highest energy deposition. The preferred beam parameters are: U^{28+} ions, 0.2 AGeV, $4{\cdot}10^{10}$ ions/bunch, the time duration 100 ns. The materials for study should be Pb and other elements. We expect to access and to detect the critical point, and to investigate the near-critical-point electrical properties in this domain of the phase plane. This information on the electrical properties of expanded substance is important for understanding the effect of metal-nonmetal transition. We also plan to use this setup for studying dielectric materials.

References

[1] V.E. Fortov, V.V. Kim, I.V. Lomonosov, A.V. Matveichev, A.V Ostrik, Intern. J. Impact Engineering, **33**, 244–253 (2006).

[2] I.V. Lomonosov, Laser and Particle Beams, **25**, 567–584 (2007).

[3] D.H.H. Hoffmann, V.E. Fortov, I.V. Lomonosov, V.B. Mintsev, N.A. Tahir, D. Varentsov, J. Wieser, Phys. Plasmas, **9**, 3651–3655 (2002).

High energy density experiments at FAIR*

S. Neff[1] *and D.H.H. Hoffmann*[2]
[1]FAIR, Darmstadt, Germany; [2]TU Darmstadt, Germany

The Facility for Antiproton and Ion Research (FAIR) will offer unique research opportunities in the fields of compressed baryonic matter, hadron physics, nuclear structure, atomic physics, materials research, biophysics and plasma physics. In the field of plasma physics, the focus of the research program will be the study of high energy density matter generated with heavy ion beams.

The equation of state of high energy density matter is important for many scientific fields, ranging from studying the interior structure of giant gas planets and the metallization of hydrogen to the dynamics of laser-driven capsules for inertial confinement fusion. To better understand the relevant processes, a knowledge of the equation of state, that is pressure as a function of density and temperature, and of the relevant transport coefficients, for example thermal conductivity and opacity, of warm dense matter (WDM, samples close to solid density with electronvolt temperatures) is essential.

Static measurements using laser-heated diamond anvil cells can only access pressures of up to about $3\ \mathrm{Mbar}$ and temperatures of up to about $1500\ \mathrm{K}$ and therefore cover only a small part of the states relevant for warm dense matter. In order to overcome this limitations, dynamic measurements, using for example shock compression or laser heating of small samples, are necessary.

For FAIR, dynamic measurements that use high energy heavy ion beams to generate warm dense matter are planned. Two main approaches will be used. In the first approach, the energy deposition of the heavy ions is used to isochorically heat macroscopic (mm-sized) samples and turn them into warm dense matter, for example in the HIHEX[1] (Heavy-Ion Heating and EXpansion) experiment. Heavy ion beams with up to $5 \times 10^{11} \mathrm{U}^{28+}$ ions with 2AGeV in a 50ns bunchs allow to heat the samples to temperatures of several electronvolts. In a second approach, which will be used in the LAPLAS[2] (LAboratry PLAnetory Science) experiment, the heavy ion beams are used to indirectly compress cryogenic samples. By using an annular beam profile to heat a payload, it is possible to quasi-isentropically compress hydrogen to a pressure of $5\ \mathrm{Mbar}$ at a temperature of only $3000\ \mathrm{K}$.

In addition to these experiments, it is also planned to use high-energy protons available at FAIR (10GeV in energy with up to $2.5 \cdot 10^{13}$ protons per bunch) to diagnose dense samples using a proton microscope with a resolution of $10\ \mu\mathrm{m}$. This can be used to either study high-energy density matter generated with secondary drivers (e.g. a laser or a gas gun) or for other applications such as imaging biological samples for the PANTERA project.

A delay in the civil construction work for FAIR has resulted in a delay of the construction and commissioning of the facility. After a review by an external expert panel, a new timeline has been determined with the experiments of the Modularized Start Version (MSV) scheduled to start in 2022. Currently several phases are planned for experiments: 'Phase 0', which covers the time up to the start of the MSV; 'Phase-1', which refers to initial experiments at FAIR which do not require the full beam intensity; 'Phase 2', which refers to experiments using the full design intensity of FAIR; and 'Phase 3', which refers to experiments beyond the MSV which require further upgrades.

The interim science program ('Phase 0') at GSI (using PHELIX, UNILAC and SIS-18) and at other facilities is essential for further R&D work, and to keep up with technological and scientific progress until the start of FAIR in 2022. Our activities in this phase will focus on further development of PRIOR and further work on diagnostics, such as laser particle acceleration.

Experiments at FAIR will take place in the so-called APPA cave, with a dedicated beamline for high energy density experiments. This beamline will be used for experiments with protons as well as with heavy ions. Originally, a dedicated second proton beamline directly from SIS-18 was also planned. To reduce costs, this second beamline was not included in the MSV. However, there is an option to add this beamline later on. In addition to the beamline, a diagnostic laser system (100 J, 0.1-20 ns, 532 nm) will be available to drive laser diagnostics (e.g. x-ray backlighting) and as a secondary driver for PRIOR experiments. The initial experiments at FAIR ('Phase 1') will concentrate on HIHEX and PRIOR, since these experiments can already start with beam intensities well below the design specifications of the SIS-100 accelerator. Once the accelerator is operating close to its design specifications ('Phase 2'), it will be possible to start the LAPLAS experiment, which needs high beam intensities in order to compress the cryogenic sample to megabar pressures. The main possible upgrade options for our experimental setup are to add the second dedicated proton beamline and to add a high energy laser to the setup. Coupling this laser with the intense ion beams from FAIR would open new fields of high energy density physics and provide new research opportunities.

References

[1] V. Mintsev et. al. Non-Ideal Plasma and Early Experiments at FAIR: HIHEX - Heavy Ion Heating and EXpansion. *Contributions to Plasma Physics*, February 2016.

[2] B.Y. Sharkov et. al. High energy density physics with intense ion beams. *Matter and Radiation at Extremes*, January 2016.

* For the HEDgeHOB collaboration.

Design of a 5 GeV Proton Microscope for FAIR*

M. Schanz† [1], *D. Varentsov*[2], *and D.H.H. Hoffmann*[1]
[1]TU Darmstadt, Darmstadt, Germany; [2]GSI, Darmstadt, Germany

The PRIOR-I (Proton Microscope for FAIR) prototype facility has recently been commissioned at GSI with 3.6 GeV proton beams delivered by the SIS-18 heavy ion synchrotron [1]. The design of this microscope is based on compact high-gradient (120 T/m) NdFeB permanent magnet quadrupole (PMQ) lenses which can facilitate imaging with protons up to 4.5 GeV. This system is capable of providing a magnified image of a dense object and correcting the most significant terms of the chromatic aberrations, which led to the achievement of micrometer-level spatial and nanosecond-scale temporal resolution with a remarkable density sensitivity during the beam time commissioning. Despite the success of the first experiments, a continuous degradation of the image quality and spatial resolution due to a severe radiation damage of the PMQ lenses has been observed. [1, 2]. It was concluded that PMQ lenses are not an appropriate choice for a radiographic facility with high-energy and high-intensity proton beams. Therefore the final design of the PRIOR proton microscope (PRIOR-II) will employ small but strong and radiation-resistant normal conducting electromagnets in order to assure high imaging quality for future experiments at GSI and FAIR.

Since the PRIOR-II microscope has to fulfill a lot of different requirements which will mainly be determined by the future experiments, new simulation tools were developed to estimate the performance of the new system [3]. The respective ion optical simulations were based on COSY Infinity 9.1 taking into account high order image aberration effects which determine the image quality of a radiographic setup. By the observation of the geometrical moments of a point spread function an entirely new approach to the calculation of the spatial resolution performance of radiographic facilities was introduced [3].

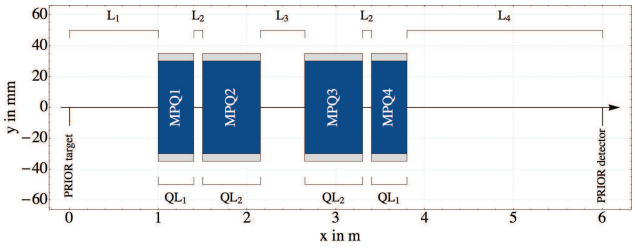

Figure 1: Geometrical layout of the PRIOR-II setup.

The PRIOR-II setup was optimized regarding the length of the individual magnets QL_1 - QL_4 as well as the distances between the magnets L_1 - L_4 (see Fig. 1) in order to obtain a compromise between the resolution and the constraints of the construction process. The shape of the yoke was chosen to guarantee an overall field deviation $\Delta G/G$ of less than $4 \cdot 10^{-4}$ and to suppress higher multipole orders ($B_n/B_2 < 4 \cdot 10^{-4}$), especially $n = 6, 10, 14$, between 80% and 90% load. The two layered coil with just 14 turns per pole will provide high field gradients up to G= 43.3 T/m (30 mm pole tip radius) while being driven by 1.7 kA current [4].

When PRIOR-II will be installed at FAIR utilizing 5 GeV protons, a magnification of 7.98 with a micrometer-level spatial resolution ($CR_x = 7.26$ μm, $CR_y = 3.83$ μm) and the maximum field of view of 26.9 x 21.5 mm^2 can be provided (see Fig. 2).

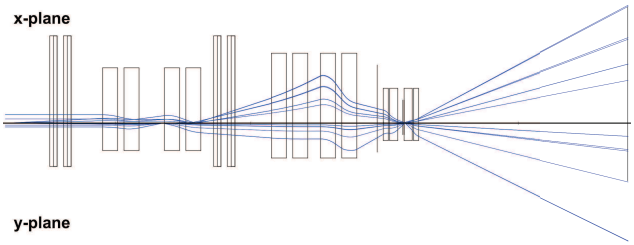

Figure 2: Ion optical layout of PRIOR-II.

It is foreseen that during the construction of FAIR, PRIOR-II will be installed first at the HHT cave at GSI and provide a magnification of 2.5 ($CR_x = 9.67$ μm, $CR_y = 6.51$ μm).

The design of PRIOR-II will offer simultaneously a variable geometry and a variable field gradient, enabling a wide range of proton energies to be used for various investigations on high energy density states in matter as well as on medical applications with an impressive image quality.

References

[1] D. Varentsov et al., "Comissioning of the PRIOR proton microscope", Rev. Sci. Instrum. **87**, 023303 (2016).

[2] M. Schanz, M. Endres et al., "High energy proton induced radiation damage on PRIOR rare earth permanent magnet quadrupoles", Laser and Part. Beams , (to be submitted) (2016)

[3] M. Schanz, "High Energy Proton Microscopy at FAIR", Master thesis, TU Darmstadt (2016)

[4] A. Kalimov, "Quadrupole for PRIOR-M", Tech. Rep. GSI (2015)

* Work supported by BMBF, grant agreement ID 05K13RDB. This report is also submitted to the *'GSI Scientific Report 2015'*.

† m.schanz@gsi.de

Short-pulse laser-driven x-ray radiography for FAIR

E. Brambrink, S. Baton, and M. Koenig
LULI - CNRS, Ecole Polytechnique, CEA : Université Paris-Saclay; UPMC Univ Paris 06 : Sorbonne Universités - F-91128 Palaiseau Cedex, France

In the context of HEDP experiments planned at FAIR x-ray radiography is an important diagnostic to characterize matter at extreme conditions. It allows for example measuring precisely mass densities or characterising the temporal evolution of hydrodynamic instabilities. Laser driven x-ray sources can deliver short high-flux x-ray pulses well adapted to this task. The simplest configuration is the point-projection geometry. We studied new experimental configurations to optimize this diagnostic.

Former experiments [1] have shown that high-quality radiographies require a close to normal incidence of the laser on the x-ray source target. Due to the size of the backlighter laser and HEDP driver beams their geometry has many constrains, often limiting the possibilities of incident angle. To overcome this limitation, we have chosen a radiography axis perpendicular to laser and drive beam. This approach is technically challenging as this axis is used for the target manipulator and laser beam path in many large laser facilities.

The experiments have been performed at the LULI2000 laser facility. The short pulse laser delivered up to 50 J in 1.5 ps at 1053 nm wavelength or 25 J in 1.5 ps at 527 nm (frequency doubled). While we used the laser at best focus (~10 µm) for the frequency doubled shots, it was defocussed to 50 µm diameter at the fundamental wavelength to reduce noise produced by hard x-rays.

Targets were Vanadium, Copper, Tungsten and Molybdenum wires of 10-20 µm diameter. To estimate the spatial resolution we used a 400 lpi gold grid as test sample.

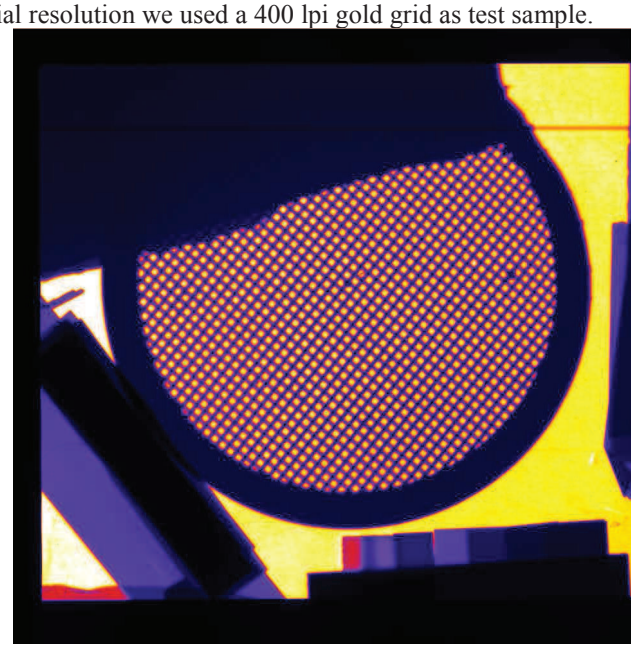

Figure 1: Radiography using a 20 µm Vanadium wire as x-ray source with a frequency doubled laser beam, the resolution is estimated to be better than 25 µm.

X-ray signals were recorded with an imaging plate (IP) type "MS" with a x24 magnification. To block light and low energy x-rays, a 13 µm Al foil was placed in front of the IP. Step wedge targets of different materials were placed onto the detector to appreciate the dynamic resolution.

Figure 1 shows a typical radiography obtained using the frequency doubled beam. The grid is well resolved and comparing the contrast (see fig. 2) with a MTF indicates a spatial resolution of less than 25 µm. The plastic step wedge at the bottom of the image is clearly resolved, indicating the majority of the signal originating from V K-shell radiation.

Radiographs using frequency doubled laser compared to the fundamental wavelength exhibit less background and stronger signal. However, even at the fundamental wavelength, we obtain similar spatial and dynamic resolution.

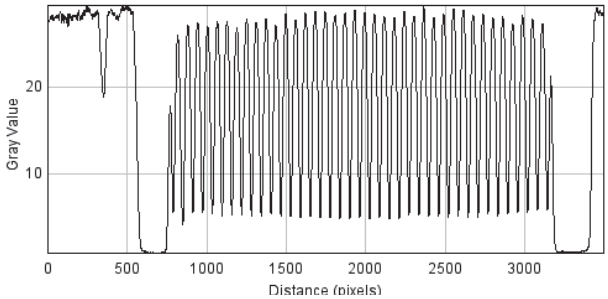

Figure 2: Lineout of the signal in the grid region

In conclusion, by using a vertical radiography axis, we were able to obtain high quality radiographies, as the laser incident angle could be optimized independently of the laser beam axis.

References

[1] E. Brambrink, H. G. Wei, B. Barbrel, et al. « X-ray source studies for radiography of dense matter », *Phys. Plasma* **16**, 033101 (2009)

[2] Park, H. -S., Maddox, B. R., Giraldez, E et al. « High-resolution 17-75 keV backlighters for high energy density experiments », *Phys. Plasma* **15**, 072705 (2008)

[3] Brambrink, E., Wei, H. G., Barbrel, B. et al. « Direct density measurement of shock-compressed iron using hard x rays generated by a short laser pulse », *Phys. Ref. E* ***80,*** 056407 (2009)

Construction, characterization and optimization of a plasma window based on a cascade arc design for FAIR*

B. Bohlender[1], J. Wiechula[1#], Marcus Iberler[1], O. Kester[1,2] and J. Jacoby[1]
[1]Goethe University, Frankfurt, Germany; [2]GSI , Darmstadt, Germany

For many different applications at GSI and for the new FAIR project, it is important and necessary to extract the ion beam from the high vacuum of the accelerator into a gas filled target chamber. In order to prevent the gas inside the chamber from flooding the accelerator section, usually thin metal membranes or differential pumping systems are used. In order to improve these systems, concerning the lifetime and the length respectively, a plasma window, similar to A. Hershcovitch's [1] design, is being built and investigated for the requirements at FAIR. Especially for the transition to the gas stripper system, where the pressure is significantly higher than inside the accelerator section the plasma window would be a benefit as a sealed off system between vacuum and high pressure. In regard to the adaption of a plasma stripper system [2] the plasma window is also thought as an improvement and alternative concept to conventional differential pumping systems. Moreover a plasma window is requested at FAIR because of the high ion beam intensities where a metal membrane as vacuum-atmosphere interface bears the risk of being destroyed.

Experimental setup and working principle

The plasma window mainly consists of a certain number of cathode tips, an anode plate and several free floating electrode plates. Similar systems are well known since the mid-50s as wall-stabilized cascade arc discharges [3]. The plasma arc is initialized between the negative cathode tips and the grounded anode plate. For first investigations, the diameter of the channel between the cathode and the anode is d=2.5 mm, the effective discharge length is about l=63 mm. Stepwise the diameter will be adapted to the requirements of FAIR. The high dissipation of heat is encountered with a water cooling system (fig.1).

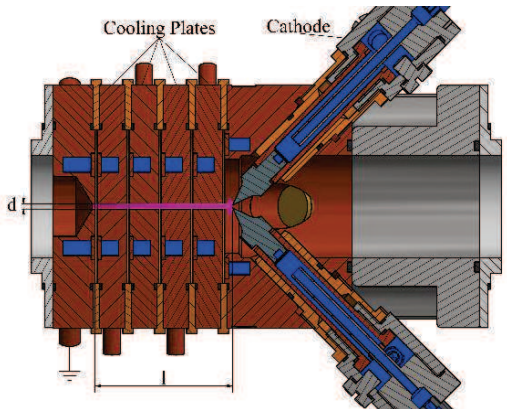

Figure 1: Schematic view of the plasma window.

According to Hershkovitch two main effects are dominant as working principle for a plasma window as a vacuum-atmosphere interface. The main effect is due to pressure equalization between arc discharge and atmosphere. In pressure equilibrium the density is reduced when the temperature is enhanced. To match atmospheric pressure at room temperature, the arc plasma and gas density needs to be a certain factor of the room temperature gas density. This factor is given by the ratio between room temperature in the low pressure part and arc discharge temperature. Therefore, a reduction in the vacuum chamber pressure by this factor is expected. The second effect is due to the fact that the viscosity in a plasma is increased at higher temperatures. Thus, a backflow of the gas from the high pressure cell into the low pressure cell is reduced. In addition the plasma window may act as a plasma lens due the Lorentz force [1].

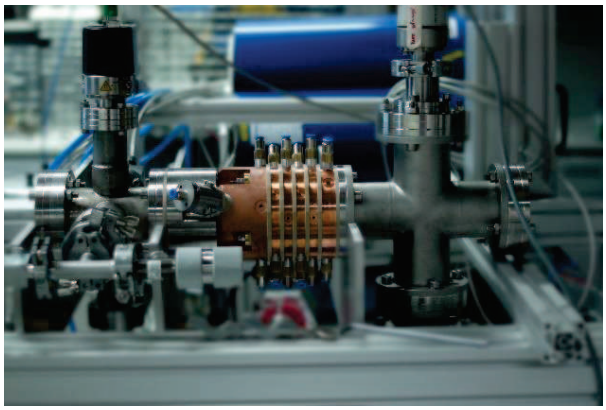

Figure 2: Present status of the plasma window.

Status and outlook

The present setup is shown in fig. 2. First investigations are directed to estimate the breakdown voltage as well as a stable burning voltage as function of the gas pressure. Next tests will include an estimation of the U-I-characteristic, the determination of the pressure gradient as well as an optical analysis for the plasma parameters density and temperature. In addition the influence of the number of cathode tips will be studied. The long term goal is the implementation of the plasma window into an accelerator section at GSI and FAIR.

References

[1] A. Hershcovitch, Journal of Applied Physics 78 (9), 1995.
[2] G. Xu et al., GSI Report 2014-1, p. 290.
[3] H. Maecker, Z. Naturforschg. 11a, 457—459, 1956

* Work supported by BMBF contract No. 05P2015.
# wiechula@physik.uni-frankfurt.de
* This report is also submitted to the GSI Scientific Report 2015

Cylindrical cryogenic targets for the LAPLAS experiments at FAIR

E.Koresheva[1,2,#], I. Aleksandrova[1], E.Koshelev[1], A. Nikitenko[1], T. Timasheva[1] and S.Tolokonnikov[1]
[1]LPI, Moscow, Russia; [2] National Research Nuclear University MEPhI, Moscow, Russia

The subject of the joint research is development on a specialized setup for fabricating and delivering multi-layered cylindrical cryogenic targets. Such targets are required for the LAPLAS (Laboratory Planetary Sciences) low-entropy compression experiment that will be constructed and run by the HEDgeHOB (High Energy Density Generatedby Intense Heavy Ion Beams) Collaboration at FAIR [1]. The targets are hydrogen or deuterium ice which is enclosed in a cylindrical shell of a high-Z material like gold or lead.

The Lebedev Physical Institute (LPI), as a member of the HEDgeHOB collaboration, considers different approaches for preparation of cylindrical cryogenic targets for the LAPLAS experiments (Fig.1) [2-4]. Main directions of the LPI research are: (1) target fabrication, (2) target manipulation, (3) target survival. The key results of this research are as follows:

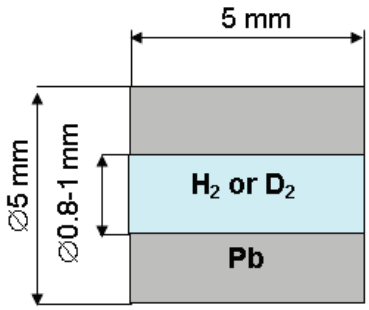

Fig.1. Cryogenic target for the LAPLAS experiment

• Target shell made at LPI from Pb is shown in Fig. 2. Softness, plasticity and malleability is the features of Pb, therefore a key moment is the shell surface survival during target transport to the experimental chamber.

Side view Top view

Fig. 2. Target shell made from Pb by mold pressing

The LPI expertise has shown that a tube from stainless steel (SS) can be successfully used for Pb-shell surface protection. In addition, at the stage of Pb-shell formation the SS-tube play a role of forming element. We also advice to use capsule from magneto-active material for target protection because at the stage of target electromagnetic delivery this element play a role of the driving body.

• A target fuel core bibliography analysis has shown that parameters combination related to fuel core in the LAPLAS targets (i.e. length to diameter ratio in the range of 5.0-to-6.25) was never realized before. Two methods of the cryogenic core formation are promising: in-sutu method and extrusion one. The specifics features of the in-situ method are: (1) short time of target fabrication – 15 min, (2) simple mechanic and electric control – there are almost no movable parts, (3) possibility to make a cryogenic core with faces of the required shape. The extrusion method features are: (1) short time of target fabrication – 1−2 s, (2) ability to supply cryogenic targets in real time, (3) minimal consumption of the liquid helium as cryogenic targets do not need a long-term storage, (4) prospects for a rep-rated target production.

• Module for cryogenic target fabrication and assembly (FAM) based on the extrusion method is shown in Fig. 3. The physical layout is as follows:

1. Pb-shell loading under gravity (Fig.3, pos. 2),
2. Solid D_2 core extrusion into Pb-shell (pos. 3),
3. Cutting off the upper & the lower parts of D_2 core using tungsten wire (pos. 3),
4. D_2 core face formation (pos. 4),
5. Target characterization (pos. 5),
6. In accordance with characterization results, the target is moved to the delivery module (pos. 6), or to the collector of the rejected targets (pos. 7),

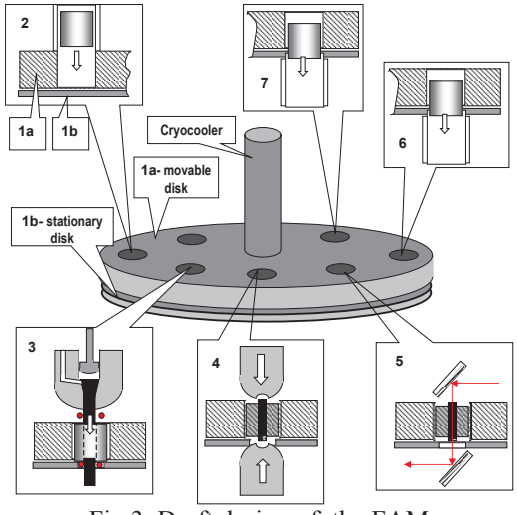

Fig.3. Draft design of the FAM

#elena.koresheva@gmail.com

7. Target loading under gravity to the corresponding unit (pos. 6 or 7),
8. High quality target delivery to the experimental chamber.

• Our calculations have shown that using the cryogenic holder for target positioning inside experimental chamber one can protect the target from the thermal radiation of the chamber wall and fix target temperature in the required ranges ($T < T_{tp}$, where T_{tp} is a triple point temperature of a fuel) [2,3].

• We have considered two options for target delivery from the FAM to experimental chamber: gravitational and electromagnetic. It is important that for both of these approaches the contamination of the experimental chamber with foreign gas is impossible. Gravitational injector seems as the most economical delivery means which requires small delivery time (1−2 s). To protect the outer target surface from the mechanical destruction due to friction we have proposed to apply a stainless steel tube [2]. Using an effect of quantum levitation of high temperature superconductors (HTSC) is another protection means,

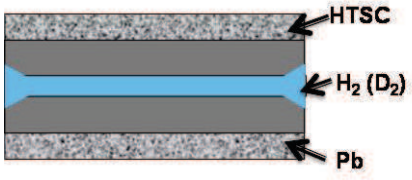

Fig.4. LAPLAS target with protecting HTSC shroud

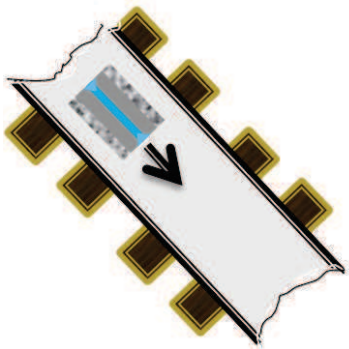

Fig.5. Target motion under gravity over the PMG: there is no contact between the target & the guiding tube

which has been proposed and examined at LPI [3,5]. To realize this approach one must use a special HTSC shroud outside of a LAPLAS target and a guiding tube with the permanent magnets guideway (PMG) for non-friction target delivery (see Fig.4, Fig.5, and Fig.6). HTSC quantum levitation effect allows shell surface protection from the scratches and fuel protection from the heat load. In addition, a target declination inside the guiding tube is excluded. This effect can be used for both gravitational and electromagnetic injectors.

On the basis of the performed research, the technical requirements to the corresponding specialized cryogenic

Fig.6. HTSC sample aligns inside the PMG with the line of minimal magnetic induction. The HTSC samples have been made at LPI from YBa_2Cu_3O ceramics (Tc ~ 91 K, Hc ~ 5.7 T at 0 K)

system (SCS) were defined. The SCS conception was proposed aiming the potential risks minimization during the system designing and functioning [2-4].

In conclusion, we would like to emphasize some open questions, which have to be solved at the next stage of the development, namely:
1. First of all: Is it possible for the LAPLAS to use the target enclosed into the protective element (SS-tube, HTSC-shroud, etc.) ?
2. Concerning the quality requirements to the cryogenic core:
− What is the permissible size of a structure inhomogeneity?
− What is the permissible roughness of the faces?
3. Another urgent question: whether the cryogenic core faces degrade before completion of target positioning?

If yes, is it necessary to perform a special face shaping in the stage of the core formation? In this connection, the problem of thermal degradation of the cryogenic core faces requires a thorough analysis at the next stage of development.
4. The LPI proposes to discuss once again the requirements to the rate of the target delivery:
− If the delivery rate is more than 1 target per day, one must work with free-standing targets: application of FAM, delivery by gravitation or electromagnetic injector are required.
− If the delivery rate is less than 1 target per day one can consider a traditional method of target fabrication and delivery: in situ method using Pb-shell pre-mounted on the holder.

References

[1] N.A.Tahir, et al. Phys. Rev. E **63**, 016402-1, 2000; HED Phys. **2**, 21, 2006
[2] E.R.Koresheva, et al. LPB **27**, 255-272, 2009
[3] E.R.Koresheva, et al. Report, 7th International EMMI Workshop on Plasma Physics with Intense Heavy Ion & Laser Beams at FAIR, December 9-10, 2014, Moscow, Russia
[4] E.R.Koresheva, et al. p.38 in: News and Reports from High Energy Density generated by Heavy Ion and Laser Beams, GSI-2015-2 Report, April 2015
[5] I.V.Aleksandrova, et al. J. Russian Laser Research **35** (2), 151-168, 2014

Status of Indirect Drive ICF Experiments on the National Ignition Facility*

The ICF Program Collaboration[1-11]

[1] *Lawrence Livermore National Laboratory, Livermore, CA, USA*
[2] *Laboratory of Laser Energetics, University of Rochester, Rochester, NY, USA*
[3] *General Atomics Corporation, La Jolla, CA, USA*
[4] *Los Alamos National Laboratory, Los Alamos, NM, USA*
[5] *Sandia National Laboratories, Albuquerque, NM, USA*
[6] *Massachusetts Institute of Technology, Cambridge, Massachusetts, USA*
[7] *Atomic Weapons Establishment, Aldermaston, Reading, Berkshire, UK*
[8] *Commissariat à l'énergie atomique et aux énergies alternatives (CEA), France*
[9] *National Security Technologies, LLC (NSTec), Livermore, CA, USA*
[10] *University of California, Berkeley, Berkeley, CA, USA*
[11] *Duke University, Durham, NC, USA*

In the quest to demonstrate Inertial Confinement Fusion (ICF) ignition of deuterium-tritium (DT) filled capsules and propagating thermonuclear burn with net energy gain (fusion energy/laser energy >1), recent experiments on the National Ignition Facility (NIF) (Fig.1a) have shown progress towards increasing capsule hot spot temperature (Tion>5 keV) and fusion neutron yield (~10^{16}), while achieving ~2x yield amplification by alpha particle deposition. At the same time a performance cliff was reached, resulting in lower fusion yields than expected as the implosion velocity was increased. Ongoing studies of the hohlraum and capsule physics are attempting to disseminate possible causes for this performance ceiling.

Experiments to understand the effect and mitigate potential sources of fuel preheat while improving the radiation symmetry in hohlraums are ongoing. Recent results show that higher energy preheat x-rays ($h\nu$>2 keV) are reduced in alternative hohlraum materials to pure Au such as uranium or by applying mid-Z liners to the inner wall surface. Furthermore, lower densities or near vacuum hohlraum fills have demonstrated a strong reduction in the amount of preheat hot electrons generated by laser-plasma instabilities. These experiments have also shown that the laser energy coupling into x-rays is improved by ~20% by reducing laser backscattering from the target.

High resolution 3D simulations, validated by inflight capsule radiography data, have also shown that the tent holding the capsule and low mode radiation asymmetries have strong negative impacts on implosions by the hydrodynamic instabilities they cause at stagnation (Fig. 1b). The relative importance of these factors depends on the ICF design, i.e. capsule ablator (CH, HDC, Be) and laser pulse (High Foot, Low Foot, adiabat shaped-AS, Fig. 1a). Studies to mitigate low-mode asymmetries and investigate alternatives to the tent mount are ongoing.

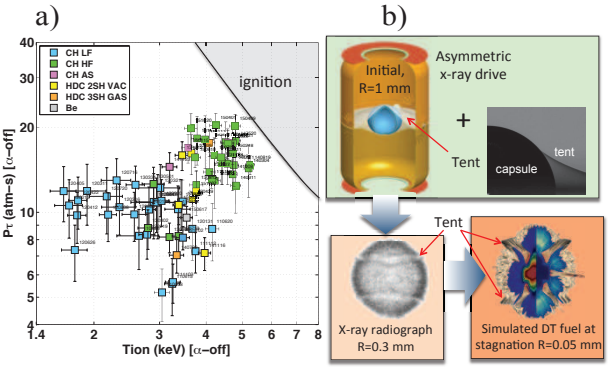

Figure 1. a) Lawson criteria Pτ of NIF DT fuel implosions vs hot spot temperature (Tion) for various ablators (plastic-CH, diamond-HDC and Be) and hohlraum fills (1.6 mg/cc for High Foot-HF and 3-Shock HDC, 0.96 mg/cc for Low Foot-LF and 0.03 mg/cc for near vacuum hohlraums-VAC). b) The tent holding the capsule inside the hohlram and low mode radiation flux asymmetries are potential culprits of performance limits; they are observed at peak implosion velocity (R=0.3 mm capsule radius) and are simulated to have a negative impact on hot spot stagnation (R=0.05 mm).

In upcoming ICF experiments with CH, HDC or Be capsules low mode asymmetries and hydro-instabilities will be mitigated by optimizing the hohlraums and laser pulses to reach nearly 1-D implosions that are well understood. These more robust designs will be then subjected to higher implosion velocities required to approach ignition.

*This work was performed under the auspices of the U.S. Department of Energy by LLNL under Contract DE-AC52-07NA27344.

Contact E-mail: dewald3@llnl.gov

Development and academic opening of the LMJ/PETAL laser facility

D. Batani[1], J.E. Ducret[1], G. Boutoux[1], S. Hulin[1], K. Jakubowska[1], J.L. Dubois[1], E. d'Humieres[1], N. Rabhi[1], V.Tikhonchuk[1], L.Serani[2], J.L.Miquel[3], I.Thfoin[3], B.Rosse[3], C.Reverdin[3], L.Lecherbourg[3], N.Blanchot[4], D.Raffestin[4]

[1]CELIA, Université Bordeaux– CNRS - CEA, France, [2]CENBG, Université Bordeaux, France, [3]CEA, DAM, DIF, F-91297 Arpajon, France, [4]CEA-CESTA, 33114 Le Barp, France

A new laser facility is under construction at the CEA/CESTA (Centre d'Etudes Scientifiques et Techniques d'Aquitaine) site in Le Barp, near Bordeaux. This will couple the Laser Megajoule (LMJ) and the short-pulse high-intensity system PETAL (PETawatt Aquitaine Laser). The combination of long ns-pulses and short high-intensity pulses will provide a unique facility at the European and also at the world scale (the only other similar facility being NIF in the US). LMJ/PETAL will be open to the European researchers for academic scientific experiments starting in 2017. Several subjects will be studied on LMJ/PETAL including in particular the direct drive approach to Inertial Confinement Fusion for the production of energy [1]. In parallel, the scientific community is working on the construction of advanced diagnostics for the facility, so-called PETAL+ project, which includes the study of induced radiation (and activation issues) and of the generation of giant EMP (Electromagnetic pulses) once PETAL is fired on target inside the LMJ interaction chamber.

1. The PETAL laser system: PETAL is funded by the Region Aquitaine, the French Ministry of Research and the European Union. The Region is the contracting owner of PETAL, the CEA is the manager and the prime contractor of the project, and the scientific assistance is provided by the ILP (Institut Lasers et Plasmas). Also, PETAL is part of the opening policy of the French Commissariat à l'Energie Atomique et aux Energies Alternatives (CEA). PETAL is a short-pulse (500 fs to 10 ps) high-energy beam (3.5 kJ compressed energy), which will be coupled to LMJ. LMJ, developed by CEA, and under construction at the CEA/CESTA site, will have 176 beams and deliver 1.3 MJ at 0.35 μm on target. LMJ is designed to provide capabilities to study High Energy Density Physics (HEDP), and the physics of ignition.

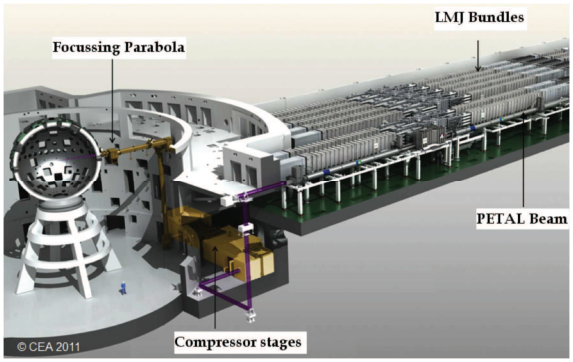

Figure 1: Implementation of PETAL in the LMJ Facility. The PETAL beam is in the equatorial plane of the target chamber.

PETAL design is based on the chirped pulse amplification (CPA) technique combined with optical parametric amplification (OPA) [2]. Furthermore, it takes the benefits of the laser developments made for the high-energy LMJ facility allowing it to reach the kilojoules level. Fig. 1 shows the implementation of PETAL in the LMJ Facility.

2. PETAL+ Diagnostics: PETAL+ is a specific project to develop diagnostics [3] adapted to the characterization of the interaction of the PETAL laser with target, mainly used as backlighter for X-ray or proton radiography of the LMJ plasmas. Also PETAL+ diagnostics must enable the measurements of the fast electron transport through plasma targets in experiments in connection with fast-ignition and shock-ignition**.**

The charged-particle diagnostics [4] include:

- A box installed close to the LMJ chamber center, which will contain a stack of RCF films to provide plasma radiography (CRACC);
- A two-channel electron, ion and proton spectrometer called SEPAGE, corresponding to low- and high-energy ranges (0.1-20 and 10-150 MeV), based on Thomson parabolas for ions/protons discrimination and energy spectra measurements with detectors for ions, protons and electrons;
- A set of two identical magnetic spectrometers called SESAME attached to the LMJ chamber wall to detect electrons above 4-5 MeV, one at 0^o and one at 40^o with respect to the PETAL axis.

The hard photon spectrometer SPECTIX is intended to be complementary with spectrometers that will be working for the first LMJ shots. SPECTIX is based on the transmission Cauchois-type optics [5, 6] and uses the combination of a cylindrical crystal used in transmission/ diffraction and a mechanical collimator. The spectrometer has been designed to measure the energy range 6 to ~ 100 keV with a signal dynamics from 10^{10} to 10^{13} photons/sr. Special care in the design has been devoted to reducing the noise on the detector [7].

All diagnostics will use passive detectors, essentially Imaging Plates (IP), in order to ensure a good protection against the effect of the giant electromagnetic pulse (EMP) launched by the interaction of the PETAL beam with its target. A systematic effort has been undertaken to calibrate such detectors with respect to X-rays [8], protons, electrons [9].

3. Radiation and Activation issues: Shooting the PETAL laser pulse on targets will generate large radiation fluxes. In turn, these may produce radionuclides in the LMJ chamber, i.e. activate the materials of the diagnostics and the chamber itself. These effects must be considered for radioprotection and nuclear safety and for correct operation of diagnostics. Activation originates from the interaction with matter of i) X bremsstrahlung photons, ii) protons originating directly from laser interaction, and iii) secondary particles generated after the interaction.

2D Particle-In-Cell simulations were performed using the code PICLS [10] to describe the electron and proton sources from the interaction of a PETAL pulse with a solid target. Laser energy on target was varied from 0.2 to 3.5 kJ corresponding to laser intensities of 1.4×10^{19} W/cm^2 to 2.5×10^{20} W/cm^2.

Unlike electrons, the proton angular distribution is strongly collimated. The emission angle decreases with the increase in proton energy and is not very sensitive to the laser energy in the conditions studied here. The energy distribution can be approximated by an exponential function characterized by a certain temperature with a sharp cut-off. These results allow using the proton characteristics directly for activation calculations and the electron characteristics for photon conversion calculations.

Simulations of the electron transport and interaction with a Tungsten target were performed using the Monte Carlo code GEANT4 [11]. The electrons produced with the PICLS simulations are used as source for the bremsstrahlung calculations. As the process of photon production is linear in the electron number, the input parameters of the GEANT4 simulations are the energy and angular distribution of the electrons. The large number of simulated particles ($\approx 10^9$) was chosen to obtain the photon spectrum with a sufficiently low level of fluctuations.

The goal of this study was to study the activation induced by PETAL experiments in its early phase of operation. A complete calculation sequence consists in the simulation of the interaction of the PETAL laser with solid targets, leading to the production of energetic particles, for two types of generic experiments – TS1 for X-ray generation through bremsstrahlung conversion of electrons in a massive target and TS2 for generation of energetic protons using a thin solid foil as target. This sequence takes into account the transport and the conversion of particles and radiation, and then estimates the global activities of the experiment system to determine regulatory levels. The irradiation conditions, the focal spot and the target structure, ensure that the obtained results constitute indeed a worst-case and that the real activity will be smaller than the calculated one.

The calculation results, performed for four different levels of irradiation from 0.2 to 3.5 kJ identify two regulatory thresholds that depend on the type of experiment envisioned: a threshold of 1 kJ for TS1 experiments and 300 J for TS2 experiments. In the energy range considered the laser pulse duration only has a small influence. Although the calculations are performed specifically for the LMJ-PETAL installation, the methodology is rather general and may be applied for design of experiments with other high power laser systems.

4. EMP Generation: The generation of strong electromagnetic pulses (EMP) when the PETAL is fired on target is critical. Comparison and extrapolation of other high-intensity facilities indicate expected in-chamber electric field exceeding MV/m, which can affect diagnostics behavior or even clearly break dedicated electronics. Hence, in the initial phase of the PETAL+ project, we did choose to rely on passive diagnostics (IP, films, etc.). Nevertheless understanding EMP generation and its impact remains a fundamental task.

Two major sources of the EMP are the bunch of energetic electrons ejected from the target during the laser pulse and the discharge current through the target support. In this context, a series of specially designed experiments was performed on the Eclipse laser at CELIA to provide direct measurements of the target polarization and the discharge current, the objective being to validate and enhance the accuracy of an analytical model of ejected charge [11, 12]. According to measurements, the charge and the maximum current depend essentially on the laser energy and much less on the laser intensity (no influence of laser pulse duration in the considered range).

A suite of numerical code integrating PIC code (CALDER) for source term and transports code of particle (MCNP) and field (SOPHIE) was used to simulate the experiment.

Conclusion: A large effort is undergoing in France to install the short-pulse high-energy laser PETAL as a high-intensity companion to LMJ. In parallel diagnostics are being developed within the PETAL+ project. The LMJ/PETAL facility will be open to academic access of European researchers starting in 2017.

References:

[1] http://www-lmj.cea.fr/en/ForUsers.htm
[2] N. Blanchot, G. Behar, et al., EPJ Web of Conferences **59**, 07001 (2013)
[3] D. Batani, M.Koenig, et al. Physica Scripta, T159 (2014) (7pp)
[4] J.-E. Ducret, S. Bastiani, et al., Nucl. Instr. Meth. A 720, 141 (2013)
[5] Y. Cauchois, J. de Physique 3, 320 (1932)
[6] J.F. Seely, et al., Applied Optics 47, 2767 (2008)
[7] I. Thfoin, Ch. Reverdin, et al., Rev. Sci. Instrum. 10, 85(11) (2014)
[8] G. Boutoux, et al., Rev. Sci. Instrum. accepted (2016)
[9] G. Boutoux, N. Rabhi, et al., Rev. Sci. Instrum. 86, 113304 (2015)
[10] Y. Sentoku, A. Kemp, J. Comput. Phys. 227, 6846-6861 (2008)
[11] S. Agostinelli et al., Nucl. Instr. Meth. A 506, 250 (2003)
[11] A. Poye, S. Hulin, et al., Phys. Rev. E 91, 043106 (2015)
[12] A. Poye, J.-L. Dubois, et al., Phys. Rev. E 92, 043107 (2015)

Status of the NICA project at JINR, Dubna

G.Trubnikov
JINR, Dubna, 141980, J.Curie, 6, Russia

Introduction

The NICA (Nuclotron-based Ion Collider fAcility) is an accelerator and experimental complex (Fig. 1) under realization at the Joint Institute for Nuclear Research (JINR) in Dubna. The main goals of the project are study of hot and dense baryonic matter at the extremeconditions in heavy ion collisions, and investigation of nucleon spin structure in the collisions of polarized p and d. The NICA includes an existing facility (an injector comprising set of particle sources (PS) and linac LU-20, Nuclotron superconducting (SC) proton synchrotron providing acceleration of completely stripped 197Au79+ ions up to the energy of 4.5 GeV/u and protons up to the energy of 12.6 GeV, and area for fixed target experiments) and those to be constructed (new injector consisting of ESIS-type ion source providing 197Au31+ ions, and heavy ion linac (HILAc) accelerating ions at A/q >8 up to the energy of 3 MeV/u, Booster-synchrotron housed inside the Synchrophasotron yoke accelerating 197Au31+ ions up to the energy of 600 MeV/u, and two SC collider rings providing gold-gold collisions at the energy range √sNN = 4 -11 GeV and p x pcollisions at the energy up to √sNN = 27 GeV. The NICA collider will provide average luminosity L=10^27 cm^-2s^-1 and 10^32 cm^-2s^-1 for gold-gold and proton-proton collisions, respectively.

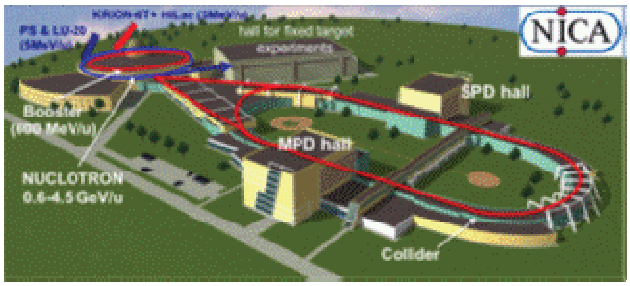

Fig. 1. The NICA complex: existing facility (blue) and to be constructed one (red) The complex comprises 2 collider experiments, MultiPurpose Detector (MPD) (Fig. 2 up) for heavy ion collisions, and Spin Physics Detector (SPD) (under design) to study collisons of polarized p and d, and a fixed target experiment – Baryonic Matter at Nuclotron (BM@N) (Fig. 2, bottom).

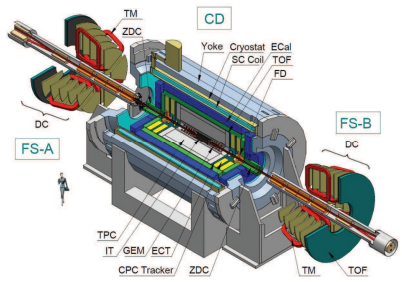

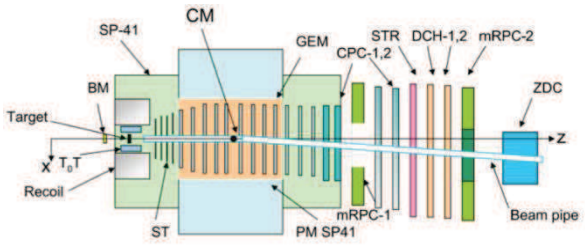

Fig. 2. The MPD experimental set-up (up) and BM@N experimental set-up (bottom)

Experimental goals

The physic program in heavy ion collisions is aimed to explore the QCD phase diagram. The NICA energy covers the region of maximum baryonic density in phase transition. The strategy is to perform energy and system size scan with an emphasis to the production of hadrons and dileptons, event-by-event fluctuations and correlations. The spin physics program is under development. It is aimed to study nucleon spin structure exploring the Drell-Yan mechanism with 8 parton distribution functions (PDFs) at leading twist. More detailed information on the NICA experimental program is available at http://nica.jinr.ru.

The MPD experiment is designed as a 4π spectrometer detecting charged hadrons, electrons and photons in heavy-ion collisions. The setup provides a precise 3D tracking and a high performance particle identification. The event rate of minimum bias interactions is ~ 7 kHz, and charged particle multiplicity exceed 1000 in central Au+Au collisions at √sNN =11 GeV. The setup includes Central Detector (CD) covering interval |η|<2 and two forward spectrometers (FSA, B) for 2 < |η|< 3 (optional). The CD is 9 m long and 6.6 m in diameter and will be constructed in two stages. At the first stage (2019) MPD will comprise a superconducting solenoid, Time- Projection Chamber (TPC), barrel Time-Of-Flight system (TOF), Electromagnetic Calorimeter (ECal), Zero-Degree Calorimeter (ZDC) and Fast Forward Detector (FFD). Feasibility study was performed using the MPDRoot comprising interfaces to event generators, Geant, detector response simulation and reconstruction algorithms.

The BM@N set-up combines high precision track measurements (12 planes of GEMs, 2 drift chambers and 4 planes of silicon strip detectors at the second stage) with time-of-flight information (two sets of RPC's) for particle identification and total energy measurements (ZDC) for the centrality definition. The T0 detector will provide a start signal for the RPC's and trigger. The Xe beam will be available in 2017 while the Au beam with intensity of 10^7 per second in planned in 2019. The first technical

run of the BM@N was performed with deuteron and carbon beams in 2015.

The project status

Design and construction of the the new facility at the JINR is in progress. The NICA will provide competitive reasearch program complementary to the BNL, CERN and planned at FAIR.

For low-mass lepton-pairs, which are critical to address medium modifications of hadrons and questions of chiral symmetry, and open charm and J/psi production, moderately significant measurements will be possible, complementing the much higher statistics experiments possible at CERN and FAIR. Also foreseen are applied physics, biology, material science and energy generation studies.

NICA project has a special status in Russian Federation and had been included to list of megascience projects. This is one of two from the list, which is already supported by State and is under active realization. JINR has made important efforts to reach beyond its traditional community. The construction of NICA and the FAIR/GSI accelerators is in fact tightly linked via a strong collaboration between GSI and JINR on the FAIR project and there is potential for a similar close detector collaboration (MPD/SPD/BM@NICA). The synergy and complementarity of the NICA and of the ESFRI Landmark FAIR and to some extent of the ESFRI Landmark SPIRAL2 make it very desirable to develop a joint coordinated effort for identifying a strong programme and for offering the best opportunities to international nuclear experimental physics. To this end ESFRI encourages these Ris both to work closely together and to pay special attention to developing NICA as a Global Research Infrastructure concept.

Now 16 institutions from Russia and 79 institutions from 24 foreign countries officially participate in the NICA project. In December 2015 China joined the project with signing protocol of understanding with JINR concerning China participation in NICA. During last 2 years, the following milestones had been achieved while NICA construction:

- in September 2015 JINR signed a general Contract for NICA civil construction with Strabag company from Europe. Civil construction works began in October 2015, the schedule is planned to commission the complex in mid. 2019;
- New unique ion sources had been designed, constrcued and commissioned with beam at Nuclotron: superconducting heavy ion source (ESIS type) had been achieved 5x108 Au ions per pulse at 50 Hz rate. Source for polarized atoms had been constructed and commissioned with 1010 polirized deuterons per pulse;
- New linear accelerator (RFQ type) for light ions had been commissioned as foreinjector for LU-20 linac. Performed in cooperation with ITEP and MEPhI. Required beam parameters had been achieved (10 mA, 170 keV);
- New heavy ion injector (2x10^9 Au ions, 3.2 MeV/u) in collaboration with IAP and Bevatech from Frankfurt had been constructed, Commissioning phase is in final stage.
- dedicated large-scale facility for assembly and cold 4K) tests of cuperconduting magnets for NICA booster and collider and also for SIS100 (FAIR) quadrupole units had been commissioned. Serial production of all types of magnets had been started in 2016. Construction of vacuum chambers, thermal shields, cryostats, pick-up station and other diagnostics is in active phase;
- NICA cryogenic plant is under commissioning it had been modernized from cooling power 4kW@4K up to 8 kW@4K to produce 2000 lHe l/h.
- JINR signed the contract for design and production of the MPD superconducting solenoid and its cold mass (whole assembly) with European producer. Parameters of the solenoid are very challenging: 0.66 Tesla field on 4.5m diameter at 5x10^-4 field homogeneity;
- Dedicated clean rooms and high-tech facility constructed and commissioned for serial production of: microstrip detectors (silicon detectors for Inner Tracker of MPD), time-of-flight detectors and time-projection chambers. Prototyping had been completed. Construction of detectors had been started;
- BM@N setup is under commissioning, dedicated beam line and diagnostics had been constructed. 3 new beam lines and dedicated research facilities for innovative tasks are under design and construction.

Recent Results with Short-Pulse, Compressed Ion Beams at the Neutralized Drift Compression Experiment*

P.A. Seidl[1#], J.J. Barnard[2], R.C. Davidson[3], A. Friedman[2], E.P. Gilson[3], D. Grote[2], Q. Ji[1], I.D. Kaganovich[3], A. Persaud[1], W.L. Waldron[1] and T. Schenkel[1,]
[1]Lawrence Berkeley National Laboratory, Berkeley, California, USA
[2]Lawrence Livermore National Laboratory, Livermore, California, USA
[3] Princeton Plasma Physics Laboratory, Princeton, New Jersey, USA

Intense ion pulses in the MeV range enable new studies of the properties of matter ranging from low intensity (negligible heating, but active collective effects due to proximate ion trajectories in time and space), to high intensity where the target may be heated to the few-eV range. By choosing the ion mass and kinetic energy to be near the Bragg peak, dE/dx is maximized and a thin target may be heated with high uniformity [1], thus enabling high-energy density physics (HEDP) experiments in the warm dense matter (WDM) regime. The Neutralized Drift Compression Experiment (NDCX-II), an induction accelerator with plasma neutralization at the exit to counteract the high space charge, was designed with this motivation [2,3]. Intense ion beams from induction accelerators have complementary advantages (e.g., benign radiation environment and low energy spread) compared to beams derived from laser-plasma acceleration [4].

The first target experiments used beam pulses of Li^+ accelerated to 1.2 MeV and focused to a beam radius, r ≅ 1mm and duration of 2 ns FWHM (peak current ~18 A/cm^2). These conditions were used, for example, to characterize dose rate effects on the ionoluminescence of yttrium aluminium perovskite (YAP). These and other results are described in Refs. [5,6].

Since last year's report, we have installed and used a new multicusp, multiple-aperture plasma ion source [7,8]. The source can generate high purity ion beams of, for example, protons, helium, neon and argon. To date, we have used it solely for the generation of He^+ ions, where the source injects significantly greater charge than did the lithium ion source. Furthermore, helium at about 1 MeV is nearly ideal for highly uniform volumetric energy deposition, because particles enter thin targets slightly above the Bragg peak energy and exit below it, leading to energy loss in the target that is uniform within several percent.

In Fig. 1 the He^+ beam distribution is peaked with 80% of the integrated charge within a radius of 1.2 mm. Warp PIC simulations indicate that the focused charge is expected to ultimately reach over 30 nC per pulse while maintaining a small focal spot size and a nanosecond bunch duration, since much more charge is now available from the new helium source. Toward that goal, we have to date measured 15 nC ($9x10^{10}$ ions/pulse) in a few-mm focal spot with the He^+ beam, in a pulse duration of ≈50 ns and 3 ns (FWHM) pulses with 2 nC. By model-derived tuning of the acceleration and bunching waveforms and the solenoid field strengths, our near-term objective is to achieve a pulse duration of 1-2 ns with higher corresponding dose rates of ≥10 nC/ns/mm^2.

Presently, we are carrying out radiation effects experiments and are probing aspects of intense beam and beam-plasma physics. We are also exploring opportunities for materials processing with intense, pulsed ion beams. Two examples areas are color center formation in diamond and tailoring of the spin properties of doped silicon [9, 10]. Here, conventional thermal annealing of specially prepared materials usually occurs on a timescale of milliseconds to minutes. With NDCX-II, we see an opportunity to excite materials with intense ion pulses on a nanosecond timescale followed by rapid quenching in order to stabilize novel phases or to optimize spin properties.

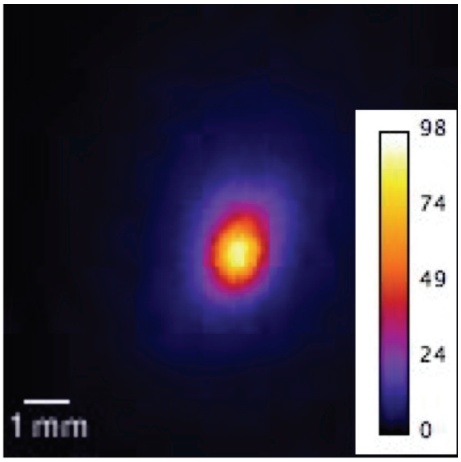

Figure 1: The transverse (x, y) distribution of the He^+ beam is shown with a color calibration bar indicating the relative intensity. With the new helium source, NDCX-II can provide 1-MeV helium ion beams with an energy deposition greater than 0.7 joules/cm^2 (~40 A/cm^2).

References

[1] L. R. Grisham 2004 *Phys. Plasmas* **11** 5727
[2] J. J. Barnard, et al. 2014 *Nucl. Inst. Meth.* **A733** 45
[3] W.L. Waldron, et al. 2014 *Nucl. Inst. Meth.* **A733**
[4] S. Busold, et al. 2015 *Scientific Reports* 5, 12459
[5] P.A. Seidl, et al. 2015 *Nucl. Inst. Meth.* **A800** 98–103
[6] A. Persaud, et al., 2015 *Phys. Procedia* **66** 604
[7] Q. Ji, et al. 2016 *Rev. Sci. Inst.* **87** 02B707
[8] P.A. Seidl et al., http://arxiv.org/abs/1601.01732
[9] J. Schwartz, et al. 2014 *J. Appl. Phys*. **116**, 214107
[10] A. Bienfait, et al. 2016 *Nature* **531** ,74

* This work was supported by the Office of Science of the US Department of Energy under contract no. DE-AC02–05CH11231.
#PASeidl@lbl.gov

Recent Progress of the Kumgang Laser : a High-Power, High-Repetition Rate Beam Combination Laser*

Hong Jin Kong[1,#], Sangwoo Park[1], Seongwoo Cha[1], Hwihyeong Lee[1], Jungsuk Oh[1], Kilsung Churn[1], Soungwoong Choi[2], Bong Ju Lee[2], and Jom Sool Kim[3]

[1]KAIST, Daejeon, Republic of Korea; [2]Handong Global University, Pohang, Republic of Korea; [3]Laser Spectronix, Seoul, Republic of Korea.

In this article we report the current status of the Kumgang laser: 4 kW coherent beam combination laser combining four 1 kW beams using self-phase controlled stimulated Brillouin scattering phase conjugate mirrors (SC-SBS-PCM).

A coherent beam combining is one of the most promising techniques to achieve a high energy and a high repetition rate laser. It has been demonstrated experimentally that the coherent beam combination using self-phase-controlled SBS-PCMs (SC-SBS-PCM) is the simplest coherent beam combination method [1-2]. For an average output power of a kW range, the experimental verification of coherent beam combination is now underway by the Kumgang laser [3-4]. The Kumgang laser system is a coherent four beam combination laser of 1 kW modules using SC-SBS-PCM.

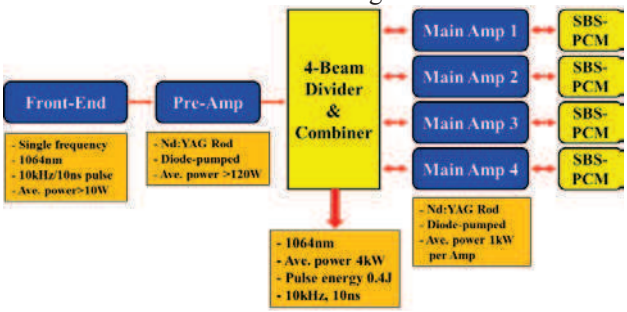

Figure 1: the schematic diagram of the Kumgang laser.

Figure 1 shows the schematic diagram of the Kumgang laser system. The front end (FE) consists of a CW laser-diode master oscillator, an acousto-optic modulator (AOM) for 10 kHz pulse generation, Yb doped fiber-based amplifiers, and a regenerative amplifier. The FE produces a single-frequency seed beam of 1064 nm at a repetition rate 10 kHz. The average output power of the FE is 11 W (1.1mJ@10kHz/8.5ns), and the M^2 of the output beam of the FE is 1.31.

The seed laser beam from the FE is amplified by the diode pumped Nd:YAG rod amplifiers in the pre-amplifier (PA) from 11 W (1.1mJ@10kHz/8.5ns) to 128 W (12.8mJ @10kHz/8.5ns), and the M^2 of the output beam of the PA is 1.8.

After the double pass amplification process by the PA, the laser beam will be divided into four sub-beams by a coherent beam divider/combiner for its main amplification process. The wave-front distortion of each sub-beam can be compensated for by SBS-PCMs.

The main amplifier stage is composed of a diode-pumped Nd:YAG rod amplifier chain and an SBS-PCM.

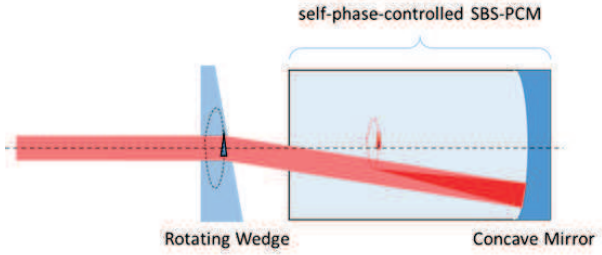

Figure 2: The rotating wedge self-phase-controlled SBS-PCM.

For high average power operation of the SBS-PCM, thermal effect at a focus point should be released to keep high reflectivity [5]. In Kumgang laser, the rotating wedge is used to reduce the thermal effect at its focal point. Figure 2 shows the schematic diagram of the rotating wedge self-phase-controlled SBS-PCM (RW-SC-SBS-PCM). The input laser beam is refracted by the rotating wedge, and reflected by the self-phase-controlled SBS-PCM.

After the reflection at the SBS-PCM and after passing through the main amplifier module (MA) again, the sub-beams will be combined by the coherent beam divider/combiner. The MA module can amplifies the laser beam from 128 W (12.8mJ@10kHz/8.5ns) to 640 W (64mJ @10 kHz/8.5ns) for single-pass amplification. In this case, the M^2 of the output beam is 1.9. The reflectivity of the SBS-PCM is 56.9% at the input power of 500 W (50 mJ@10kHz/8.5ns). The coherent beam divider/combiner and main amplifier stage will be completed in this year.

References

[1] H. J. Kong, J. W. Yoon, J. S. Shin, D. H. Beak, and B. J. Lee, Laser and Particle Beams 24, 519-523 (2006).
[2] J. S. Shin, S. Park, H. J. Kong and J. W. Yoon, Applied Physics Letters 96, 131116 (2010).
[3] H. J. Kong, S. Park, S. Cha, and J. S. Kim, Physica Status Solidi (c) 10(6), 962-966(2013).
[4] H. J. Kong, S. Park, S. Cha, H. Ahn, H. Lee, J. Oh, B. J. Lee, S. Choi, and J. S. Kim, Optical Materials Express, 4(12), 2551–2558 (2014).
[5] H. Yoshida, A. Ohkubo, H. Fujitah, and M. Nakatsuka, Review of Laser Engineering 29(2), 109–114 (2001).

* Work supported by Republic of Korea, Agency for Defense "Dual-Use Technology Program" (UM12012RD1)
#hjkong@kaist.ac.kr

Status and prospects of large-scale accelerator projects and high-energy density physics program in Korea *

Moses Chung †
Ulsan National Institute of Science and Technology, Ulsan 689-798, Korea

Status of Accelerator Projects in Korea

Several large-scale accelerator facilities are operational or under construction in Korea, such as Korea Multi-purpose Accelerator Complex (KOMAC) in Gyeongju area, Synchrotron Light Source (PLS-II) and X-ray Free Electron Laser (PAL-XFEL) in Pohang area, Rare Isotope Science Project (RISP) in Daejeon area, and Korea Heavy Ion Medical Accelerator (KHIMA) in Gijang area. These accelerator projects open up new opportunities in basic science researches in Korea, and can also provide excellent platforms for various accelerator R&D activities.

The KOMAC project [1] started in 2002 and completed the linac commissioning in 2013. The KOMAC linac consists of a 50-keV proton injector, a 3-MeV four-vane RFQ, and a 100-MeV drift tube linac (DTL). The RF frequency is 350 MHz and the maximum beam pulse current is 20 mA. So far, two beamlines are available for users. One is located at the end of the 20 MeV DTL and the other at the end of the 100 MeV DTL.

The PAL-XFEL project [2] started in 2011 and is expected to be operational in 2016. The PAL- XFEL will have a dog-leg branch line at 3-GeV point of the linac for two soft X-ray undulator lines, and three hard X-ray undulator lines at the end of 10-GeV linac. A 1.6-cell type photocathode RF gun is used to inject 0.2 nC of electron beam pulse with 120 Hz repetition rate. The main accelerating structure is S-band normal conducting linac.

The RISP project [3] will be composed of a 70 kW proton cyclotron as a low-power ISOL driver, an 18 MeV/u linac for ISOL post-accelerator, and a 200 MeV/u main linac for high-power ISOL and IFF driver. The main driver linac named RAON will accelerate all masses up to Uranium with beam power up to 400 kW. To maximize the average currents of the primary beam on target, continuous wave (CW) operation is preferred, and therefore superconducting RF (SCRF) technology has been adopted for the linac design.

High-Energy Density Physics Program

No concrete high-energy density physics (HEDP) program has been established within the scope of those accelerator projects yet. However, several long-term accelerator R&D programs revelent to the HEDP can be readily pursued. For example, the KOMAC linac can be used to study beam halo dynamics and its diagnostics, which are critical for future high-intensity accelerators. Using the intense short-pulse X-ray available from the PAL-XFEL, warm dense matter (WDM) physics relevant to astrophysical phenomena can be investigated. For the RISP, basic studies on the beam-gas-plasma interactions will play key roles in many beam-line components, such as ECR ion source, electron beam ion source, RF cooler, and gas catcher.

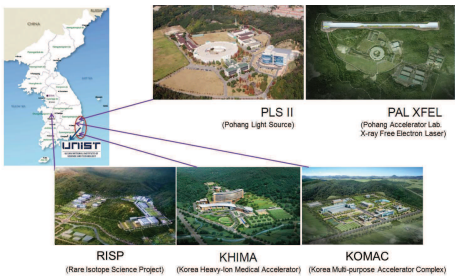

Figure 1: Large scale accelerator projects in Korea.

For the laser-based HEDP researches, several university-based programs are underway. The Korea Advanced Institute of Science and Technology (KAIST) group is developing coherent beam combination technology, which would enable a laser system with both high-repetition rate and high power. The Handong Global University (HGU) group is developing a concept for the fusion-fission hybrid reactor utilizing high-power and high-repetition rate lasers. The Gwangju Institute of Science and Technology (GIST) recently hosted IBS center for relativistic laser science [4]. Relativistic laser-matter interactions will be explored using petawatt lasers.

In the Ulsan National Institute of Science and Technology (UNIST), a laboratory astrophysics group has been recently formed to investigate the matter in extreme conditions using accelerator and laser facilities in Korea. High energy astrophysical phenomena in clusters of galaxies, particularly those involving shock waves, turbulence, magnetic fields, and cosmic rays in high temperature and low beta plasma will be studied.

References

[1] KOMAC web page, http://www.komac.re.kr.

[2] PAL web page, http://pal.postech.ac.kr.

[3] RISP web page, http://www.risp.re.kr.

[4] CoReLs web page, http://corels.ibs.re.kr.

* Work supported by the 2014 Research Fund (1.140075.01) of UNIST (Ulsan National Institute of Science and Technology)

† mchung@unist.ac.kr

High Energy Density Research at the future project HIAF in China

Y. Zhao[1,2,#], R. Cheng[1*], Y. Wang[1], X. Zhou[1], Y. Lei[1], Y. Sun[1], G. Xu[1], J. Ren[1], and G. Xiao[1]
[1]XJTU, Xi'an, China, [2]IMP, Lanzhou, China

A large scale scientific research platform, named the High Intensity heavy-ion Accelerator Facility (HIAF), was proposed in light of the trend and development in nuclear physics and the associated high energy heavy ion research fields. HIAF is one of the 16 approved national projects for basic sciences and technologies as the 12th five-year-plan in China; it will be a laboratory open to the outside world, similar to CSR which was built as the 9th five-year-plan in China [1]. The HIAF complex, as shown in Fig. 1, includes a SECR (Superconductive Electronic Cyclotron Resonance) ion source, an ion linear accelerator (i-Linac), a Booster Ring (BRing), a Spectrometer Ring (SRing), a Compression Ring (CRing) and about 8 experimental terminals.

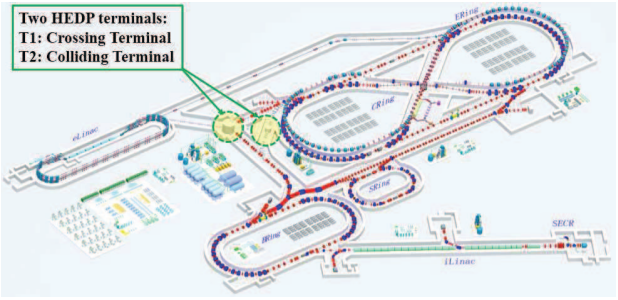

Figure 1: Layout of the HIAF complex and the two terminals for HEDP research

Since both BRing and CRing can produce high-energy and high-intensity ion beams (please see Fig. 2), two terminals for HEDP (High energy density physics) research were proposed at HIAF, one for crossing (T1) and the other for colliding (T2) of the beams from BRing and CRing at the target area.

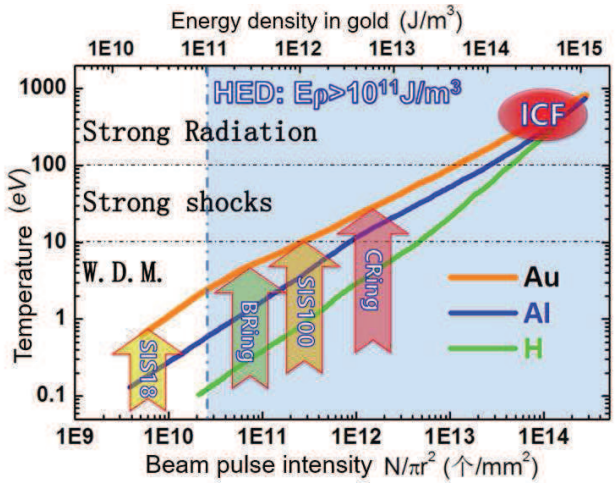

Figure 2, the temperature and energy density cuold be achieved with the beam from diffferenct accelerators.

However, mainly due to the budget limitation and technique challenges, CRing will NOT be included in the first stage of the HIAF project.

The key parameters related to HEDP research at HIAF and other advance heavy ion drivers is listed in Table 1, where E_0, N, E_{total}, S_f, t and $E\rho$ is the particle energy, the beam intensity (unit, ppp), the total beam energy per pulse, FWHM of the beam spot, the pulse duration and energy density in a lead target (J/m^3), respectively.

Table 1. Key parameters related to HEDP research at HIAF and other heavy ion drivers (for uranium beam).

	SIS-18	FAIR(Ph-I)	HIAF (Ph-I)[a]
E_0	0.4GeV/u	1 GeV/u	1.1 GeV/u
N	4×10^9	4×10^{11}	$1\text{-}3\times10^{11}$
E_{total}	0.06 kJ	15 kJ	4-12kJ
S_f	~1 mm	~1 mm	1 mm
t	130 ns	50 ns	130-400 ns
E_ρ	2×10^{10}	2.4×10^{12}	$6\text{-}18\times10^{11}$

[a] The upper limit may rely on the budgets of HIAF, and Ph-I means that we take the beam parameters of BRing.

References

[1] Y. Zhao, et al, High energy density physics research at IMP, Lanzhou, China. High Power Laser Science and Engineering, 2, (2014) e39 doi:10.1017/hpl.2014.44.

[2] ZHAO Yong-Tao , XIAO Guo-Qing and LI Fu-Li. The physics of inertial confinement fusion based on modern accelerators: status and perspectives. Physics, 2016, 45(2): 98-107.

[3] J. Ren et al, High energy density state generated by intense heavy ion beams from HIAF, under preparing

zhaoyongtao@xjtu.edu.cn
* chengrui@impcas.ac.cn

2 Interaction Experiments with Ion - and Laser Beams

Energy Deposition and Excitation of Wakefield in Case of 100keV/u Ion Beam Passing through a Plasma Target*

Y.Zhao[1,2#], R.Cheng[2#], X.Zhou[2], Y.Wang[2], Y.Lei[2], S.Liu[2], H.Peng[2], J.Deng[2], G. Xu[2], J. Ren[1,2], S.Savin[3],R.Gavrilin[3], A.Golubev[3],D.Hoffmann[4], G.Xiao[2]

[1]XJTU, Xi'an, [2]IMP, Lanzhou, [3]ITEP, Moscow, [4]TUD, Darmstadt

Recently our team investigated the energy deposition and excitation of wakefield in case of hundreds keV proton/helium ion beams passing a gas-discharged plasma target. The plasma target was produced by igniting an electric discharge of hydrogen gas in two-collinear quartz tubes, each of 5mm in diameter and 78mm in length, the electrical current even up to kA will flow in two opposite directions in either of the two quartz tubes. This device could produce the hydrogen plasma with the line-integrated free electron density of up to $10^{17\text{-}18}$ /cm^2, and with the temperature of around 2eV when the discharge current was reaching the maximum, as shown in figure1.

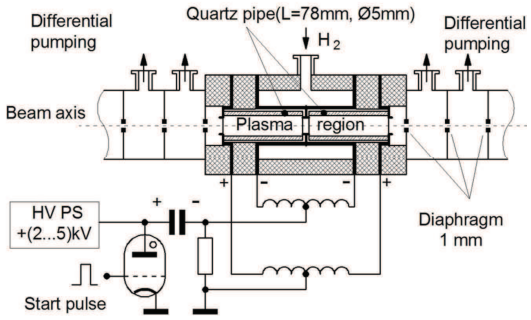

Figure 1 the scheme of the plasma target

The experiments were performed at the HV-ECR platform at IMP (see details in ref [1, 2]).

As an example. figure 1 shows the measured beam after 100keV proton beam penetrating the hydrogen plasma target (with initial gas pressure of 3mbar, and discharging high-Voltage of 3kV) in terms of time after discharging. Enhanced energy loss comparing to that for neutral gases has been observed. Moreover, we found that the proton beam was strongly focused while energy of the focused beams is uniform. We carried out some PIC simulations, which suggests that the wake-field could form a self-modulated, periodic(pulsed), focusing, collision-less tunnel. More details will be reported later [3,4].

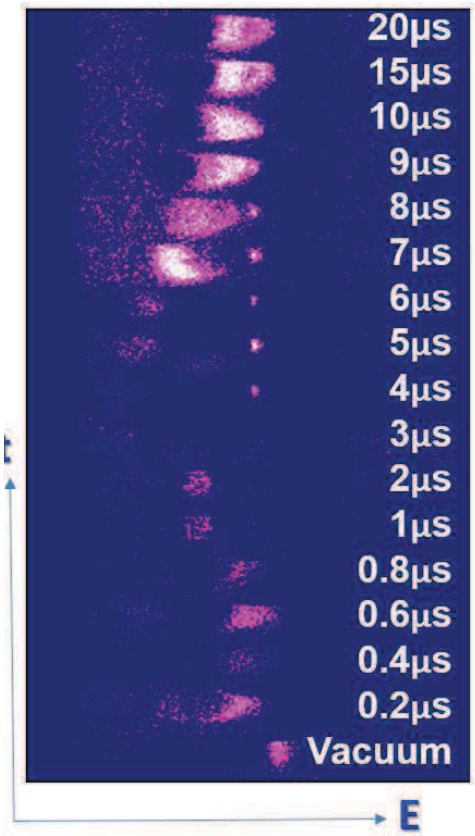

Figure 1 the measured beam after 100keV proton beam penetrating the hydrogen plasma target.

References

[1] Zhao Y. et al. 2012 Laser and Particle Beams 30 679–706

[2] Cheng R. et al. 2013 Phys. Scr. T156 014074

[3] R. Cheng et al 2016 Measurement of the energy loss by slow protons in a plasma target, to be submitted

[4] Y. Zhao, et al, Excitation of Plasma Wakefield by 100keV/u proton Beam, under preparing

* Work supported by NSFC (11275241, 11375034 and U1532263)

Corresponding authors: zhaoyongtao@xjtu.edu.cn, chengrui@impcas.ac.cn

Development of experimental setup for energy loss measurements in gas-discharge plasma on TIPr accelerator in ITEP

R.O Gavrilin[1], E.R Khabibullina[1], S.A. Visotskiy[1], A.V. Kantsyrev[1], I.V. Roudskoy[1], A.A. Golubev[1], R.P. Kuibeda[1], B.B. Chalykh[1], T.V. Kulevoy[1], A.P. Kuznetsov[2], R. Cheng[3], Y. Zhao[3]*

[1]SSC RF ITEP of NCR "Kurchatov Institute", Moscow, Russia; [2]National Research Nuclear University MEPhI, Moscow, Russia; [3]Institute of Modern Physics, CAS, Lanzhou, China

Introduction

The energy losses of ion beam in plasmas remains a key question for high energy density physics during the last several decades. To investigate this problem in the low energy range of projectile heavy ions (40- 500 keV/n) a gas-discharge plasma target, which can be integrated into high vacuum system of beam lines, was developed [1] and diagnosed [2] in ITEP (see fig. 1)

Experimental setup at IMP

The first experements were performed on linear accelerator in collaboration with Institute of Modern Physics (IMP CAS, Lanzhou, China).

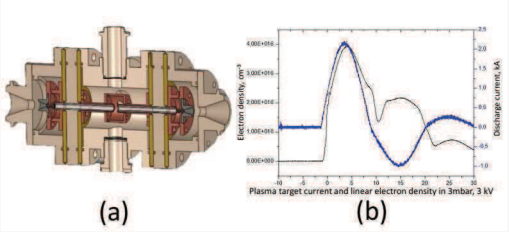

Fig.1 (a) Gas-discharge plasma target, (b) Current and linear electron density curve example.

The scheme of experimental setup at IMP presented in fig. 2. The measurements of energy losses were carried out using bending magnet and MCP+CCD detector. Energy losses of projectile ions H^{+}, He^{+1},He^{+2}, O^{+4},O^{+5} with energies 100-500 keV/q in cold gas and plasma were obtained [3].

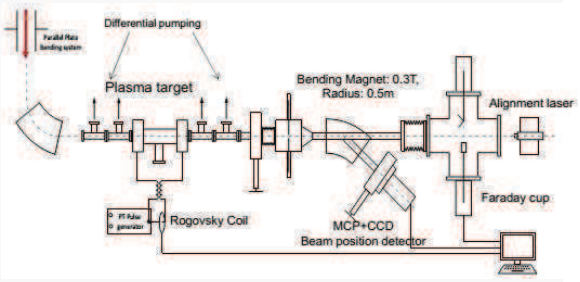

Fig. 2 Experimental setup scheme.

Since the beam current after passing through plasma target is quite low (about several nA) it is difficult to achieve high precision. The long time intergation method with several beam shots was used to achieve reasonable accuracy. The sample of experimental results are shown in fig.3.

New experimental setup at TIPr accelerator

To increase the accuracy of the energy loss measureents and to use more heavy ions as projectiles

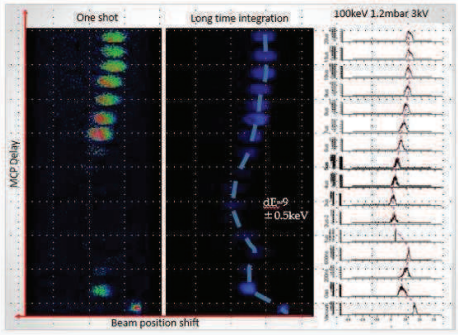

Fig. 3. Example of beam shots integration method.

a new experimental setup (see fig. 4) on a beam line of the linear accelerator TIPr at ITEP is under construction now. It will provide measurement of energy loses of heavy ions (Al^{+2} Cu^{+2},Cu^{+3},Ag^{+2}) with energies 100kev/n in the gas-discharge plasma target. The time of flight (TOF) method will be used for such experiments. The FC detector, fast scintillator with PMT and FCT detectors will be used to measure the micro-bunch structure of the beam (27 MHz). TOF method may provide better quality of energy loss measurement. In addition a bending magnet with scintillator and CCD camera is planned to use for the measurements of charge state of particles after its interaction with plasma.

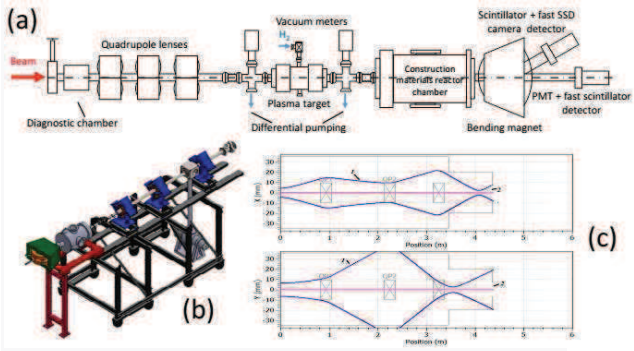

Fig.4 (a) Scheme of experimental setup at TIPr accelerator; (b) Modeling of experimental setup; (c) Beam dynamics calculation.

References

[1] G.E. Belyaev et al. Phys. Rev. E 1996, v.53, N3, pp.2701-2707

[2] A. P. Kuznetsov et al. Plasma Physics Reports 03/2013; 39(3)

[3] Rui Cheng et al. Journal of Physics Conference Series 04/2014;488(9):092005.

Work supported by RFBR grant № 15-02-08963_a

roman_gavrilin@mail.ru

X-ray Imaging of Shock Waves Generated by Intense Pulsed Ion Beams*

G. E. Remnev[1#], D. H. H. Hoffman[2], A. V. Stepanov[1], S.K. Pavlov[1], M. V. Zhuravlev[1]
[1]TPU, Tomsk, Russia; [2]MEPhI, Moscow, Russia.

In the report, we present the concept of the experiments for research of the shock wave generation and propagation processes in solids under the impact of intense pulsed ion beams.X-ray radiographic measurments are used for diagnosis of shock waves.

Introduction

Design of the intense pulsed ion beams (IPIB) sources was initiated by researches in the inertial confinement fusion direction[1]. In succeeding years, IPIB have been further developed for material modification [2,3]. For these purposes, IPIB with the following parameters are used: 100-500 keV ion energy, 50-500 ns pulse duration, 5-500 A/cm^{2}current density. Such impact of a concentrated flow of energy on the surface of solid causes the formation of thermomechanical compression waves, and at an energy density above the ablation threshold - the formation of the recoil pulse propagating deeper into the target material and, under certain conditions, forming a shock wave [4]. The study of the impact of these processes on phase transformations and mass transfer in the target at the IPIB processing is important for the further development of this treatment method.

The experimental setup

The experimental setup shown in Fig. 1is supposed to be used to study the shock wave generation by IPIB. Shock-wave compression of the sample is carried out by the IPIB generated by TEMP accelerator [5, 6] with the following parameters: accelerating voltage - up to 250 kV, pulse duration - 100 ns (at half-height accelerating voltage), beam composition - carbon ions (C^+, C^{n+}) 85% and protons 15%, energy density at the sample surface - up to 5 J/cm^2. The density of matter is determined by transmission X-ray radiography [7]. X-ray source is an electron gun with a tungsten anode (target) generating bremsstrahlung spectrum. The parameters of the electron gun: 300 kV accelerating voltage, 10 ns pulse duration (at half-height accelerating voltage). Timing unit is used for the synchronization of the pulse generation by ion and electron accelerators with a certain pause (jitter is 10 ns). This approach enables to obtain the image of the distribution of the density of matter in the sample at different times with a spatial distribution ~ 20-30 μm (depending of the material of sample).

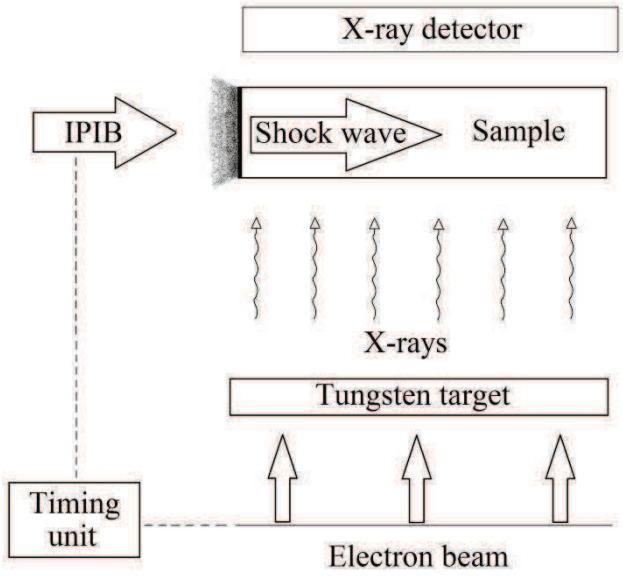

Figure 1. The experimental setup.

Thus, the dynamics of the formation and propagation of shock wave in the solid will be studied. Subsequently, this technique is supposed to be used for the study of the parameters of plasma formed on the surface of solid by IPIB.

References

[1] S. Humphries, Nucl. Fusion 20 (1980) 1549.
[2] H. A. Davis, G. E. Remnev,R. W. Stinnett, K. Yatsui, MRS Bull. 21 (1996) 58.
[3] T. J. Renk, P. P. Provencio, S.V. Prasad, S. V. Shlapakovski, A. V. Petrov, K. Yatsui, W. Jiang and H. Suematsu, Proc. IEEE 92 (2004) 1057.
[4] S. A. Chistjakov, A. D. Pogrebnjak and G. E. Remnev, Nucl. Instr. Meth. Phys. Res. B42 (1989) 342.
[5] I. F. Isakov, V. N. Kolodii, M. S. Opekunov, V. M. Mat-vienko, S. A. Pechenkin, G. E. Remnev and Yu. P. Usov, Vacuum 42 (1991) 159.
[6] V. S. Lopatin, G. E. Remnev, E. G. Furman, V. A. Makeev, A. V. Stepanov, Instrum. Exp. Tech. 47 (2004) 484.
[7] B. A. Hammel, D. Griswold, O. L. Landen, T. S. Perry, B. A. Remington, P. L. Miller, T. A. Peyser and J. D. Kilkenny, Phys. Fluids B 5 (1993) 2259.

*Work supported by Russian Science Foundation, Grant 14-19-00439.
#remnev@hvd.tpu.ru

Warm Dense Matter Created by a Plasma-Filled Rod-Pinch Diode *

B. V. Weber[1], T. A. Mehlhorn[1], S. Richardson[1], J. W. Schumer[1],
J. P. Apruzese[2], D. Mosher[2], N. Pereira[3],
[1]Naval Research Laboratory, Washington, DC, USA; [2] consultant to NRL through Engility, Corp., Chantilly, VA, U.S.A,
[3]Ecopulse, Inc. Alexandria, VA, USA.

High energy-density plasma (HEDP) is created using a plasma-filled rod pinch diode (PFRP) [1] on the Gamble II pulsed-power generator. HEDP is produced by a 1-2 MeV, 500 kA electron beam that deposits energy at the end of a tapered tungsten rod. The plasma pressure is estimated to reach 16 Mb in about 5 ns, before rapid expansion decreases the energy density.

Recent measurements [2] show that the temperature peaks at about 30 eV at the time of maximum energy density, and that the time-averaged ionization is about +17, similar to MHD model predictions [3]. The plasma mass distribution is inferred from x-ray distribution measurements. The time-dependent mass distribution is used to calculate the plasma pressure. These measurements indicate the HEDP is strongly coupled (Γ = 35) with peak pressure (16 Mb) about 7 times greater than $n_e kT$.

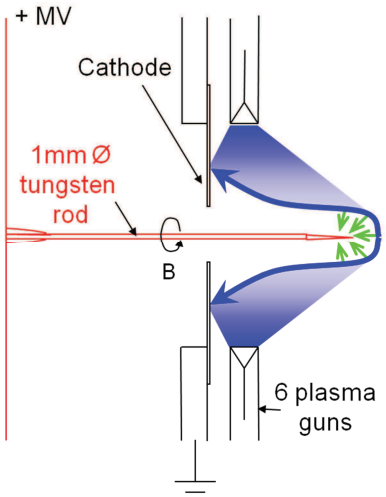

Figure 1: Plasma-Filled Rod Pinch setup.

Figure 1 illustrates the PFRP technique. An injected plasma (blue in Fig. 1) connects the grounded cathode to the tungsten rod anode prior to firing the generator. The generator current increases to 500 kA while the plasma is distorted and displaced toward the rod tip. As the current increases further, a 2 MeV electron beam forms that bombards the tip of the tapered rod (green arrows in Fig. 1). The strong self-magnetic field confines the electrons to the tip region, rapidly heating the tungsten and creating warm dense matter conditions.

The plasma pressure is inferred from time-dependent measurements of the x-ray distribution in the vertical and axial directions. These distributions are fit by Gaussians functions with 1/e widths a_y and a_z. The mass per unit length, μ, is determined from the initial rod tip shape and a_z. Newton's second law is formulated for a radially-expanding Gaussian with time dependent mass, giving:

$$P_0(cgs) = \frac{1}{2\pi a_y}\left(\mu\frac{d^2 a_y}{dt^2} + \frac{d\mu}{dt}\frac{da_y}{dt}\right) + \frac{I^2(A)}{200\pi a_y{}^2}$$

where P_0 is the pressure on axis. Figure 2 shows that the magnetic pressure term is negligible compared with the $d(mv)/dt$ terms.

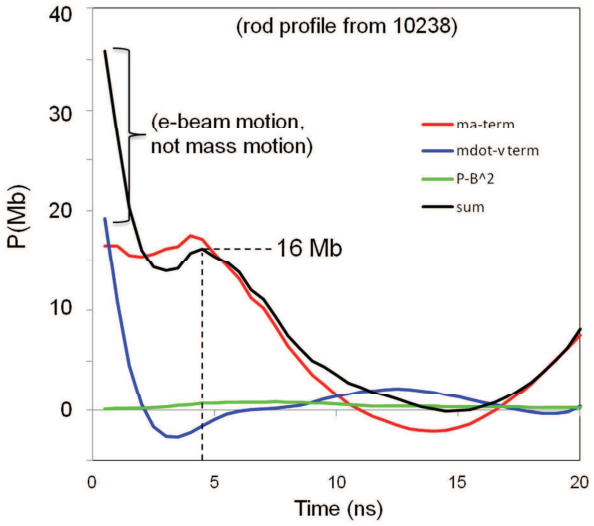

Figure 2: Plasma pressure inferred from mass-density dynamics.

This approach will be used to explore WDM parameters that can be obtained with this technique. The creation of WDM by electron beams is complementary to future research using heavy ion beams as part of Plasma Physics at FAIR (GSI).

References

[1] B.V. Weber, *et al.*, "Ultra-High Electron Beam Power and Energy Densities Using a Plasma-Filled Rod-Pinch Diode," *Phys. Plasmas*, **11**, 2916-2927, May 2004.

[2] B. V. Weber, *et al.*, "High Energy-Density Plasma Dynamics in Plasma-Filled Rod-Pinch Diodes,"in Proc. 19th IEEE Int. Pulsed Power Conference, (San Francisco, CA, June 2013), p. 316.

[3] D. Mosher, *et al.*, "Electrode-Expansion MHD in a Plasma-Filled Rod Pinch," in Proc. 14th IEEE Int. Pulsed Power Conference, (Dallas, TX, June 2003), p. 503

* Work supported by the US Office of Naval Research and the US DOE Office of Science.

X-ray emission induced by highly charged heavy ions

Xiaoan Zhang*, Cexiang Mei, Chuanghui Liang, Yaozong Li
School of Physics and Electronic Engineering, Xianyang Normal University, Xianyang, China

The investigation of the X-ray emission is useful method to study the mechanism of ion–solid collisions. Accurate measurement of the inner-shell ionization cross section is essential for the development of ion-atom collision models and moreover significant to complete atomic data library for science research.

The experiment was partly performed at the cancer therapy terminal, which was specially designed for the heavy ion tumor therapy, at the national laboratory of Heavy Ion Research Facility in Lanzhou (HIRFL). The highly charged C6+ ions, produced and extracted from the electron cyclotron resonance (ECR) ion source, were accelerated by the main cooling storage ring (CSRm) with energy of 292.7, 343.3 and 423.9 MeV/u, and the beam quality was improved by the new generation electron cooler. The C6+ ion beam pulses impacted on Au taget surface, the Lα and L□ X spectra of Au atom were measured[1]. Results showed that the production cross section of Lα was larger than that of L□. The production cross sections increase with the kinetic energies of the projectiles.

Table1. Target atomic L-shell X-ray production cross sections induced by C^{6+}.

C^{6+}energy/Mev/u	L_α			L_β		
	PWBA	ECPSSR	Exp	PWBA	ECPSSR	Exp
292.7	3.75E+03	3.81E+03	3.30 E+02	1.17E+03	1.18E+03	1.91 E+02
343.3	3.33E+03	3.39E+03	3.69 E+02	1.04E+03	1.05E+03	2.47 E+02
423.9	2.84E+03	2.88E+03	4.26 E+02	8.82E+02	8.91E+02	2.59 E+02

The PWBA and ECPSSR theoretical models were compared with the experimental results as was shown in table 1.

Results showed that theory calculation was small one order of magnitude than experimental results. The significant difference between experimental data and theoretical models was studied. It can be seen from the analysis that the relativistic effect made the 2p electron renormaliza tion process be delayed and the L2 & L3 subshell ionization effect became very small. Moreover gamma ray radiation is an important way of the projectile energy transfer in high energy region.

Another experiment was performed at the 320 kV high voltage experimental platform at the institute of modern physics, Chinese academy of science in Lanzhou. The characteristic X-ray spectra produced by the impact of 129Xe26+ with kinetic energies from 350 to 600 keV and from 1.8 to 3.9 MeV on Au surface was measured. It was found that 129Xe26+ with kinetic energies from 350 to 600 keV can excite only the characteristic X-ray spectra of Mα of Au, but 129Xe26+ with kinetic energies from 1.8 to 3.9 MeV can excite the characteristic X-ray spectra of Mζ, Mγ, Mδ and Mα. The characteristic X-ray intensity probably increased with increasing projectile energy. X-ray yield was not related with the ion kinetic energy. The kinetic energy threshold of L X-ray of Xe emitted by Xe26+ is 3.0 MeV.

The X-ray spectra produced by the impact of Xeq+ (q = 10, 15, 20, 26) with 2.4 MeV kinetic energy on Au surface was also measured[2]. Results showed that there was different broadening of Au M X-ray owing to multiply ionized effect in the collision with heavy ions, the degree of ionization mainly depend on the distribution of the electronic states in the ions' outer shell. The yield of X-ray was calculated and compared with BEA. The BEA model can give a better prediction of the experimental results after taking into account the effective of multiple ionization on the fluorescence yield as shown in Fig 1.

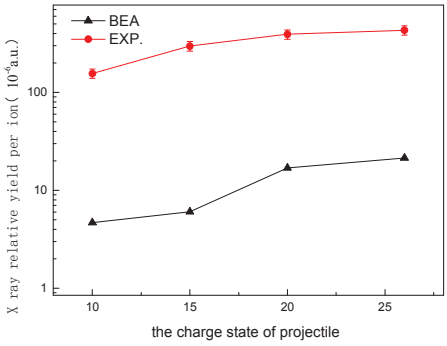

Fig. 1. X-ray yields are shown for both experimental and theoretical results.

References

[1] Zhang X A, et al, Acta Phys. Sin. 62 173401(2013) (in Chinese)
[2]Liang C H et. al, Acta Phys. Sin. 64, 053201 (2015) (in Chinese

---

*zhangxiaoan2000@126.com

Multiscale description of the laser plasma interaction, application to the physics of Shock-Ignition in Inertial Confinement Fusion

A.Colaïtis[1], G. Duchateau[1], Ph. Nicolaï[1], X. Ribeyre[1], S. Hüller[2], D. Pesme[2], D. Batani[1], and V. Tikhonchuk[1]

[1]*CELIA, Université de Bordeaux – CNRS - CEA, France*

[2]*CPHT, Ecole Polytechnique, CNRS, Université Paris-Saclay, France*

The state-of-the-art description of laser propagation on large scales relies on reduced approaches compatible with the performances of modern computers. The most common one is the *Ray-Tracing* model [1], that describes laser beams by bundles of needle-like rays following the *Geometrical Optics* (GO) propagation laws and characterized by a power density. In situations where collective effects and nonlinear couplings are unimportant ($I\lambda^2 \lesssim 5x10^{13}$ Wμm^2/cm^2), GO-based models are sufficiently precise and computationally efficient. They describe the laser refraction and plasma heating due to collisional energy absorption. Conversely, modelling of the Laser-Plasma Interaction (LPI) at higher interaction parameters requires knowledge of quantities such as the electric field amplitude and direction of the wavefront, which are not readily described by GO.

The physics of linear and nonlinear LPIs at these hydrodynamic scales is usually addressed by using limitations of the maximum electron thermal flux or by adjusting the energy deposition of laser beams so as to reproduce experimental results. Such approaches hinder the understanding of the physical processes at play and limit the predictive capability of existing numerical tools. This is a strong motivation for the development of alternative models to study and design experiments at high laser intensities on the nanosecond timescales.

1. A novel laser propagation model The description of nonlinear LPIs relies on the knowledge of the laser intensity distribution in plasma. In order to access this quantity at the large scales of hydrodynamics codes, we have adapted the method of Paraxial Complex Geometrical Optics (PCGO) to the case of plasmas. The resulting wave front equation includes information on the radius and intensity of a wave field described as a fundamental Gaussian mode in the paraxial approximation, which propagation axis is a Geometrical Optics ray. Our formulation includes the effects of collisional absorption in the under-dense corona and at the critical density on the skin-depth length. Furthermore, by pseudo-randomly focusing PCGO beamlets in a region of the beam focus where the speckle radius varies slowly, we are able to reproduce the main features of the intensity distribution of a beam transformed by a Phase Plate. The model performance was confirmed using theoretical models and standard paraxial wave solvers. This model, specially formulated for the framework of a Lagrangian code, was implemented in the radiative-hydrodynamic code CHIC [2,3] of the CELIA.

2. Large-Scale description of nonlinear LPIs Building on the novel formulation of the laser propagation, we have proposed several models to account for the nonlinear LPI. The physical processes that were considered are: (i) the nonlinear energy transfer between crossed laser beams, arising from the light diffraction on density fluctuations excited by the ponderomotive beating of the waves, and (ii) the nonlinear coupling of the wavefield with EPWs that generate hot electron populations.

2.1 Cross-Beam Energy Transfer Our formulation of Cross-Beam Energy Transfer (CBET) relies on the discretization of the interaction region by many elementary energy exchanges between Gaussian PCGO rays. Each exchange is assumed to occur within a plasma with locally constant parameters. The set of elementary energy transfers is resolved chronologically in order to be consistent. This inline model based on PCGO and implemented in CHIC has been validated against a time-dependent conventional paraxial propagation of smoothed laser beams coupled to a hydrodynamics code. Both approaches were compared in a well-defined plasma configuration, with density- and velocity- profiles corresponding to an inhomogeneous plasma, including a resonance zone in which the matching conditions for a resonant coupling between the two laser beams are fulfilled. A very good agreement was found between the PCGO simulations and the fully time-dependent paraxial-type simulations carried out with the code HARMONY [4]. The comparison showed that the code based on the PCGO approach correctly describes the CBET in situations where a resonant energy exchange occurs, past a transient period on the picosecond time scale. The PCGO-based CBET model was applied to the hydrodynamic simulation of a CBET experiment. The results are in overall good agreement with the experimental data. Based on these results, the PCGO approach for CBET has proven to be a reliable method to be implemented in hydro codes for mm-scale modelling.

2.2 Hot Electrons generated by nonlinear Laser-Plasma Interactions The description of electrons heated to supra-thermal temperatures by nonlinear LPIs has been included into the PCGO framework. This inline model has two components. First, it describes the transport and energy deposition of high energy electrons in the plasma. Electron beams are modelled in the Angular Scattering Approximation, derived from the kinetic Vlasov-Fokker-Planck equation by considering the diffusion of electrons on a background of electrons and ions. This formulation is adapted to two-dimensional, transversally Gaussian, multi-group HE beams of arbitrary angular distribution. Secondly, this transport model is interfaced with HE sources computed from the laser optical module (PCGO). Considering the case of Hot Electrons accelerated by EPWs excited by Resonant Absorption at the critical density, Stimulated Raman Scattering (SRS) and Two Plasmon Decay (TPD) at the

quarter critical density, we proposed various formulations for computing the hot electron fluxes, temperatures and angular distribution with respect to the pump wave. These formulations are based on theoretical models and analysis of the most unstable modes, experimental observation of the scattering angles and competition between processes, experimental scaling laws and Particle-In-Cell simulations. Additionally, backward propagating electrons from the TPD and backward scattered light from SRS are accounted for in the energy balance. Results obtained with this model are in good agreement with various experimental in different interaction geometries and across different intensity regimes [5,6,7].

3. Applications to the physics of Shock Ignition ICF Shock Ignition (SI) in Inertial Confinement Fusion is an alternative ignition scheme where the compression and ignition phases are separated: the target compression is conducted at a low velocity using lasers of moderate energy and the ignition is achieved at the end of the compression phase with a dedicated intense laser pulse. While the compression phase is less sensible to nonlinear LPIs compared to the standard hotspot ignition, the laser spike employed for the generation of the strong shock lies in a strongly nonlinear interaction regime. Considering typical spike durations of 500 ps at peak intensity, nonlinear LPIs have ample time to develop and (i) drive copious amounts of high energy supra-thermal electrons, notably via the excitation of EPWs from the SRS and TPD instabilities, and (ii) significantly reduce the laser-target coupling for the strong shock generation through CBET.

First, we have studied the CBET in the context of direct-drive ICF for a laser beam configuration corresponding to that of the OMEGA laser facility [8]. We conducted simulations of a capsule implosion in which certain beams are allowed to interact through CBET, following the co-planar beam angles of the OMEGA chamber. It was found that (i) Deuterium-Tritium ablators are more prone to CBET-induced deformations than plastic ablators, (ii) the CBET decreases the laser-target coupling by displacing intensity maxima away from the critical density, thus decreasing the target convergence ratio by up to 25%, (iii) the CBET causes significant low-mode deformations of the target.

The effects of Hot Electrons (HE) generated by the nonlinear LPI on the properties of shocks in plasma [9,5] and on the dynamics of shock ignition targets has been investigated [10,11]. Two targets were considered: the pure-DT HiPER target and a CH-DT design with baseline spike powers of the order of 200-300 TW. In both cases, accounting for the LPI-generated HEs leads to non-igniting targets when using the baseline spike powers. While HEs were found to increase the ignitor shock pressure, they also preheat the bulk of the imploding shell, notably causing its expansion and the contamination of the hotspot with the dense shell material before the time of shock convergence. The associated increase in hotspot mass (i) increases the ignitor shock pressure required to ignite the fusion reactions and (ii) significantly increases the power losses through Bremsstrahlung X-ray radiation, thus rapidly cooling the hotspot. These effects are less prominent for the CH-DT target where the plastic ablator shields the lower energy LPI-HE spectrum. Simulations using higher laser spike powers of 500 TW suggested that the CH-DT capsule marginally ignites, with an ignition window width significantly smaller than without LPI-HEs, and with a half of the baseline target yield. The latter effect arises from the relation between the shock launching time and the shell areal density, which becomes relevant in presence of a LPI-HE preheating.

4. Conclusion A significant effort has been made in including the basic features of the nonlinear LPI in the context of a large scale hydrodynamics code. This physical model has allowed to identify key mechanisms in experiments conducted in the context of SI at high interaction parameters. These mechanisms have been shown to be of great importance in the understanding and design of SI experiments.

5. References

[1] T. B. Kaiser. Phys. Rev. E 61, 895 (Jan. 2000).
[2] J. Breil, et al. Computers & Fluids 46 (2011).
[3] A. Colaïtis, et al. Phys. Rev. E 89, 033101 (2014).
[4] S. Hüller, et al. Phys. Plasmas 13, 022703 (2006).
[5] A. Colaïtis, et al. Phys. Rev. E 92, 041101 (2015).
[6] D. Batani, et al. Phys. of Plasmas 21, 032710 (2014).
[7] W. Theobald, et al. Phys. of Plasmas 22, 056310 (2015).
[8] A. Colaïtis, et al. Phys. Rev. E 91, 013102 (2015).
[9] P. Nicolaï, et al. Phys. Rev. E 89, 033107 (2014).
[10] V. T. Tikhonchuk, et al. PPCF 58, 014018 (2016).
[11] A. Colaïtis, et al. Submitted to PPCF.

Surface parallel electron acceleration using ultra-intense sub-picosecond pulses

J. Y. Mao[1], O. Rosmej[2,3], M. H. Li[4], J. Urbancic[1], F. Gaertner[2,3], K. Dimitri[2], S. Zaehter[2,3], D. Aslituerk[2,3], M. Z. Tao[4], C. Brabetz[2], V. Bagnoud[2,5], F. Wagner[2,3], B. Zielbauer[2], P. Neumayer[2], S. Mattias[1], M. Aeschlimann[1], L. M. Chen[4], T. Kuehl[2,5,6]

[1]University of Kaiserslautern and Research Center OPTIMAS, Kaiserslautern, Germany; [2]GSI Helmholtzzentrum, Darmstadt, Germany; [3]Goethe University, Frankfurt, Germany; [4]Beijing National Laboratory for Condensed Matter Physics, Institute of Physics, CAS, Beijing 100190, China; [5]Helmholtz Institute Jena, Jena, Germany; [6]Johannes-Gutenberg University, Mainz, Germany.

INTRODUCTION

As a continuation of the experiment P090, we investigate the optimization of highly collimated target surface electron (TSE) beams with high electron energy and monoenergetic property from the interaction of a Cu bulk target irradiated by an ultra-intense laser at PHELIX, which could make it possible to generate high-energy Gamma rays for backlighting of HIHEX (up to 300 μm Pb).

EXPERIMENT

The experiments in Jun. 2015 were carried out by working at the fundamental wavelength of 1053 nm with a peak power of around 40 TW. The s – polarized laser beam with a duration of τ_0 = 500 fs was focused by an f40 off-axis paraboloidal mirror at a grazing incidence angle onto a Cu bulk target with the focus diameter of 5 μm. An additional prepulse with adjustable intensity from 1×10^{-4} to 1×10^{-8} was applied 3ns-5ns in advance of the main pulse. A schematic picture of the experimental setup is shown in Figure 1. Also, 1% leakage of the main beam was frequency-doubled and applied as a probe beam to monitor the preplasma scale and density by using the M-Z interferometry method in the mean time.

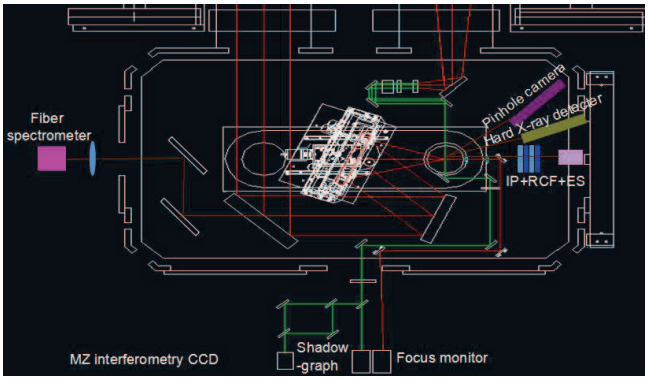

Figure 1: Experiment setup.

We investigated the prepulse dependence on the TSE generation, including the prepulse intensity ratio and the delay time. According to our previous experimental results [1], an optimized intensity ratio of the prepulse is essential to achieve an effective underdense preplasma. In the experiment, we found that when the laser power is lower, the required preplasma density is correspondingly lower. The phenomena are supported by numerical simulations [2]. In detail, both the intensity ratio of the prepulse and the delay time between the prepulse and the main beam were controlled, while the consequent preplasma density and scale were simultaneously monitored. At the optimized intensity ratio between prepulse and main pulse of around 5×10^{-7}, well concentrated and intense TSE electron jets with low divergence were observed at a laser incident angle of 72o, as shown in Figure 2(a). The divergence of the TSE electron jet was measured to be around 3° (FWHM). And the corresponding electron spectrum is detected, as shown in Figure2(b). Compared to the last experiment, the electron energy becomes lower. It might suggests that the generated TSE beam quality depends more on the laser power, than the laser intensity.

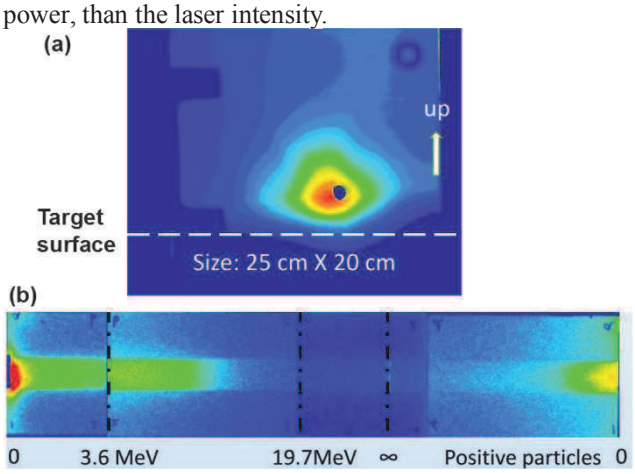

Figure 2(a): Spatial angular distribution of the TSE beam in the case with the prepulse intensity ratio of 5×10^{-7}. Figure 2(b): Corresponding electron spectrum. The hole is in a diameter of 5 mm.

PROSPECT

In the next step, we will continue the experiments above and to deepen our understanding of surface electron acceleration.

References

[1] J. Y, Mao, L. M. Chen, K. Huang *et al.,* Appl. Phys. Lett. 106, 2015, p.131105.

[2] W. M. Wang, L. M. Chen, J. Y. Mao *et al.*, High Energy Density Physics 9, 2013, p. 578.

Spatially resolved temperature diagnostic of a thin Ti-wire heated by laser-accelerated relativistic electrons* †

A. Schoenlein[1], *G. Boutoux*[2], *S. Pikuz*[3], *L. Antonelli*[2], *D. Batani*[2], *A. Debayle*[4], *L. Giuffrida*[2], *J. Honrubia*[5], *J. Jacoby*[1], *D. Khaghani*[6], *P. Neumayer*[6], *O. Rosmej*[1,6], *J. J. Santos*[2], *and A. Sauteray*[2]

[1]Goethe University, Frankfurt, Germany; [2]Univ. Bordeaux, CNRS, CEA, CELIA; [3]JIHT, Moscow, Russia; [4]CEA DAM DIF, Bruyres-le-Chatel, France; [5]ETSI Aeronauticos, Universidad Politcnica de Madrid, Madrid, Spain; [6]GSI, Darmstadt, Germany

In the reported experiment, warm dense matter (WDM) was generated by irradiating a wire target with a high intensity PHELIX-laser pulse. The wire geometry lead to a confinement of relativistic electron currents which are generated during the laser-matter interaction. Due to this confinement, the process of volumetric heating by the relativistic electrons is maintained in large target depths.

The experiment was carried out at the PHELIX-laserbay. Ti-wires with a diameter of $50\,\mu m$ and a length of $3-4\,mm$ were irradiated. The laser was focused on the tip of the wires to intensities up to $10^{21}\,W/cm^2$, with a contrast of 10^{-10}.

High spatial resolution K-shell X-ray spectroscopy was used to measure the isochoric heating process induced by the laser-accelerated relativistic electrons propagating along the Ti-wire. Radiation of highly charged He- and H-like Ti-ions and Kα-satellites have been measured with high spectral resolution ($2\,m\AA$) using a focusing spectrometer with spatial resolution (FSSR). The FSSR consists of a spherically bend quartz crystal as a dispersive element and X-ray films as detectors.

The energy of photons emitted due to K-shell tranistions depends on the charge state of the atom. Inside the matter rather a charge state distribution than a single charge state is present. This leads to a broadening of the observed Kα-line (fig. 1).

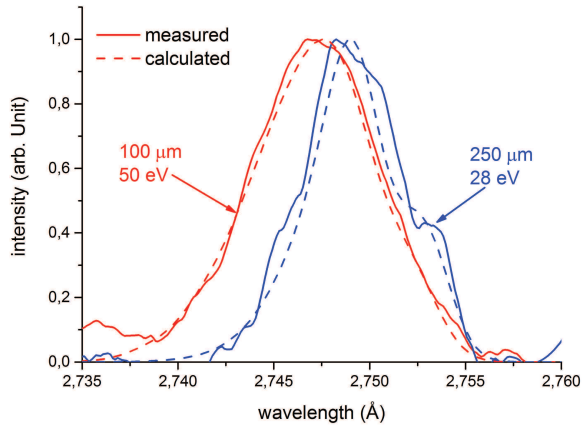

Figure 1: Comparison of modelled and measured Kα broadening.

The observed line is a superposition of all lines emitted by atoms of different charge states, which appear at a corresponding temperature of plasma bulk electrons. The broadening of the Kα-line is modelled by superposition of every charge state transistion energy, weighted with a charge state distribution. The charge state distribution for different temperatures is calculated using FLYCHK[1]. Figure 1 shows a comparion of the modelled and the measured broadening of the Kα-line. It is shown that the measured broadening can be modelled very satisfactorily by variing the charge state distribution by means of temperature.

The comparison of modelled and measured broadening can be used to determine the temperature of the heated target along the wire axis. The results are presented in figure 2.

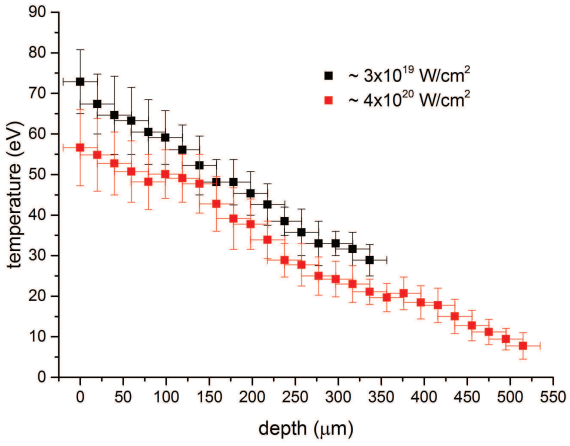

Figure 2: Temperature profile of warm dense matter heated by relativistic electrons.

It is observed, that the wire is heated to WDM temperatures of $10-70\,eV$ into a depth of $500\,\mu m$. We conclude, that using a wire geometry of high aspect ratio in laser-matter experiments, gives the possibility to generate WDM with volumetric character.

Our results are compared to simulations [2] that highlight both the role of electron confinement inside the wire and the importance of resistive stopping powers in warm dense matter.

References

[1] http://nlte.nist.gov/FLY/

[2] G. Boutoux in this report

* Work supported by GSI(PHELIX) / HIC4FAIR / HGSHire.

† This report is also submitted to the GSI Scientific Report 2015

Collisional versus Resistive Energy Losses of Laser-Accelerated Electrons in a Warm Dense Titanium Wire

G. Boutoux[1], A. Schönlein[2], S. Pikuz[3], L. Antonelli[1], D. Batani[1], A. Debayle[4], A. Franz[2], L.Giuffrida[1], J.J. Honrubia[5], J. Jacoby[2], D. Khaghani[6], P. Neumayer[6], O.N. Rosmej[2, 6], T. Sakaki[1], J.J. Santos[1]
[1]CELIA, Université de Bordeaux, France; [2]Goethe University, Frankfurt, Germany; [4]JIHT RAS, Moskau, Russland; [4]CEA DAM DIF, France; [5]ETSI Aeronauticos, UPM, Madrid, Spain; [6]GSI, Darmstadt, Germany

Ultrahigh intensity laser interactions with dense targets stand out as an effective way to produce high-current relativistic electron beams (REB). In this context, it is important to understand the REB transport, at high electron current densities and through warm dense and highly resistive plasmas. To investigate this topic, we studied the interaction of the PHELIX laser (E_L=120 J on target, t_p=500 fs, λ=1064 nm) with a free-standing mass-limited Ti-wire (experiment P-077). In this report, we consider a laser shot with a ns-contrast up to 10^{-10} and with a focal spot size down to 6 µm, leading to a laser intensity on target of I_L=7.10^{20} W/cm^2. The REB, accelerated during interaction between relativistic laser pulse and short scale length preplasma, penetrate the wire and deposit energy therein. In [1,2], we have already discussed how isochoric heating due to laser-accelerated electrons can generate Warm Dense Matter (WDM) in depth and how we can diagnose this extreme state of matter. In this report, we focus on hot electrons and how they lose energy in WDM. When electrons propagate the wire, they ionize it and subsequent K-shell and Bremsstrahlung emission occurs, making the electrons propagation experimentally traceable. To characterize their energy distribution as well as their transport, we used two main diagnostics and a comprehensive set of simulations. First, a "Bremsstrahlung cannon" acted as a hard X-ray spectrometer. It was made of a stack of image plates (IP) and differential filtering at the front and rear sides. Monte-Carlo modelling of the Bremsstrahlung dosimetry was then used to infer the internal hot electron energy distribution. Both experimental data from this diagnostic and from dedicated "Particle-In-Cell" calculations (using the code PICLS-2D [3]) demonstrate that hot electrons with temperature of about 2 MeV were generated. Secondly, a Focusing Spectrometer with Spatial Resolution (FSSR) enabled highly spatially and spectrally resolved X-ray spectroscopy. In particular, the Kα emission intensity profile along the wire gives rather direct information on the REB propagation. The Kα signal was surprisingly found to decrease exponentially up to ~0.8 mm deep, though a stopping range of 1.8 mm was expected in cold Ti, see Fig. 1(a). Energy losses of an electron beam propagating within a material are commonly associated with inelastic collisions with bound and free electrons in the matter. However, this process is insufficient at the extremely high current density j_h achieved in relativistic laser-plasma experiments, where resistive losses induced by the neutralizing return current, of density j_e, become important. Indeed, while the rate of collisional energy loss by the electron beam per unit volume is proportional to $\rho.j_h$, with ρ the material density, by assuming a perfect current neutralization j_e=-j_h, the rate for the resistive energy loss is around $\eta.j_h^2$, with η the material resistivity. This last process has been recently experimentally evidenced in the warm dense matter regime [4]. To quantify the resistive losses, we performed hybrid PIC simulations [5]. Our simulations are able to reproduce the Kα emission intensity profile along the wire, see Fig.1(a). The predicted electron current density inside the wire is up to 10^{12} A.cm^{-2} (time-averaged), which is higher than in [4]. Resistive effects are found to be dominant in the first 200 µm of the target, where the electron current density is important. In total, resistive losses exceed collisional losses by a factor 2.35, hence justifying the observed reduction of the electron stopping range. Fig. 1(b) illustrates the competition between collisional and resistive losses as a function of the wire depth. As expected, the resistive losses, proportional to the square of the current density, are dominant near the laser-plasma interaction region. Yet, in comparison to experiments on foils, e.g. [4], the collective effects remain dominant over a relatively larger distance.

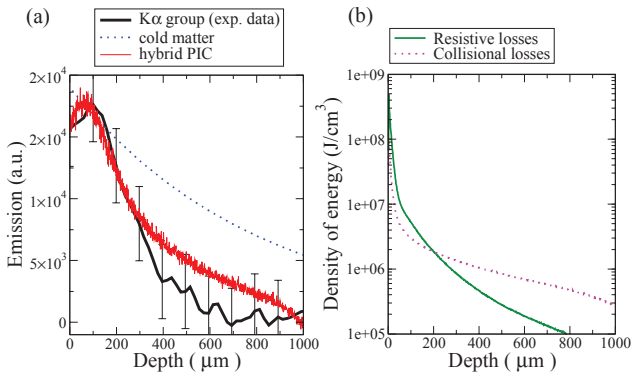

Figure 1: (a) Experimental Kα emission intensity profile along the wire using the FSSR compared to hybrid PIC simulations and a standard Monte-Carlo simulation in cold matter. (b) Resistive and collisional density of deposited energy as a function of wire depth predicted by the hybrid PIC code.

References

[1] GSI Sci. Report 2014, APPA-MML-PP-11, p. 285
[2] GSI Sci. Report 2014, APPA-MML-PP-08, p. 282
[3] Y. Sentoku et al., J. Comput. Phys., 227, 6846 (2008)
[4] X. Vaisseau et al., Phys. Rev. Lett. 114, 095004 (2015)
[5] J.J. Honrubia et al., Laser and Particle Beams 24, 217 (2006)

OAM effects in relativistic laser plasma interactions *

Y.Shi[1], B.F.Shen[1], X.M.Zhang[1], W.P.Wang[1] and Z.Z.Xu[1]
[1]State Key Laboratory of High Field Laser Physics, Shanghai Insitute of Optics and Fine Mechanics, Chinese Academy of Sciences, Shanghai 201800, China

Prompted by the fast development of laser techniques, light-matter interaction has entered the regime of relativistic laser-plasma interaction. How to observe the orbital angular momentum (OAM) in laser-plasma interaction and how the appearance of OAM would essentially affect the process are of special interests. Circularly polarized light carries a spin angular momentum of $\pm\hbar$ per photon; however, the total OAM of a normal Gaussian pulse, commonly found in the current chirped pulse amplification technology, is zero. Therefore, observation of the torque and OAM in relativistic laser-plasma interaction is rare.

We propose a simple and effective method for generating a relativistic twisted laser pulse and showing the OAM effect. It is called "Light Fan": a relativistic laser pulse (with very high photon density) impinges on a spiral foil (the fan); hence, both the fan and the reflected pulse achieve a net large OAM [1]. The proposed scheme is verified by the following three-dimensional (3D) particle-in-cell (PIC) simulations. The set-up is sketched in Figure 1. A relativistic laser pulse normally incidents on the foil from the left, interacts with the matter and is then reflected. If we see the rotator as a protons disk with r = 3 μm , h = 0.8 μm and ρ = $100m_p n_c$, the angular velocity corresponding to $L = 2.0\times10^{17}$ kg m^2 s^{-1} is about $\omega = 7\times10^8$ rad s^{-1}. It can be one order higher than man-made rotational speed record 6×10^7 rad s^{-1}, which is also laser-induced. In our case, the OAM density of relativistic twisted light, defined with OAM over volume, can be as high as $u = L_x / V = 0.56$ kg m^{-1} s^{-1}. Considering that high energy density is an important concept, this high OAM density may bring some new effects.

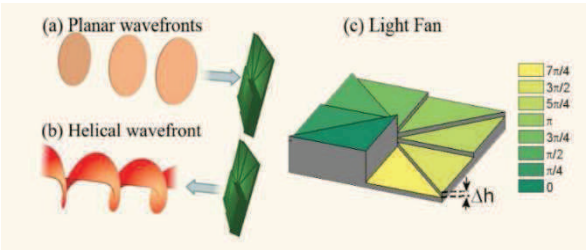

Figure 1: (a) the normally incident laser pulse has planar wavefronts. (b) The reflected laser pulse gets a helical wavefront. (c) The foil used in the simulation has eight parts, with the same step height $\Delta h = \lambda/16$ to mimic a $h = \lambda/2$ spiral phase plate. The maximum thickness of the foil is set as 0.8 μm to ensure that laser pulse is not transmitted. The colors represent different phase changes when a laser pulse incidents normally and the foil act as a mirror. [1]

When an intense linearly polarized driving vortex beam with low-order mode impinges on a solid target, both the reflected and transmitted light include high-order harmonics, the phase of which scales with the harmonic order [2]. In this nonlinear process, OAM carried by the driving helical light is readily transferred to the harmonics. Moreover, plasma as the nonlinear medium shows superiority in the damage threshold compared with the optical component. Also the PIC simulations show that the Laguerre-Gaussian (LG) pulse can drill into the plasma like a screw [3]. The well-confined acceleration of externally injected protons in the wakefield driven by LG laser pulse is also studied by using 3D PIC simulations [4]. It is found that, different from the regular bubble induced by a Gaussian laser pulse, a special bubble with an electron pillar on the axis will be formed when a LG laser pulse irradiates in underdense plasma. This structure provides an efficient and strong focusing force for protons in the transverse direction; thus, protons can be accelerated continuously for a long time.

As an important character, relativistic laser has strong torque. This strong torque can lead to strong OAM when the laser interacts with structured matter (like Light Fan in our case) or when twisted light (like the reflected light in our case) interact with uniform matter. Like strong ponderomotive force of relativistic laser can produce a finite linear momentum in many applications (for example LWFA), such a strong torque should also be expected to produce a finite OAM in many potential applications. Also a relativistic twisted laser has an ultra-high OAM density accompanying ultra-high energy density.

References

[1] Yin Shi, Baifei Shen et al. "Light fan driven by a relativistic laser pulse." Phys.Rev.Lett.112.235001 (2014).
[2] Xiaomei Zhang, Baifei Shen, Yin Shi et al. Generation of Intense High-Order Vortex Harmonics. Phys.Rev.Lett.114.173901 (2015).
[3] Wenpeng Wang, Baifei Shen, Xiaomei Zhang et al. Hollow screw-like drill in plasma using an intense Laguerre-Gaussian laser. Sci. Rep., 2015. 5.
[4] Xiaomei Zhang, Baifei Shen, Lingang Zhang et al. Proton acceleration in underdense plasma by ultraintense Laguerre-Gaussian laser pulse. New Journal of Physics, 16(12), 123051. (2014)

* Work supported by the Ministry of Science and Technology, the National Natural Science Foundation of China

Observation of hollow ion emission from Si ions pumped by ultraintense X-ray radiation of relativistic laser plasma

A. Ya. Faenov[1,2] J. Colgan[3], S.A. Pikuz[2,4] , E. Tubman[5], N. Butler[6], J. Abdallah, Jr.[2], R. Dance[6], T.A. Pikuz[2,7], I.Yu. Skobelev[2,4], M.A. Alkhimova[2,4], N. Booth[8], A. Andreev[9,10], A. Zhidkov[7], R. P. McKenna[6], N. Woolsey[5], Kodama[1,7]

[1]Institute for Academic Initiatives, Osaka University, Suita, Osaka 565-0871, Japan; [2]Joint Institute for High Temperatures, Russian Academy of Sciences, Moscow 125412, Russia; [3]Theoretical Division, Los Alamos National Laboratory, Los Alamos, NM 87545, USA; [4] National Research Nuclear University MEPhI, Moscow 115409, Russia; [5]York Plasma Institute, Department of Physics, University of York, York YO10 5DD, UK, [6]Department of Physics, SUPA, University of Strathclyde, Glasgow G4 0NG, UK, [7]PPC and Graduate School of Engineering, Osaka University, 2-1, Yamadaoka, Suita, Osaka 565-0871, Japan, [8]Central Laser Facility, STFC Rutherford Appleton Laboratory, Didcot OX11 0QX, UK; [9]Max Born Institute, Berlin 12489, Max-Born str.2a, Berlin, Germany; [10]ELI-ALPS, Szeged H-6720, Hungary

The radiation properties of high energy density plasma are under increasing scrutiny in recent years due to their importance to our understanding of stellar interiors, the cores of giant planets, and the properties of hot plasma in inertial confinement fusion devices. Recently, it was demonstrated [1-4] that conventional optical lasers with pulse duration of 40 – 1000 fs and laser intensity (0.3-1.0)x10^{21} W/cm^2 irradiating Al foils could generate very bright X-ray radiation with intensities exceeded 10^{17} W/cm^2 and efficiently produce exotic states of matter (so called Hollow ions), which are very far from equilibrium (See Fig.1).

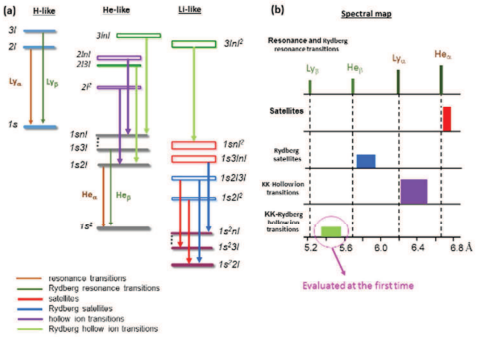

Figure 1: Schematic diagram of the Si hollow ions

New set of measurements of high spectrally resolved K-shell emission of Si foils irradiated by sub picosecond laser pulses of Vulcan laser facility was provided [5] (see Fig.2).

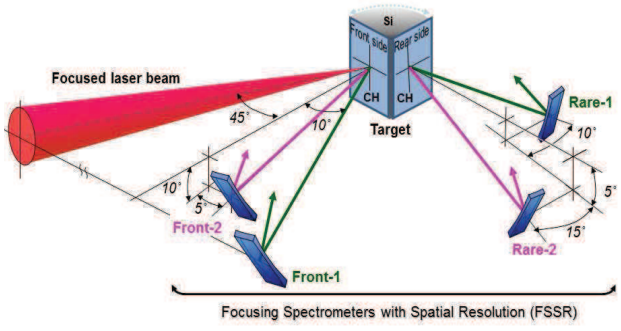

Figure 2: Experimental set up [5].

Comparison of experimental and modelled by Atomic code Si spectra is presented in Fig.3 and clear demonstrated that the measured bulk electron temperature of Hollow ions is reached 180 eV with ionization up to Li-like. Our investigations asserts that exotic Hollow ions states can be probed not only by X-ray radiation of XFEL lasers, but also upon using optical laser technology. In the latter case the generated X-ray radiation is polychromatic with its energy and intensity (~10^{18} W/cm^2) comparable or even exceeding that of current XFELs and complements the recent observations of such exotic states using XFELs. The results reported here suggest that Hollow ions spectral diagnostics provide a unique opportunity to characterize warm dense plasma and particular powefull X-ray radiation of laboratory and astrophysical plasmas. Additionally it follows that radiation dominated atomic physics processes could be efficiently studied at high optical laser intensities.

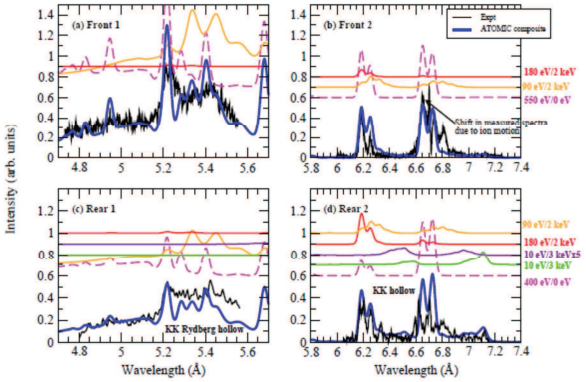

Figure 3: Comparison of measured Si spectra and ATOMIC calculations [5].

References

[1] J. Colgan et al. Phys. Rev. Lett. **110,** 125001 (2013)
[2] S.A. Pikuz et al. High Energy Density Physics **9**, 560-567 (2013)
[3] S.B. Hansen et al. Physics of Plasma 21, 031213 (2014)
[4] A. Faenov et al. *Sci. Rep.* **5**, 13436 (2015)
[5] J. Colgan et al. EPL, 2016 (submitted)

Flute-like instability structure observed at the diamagnetic cavity edge in a large magnetized plasma*

B.R. Lee[1,#], A. Bondarenko[2], S.E. Clark[2], C. Constantin[2], E. Everson[2], D. Schaeffer[2], D.H.H. Hoffmann[1], and C. Niemann[2]
[1]Technische Universität Darmstadt, Germany; [2]University of California, Los Angeles, CA, USA

When magnetized plasmas with different densities interact with each other, various hydromagnetic waves are launched including magnetized collisionless shocks. As the galactic cosmic rays are believed to arise in the shock, the importance of its study has already been emphasized, however, many questions still remain open. A well-scaled laboratory experiment helps study the microphysics of shocks and complement *in situ* spacecraft measurements of shocks in the Earth's magnetosphere. This work presents the result of the recent experimental campaign [1] where a kJ-laser from the Phoenix Laser Facility [2] at the University of California, Los Angeles, irradiates a polyethylene target which is embedded in a pre-formed magnetized plasma created in the Large Plasma Device [3]. A diamagnetic cavity launches a magnetized collisionless super-Alfvénic pulse (~$1.2v_A$ with $v_A=B/(\mu_0 n_i)^{1/2}$) which has the potential to become a shock if the shock formation requirements are met [4]. Here, the focus is on the flute-like instability feature at the diamagnetic cavity edge observed in the electric as well as in the magnetic field.

The free energy for instability originates from the relative ion and electron drift at the cavity edge and gives rise to dissipative wave-particle interactions [5]. Large fluctuations in the electromagnetic field as shown in Figure 1a) display instability features detected by the measuring probe before the cavity (blue dip) reaches the probe location. The electric field (black and red) and the magnetic field (blue dotted) oscillations show that the fluctuation lies in the frequency range around 8 MHz and moves with the same velocity as the cavity edge expansion velocity indicating that these fluctuations are triggered at the front cavity edge. The outcome corresponds to the observation of the flute patterns from the fast photography on the ion dynamics. The possible candidates for instability structures are the lower-hybrid-drift (LHDI) [6] and the modified two-streaming instability (MTSI) [7]. However, with their characteristic frequencies of f_{LHDI}~46.3MHz and f_{MTSI}~41.7MHz with the corresponding experimental parameters, none of the frequency of the proposed instabilities matches the measurement. The discrepancy from the theory can be explained by the frequency modes of longer- wavelength structures becoming dominant over time as the instability progresses and the unstable density profile disruption which could influence the instability structure [8]. The excitation of the instabilities at the cavity edge could be one cause for the short cavity lifetime compared to the classical diffusion time, thus the energy dissipation.

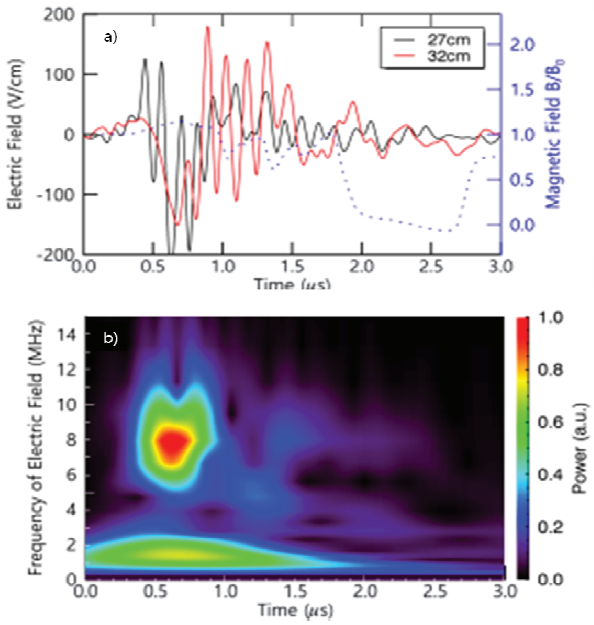

Figure 1: a) Temporal evolution of the radial electric field 27cm (black) and 32cm (red) away from the target across the magnetic field, compared to the magnetic field (blue dotted) at E_{laser}~160J and B=1420G. b) The auto-spectrum of the electric field fluctuation shows that the high frequency mode is around 8MHz consistent with the magnetic field oscillations in the same frequency range (not shown).

References

[1] B.R. Lee *et al.* (2016) to be submitted
[2] C. Niemann *et al.*, Phys.Plasmas, 20 1 012108 (2013)
[3] W. Gekelman *et al.*, Rev.Sci.Instrum., 62 2875 (1991)
[4] D. Schaeffer *et al.*, Phys.Plasmas, 21 5 056312 (2014), C. Niemann *et al.*, Geophys.Res.Lett., 41 21 7413 (2014), D. Schaeffer *et al.*, Phys.Plasmas 22, 113101 (2015)
[5] C.S. Wu, Space Sci.Rev., 32 1 83 (1982)
[6] J. McBride *et al.*, Phys.Fluids, 15 12 2367 (1972); M. Thomsen *et al.*, J.Geophys.Res., 90 A1 137 (1985)
[7] K. Papadopoulos *et al.*, Phys.Fluids, 14 4 849 (1971)
[8] J. Huba *et al.*, Phys.Rev.Lett., 59 26 2971 (1987)

*This work was supported in part by the Deutsche Forschungsgemeinschaft within the framework of the Excellence Initiative, Darmstadt Graduate School of Energy Science and Engineering under Grant GSC1070 and in part by the U.S. Department of Energy.
boramlee@skmail.ikp.physik.tu-darmstadt.de

3 New Diagnostic Methods, Particle - and Plasma Sources and Target Design

A laser-driven neutron source at PHELIX *†

A. Kleinschmidt‡ [1], *V. Bagnoud*[2], *O. Deppert*[1], *A. Favalli*[3], *S. Frydrych*[1], *J. Hornung*[1], *D. Jahn*[1], *G. Schaumann*[1], *A. Tebartz*[1], *F. Wagner*[2], *G. Wurden*[3], *and M. Roth*[1]

[1]Institut für Kernphysik, TU Darmstadt, Germany; [2]GSI Helmholtzzentrum für Schwerionenforschung GmbH, Darmstadt, Germany; [3]Los Alamos National Laboratory, New Mexico, USA

Neutrons can be used in a wide field of applications to probe and alter materials. Laser-driven neutron sources have the potential to complement common accelerator-based spallation sources because of their compact design and the possibility of easy impelementation in other facilities.

The principle of laser-driven neutron sources has already been demonstrated at different laser systems like, amongst others, the Trident laser facility at Los Alamos National Laboratory, New Mexico, USA [1] or the VULCAN laser at Rutherford Appleton Laboratory, Harwell Oxford, UK [2].

These neutron sources are based on laser-ion acceleration and their subsequent convertion into neutrons. The acceleration of deuterons in the transparency regime is of particular interest for the generation of neutrons, because of the so-called *deuteron break-up* reaction. Therefore such sources require a high energy short pulse laser with intensities above 10^{18} W/cm^2 and high temporal contrast. The improvement of the PHELIX laser during the last years, especially with respect to temporal contrast [3], made it possible to perform a first neutron experiment at GSI.

Neutron generation at PHELIX

Using the PHELIX short pulse beam with an energy of 200 J and intensities between 10^{20} and 10^{21} W/cm^2 within a pulse length of 0.5 ps, protons and deuterons were accelerated from thin deuterated plastic foils in the thickness range of a few hundred nanometers and characterized with Thomson parabolas and RadioChromic Films (RCF). The ions were driven into a beryllium catcher that was built out of several beryllium disks of various thicknesses and layers of RCF inbetween. The sandwich type catcher was wrapped in tungsten foil with an overall thickness of 1 cm to reduce the number of neutrons scattered out of the catcher.

Neutrons are produced via nuclear reactions of the accelerated ions in the catcher material. (p,n) or (d,n) reactions generate a homogeneous angular neutron distribution, whereas pre-equilibrium emissions or the deuteron break-up result in a more forward directed emission with higher energies. This results in an angular neutron distribution with a 4π component and an overlapping forward directed neutron beam.

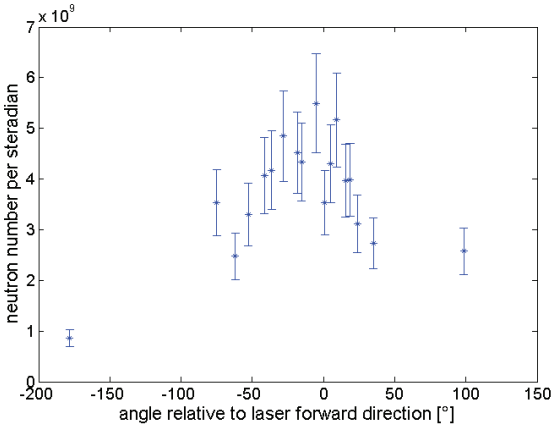

Figure 1: Angular neutron distribution with respect to the laser forward direction (0°).

The energy spectrum of the neutrons, their flux, and angular distribution were measured with three neutron time of flight detectors, using liquid scintillators coupled to photomultiplier tubes, and BD-PND Bubble Detectors. Both detector types were set up in different angles around the target chamber.

Especially the simultaneous measurement with up to 30 Bubble Detectors per shot allowed a detailed analysis of the angular neutron distribution. An example of such a distribution can be seen in Figure 1 showing neutron number per steradian over angle with respect to the laser forward direction defined as 0°. The laser incident angle on target was -10°. The data clearly reflects the forward directed characteristics of neutron emission from non-equilibrium reactions.

The maximum dose measured in the laser forward direction scaled to a distance of 1 m to the center of the beryllium catcher was about 43 mrem, which is the highest neutron flux measured at a laser-driven neutron source so far.

References

[1] M. Roth et al., "Bright Laser-Driven Neutron Source Based on the Relativistic Transparency of Solids", Phys. Rev. Let., 110 (4), (2013)

[2] S. Kar et al., "Beamed neutron emission driven by laser accelerated light ions", Phys. Plasmas (2015)

[3] F. Wagner et al., "Temporal contrast control at the PHELIX petawatt laser facility by means of tunable sub-picosecond optical parametric amplification", Appl. Phys. B, 116 (2) pp. 429-435., (2013)

* Work supported by GSI(PHELIX) /HIC4FAIR

† This report is also submitted to the GSI Scientific Report 2015

‡ a.kleinschmidt@gsi.de

First steps towards the generation of intense, subnanosecond heavy ion bunches at LIGHT *

J. Ding[1], *D. Schumacher*[2], *D. Jahn*[1], *O. Deppert*[1], *C. Brabetz*[2], *S. Weih*[1], *F. Kroll*[3,4], *U. Schramm*[3,4], *T.E. Cowan*[3,4], *V. Bagnoud*[2,5], *A. Blazevic*[2,5], *and M. Roth*[1]

[1]TU Darmstadt, Darmstadt, Germany; [2]GSI, Darmstadt, Germany; [3]TU Dresden, Dresden, Germany; [4]HZDR, Dresden, Germany; [5]HI Jena, Jena, Germany

The LIGHT collaboration, consisting of several Helmholtz institutes and universites, has been founded for the purpose of Laser Ion Generation, Handling and Transport. For this a test beam line has been established at the Z6 experimental area at GSI [1]. The laser ion generation is based on the Target Normal Sheath Acceleration (TNSA) mechanism and driven by the PHELIX 100 TW beam line. A pulsed solenoid captures and collimates a part of the divergent ion beam with a continous energy spectrum by means of achromatic focusing [2]. The resulting collimated beam with a much narrower energy spread can then be compressed in phase or energy in a radiofrequency cavity, which is situated two meters behind the ion source. Two quadrupole doublets transport the ion beam to a second target chamber. The resulting ion beam is then diagnosed with a diamond detector for a temporal depiction of the achieved phase focus or with a stack of radiochromatic films for an energy spectrum.

Two campaigns in 2015 examined the acceleration of fluorine ions with TNSA and the handling and transport of the resulting ion beams. The first campaign focused on the generation of fluorine ions. For this purpose a 13 μm tungsten foil with a submicrometer coating of CaF_2 on the rear side was heated to 1100 degrees celsius in order to get rid of hdyrogen and hydrocarbon pollution. By removing these pollutions an efficient acceleration of fluorine ions of varying charge states was achieved. In figure 1 an extrapolation of the energy spectrum of the observed fluorine ions and their charge states can be found. It was measured with a Thomson parabola, which was set up at 0.12 m behind the target. Since the pinhole of the Thomson parabola covers only a very small solid angle of 1.1 mrad in the centre of the beam, the spectrum of the whole beam can only be extraced by extrapolating the measured part of the beam. This was done by assuming a two dimensional gaussian beam distribution with an energy dependent standard deviation. The divergence of the fluorine ion beams as a function of their energy was taken to be the same as the divergence of TNSA proton beams [3]. In addition to that the photo stimulated luminescence values from the image plates had to be converted to particle numbers by means of energy loss calculations with GEANT and fitting to existing models [4].

In the second campaign the transport and phase focusing of a part of the fluorine ion spectrum in the LIGHT beamline was approached. Six metres behind the target a diamant detector recorded time of flight (TOF) data. Figure 2 shows the comparison of TOF data of a phase focused fluorine ion and proton beam, converted to energy per nucleon. The central energy of the transported fluorine ion bunch was 0.85 MeV/u with an energy spread of $\pm$0.3 MeV. The relative energy spread of the fluorine ion bunch is much bigger than that of the proton bunch. Therefore the fluorine ion beam is longitudinaly much longer at the entrance of the rf cavity than the proton beam and exceeds the cycle duration of the rf cavity. This leads to the formation of multiple phase focused ion bunches. Simulations with TraceWin suggest, that the fluorine ion tof data in figure 2 stem from F^{7+} and F^{6+} only, because the particle numbers of the other accelerated charge states are strongly suppressed at the selected energy range.

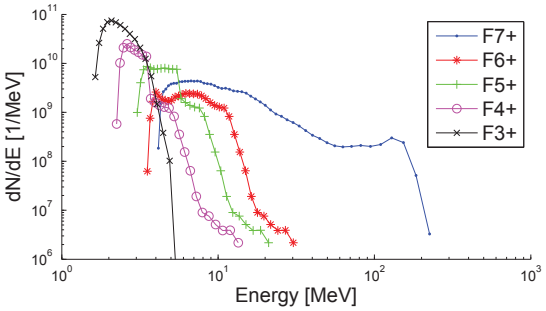

Figure 1: Energy spectrum of TNSA fluorine ions

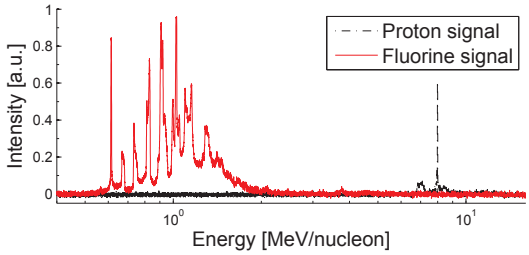

Figure 2: Diamond detector signal of phase focused ions

References

[1] S. Busold et al., NIMA 740, 94-98 (2014).

[2] S. Busold et al., PRSTAB 16, 101302 (2013).

[3] E. Bambring et al., Phys. Rev. Lett 96, 154801 (2006).

[4] P. Poth, Master thesis (2015).

* also published in 'GSI Scientific Report 2015'

Generation of subnanosecond, intense ion bunches with the laser-driven LIGHT beamline*

D. Jahn[1], *D. Schumacher*[2], *C. Brabetz*[2], *J. Ding*[1], *S. Weih*[1], *F. Kroll*[3,4], *U. Schramm*[3,4], *T. E. Cowan*[3,4], *V. Bagnoud*[2,5], *A. Blazevic*[2,5], *and M. Roth*[1]

[1]Technische Universität Darmstadt, Darmstadt, Germany; [2]GSI Helmholtzzentrum für Schwerionenforschung, Darmstadt, Germany; [3]Technische Universität Dresden, Dresden, Germany; [4]Helmholtzzentrum Dresden-Rossendorf, Dresden, Germany; [5]Helmholtz-Institut Jena, Jena

Within the Laser Ion Generation Handling and Transport (LIGHT) project at GSI laser-driven ion acceleration and, especially, ion beam shaping with conventional accelerator technology are investigated using the worldwide unique LIGHT test beamline in the Z6 experimental area [1]. The project is based on a Target Normal Sheath Acceleration (TNSA) source driven by the Petawatt High-Energy Laser for Heavy Ion EXperiments (PHELIX) 100 TW beam resulting in a continuous proton energy spectrum up to a maximum energy of 28.4 MeV. The ions of the TNSA source are captured by a high-field solenoid for energy selection of protons in a range of 8 to 10 MeV via chromatic focusing. In 2 m distance to the source, an implemented radiofrequency (rf) double spiral resonator operating at -90 degrees synchronous phase is used for phase rotation of the accelerated single bunch. This way, the bunch can be energy-compressed or longitudinally phase-focused down to a subnanosecond pulse [2]. Behind the resonator, the beam is transported through two permanent quadrupole doublets (50 mm, 25 T/m) into a second target chamber. In this second target chamber at 6 m distance, a second high-field solenoid system was installed for steep focusing to access highest peak intensities. Behind this solenoid, the diagnostic instruments are placed.

The LIGHT project dealing with proton acceleration follows two main objectives: The longitudinal phase focusing should be improved and the focal spot size should be minimized. For the first objective, a newly developed fast diamond detector based on a $5 - 7$ μm thin membrane with a time resolution up to (65 ± 5.5) ps and a field gradient of 5 V/μm was positioned at 6 m distance from the source. With this device a new optimum in phase focusing was reached: The shortest measured proton bunch lasted (209 ± 18) ps (FWHM) with a proton energy of 8 MeV. For comparison, a bunch duration of (462 ± 40) ps (FWHM) was measured in 2014. Figure 1 shows the temporal bunch profile. For the second objective, the second solenoid was installed at 6 m distance for steep focusing: A focal spot size of 2.3 mm x 2.3 mm with 2.5×10^8 protons was achieved resulting in a current of 1.2×10^9 1/ns $\sim$ 190 mA and an intensity of 2.3×10^{19} 1/(s cm^2). In the next experimental campaign in 2016, the beam homogeneity will be improved. After this crucial step, this beam can be applied for proton imaging.

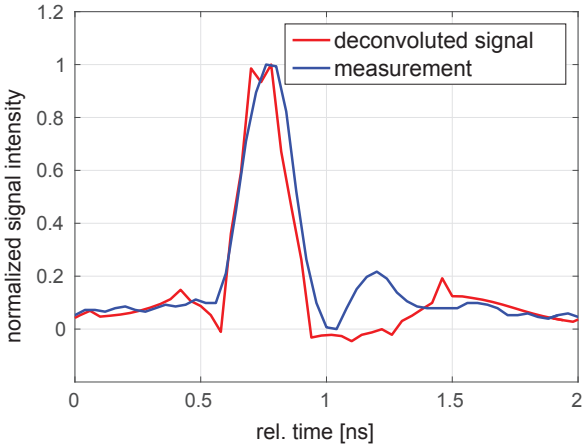

Figure 1: Measured temporal profile of the shortest proton bunch with a duration of (209 ± 18) ps after deconvolution.

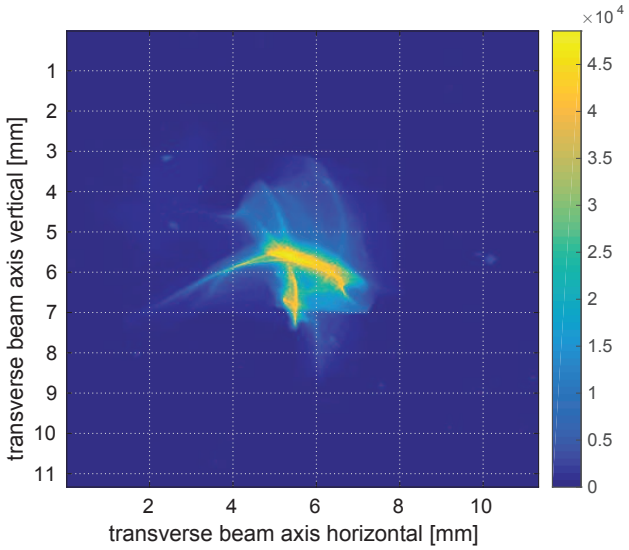

Figure 2: Measured focal spot size of 2.3 mm x 2.3 mm with color scale describing particle numbers per mm^2.

References

[1] S. Busold *et al.*, NIMA **740**, 94-98 (2014)

[2] S. Busold *et al.*, Scientific Reports **5**, 12459 (2015)

* This report is also published in *GSI Scientific Report 2015*.

Pepperpot emittance measurements for LIGHT beam characterization *

S. Weih[1], D. Jahn[1], J. Ding[1], D. Schumacher[2], C. Brabetz[2], A. Blazevic[2,3], V. Bagnoud[2,3], F. Kroll[4,5], U. Schramm[4,5], T. E. Cowan[4,5], and M. Roth[1]

[1]Technische Universität Darmstadt, Darmstadt, Germany; [2]GSI Helmholtzzentrum für Schwerionenforschung, Darmstadt, Germany; [3]Helmholtz-Institut Jena, Jena, Germany; [4]Helmholtz-Zentrum Dresden-Rossendorf, Dresden, Germany; [5]Technische Universität Dresden, Dresden, Germany

The Laser Ion Generation, Handling and Transport (LIGHT) project at the Z6 experimental area investigates the possibility of beam transport and shaping of laser- accelerated protons and heavier ions with conventional accelerator technology [1]. In the past experiments, ultra-short bunches with an energy of 8 MeV were generated and measured for protons [2], and the transport of flourine and carbon ions along the 6 m long beamline was shown. During the experiments in October 2015, first emittance measurements were performed for protons to characterize the beam quality and transverse beam dynamics. Since the TNSA particle bunches are only provided in single-shot mode, the pepperpot measurement method was suited the best.

The measurement was realized with a conventional beam diagnostics pepperpot device which was placed directly behind the first solenoid in the beamline, which is used to collect and focus the diverging particles directly behind the source. Since this is the main transverse focusing element, its influence on the emittance was of major interest. A radiochromatic film (RCF) stack was used 60 cm behind the pepperpot as screen.

To measure the emittance of the TNSA source (based on a 0.01 mm gold target), the solenoid first stayed turned off during the shot. The pattern on the RCF screen showed a magnified image of the pinholes with the magnification corresponding to the geometrical distances of the setup. The TNSA source can therefore be seen as an almost ideal point source. The evaluation of the phase space was performed in the radial dimension (r - r') and confirmed this result (fig. 1), but since the obtained numerical value of $\epsilon = 2.7$ mm mrad was already the resolution limit of the experimental setup, the measured value yields only an upper limit for the source emittance. The real source emittance might be much lower, like [3] indicates.

The second measurement was carried out with the solenoid turned on during the shot, which is the operation mode for the 6 m long transport along the beamline. Since there is no energy selection in front of the solenoid, the protons enter it with their full energy spectrum and get separated radially due to the solenoid chromaticity. On the screen, the image of the pinholes therefore becomes radially streaked. The radial positions within one streak can be assigned to the corresponding proton energies (fig. 2), which allows an energy-resolved emittance analysis. In practice, due to small signals, it was difficult to analyze the RCF images for the solenoid emittance measurement. It could be seen qualitatively, that the solenoid field distorts the symmetry of the pattern on the screen (fig. 2).This explains the measured emittance blow-up of a factor around 10 compared to the upper limit of the source emittance. Further investigations on this effect will be performed following the aim to maintain the small source emittance along the beamline. Additionally, the resolution of the source emittance measurement setup will be improved.

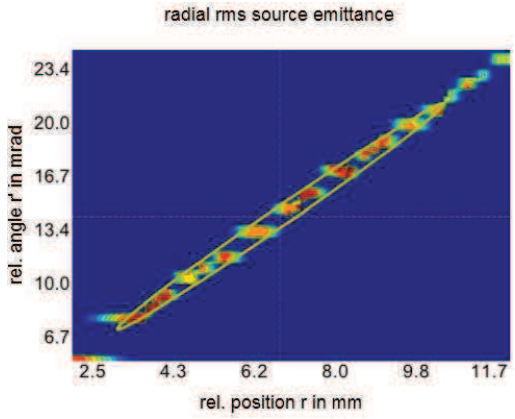

Figure 1: Radial phase space diagram of the TNSA proton source with rms emittance ellipse.

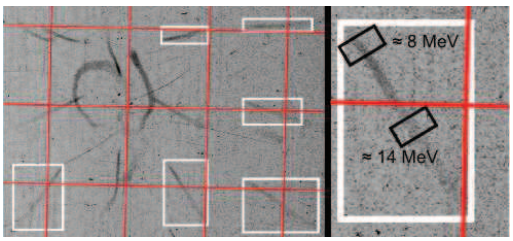

Figure 2: Section of the RCF image from the measurement with the solenoid turned on (left). The grid shows the calibration of the setup. Some streaks are shifted away from their original position in a non-radial way, which disturbs the symmetry. On the right, the energy selection within one streak is illustrated.

References

[1] S. Busold et al., NIM-A **740**, 94-98 (2014)

[2] S. Busold et al., Scientific Reports 5, 12459 (2015)

[3] T. E. Cowan et al., Phys. Rev. Lett. **92**, 204801 (2004)

* This report is also published in *GSI Scientific Report 2015*

Laser-driven proton acceleration with cone-guided hemispherical targets*

O. Deppert[†1], *C. Brabetz*[2], *S. Busold*[1], *D. Jahn*[1], *A. Kleinschmidt*[1], *K. Philipp*[1], *P. Poth*[1], *G. Schaumann*[1], *D. Schumacher*[2], *A. Blazevic*[2], *V. Bagnoud*[2], *and M. Roth*[1,2]

[1]Technische Universität Darmstadt, Germany; [2]Helmholtzzentrum für Schwerionenforschung GmbH - GSI, Germany

With the advent of new high power laser-systems, like the National Ignition Facility (NIF), the concept of Inertial Confinement Fusion (ICF) is now accessible experimentally. One of the major problems in ICF are based on an asymmetric implosion due to plasma instabilities and fuel mixing inside the hot spot. At this point, the concept of Fast Ignition (FI) is a promising scheme to overcome these problems and to pave the way for future ignition campaigns at NIF.

In the FI scheme the compression and ignition of the fuel capsule are decoupled, leading to moderate pressures which minimize potential instabilities. **P**roton-driven **F**ast **I**gnition (pFI) makes use of laser-driven protons which are dumped into the hot spot to ignite a burn wave. The upcoming ARC laser-system at NIF will be a short-pulse, petawatt, 10 kJ class diagnostic laser which allows for the first time the realization of a combined ICF and pFI scenario. In order to scale the laser-driven proton acceleration concept, the key mechanism of pFI, detailed laser-parameter studies on realistic pFI target geometries need to be carried out at high class petawatt laser-systems worldwide. First steps have been made by an experimental campaign in 2015 at the PHELIX laser-system at the Helmholtzzentrum für Schwerionenforschung GmbH - GSI at Darmstadt. During this campaign several important pFI parameters, e.g. the focusing behavior of the laser-driven proton beam, the influence of the laser-pulse length onto the conversion efficiency as well as the spatial and angular proton beam profile have been studied in detail.

Experimental and Diagnostic Setup

A PHELIX short pulse laser beam with varying pulse length and energy for constant intensities of the order of 10^{19} W/cm^2 was used to primarily accelerate protons from the surface of a complex cone-guided hemispherical target geometry (Fig. 1, left) by the **T**arget **N**ormal **S**heath **A**cceleration (TNSA) mechanism. The target consists of a hemispherical part which produces a focusing proton beam and a cone part to transport it through the outlet port. In a typical pFI scenario the fuel capsule would be attached close to this outlet port. The targets been investigated additionally modify the angular distribution of the guided proton beam due to the interaction with strong electric ($\sim$ TV/m) as well as azimuthal magnetic fields ($\sim$ kT) inside the geometry, thus allowing to produce an annular shaped proton beam which is proposed to be more efficient to ignite the pre-compressed hot spot. To diagnose the emerging ion beam three Thomson Parabola spectrometers, a newly developed **I**on **W**ide-**A**ngle **SP**ectrometer (iWASP) as well as **R**adiochromic film **I**maging **S**pectroscopy (RIS) and **N**uclear **A**ctivation based **I**maging **S**pectroscopy (NAIS) were applied. The interaction of the proton beam with the electric and magnetic fields inside the cone produces an annular proton beam for higher ($\geq$ 9 MeV) and a typical TNSA beam profile for lower proton energies (Fig. 1, right). Additionally, a complementary spectral measurement with a newly developed iWASP allows for angular and energy resolved proton beam characterization from a larger solid angle to determine more precisely the proton conversion efficiency. Fig. 2 shows the energy resolved angular distribution for proton energies between 3.3-28 MeV for the half emission cone of the beam. The annular structure can be clearly seen for energies $\geq$ 9 MeV due to the hole of the distribution for small emission angles left hand side. The time-stamps shown in Fig. 2 corresponds to a time-of-flight (ToF) distance of 1 mm behind the outlet port where the compressed fuel capsule would be placed. In the first 14-24 ps the high energy part of the proton beam will deposit its energy circular around the hot spot to drive a shock wave to further compress the core. Between 24-40 ps the low energy, but high intensity part of the spectrum then will be used to ultimately ignite the hot spot. Such a scenario is proposed to reduce the total required ignition energy by almost a factor of two. The preliminary results presented show the first time the experimental realization of this promising concept.

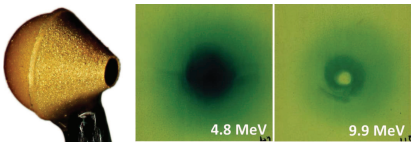

Figure 1: Dedicated target design for pFI (left); Annular proton beam measured by the RIS method (right).

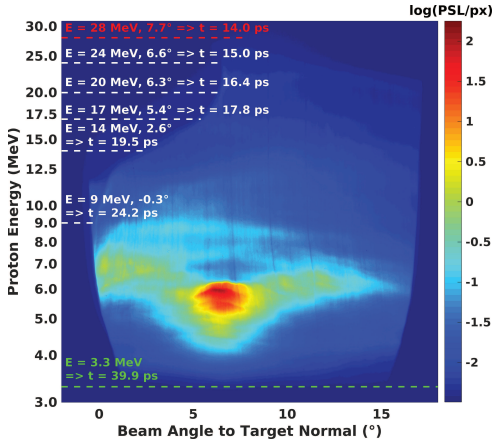

Figure 2: Angular and energy resolved proton distribution with ToF marks for passing the target outlet port.

* This report is also published in *GSI Scientific Report 2015*.

† O.Deppert@gsi.de

Line-imaging velocimeter in Laser-Driven EOS Experiments

A. Mikhaylyuk[1], D. Koshkin[1], K. Gubskii[1], A. Kuznetsov[1], A. Golubev[1,2]
[1]National Research Nuclear University MEPhI (Moscow Engineering Physics Institute), Moscow, Russia
[2] SSC RF Institute for Theoretical and Experimental Physics of National Research Centre „Kurchatov Institute“, Moscow, Russia

The paper presents diagnostic system for velocity measurements in laser-driven EOS experiments. The system includes two vernier Mach-Zehnder VISAR interferometers designed to measure velocity in the interval of 5 to 50 km/s. A passive channel records luminescence in the shock wave front. Spatial resolution of the optical layout is about 10 µm.

One of the main methods that allows getting information about the passage of powerful shock waves through matter in high energy physics is Doppler interferometry. This method is non-contact and provides information about the object with high spatial and temporal resolution.

Diagnostic method and measuring system based on line-imaging Doppler interferometry has been developed for the experimental study of shock-wave processes occurring in the interaction of intense laser radiation with matter. The system allows for remote non-contact measurement of the shock wave velocity in the range of 5 - 50 km/s with a spatial resolution of about 10 microns.

The principle of continuous velocity measurements is based on the Doppler frequency shift analysis of a probe monochromatic wave reflected by the moving surface of the sample. This system is based on two vernier Mach-Zehnder unequal path interferometers of VISAR-type (Velocity Interferometer System for Any Reflector) [1].

Optical scheme of the system was implemented in ZEMAX for getting proper spatial resolution of the target image on streak cameras (Figure 1). Functions of the optical layout include: target illumination by the probe laser beam, collecting and collimating reflected light and passing it through the interferometers, followed by the target imaging on the streak cameras with a predetermined magnification. Interferometers impose interference fringes on the target image. Displacement of fringes in every point of the image corresponds to the Doppler shifts of the light reflected from corresponding point of the target. Optical layout conditionally divided into several sections, limited by intermediate images. This solution makes it possible to adjust parts of the optical path independently. Using the zoom lenses in optical layout enables to change the magnification and make experiments with different-size field of view on target (in range of 0.3-0.6 mm). Time resolution is limited 10 ps by the streak-cameras.

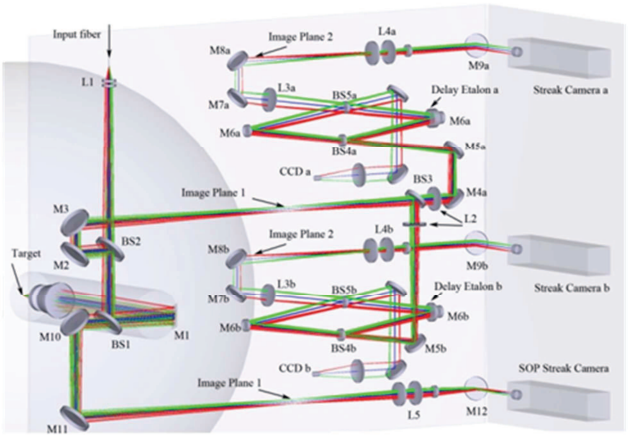

Figure 1. Vernier line-imaging VISAR layout. M - mirrors, BS – beam splitters, L – lenses

Additional optical path with streak camera is used to realise SOP measurements of target surface luminescence with the same spatial and time resolution as VISAR data.

Figure 2 shows 3D view of vernier line-imaging VISAR setup in conjunction with target chamber.

Probe light source is a pulsed Nd laser at a wavelength

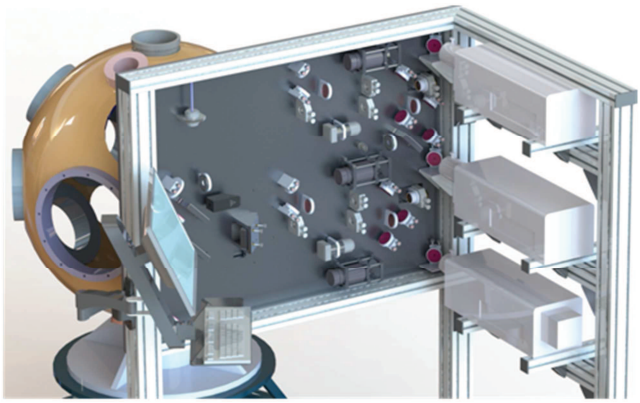

Figure 2. Vernier line-imaging VISAR work area

of 660 nm. Chosen wavelength is outside the wavelengths of the main laser harmonics (1064 and 532 nm), that allows us to separate probe and main light simply. Probe laser consists of semiconductor master oscillator and regenerative amplifier. This scheme allows obtaining the pulse with energy of 30 mJ, time duration ~100 ns with the frequency of 10 Hz. Several light sources are used for adjusting the system, including a continuous Nd laser at a wavelength of 660 nm and white light source. Probe and adjusting lasers are mounted on the separate table and connected to measuring system by 40 meters of 1-mm core fiber.

References

[1] P.M. Celliers, D.K. Bradley, G.W. Collins andD.G.Hicks,“Line-imaging velocimeter for shock diagnostics at the OMEGA laser facility”, Rev. Sci. Instrum., 2004, Vol. 75, No. 11

X-ray emission from a laser-induced plasma with ZnO nanostructured targets*

Z. Samsonova† [1,2], *E. Förster*[1,2], *S. Höfer*[1], *A. Hoffmann*[1], *D. Kartashov*[1], *D. Khaghani*[3], *B. Landgraf*[1], *P. Neumayer*[3], *R. Röder*[4], *C. Ronning*[4], *O. Rosmej*[3], *C. Spielmann*[1,2], *L. Trefflich*[4], *I. Uschmann*[1,2], *and M. Zürch*[1]

[1]Institute of Optics and Quantum Electronics, Abbe Center of Photonics, FSU Jena, Germany; [2]Helmholtz Institut Jena, Germany; [3]GSI, Darmstadt, Germany; [4]Institute of Solid State Physics, FSU Jena, Germany

Utilization of nanostructured targets for laser-produced plasma sources allows one to overcome the limited absorption of laser energy [1, 2] and to archive simultaneously very hot and dense plasma by volumetric heating [3]. Generation of such plasmas is of particular interest for both astronomical studies and table-top hard X-ray laser development. In this contribution we present the results of experimental investigation of hard X-ray generation from nanostructured solid targets irradiated by relativistically intense ultrashort laser pulses. The targets are made of zinc oxide, a dielectric, trasparent in the visible and NIR/MID range.

Experiment

The experiment was carried out at the Ti:Sapphire laser system in Jena (JETi-40). Ultra-short (45 fs) 130-mJ laser pulses at 400 nm wavelength are focused close to the normal incidence on a nanostructured target providing the peak intensity of 2.7×10^{19} W/cm^2. To minimize preplasma formation and ablation of nanostructures before the arrival of the main pulse, it is essential to have a high pulse contrast, which is about 10^{-10} on 1-ps scale in our case. The main diagnostics of X-ray emission from the plasma is a bent crystal spectrometer, based on LiF 220 crystal with a CCD camera. The samples have morphology of a disordered array of single crystalline nanowires ("grass-like") with diameters of 100-400 nm and a length of 1-5 μm (Fig. 1). For investigating the influence of the morphology on the X-ray yield, we have also measured X-ray spectra emitted from polished single crystalline ZnO.

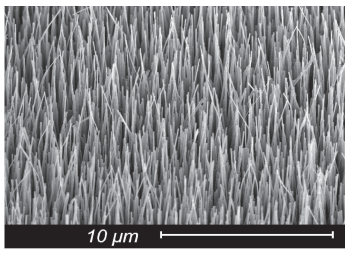

Figure 1: SEM image of "grass-like" nanostructured ZnO sample.

Results and discussions

The observed characteristic lines in the spectral energy region 8.7-9.0 keV demonstrate generation of highly charged states of Zn up to He-like Zn from both, nanostructured and polished sample (Fig. 2). However, in comparison with a polished sample, the obtained flux of photons at the Kα transitions in He-like Zn is more than 2.5 times higher for nanostructured targets. Remarkably, the intensity of observed K$_\alpha$ emission from Zn^{28+} generated in nanostructured target is almost equivalent to the intensity of the K$_\alpha$ emission from neutral Zn, pointing on the possibility to achieve very high density of highly charged plasma. Measurements with samples having different length and diameter of nanowires have shown that the longer and the thinner wires are advantageous for the production of hot and dense plasma. To investigate the temporal evolution of generated plasma, we are currently working on simulations of experimental spectra using FLYCHK code with time-dependent electron density and temperature.

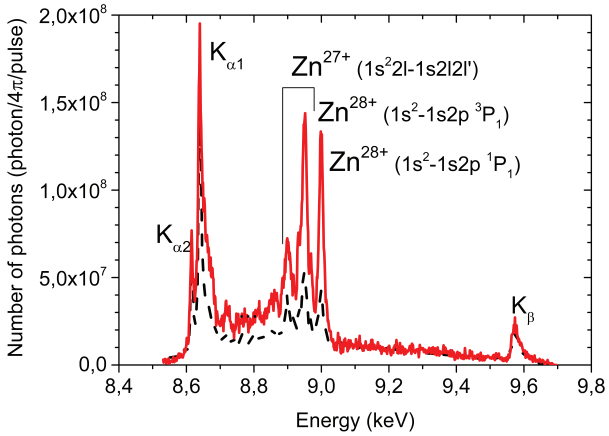

Figure 2: Calibrated spectra of X-ray emission obtained from "grass-like" (red solid line) and polished (black dashed line) ZnO targets.

References

[1] A. A. Andreev and K. Yu. Platonov, "Interaction of ultra high intensity laser pulse with structured target and fast particle generation in a stable mode", Contr. to Plasma Phys. 53, 2 (2013)

[2] G. Kulcsar et al., "Intense picosecond x-ray pulses from laser plasmas by use of nanostructured "velvet" targets", Phys. Rev. Lett. 84, 22 (2000)

[3] A. Purvis et al., "Relativistic plasma nanophotonics for ultrahigh energy density physics", Nature Photonics 7 (2013)

* This report is also submitted to the GSI Scientific Report 2015

† zhanna.samsonova@uni-jena.de

Experimental developments on proton acceleration and proton imaging in SIOM

W. P. Wang, B. F. Shen, H. Zhang, X. M. Lu, C. Wang, Y. Q. Liu, L. H. Yu, Y. X. Chu, Y. Y. Li, T. J. Xu, H. Zhang, S. H. Zhai, Y. X. Leng, X. Y. Liang, R. X. Li, and Z. Z. Xu

State Key Laboratory of High Field Laser Physics, Shanghai Institute of Optics and Fine Mechanics, Chinese Academy of Sciences, Shanghai 201800, China

Proton acceleration and its applications are carried out on the self-developed ultra-short ultra-high laser system in State Key Laboratory of High Field Laser Physics, Shanghai Institute of Optics and Fine Mechanics, Chinese Academy of Sciences. 14.3-MeV proton beam is obtained in the TNSA experiments. The effects of laser intensity, prepulse, and focal spot on the qualities of the proton beams (maximum proton energy and divergence) have been experimentally proved by the PW laser system [1-3].

High contrast is an important factor influencing the generation of high-energy proton beam in TNSA experiments. The maximum proton energy is usually achieved at the optimum foil thickness d_o for a laser with certain intensities of pulse and prepulse. According to the scaling law, higher laser intensity has been used to increase the maximum proton energy. However, the intensity of the prepulse also increases for laser systems with a similar contrast. Thus, the optimum foil thickness changes. The scaling laws between the optimum foil thickness and laser intensity should be given to guide efficient TNSA experiments.

A simple scaling law between laser intensity and d_o is proposed for our high-contrast laser system considering the prepulse effects on the expending foil[3]. d_o scaled by $d_o \propto \sim I^{0.25}$ can be obtained, which is similar to the scaling law ($d_o \propto \sim I^{0.33}$) derived in our experiments (see Figure 1).

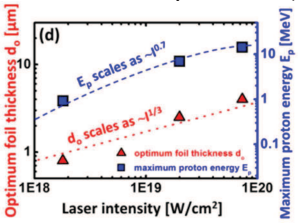

Figure 1: Variations in optimum foil thickness d_o (triangle) and maximum proton energy E_p (square) as a function of laser intensity [3]

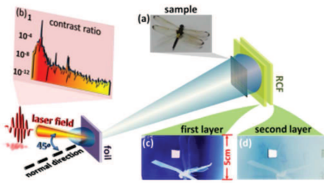

Figure 2: Schematic of experimental setup. (a) Dragonfly sample. (b) Contrast ratio of laser system. Dragonfly imaging on (c) first and (d) second RCF layers [4]

An image of dragonfly with many details is obtained by the fundamental property of such high-energy proton source on a femtosecond petawatt laser system[4]. Equal imaging of the dragonfly (~5 cm) and high spatial resolution (~5um) on the micrometer scale are simultaneously obtained. The head, wing, leg, tail, and even the internal tissue structures are clearly mapped in detail by the proton beam (see Figure 3). Experiments show that image blurring caused by multiple Coulomb scattering can be reduced to a certain extent and the spatial resolution can be increased by attaching the dragonfly to the RCFs.

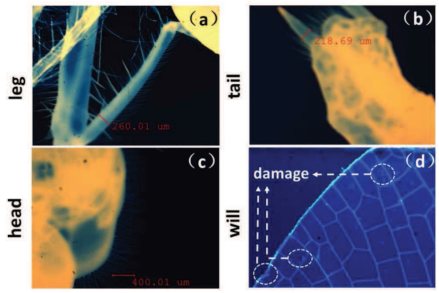

Figure 3: Structures of dragonfly (a) leg, (b) tail, (c) head, and (d) wing on RCF [4]

References

[1] W.P. Wang, H. Zhang, B. Wu, C.Y. Jiao, Y.C. Wu, B. Zhu, K.G. Dong, W. Hong, Y.Q. Gu, B.F. Shen, Y. Xu, Y.X. Leng, R.X. Li, Z.Z. Xu, Appl. Phys. Lett., 101 (2012) 214103.

[2] W.P. Wang, B.F. Shen, H. Zhang, Y. Xu, Y.Y. Li, X.M. Lu, C. Wang, Y.Q. Liu, J.X. Lu, Y. Shi, Y.X. Leng, X.Y. Liang, R.X. Li, N.Y. Wang, Z.Z. Xu, Appl. Phys. Lett., 102 (2013) 224101.

[3] W.P. Wang, B.F. Shen, H. Zhang, X.M. Lu, C. Wang, Y.Q. Liu, L.H. Yu, Y.X. Chu, Y.Y. Li, T.J. Xu, H. Zhang, S.H. Zhai, Y.X. Leng, X.Y. Liang, R.X. Li, Z.Z. Xu, Plasma Physics and Controlled Fusion, 58 (2016) 025010.

[4] W.P. Wang, B.F. Shen, H. Zhang, X.M. Lu, C. Wang, Y.Q. Liu, L.H. Yu, Y.X. Chu, Y.Y. Li, T.J. Xu, H. Zhang, S.H. Zhai, Y.X. Leng, X.Y. Liang, R.X. Li, Z.Z. Xu, AIP Advances, 5 (2015) 107214.

Ultrashort megaelectronvolt positron generation at SIOM

T. J. Xu, B. F. Shen,* J. C. Xu, S. Li, Y. Yu, J. F. Li, X. M. Lu, C. Wang, X. L. Wang, X. Y. Liang, Y. X. Leng, R. X. Li, and Z. Z. Xu

State Key Laboratory of High Field Laser Physics, Shanghai Institute of Optics and Fine Mechanics, Chinese Academy of Sciences, Shanghai 201800, China

Relativistic electron-positron pairs are ubiquitous in some of the most energetic objects in the Universe, such as black holes and pulsars. Meanwhile, relativistic positron source has many important applications, such as positron emission tomography (PET) for the cancer diagnosis and positron annihilation spectroscopy (PAS) for materials science as a nondestructive probe. The high-intensity laser offers a novel approach to generating positron beams prompted by the fast development of laser techniques. Shen *et al*. has made a theoretical research of the electron-positron production by using the intense laser as early as 2001, where electron-positron production is investigated for a very thin foil target [1]. In the following we introduce the experimental generation of ultrashort MeV positron beams in our laboratory [2].

A femtosecond petawatt laser system at Shanghai Institute of Optics and Fine Mechanics (SIOM), Chinese Academy of Sciences (CAS) was employed in our experiments. It delivered laser beams with a central wavelength of λ_L = 0.8μm, a duration of 45fs, a focal spot of 12μm and a peak intensity of 3.5×10^{19} W/cm^2. A supersonic argon gas jet offers an electron density of n_e=3.8×10^{20} cm^{-3}. The experimental setup is shown in Figure 1. A huge number of relativistic electrons were produced during the laser-gas interaction. Then the electrons irradiated on the high-Z materials, and high intensity gamma rays were generated through bremsstrahlung process, which in turn interacted with nuclei and produced electron-positron pairs. A magnetic positron spectrometer is well-designed and vastly reduces the gamma rays noise. Positrons are recorded experimentally in the image plates (IPs) in single-shot working mode due to the different dispersion characteristics.

The relativistic electrons produced during the laser-gas interaction has a spectrum shown in Figure 2(a). The electron beam with an energy exceeding 1.2 MeV contains 7.7×10^9 electrons, corresponding to the charge of 1.23nC, which is more relevant to positron generation.

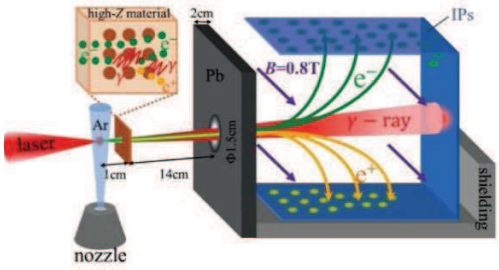

Figure 1: Schematic of the experimental setup.[2]

The spectrum of positrons generated with a 2-mm-thick lead target is shown in Figure 2(b), which is confirmed by the Geant4 simulations. Analysis shows that a maximum positron yield of 3.5×10^8 is obtained with a temporal duration of $\tau_p \leq$ 45fs, and the density of the positron beam is $n_p \approx 3 \times 10^{12}$ cm^{-3}. The ultrashort MeV positron beams are inspiring for the study of laboratory astrophysics and have great potential for PAS applications.

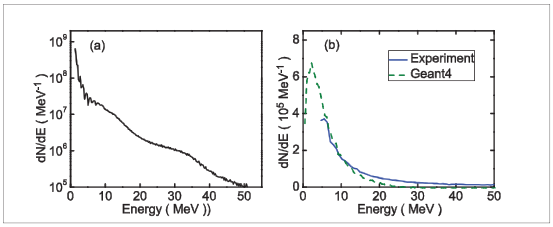

Figure 2: (a) Spectrum of the electron beam. (b) Experimental and simulated positron spectra. [2]

References

[1] B. F. Shen *et al.*, Phys. Rev. E: Stat. Nonlinear Soft Matter Phys. 65, 016405 (2001).

[2] T. J. Xu *et al.*, Phys. Plasmas 23, 033109 (2016).

#Work supported by Nat. Natural Science Foundation of China

* Corresponding author: bfshen@mail.shcnc.ac.cn

Demagnetization of PRIOR Permanent Magnet Quadrupoles*

M. Endres †[1], *M. Schanz*[1], *P. M. Lang*[2], *and D.H.H. Hoffmann*[1]
[1]TUD, Darmstadt, Germany; [2]European XFEL, Hamburg, Germany

The PRIOR-I Proton Microscope was commissioned at GSI in 2014. [**?**] The setup consists of four Permanent Magnet Quadruople (PMQ) Lenses, each one assembled from several Halbach-Style arrays (PMQ modules). The PMQ modules itself consist of 48 single NdFeB wedges arranged in two (inner and outer) circles with 24 segments each (see fig. 1). During the beam time with 4.5 GeV protons the lenses were hit and therefore damaged by radiation, resulting in a decreased quality of the magnetic field and a worse image quality. Measurements of the magnetic field after the first experiments showed a degradation of the field gradient by $10-13\%$, in addition an increase of higher multipole components was observed. Following those investigations, various NdFeB magnetic material was deliberately irradiated and analyzed.

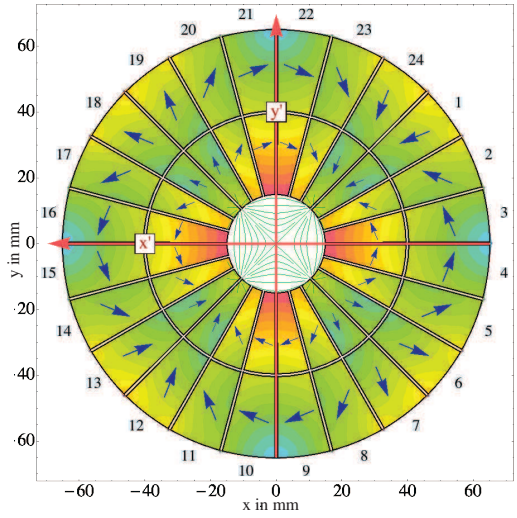

Figure 1: Geometry of the PRIOR PMQ Modules. The colour shows the internal Field H.

At first single wedges were irradiated with protons with different doses. The irradiated ones and one non-irradiated wedge were cut into small samples to scan the magnetic properties. Here a correlation between the absorbed dose and degradation was already visible. [**?**] To investigate the influence of the $\vec{H}$-Field inside an assembled module a PMQ module was deliberately irradiated. The module was irradiated with approximately $8.3 \cdot 10^{11}$ protons at 3.6 GeV. The Dose for each Wedge was measured with radiochromatic films (RCF). The field gradient was measured on the x' and y' axes each on five points (see figure 1).

The RCF showed that wedge 23 and 24 from the inner ring had absorbed the highest dose while wedge 11 and 12 from the inner ring were barely affected by radiation. These wedges were replaced with non-irradiated ones. The "repaired" module was scanned again. No increase of the field gradient in comparison with the measurement directly after the irradiation was visible. The disassembled wedges were individually scanned for their magnetic properties. No correlation between the dose and the observed degradation could be proved. This led to the conclusion that – assembled in an array – the wedges which absorbed the highest dose are not the most damaged ones.

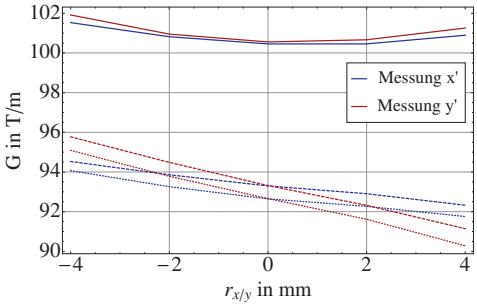

Figure 2: Gradient before (solid), after irradiation (dashed) and after exchange of segments with highest dose (points).

The replaced and analyzed wedges were located in regions which are the magnetic poles of the quadrupole. This are regions with a low $\vec{H}$-Field. It seems possible that the influence of the this field is higher than the the influence of the dose. To proof this hypothesis, more wedges have been disassembled and will be analyzed.

To overcome the issue of demagnetization, a new mircoscope facility (PRIOR-II) – based on electromagnetic quadrupoles – has been developed at GSI in 2015. [**?**] Simultaneously a setup for the remagnetization of the PRIOR-I facility is assembled at the collaborating institute ITEP.

References

[1] P. Lang, "Aufbau und Test des Protonenmikroskops PRIOR", Dissertation TU Darmstadt 2014.

[2] D. Varentsov et al., "Commissioning of the PRIOR proton microscope", Rev. Sci. Instrum. arXiv:1512.05644, (submitted) (2016).

[3] M. Schanz, "Design of a 5 GeV Proton Microscope Facility for FAIR", GSI Report 2015.

* Work supported by BMBF. This report is also submitted to *GSI Scientific Report 2015*
† m.endres@gsi.de

New elements of data acquisition system for PRIOR and HHT experiments*

A. Kantsyrev[1#], A. Bakhmutova[1], A. Bogdanov[1], E. Ladygina[1], N. Markov[1], V. Panyushkin[1], D. Varentsov[2], L. Shestov[2]
[1]ITEP NRC KI, Moscow Russia; [2]GSI, Darmstadt, Germany

Control units for HV generators

High energy proton microscopy facility PRIOR (Proton Microscope for FAIR) has been designed, constructed, and successfully commissioned at GSI [1]. For dynamic comissioning of PRIOR was developed dynamic target based on underwater electrical wire explosion UEWE[1]. The pulsed power generator for UEWE (10 μF, up to 50 kV charging voltage and 12.5 kJ stored energy) consists of four modules and can drive currents of about 200 kA in amplitude and 1.8 μs rise time through a load at charging voltage of 35–40 kV. Main capacitor set and capacitors of trigger generator (Marx 75 kV) are charged by two high-voltage (HV) generators TDK-Lambda 402-50 with output voltage up to 50 kV.

To effectively control (in frame of data acquisition system (DAQ) of HHT and PRIOR facility [2]) of HV generators were developed two independent automated units. Each unit are based on ICPDAS μPac7186 microcontroller with IO modules: i7021 (DAC), i7017 (ADC), i7063D (discrete I/O), i7520 (communication) and TPD280U touchpad. Fig. 1 shows a photo of developed units. One of the units, equipped with input voltage divider with ratio of 67.5 kV/V, is used for measure of charge voltage level of capacitors, another unit used to control of trigger HV generator. Software for μPac7186 microcontroller was written in the Borland C ++ V5 in frame of MiniOS7 Studio V1.07 software environment. Communication between the microcontroller and touch panel carried through Modbus RTU protocol via the RS232, RS485 interfaces with conversions by i7520 module. Data transfer between μPac7186 and modules i7021, i7017, i7063D occurs via DCON protocol and RS485 interface.

Developed units are provides: automatically charging of external capacitors with control and stabilizing of charging voltage level, control of emergencies (self-discharge of capacitors, lack of charging capacitors, shortcut in the capacitors), synchronization with the beam extraction system and PRIOR DAQ system, controlling of main functions and settings through touchpanel.

Figure 1: Two units for control of HV generators of UEWE dynamic target for PRIOR.

Tests of units were performed in the first experiments with UEWE target at PRIOR facility at GSI.

Synchronization scheme for PRIOR and HHT

In frame of experiments at PRIOR and HHT facility is required to ensure accurate synchronization of beam shot pulse with the start of experimental equipment such as oscilloscopes, CCD imaging system, dynamic target (e.g. UEWE). The minimum duration of the bunch beam in experiments at the PRIOR proton microscope at GSI is about 40 ns, which requires the accuracy of timing at the level of ~1 ns. Existing synchronization scheme, had synchronization error (jitter) at ~20 ns, due to using of synchro pulse from kicker extraction magnet. To improve the accuracy of timing was developed new synchronization scheme (fig. 2). It is provides synchronization of such events: beam request, triggering of kicker magnet, high frequency of accelerator and operation of the virtual accelerator machines of SIS-18. The output trigger signal is formed with accurate timing relative to a high frequency of accelerator. Controlling of scheme provided by Apeman[2] software client of existing DAQ system or manually from front panel.

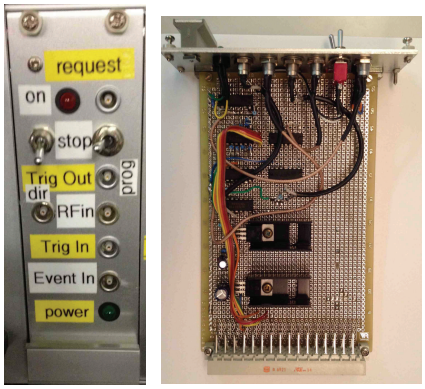

Figure 2: The photos of the front panel (left) and electronic board of new synchronization scheme.

The scheme is based on two RS-D-T flip-flops 7474 chips with a set of logic circuits. Communication and control between new synchronization scheme and DAQ provided by ICPDAS I7055D module and MOXA NPORT_5450 interfaces converter RS485-Ethernet. Transmission is produced in frame of TCP/IP Sockets and DCON data transfer protocols.

References

[1] D. Varentsov et al., “Commissioning of the PRIOR proton microscope”, Review of Scientific Instruments, 2016, 87, issue 2, p. 023303/1–023303/8.
[2] A. Hug et al, “Data acqusition system for HHT experiments”, GSI Scientific Report 2011, p. 464

* Work supported by FRRC Contract No. 29-11/13-17.
# kantsyrev@itep.ru

Recent progress in research of underwater electrical explosion of wires and wires arrays

Ya. E. Krasik, S. Efimov, D. Sheftman, O. Antonov, D. Shafer, D. Yanuka, M. Ntishinski, and V. Tz. Gurovich
Technion – Israel Institute of Technology, Haifa 32000, Israel

Underwater electrical explosion of wires can be used for research of extreme state of matter. Indeed, formation of the parasitic plasma channel along exploding wire typical for wire explosion in gas of vacuum is prevented due to high (300 kV/cm) threshold of water breakdown and water small compressibility prevents fast wire radial expansion. Thus, almost 90% of the energy initially stored in capacitor banks can to be transferred into the wire keeping high energy density deposition rate. Also, due to ~24% efficiency of the energy transfer to the water by expanding wire, one obtains generation of strong shock waves (SW). In the case of either cylindrical or spherical wire array underwater electric explosion, extreme state of water with pressure up to 10^{12} Pa, compression up to factor 10 and temperature of several eV can be obtained in the vicinity of implosion axis or origin.

Research of single wire explosion was carried out in 10^{-7} – 10^{-6}s time-scale. It was found that in a microsecond timescale, good agreement was attained between the results of experiments and the results of magnetohydrodynamic calculations coupled with equations of state (EOS) and modern conductivity models. Conversely, in a nanosecond timescale wire explosion, the wire resistance and the EOS were modified in order to fit experimental data. Thus, it was shown that this approach can be successfully used for studies of EOS and transport parameters of different metals in a broad range of temperature, pressure, density, and internal energy. The results obtained indicate that in the case of extremely fast energy density deposition, which is typical of nanosecond and submicrosecond timescales of explosion, additional research is strongly required in order to explain the difference between the experimental data and existing EOS database and conductivity models.[1,2,3]

Experiments with underwater electrical explosion of cylindrical and spherical wire arrays (see Fig. 1) were carried out using high-current pulse generators with stored energy of a several kJ only. An extreme state of water in the vicinity of the implosion of converging SWs was generated by either cylindrical (see Fig. 1) or spherical wire array explosions.

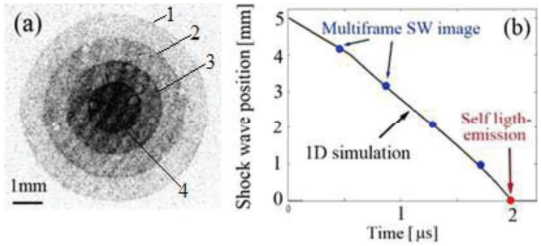

Fig. 1. (a) Sequence of four shadow images of the converging SSW indicated by 1–4, in which each frame duration is 5 ns and the time delay between the frames is 300 ns. (b) Experimentally obtained and simulated SW propagation with respect to the current beginning. Underwater electrical explosion of 30-Cu wire array of 10-mm diameter and 50-mm length. Each wire was 0.114 mm in diameter. The generator charging voltage was 80 kV. The maximal amplitude of the discharge current was ~380 kA with a rise time of ~270 ns. The energy deposited into the wire array was 4.3 kJ.

The results of HD simulations based on TOF of the SW and deposited energy into the water flow showed that in the case of a spherical SW implosion (see Fig. 2), one can expect to obtain the pressure, density, temperature of water plasma at the distance ≤10 μm from the origin of implosion, ≤6 TPa, ≤17 eV, and ≤8, respectively.[5-8] In addition, iIn order to increase the pressure in the vicinity of the SW implosion, experiments with convergence of SW in super-spherical geometry was carried out. The results of this preliminary research[9] showed that indeed this geometry allows one to achieve larger

values of pressure, density, and temperature of water in the vicinity of the axis of convergence.

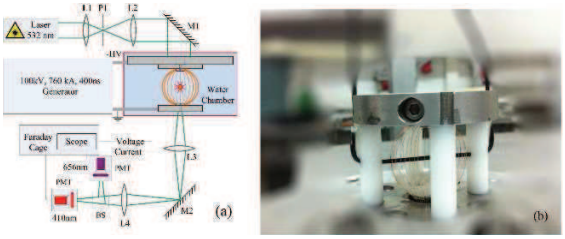

Fig. 2. (a) Experimental setup for spherical wire array explosion. (b) External view of 40-Cu-wire array of 30-mm diameter, each wire being 114 μm in diameter.

Another interesting results were obtained in experiments with X-configuration of underwater exploding wires. It was shown that the collision of the exploding wires generated by underwater electrical explosion in the X-pinch configuration creates fast-moving (2.5×10^5 cm/s) cumulative jets (see Fig. 3) similar to those generated by the collision of metal slabs, accelerated by the chemical explosion. The properties of these jets are determined by the parameters of the explosion and their interaction with the water, compressed by the SW generated by the exploded wires. This method of generation of cumulative jets is significantly simpler than common methods, and allows the application of optical diagnostics for the observation of the dynamics of the jets.[10] Using conical wire array underwater electrical explosion, a fast water jets were generated with velocities up 2 km/s.[11]

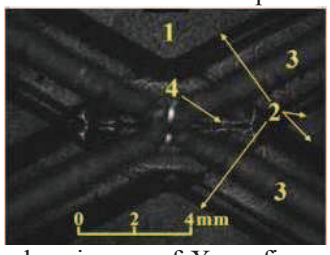

Fig. 3. Shadow image of X-configuration wires explosion. 1.Undisturbed water. 2. SW front. 3. Exploding wire. 4. Fast copper jet.

Finally, the generation of strong magnetic fields (~50 T) using single- or multi-turn coils immersed in water was studied (see Fig. 4). A pulse generator with stored energy of ~3.6 kJ, discharge current amplitude of ~220 kA, and rise time of ~1.5 μs was used in these experiments.

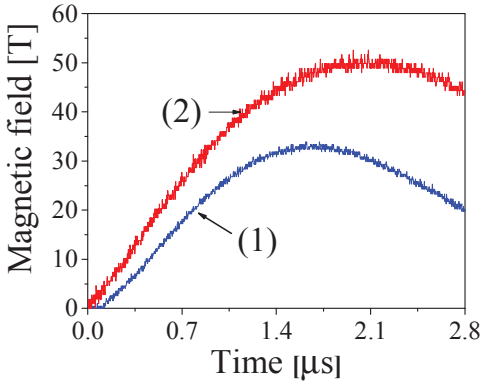

Fig. 4. Calculated magnetic fields at the center of a single-turn coil (1) and three-turn coil (2).

Using the advantage of water that it has a large Verdet constant, the magnetic field was measured using the non-disturbing method of Faraday rotation of a polarized collimated laser beam. In addition, it was shown that this approach can be used successfully to investigate the interesting phenomenon of magnetic field enhanced diffusion into a conductor.[12]

References

1. D. Sheftman and Ya. E. Krasik, *Phys. Plasmas* 18, 092704 (2011).
2. D. Sheftman, *et al.*, *Phys. Plasmas* 19, 034501 (2012).
3. D. Sheftman and Ya. E. Krasik, *Phys. Plasmas* 17, 112702 (2010).
5. O. Antonov, *et al., Phys. Plasmas* 19, 102702 (2012).
6. O. Antonov, *et al.*, *Appl. Phys. Lett.* 102, 124104 (2013).
7. O. Antonov, *et al.*, *J. Appl. Phys.* 115, 223303 (2014).
8. O. Antonov, *et al.*, *Phys. Plasmas* 22, 053507 (2015).
9. D. Yanuka, *et al.*, *J. Appl. Phys.* 117, 163305 (2015).
10. D. Shafer, et al., *J. Appl. Phys.*114, 203301 (2013).
11. D. Shafer *et al.*, *J. Appl. Phys.* 117, 015901 (2015).
12. D. Yanuka, *et al.*, J. Appl. Phys. Accepted for publication, 2016.

Investigation of Porous Materials for Shock-Wave Experiments at PRIOR*

A. Zubareva[1,2,#] and A. Utkin[1]
[1]IPCP RAS, Chernogolovka, Russia; [2]ITEP, Moscow, Russia

Research on shock-wave processes provides information on thermodynamic and rheological properties of materials in a wide range of pressures and temperatures under conditions of high strain rates. Investigation of shock compression features of porous materials is of particular interest, since the experimental study of the same material at different densities can significantly expand the area of thermodynamic states accessible by pulse loading [1-3].

Experimental setups were developed to obtain low pressures for studies of the threshold and mechanism of pore collapse under shock-wave action. Parameters of loading conditions, which are realized in this work, correspond to those assumed in the experiments on the light-gas gun at the PRIOR facility.

Samples of different porosity with the use of matrices from materials with different compressibility were selected and prepared for studies of shock waves properties and spall strength. Silicone rubber and epoxy resin were used as matrices. Glass microspheres with an average size of about 80 microns were used as a filler.

The volume ratio of silicone rubber and glass microspheres in the investigated samples was equal to 100/39 which corresponds to the density of 0.55 g/cc. The thickness of samples in all experiments was the same and equal to 4 mm. The diameter of samples was 40 mm.

In the samples of epoxy resin and glass microspheres the volume ratio of components was equal to 100/52. The density of the samples was 0.56 g/cc. The thickness of the samples varied in the range of 6.5 to 7.5 mm.

Typical particle velocity profiles obtained by VISAR laser interferometer are shown in Figure 1 and Figure 2.

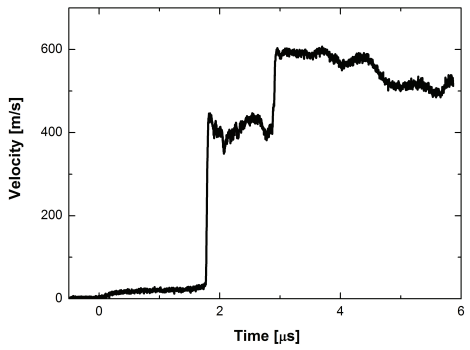

Figure 1: particle velocity profiles at the sample – water window boundary for porous rubber.

Velocity profiles for two investigated materials are similar. A difference between them is of purely quantitative nature, due to differences in shock-wave properties of matrix materials. The complicated structure of the shock wave front was observed for both materials.

First, the precursor wave propagates ahead of the shock wave, i.e. the two-wave configuration is formed which is most clearly expressed at low pressures. The speed of the second wave increases sharply with increasing pressure, while the velocity of the first wave is practically constant. This leads to the disappearance of the two-wave configuration in the porous rubber at the pressure of 1 GPa and in the porous epoxy resin at the pressure above 2 GPa.

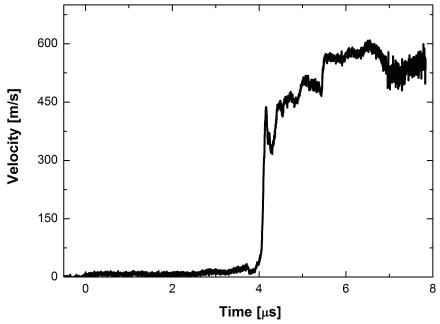

Figure 2: particle velocity profiles at the sample – water window boundary for porous epoxy resin.

Second, the heterogeneous structure of the investigated samples leads to significant oscillations on velocity profiles behind the shock jump. Since oscillations are not smoothed by the passage of the shock wave through the 7-micron aluminum foil which is used to reflect the probe laser beam, it means that the spatial size of inhomogeneities is greater than the thickness of a foil, i.e. not less than 10 microns. This estimate correlates with the size of glass microspheres which determines the characteristic size of inhomogeneities.

Third, the wave profiles have a feature that is associated with the registration technique. In all experiments, an additional velocity jump is recorded after 1 microsecond after the second wave comes to the water window border. It is due to the fact that the shock compressibility of samples is higher than that in water. Therefore, after a shock wave comes to the border with water, it is reflected back into the sample, after which it is again reflected by the shield plate and returns to the water border as a shock wave. The circulation time decreases with the increase of pressure.

References

[1] A.V. Ostrik and A.I. Potapenko, Composite Materials Constructions, 2001, (1) 48–53.
[2] V.P. Efremov, A.V. Ostrik, A.I. Potapenko and V.E. Fortov, Problems of Atomic Science and Technology: Plasma Electronics and New Methods of Acceleration Series, 2000, (1) 152–154.
[3] R.M. Christensen, Mechanics of Composite Materials (New York), 1979.

* Work supported by FAIR-Russia Research Center
#zan@ficp.ac.ru

Experimental Investigation of Shock Wave Compression of Heterogeneous Anisotropic Materials*

Valentina Mochalova[1,2,#], Alexander Utkin[1]

[1]Institute of Problems of Chemical Physics RAS, Chernogolovka, Russia; [2]FSBI "SSC RF ITEP" of NRC "Kurchatov Institute", Moscow, Russia.

Carbon fibers are composite materials, which consist of fibers from carbon with a diameter of 5-10 microns, bonded with epoxy resin. Main feature of these materials is strongly expressed anisotropy of properties. The aim of this work was to investigate the shock compressibility of carbon fiber with different fibers orientation relatively to the direction of shock waves propagation. The average density of the samples was 1.55 g/cm^3. The sound speed transversally to the fibers is equal to 3.0 km/s, and parallel is about 10 km/s.

Shock wave profiles were recorded by a laser interferometer VISAR. Probing radiation was reflected from the aluminum foil, placed between the end of the charge and the water window. Experimental data are the velocity of movement of the foil surface at the boundary with water, and show all the details of the structure of compression pulse. In each experiment the structure of compression pulse and the shock wave velocity of carbon fiber were obtained. Pressure of shock compression was varied by changing of the thickness and the velocity of projectiles.

Hugoniots of carbon fiber were obtained for two orientations of the fibers in the coordinates of the shock wave velocity D - particle velocity u. In the investigated range of pressures at the transverse orientation of the fibers experimental data are approximated by a linear dependence of D = 1.70 + 2.3*u, km/s (see fig.1). And the first factor C_0 = 1.70 km/s differs significantly from the sound speed, measured at zero pressure. Such situation is often observed for porous samples. In this case the Hugoniot is non-linear at low pressures. The coefficient C_0, which is result of extrapolation, not only may significantly differ from the sound speed under normal conditions, but often doesn't have any physical meaning.

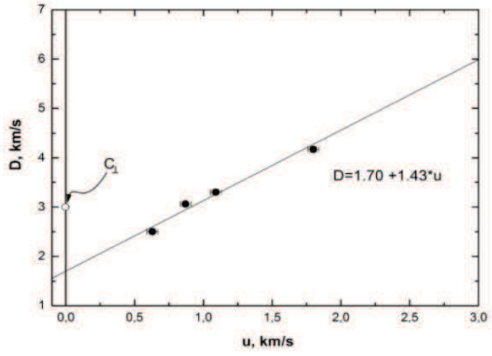

Figure 1: Hugoniot of the sample for transverse orientation of the fibers.

The Hugoniot for the parallel orientation is satisfactorily approximated by the dependence D = 2.3 + 2.0*u, km/s (see fig.2). Unlike the transverse orientation, in this case a complex structure of the shock wave is observed. Almost in the entire pressure range two-wave configuration is recorded which is most clearly expressed at low pressures. In this case the two-wave configuration is due to anisotropic structure of the sample. The velocity of propagation of disturbances along the carbon fibers is in several times higher than the velocity of the shock wave, that results in the formation of a precursor. Since the amplitude of the running ahead perturbations decays, the front of the first wave degenerates into a sound pulse, so the velocity of its propagation is close to the sound speed C=10 km/s, which was measured by ultrasonic method.

Thus, it was found that Hugoniots were different for two orientations of fibers. There is a tendency to their convergence with the pressure increasing.

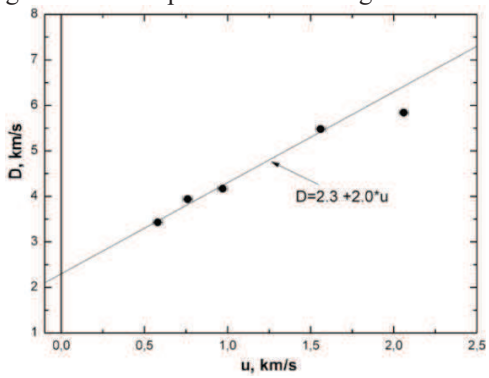

Figure 2: Hugoniot of the sample for parallel orientation of the fibers.

Also a study of spall strength for carbon fiber was conducted. It was shown that for a given material the character of spall fracture was rather complicated. For unambiguous definition of spall strength, together with recording of the free surface velocity, an additional recording of particle velocity was made. The value of spall strength along the fibers is about four times higher than the spall strength for the transverse direction. For longitudinal direction of the fibers it is equal to 175 MPa, for transverse direction – is about 40 MPa.

Thus, from the results obtained in this work it can be concluded that the correct description of the dynamic deformation of carbon fiber is possible only within the framework of the two-component model considering the real motion of the fibers and their interaction with the matrix.

* The work is carried out with the financial support of FAIR-Russia Research Center.

#roxete20000@hotmail.com

Investigation of plasma-accelerated flyer plates

S. Sander[1], *J. Helfrich*[1], *S. Frydrych*[1], *J. Ohland*[1], *C. Bläser*[1], *G. Schaumann*[1], *D. Schumacher*[2], *A. Blazevic*[2], *and M. Roth*[1]

[1]Technische Universität Darmstadt, Institut für Kernphysik, Schlossgartenstraße 9, 64289 Darmstadt, Germany;
[2]GSI Helmholtzzentrum für Schwerionenforschung GmbH, Planckstraße 1, 64291 Darmstadt, Germany

Introduction

Man-made space debris is exponentially increasing in the low earth orbit, posing a big threat on current and future space missions [1]. To remove this space debris, high velocity impacts ($v > 10\,\mathrm{km\,s^{-1}}$) of tungsten balls with a presumed momentum transfer of $\sim 10 - 15$ are proposed to slow down space debris [2]. Thereby, it will decrease in orbit and burn up in the atmosphere earlier.

Experiment

The first objective is to reach a high velocity with a tungsten flyer plate that remains in a solid state. For preliminary experiments, a special target design has been developed as seen in figure 1.
The first layer is a 270 µm thick polyethylene (PE) sample. A tungsten thumbtack construction with a 50 µm thick and 600 µm long stalk and a head diameter of 600 µm and 25 µm thickness is glued on the PE rear side. In this setup, the accelerated head is free and not glued to any structure other than the PE itself.
The experiments are performed at the target area *Z6* at GSI, where the *nhelix* laser system is used to drive a shock wave into the PE. After the shock breakout, the expanding material hits the disk of the thumbtack. This is supposed to accelerate the thumbtack to high velocities, while retaining the solid state of the disk.
With a streak camera the shock breakout on the rear side of the PE is determined to calculate the shock velocity in the PE. This information is used to benchmark future simulations. The temporal behaviour of the plate is measured with two *DICAM Pro* in a side view configuration (see figure 1). Over several shots, a time evolution of the flyer plates reaction has been obtained (see figure 2).
In figure 2a, the tungsten disk can be seen undisturbed. 100 ns after the *nhelix* impact, the expanding material reaches the flyer plate (2b). In figure 2c, at $t = 150\,\mathrm{ns}$, the flyer plate starts to expand and eventually breaks apart as seen in figure 2d. Over multiple shots an average expansion velocity of the PE was estimated to $\sim 1\,\mathrm{km\,s^{-1}}$. A rough estimate of the expansion of the tungsten in figure 2c and d results in $v_{\mathrm{expansion}} \approx 7\,\mathrm{km\,s^{-1}}$. A movement of the flyer plate prior to break up could not be confirmed. This phenomenon is currently under investigation. Possible explanations are a pre heat of the flyer plate due to radiation from the *nhelix*-PE interaction or a generation of a strong shock wave in the tungsten.

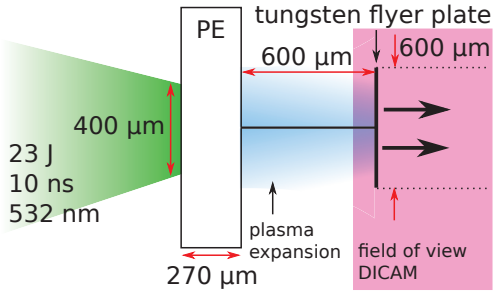

Figure 1: Schematic setup of experiment: The shock wave is driven with the *nhelix* laser (with 23 J, 532 nm, 10 ns, spotsize 400 µm and intensity homogenized flat top) into 270 µm thick PE samples. A streak camera determines the shock breakout on the PE rear side. The flyer plate is observed with two *DICAM Pro* in a side view configuration.

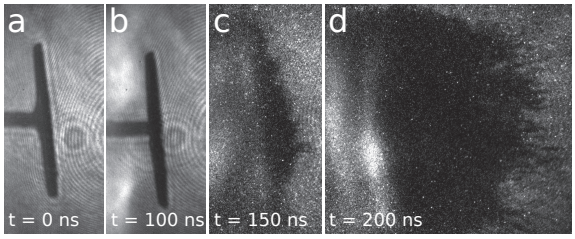

Figure 2: *DICAM Pro* measurements show the temporal development of the impacting plasma expansion on the flyer plate and the reaction of the plate.

Simulation

Simultaneously, hydrodynamic fluid simulations are prepared to further study possible target designs. In a first step, the FEOS code has been analysed and is now used to produce the equations of state (EOS) for tungsten and PE which are required for the simulations. These simulations will be benchmarked with the already received experimental results.

References

[1] McKnight, Darren and Donald Kessler, IEEE Spectrum, Retrieved (2012).

[2] G. Ganguli, C. Crabtree, L. Rudakov, S. Chappie, Aerospace Conference, 2012 IEEE (2012).

This report is also submitted to the GSI Scientific Report 2015.

4 Accelerator and Beam Physics

Optical Beam Profile Measurements Using Light Emission from Nitrogen at Various Pressures *

Y. Shutko† [1], *D. H. H. Hoffmann*[1], *P. Forck*[2, 3], *F. Becker*[2], *C. Dorn*[2], *R. Haseitl*[2], *B. Walasek-Höhne*[2], *S. Udrea*‡ [3], *T. Dandl*[4], *J. Wieser*[4], *and A. Ulrich*[4]

[1]TU Darmstadt; [2]GSI, Darmstadt; [3]Goethe Universität Frankfurt am Main; [4]TU München

A Beam Induced Fluorescence (BIF) monitor is a diagnostic tool, based on the detection of photons emitted from residual gas excited by the ion beam [1]. To apply this method to the FAIR facilities, the influence of different parameters such as gas pressure, beam energies, etc. has to be investigated. Imaging spectroscopy has been performed in a gas cell with a titanium entrance foil at the Munich Tandem van de Graaff accelerator with a continuous 200 nA S^{8+} beam at 3.75 MeV/u. Experiments were performed for nitrogen in a gas pressure range from 0.001 to 30 mbar. A detailed description of the experimental set-up can be found in [2].

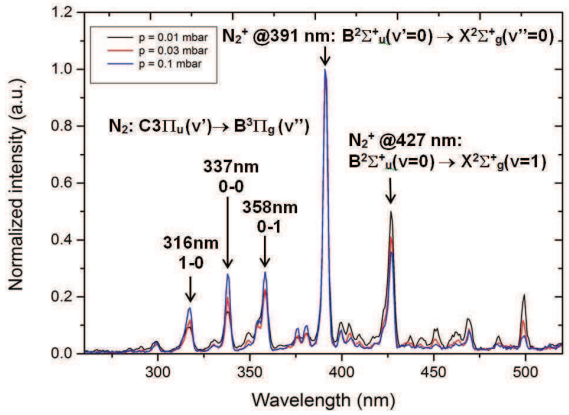

Figure 1: Nitrogen spectra obtained at different gas pressures with labeled dominant molecular transitions.

Nitrogen spectra obtained at different pressures are presented in Fig. 1. Two emission bands were investigated in detail: the 337 nm band corresponding to neutral nitrogen ($C^3\Pi_u(v' = 0) \rightarrow B^3\Pi_g(v'' = 0)$), and the 391 nm band corresponding to ionized nitrogen ($B^2\Sigma_u^+(v' = 0) \rightarrow X^2\Sigma_g^+(v'' = 0)$) [3]. Profiles of the imaged beam based on these transitions are shown in Fig. 2. The imaged beam profile width of the neutral N_2 $C \rightarrow B(0-0)$ transition shows a strong dependence on pressure, while the width of N_2^+ $B \rightarrow X(0-0)$ transition remains almost constant [2]. This behavior can be interpreted by different excitation mechanisms of these two molecular transitions. The 391 nm band, which represents the correct transverse profile of the imaged beam in the entire measurement range, is caused only by collisions of the beam projectiles and gas molecules which lead to ionization of the nitrogen and secondary electron emission. These electrons excite N_2 molecules to the electronic state $C^3\Pi_u$ and transition to $B^3\Pi_g$ levels are observed at the 337 nm band. The mean free path of the secondary electrons emitted from the beam path depends on the gas pressure. This fact in combination with larger excitation cross section of secondary electrons for neutral molecules effects on an correct transverse profile of the imaged beam representation, see Fig. 3. A detailed discussion is given in [4].

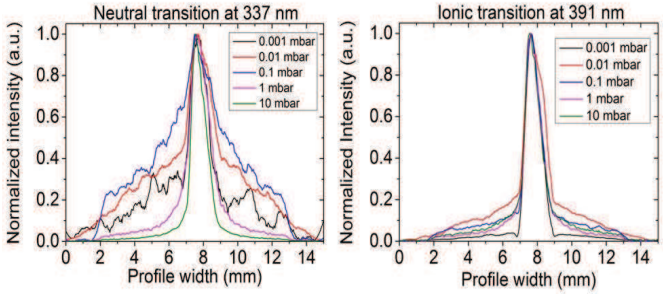

Figure 2: Profiles of the imaged beam measured for different pressures using the neutral (337 nm) and ionic (391 nm) nitrogen emission bands.

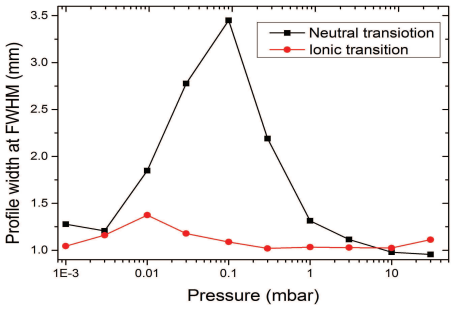

Figure 3: Profile width of the imaged beam, characterized by FWHM, of the neutral (337 nm) and ionic (391 nm) nitrogen emission bands.

References

[1] C. A. Andre, et al.,Proc. of DIPAC2011, p.185.

[2] F. Becker, et al., Proc. of IPAC2012, p. 798.

[3] A. Lofthus and H. Krupenie. J. Phys. Chem. Ref. Data, Vol. 6, No. 1, 1977. p.113.

[4] Y. Shutko, PhD thesis, TU Darmstadt, in preparation.

* Work supported by BMBF project No. 05P12RDRBN and Graduate School of Excellence ESE TU- Darmstadt.

† y.shutko@gsi.de

‡ Work supported by LOEWE-HIC for FAIR

Gas Dynamics Simulations for Heavy Ion Induced Desorption Measurements with the Single Shot Method *

Ch. Maurer[† 1,2], *L. Bozyk*[1], *P. Spiller*[1], *and D.H.H. Hoffmann*[2]
[1]GSI, Darmstadt, Germany; [2]TU Darmstadt, Institut für Kernphysik, Germany

Introduction

Beam induced gas desorption is a key process that drives beam intensity limiting ionization losses in heavy ion synchrotrons in general and in the upcoming SIS100 in particular. Measuring the beam impact induced desorption yield of (cryogenic) collimator materials behind from a synchrotron presents a challenge in itself, since the well established continuous bombardment method [1] cannot be used. Instead, a technique suitable for repetition rates in the mHz-regime is needed. The key task is to find a way to compute the number of desorbed particles from the measured pressure pulse. The gas dynamics simulations presented here are used to gain a better understanding of the influence of adsorption/redesorption processes, the experiment's geometry and temperature on the shape of the pressure pulse and to improve the accuracy of the data analysis.

Current Method

An important component of a typical single shot desorption experiment is its diagnostic volume V, which also contains the target. Gas desorbed from the target after beam impact disperses in this region, giving rise to a characteristic pressure pulse, called "desorption peak". Using the ideal gas law, the number ob desorbed particles ΔN is then calculated as

$$\Delta N = \frac{\Delta p V}{k_{\mathrm{B}} T}, \qquad (1)$$

where Δp is the desorption peak's height and T is the gas temperature. This method assumes a uniform gas temperature and the coincidence of the desorption peak's maximum with a homogenous distribution of all desorbed gas in the diagnostic volume. Furthermore, this spreading is supposed to take place on a faster timescale than pumping, so that gas escaping from V before a homogenuous distribution is reached can be neglected. Comparing measurements with different geometries [2, 3] shows significant deviations in the time structure of the desorption peak. Therefore, a deeper understanding of the dynamics involved is needed to facilitate a more accurate analysis.

Gas Dynamic Simulations

A gas dynamic simulation code, such as Molflow+, provides a means to model the desorption peak's formation [4]. It tracks gas particles in a given geometry and can compute pressure profiles from the results. The latest version is capable to simulate time dependent pressure evolutions with regard to adjustable sojourn times t between adsorption on and redesorption from the chamber walls. First simulations show the influence of sojourn times on the peak height (Fig. 1), pointing out the need for an improved analysis.

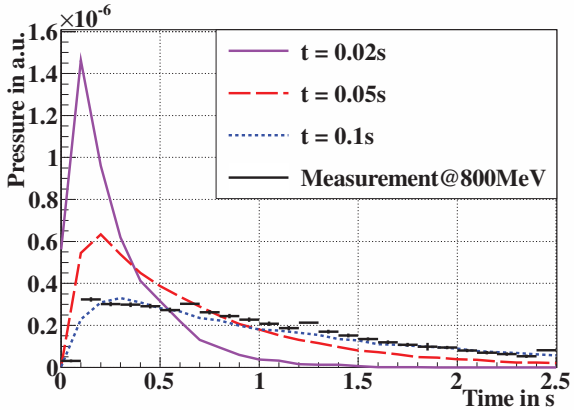

Figure 1: A Measurement and simulated desorption peaks with different sojourn times t for the geometry in [2].

Outlook

Gas dynamics simulation with Molflow+ promise a significant gain in accuracy for high energy desorption measurements. Improving future desorption experiments as well as reevaluation of already existing data will boost our understanding of the desorption process, improve the prediction by simulations, and might to better solutions regarding beam loss due to dynamic vacuum effects.

References

[1] D. P. Holzer et al., "Heavy-ion-induced desorption yields of cryogenic surfaces bombarded with 1.4 MeV/u xenon ions", in PhysRefSTAB **16**, p. 083201 (2013)

[2] L. Bozyk, H. Kollmus, P.J. Spiller, "Development of a Cryocatcher-System for SIS100", in Proc. of IPAC 2012, p. 3239

[3] Ch. Maurer et al., "Heavy Ion Induced Desorption Measurements on Cryogenic Targets," in Proc. of IPAC 2014, p. 867

[4] M. Ady, R. Kersevan "Introduction to the Latest Version of the Test-particle Monte Carlo Code Molflow+" in Proc. of IPAC 2014, p.2348

* This report is also submitted to the GSI Scientific Report 2015

† C.Maurer@gsi.de

State of development of the inductive coupled plasma stripper device *

K. Cistakov[1#], A. Fedjuschenko[1], G. Xu[1,2,3], Ph. Christ[1], M. Iberler[1], T. Ackermann[1], T. Rienecker[1], A. Blazevic[4], K. Weyrich[4], O. Rosmej[4], A. Schönlein[1], J. Wiechula[1], T. Manegold[1], S. Zähter[1] and J. Jacoby[1]

[1]Goethe University of Frankfurt, Frankfurt am Main, Germany; [2]IMP, Lanzhou, China; [3]UCAS, Beijing, China; [4]GSI, Darmstadt, Germany;

At the present time gas and solid foils are mainly used as stripper in accelerator facilities like GSI to achieve an increase in the charge state of the ions. As an alternative to these methods a dense pinch plasma is proposed as stripper medium. Compared to a gas stripper, which shows much less effectiveness, and a foil stripper, which has a shorter life time, a plasma stripper has both higher efficiency and longer lifetime. As a consequence, this novel stripper is recommended for the requirements at FAIR.

The effect of a plasma for the increase of the equilibrium charge states has been already proved in experiments with a Z-pinch [1]. However, a disadvantage of the Z-pinch is the erosion of the electrodes, which has a negative impact in the lifetime of the systems. Apart from that, the high magnetic fields have an adverse effect in the beam optic. In contrary to the Z-pinch a Theta-pinch has no erosion and the magnetic field of the coil is mainly in the center of the coil. The magnetic field distribution is mainly parallel to the beam and has therefore no influence to the beam dynamics [2] [3] [4]. For the ignition of a dense plasma, a spherical Theta-pinch was developed and successfully tested at a beam time at GSI. A major feature of the Theta-pinch is the use of a large spherical discharge vessel surrounded by a multi-turn induction coil, which is connected to a capacitor bank via low inductance transmission line, thus forming a resonant circuit. The stored energy in the capacitors was 3.6 kJ. As switch a high power thyristor stack was used. During the pinch a maximum electron density of about $3.5 \times 10^{22} m^{-3}$ (Figure 1) were achieved.

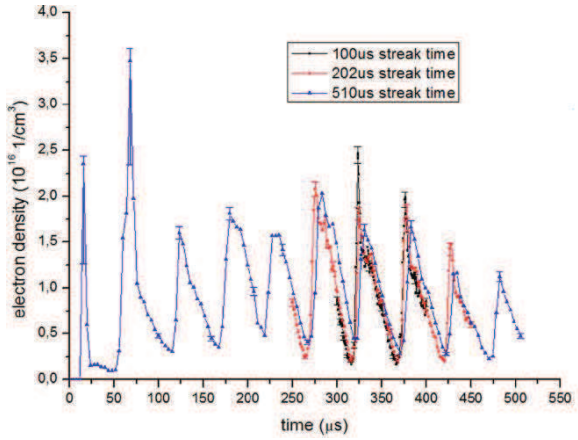

Figure 1. Electron density of a 14 kV, 110 Pa discharge, measured with different streak times [5].

The charge state of the ion beam was increased. In experiment on Z6 Area during beam time 2014, the initial state of the ion beam Au^{26} was increased to the final state of Au^{31}.The measurements made with the spherical Theta-pinch during the beam time showed, however, a negative impact in the beam optic due to distortion of the magnetic field at the ends of the coil. The reason is an asymmetrical current flow at the connecting elements of the coil. Therefore a maximum ion transmission of about 58% was achieved. A modified form of the Theta-pinch is being developed to increase the electron density and the transmission.

A new stripper cell with cylindrical coil and symmetrical power connection was designed, in order to eliminate asymmetric magnetic fields. Through the diamagnetism of the plasma along the entire z-axis, the ion beam will be sufficiently protected from the influence of asymmetric magnetic fields.

Because of the cylindrical design of the coil, the efficiency of the energy transfer will be decreased from 85% to a maximum of 50%. Due to the new coil design the energy storage system has been increased from 3.6 kJ to 49 kJ. Thus, the energy deposition into the plasma is expected to be increased by a factor of 8. Within this configuration the expected plasma densities are of $3 \times 10^{23} m^{-3}$.

References

[1] J. Jacoby, „Stopping of Heavy Ions in a Hydrogen Plasma," *Physical Review Letters,* 27 Februar 1995.

[2] C. Teske, J. Jacoby, F. Senzel und W. Schweizer, „Energy transfer efficiency of a spherical theta pinch," *Phys. Plasmas,* Bd. 17, Nr. 043501, 2010.

[3] C. Teske, Y. Liu, S. Blaes und J. Jacoby, „033505," *Physics of Plasmas 19,* 2012.

[4] G. Loisch, G. Xu, C. Teske, K. Cistakov, A. Fedjuschenko, M. Iberler, Y. Liu, T. Rienecker, A. Schönlein, F. Senzel, J. Wiechula und J. Jacoby, „IEEE Transactions on 42," *Plasma Science,* 2014.

[5] G. Loisch, G. Xu, A. Blazevic, B. Cihodariu-Ionita und J. Jacoby, „Hydrogen Plasma Dynamics in the Spherical Theta Pinch Plasma Target for Heavy Ion Stripping," *Physics of Plasmas 22,* 2015.

* Work supported by BMBF contract No 05P2015.
# cistakov@iap.uni-frankfurt.de
* This report is also submitted to the GSI Scientific Report 2015

Detailed simulation of the beam forming system for LAPLAS

D. Liakin[1], A. Golubev[1], and O. Rosmej[2]
[1]ITEP, Moskwa, Russia; [2]GSI, Darmstadt, Germany.

Detailed simulation of the beam transport has been performed to get a most realistic estimation of the beam quality in the volume of the experimental target. The particular interest was the observing of distortions in the optic system including superconducting quadrupoles and the radio-frequency deflector described in the technical design report (TDR) of the LAPLAS experiment[1]. Different system detailing levels starting from linear optics to numerical system with use of particle dynamics in realistic 3D electromagnetic fields were used to get values for the final beam quality. Due to functional limitations of programs GICOSY and SIMON, used for TDR, it was necessary to develop a new beam transport analysis code. This code is based on proved algorithms of the matrix algebra, multidimensional interpolation algorithms, ODE solvers etc. presented in MATLAB. It includes a possibility to import time-dependent 3D electromagnetic field distributions from commercial solvers like CST studio or COMSOL.

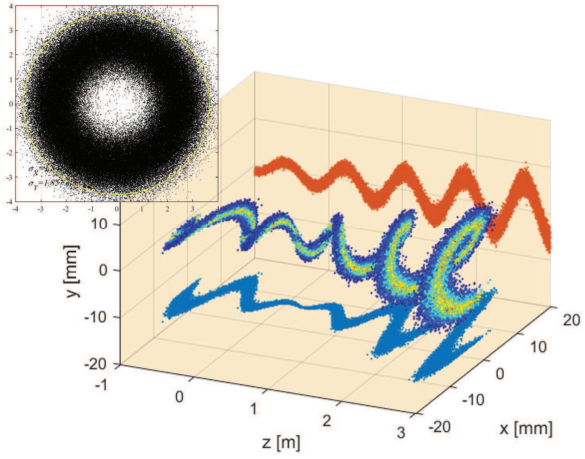

Figure 1: The beam profile and the snapshot of the 3D particles density distribution for the monochromatic beam.

As a result, the program could produce varied in time 3D beam density distribution, similar to one shown on Fig. 1.

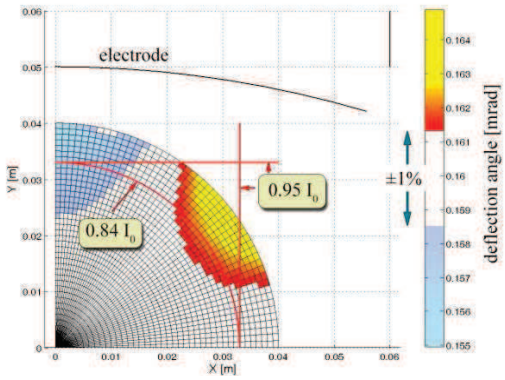

Figure 2: A one-percent uniformity area of the single cell of the RF deflector.

It is important to investigate particular contributions of various effects on the final beam quality. With developed code it is possible to switch off all except one distortion mechanisms to get a specific value. Figure 2 shows the quality area chart comes from beam transport 3D simulations performed for a single RF deflector cell. Figure 3 presents another result of simulation made for monochrome beam. Only high order non-linear effects in quadrupoles are “switched” on.

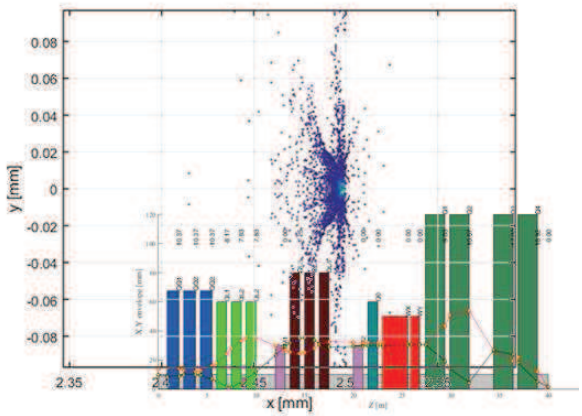

Figure 3: Beam spot distortions caused by nonlinear effects in superconducting lenses.

The table below presents the refined specific ring width for different effects applied to monochrome beam with ring radius of 2.5 mm.

	σ
Chromatic effect	140 um
Wobbler	40 um
Lenses nonlinearity	13 um
Lens production error.	14 um
Target depth effect	9 um

One can see the most significant contribution of chromatic aberrations. Those effects define the minimal achievable spot size sigma in the range of hundred micrometers. The density distribution of a such spot, formed purely by chromatic aberrations and the system nonlinearities is far from Gaussian, which leads to some azimuthal symmetry violation during the spot rotation. This may constrain the lowest usable beam spot size sigma to 200 um. At the same time even a thoroughly modeling shows no perceptible azimuthal variation for the case of the beam spot size used in the TDR(about 500um).

References

[1] Technical Design Report for the RF multicell deflector(wobbler) for LAPLAS experiment.

Beam-loss criteria for heavy-ion accelerators*

P. Katrík[1 #], D. H. H. Hoffmann[2], E. Mustafin[1], I. Strašík[1], M. Pavlovič[3]
[1]GSI, Darmstadt, Germany; [2]TU Darmstadt, Darmstadt, Germany, [3]FEI STU, Bratislava, Slovakia.

Activation of high-energy heavy-ion accelerators due to beam losses is a serious issue for some accelerator components. Knowledge about accumulated nuclides inside the activated accelerator components is important for their handling, treatment, storage, transportation and final disposal [1].

The beam losses below 1 W/m are considered as tolerable for "hands-on" maintenance on proton machines [2]. In our previous studies, a scaling law has been established to expand the existing proton beam-loss tolerance to heavy-ion beams using the FLUKA 2008 code [3]. Cross-checking of two Monte Carlo code versions was triggered by the release of the FLUKA 2011 with the new feature for nucleus-nucleus interactions calculated below 100 MeV/u [4].

Simulations

A bulky target has been chosen to represent compact structures like magnet yokes or coils. The cylindrical bulky target was 60 cm long and had a diameter of 20 cm. The target material was high-purity (better than 99.9%) copper (density of 8.92 g/cm^3). Irradiation was simulated using a continuous ^{238}U ion beam normalized to the beam power of 1 W during 100 days, and 20 years, respectively. Different beam energies ranging between 25 MeV/u and 1 GeV/u have been chosen. The produced nuclides, their activities and effective dose-rates were scored at several defined time-points: immediately at the end of irradiation, 1 day, 100 days, 1 year and 20 years after the end of irradiation. This paper presents a selection of the obtained data.

Results and Discussion

The new feature in the FLUKA 2011 does show an impact on the induced activity resulting in stricter beam-loss criteria compared to older versions (see Table 1, the 1st and the 2nd column). The simulation shows that there is an accumulation of the long-living nuclides at irradiation lasting 20 years. That is why the beam-loss criteria are even decreasing compared to the ones for 100 days of irradiation (see Table 1, the 3rd column). The scaling law based on proton losses cannot be applied for heavy-ion beams at energies below 150 MeV/u, because one of the main assumptions – the same population of produced nuclides – is not valid anymore below this energy [3]. For the same reason, the effective dose-rate becomes the keystone instead of induced activity (see Table 2).

Table 1: The beam-loss criteria for ^{238}U beams with different energies calculated by previous and recent FLUKA versions at the end of irradiation.

		Beam-loss criteria [W/m]		
	Irradiation time:	100 days	100 days	20 years
Beam energy:	1 GeV/u	5	5	4
	500 MeV/u	12	12	9
	200 MeV/u	60	40	30
	150 MeV/u		52	39
		FLUKA 2008.3.6	FLUKA 2011.2b.5	

The list of the nuclides with dominant contribution to the effective dose-rate from proton and uranium accelerators after 20 years of operation and 20 years of cooling is shown in Table 2. The production of the nuclides depends on the ion species and the beam energy. Comparison within the same beam species shows that pole positions for 1 GeV/u and 200 MeV/u is engaged by target fragments and projectile fragments, respectively.

References

[1] International Atomic Energy Agency, "Classification of Radioactive Waste", Safety Series No. 111-G-1.1(1994).

[2] N. V. Mokhov et al., "Proceedings of the 7th ICFA Mini-workshop on High Intensity High Brightness Hadron Beams", Wisconsin, September 1999, p 51-61

[3] I. Strašík et al., Phys. Rev. ST Accel. Beams 13, (2010) 071004.

[4] P. Katrík et al., "New results on the beam-loss criteria for heavy-ion accelerators", SATIF 12, Batavia, Illinois, USA, June 2015, p. 124

Table 2: Effective dose-rates (EDR) of nuclides produced by proton and uranium beams with different energies after 20 years of irradiation of Cu target followed by 20 years of cooling simulated by FLUKA 2011.2b.5.

	Effective dose-rates [mSv/h]		Effective dose-rates [mSv/h]		Effective dose-rates [mSv/h]
Beam:	^{1}H with E = 1 GeV/u		^{238}U with E = 1 GeV/u		^{238}U with E = 200 MeV/u
Sc-44	$1.0\times10^{-10}\pm8\times10^{-13}$	Sc-44	$1.2\times10^{-11}\pm3\times10^{-14}$	Bi-207	$2.0\times10^{-12}\pm5\times10^{-14}$
Ti-44	$5.7\times10^{-11}\pm4\times10^{-13}$	Ti-44	$7.1\times10^{-12}\pm2\times10^{-14}$	Tl-208	$6.1\times10^{-13}\pm2\times10^{-14}$
Co-60	$1.7\times10^{-11}\pm3\times10^{-14}$	Co-60	$3.7\times10^{-12}\pm3\times10^{-15}$	Co-60	$4.9\times10^{-13}\pm1\times10^{-15}$
K-42	$6.6\times10^{-12}\pm3\times10^{-13}$	Bi-207	$3.1\times10^{-12}\pm2\times10^{-14}$	Bi-210	$3.3\times10^{-13}\pm8\times10^{-15}$
Na-22	$5.4\times10^{-12}\pm1\times10^{-13}$	K-42	$1.2\times10^{-12}\pm8\times10^{-15}$	Sc-44	$2.2\times10^{-13}\pm7\times10^{-15}$
Ar-39	$2.3\times10^{-13}\pm1\times10^{-15}$	Tl-208	$7.5\times10^{-13}\pm9\times10^{-15}$	Pm-145	$1.5\times10^{-13}\pm3\times10^{-15}$
Fe-55	$2.6\times10^{-14}\pm4\times10^{-17}$	Na-22	$7.5\times10^{-13}\pm3\times10^{-15}$	K-42	$1.4\times10^{-13}\pm6\times10^{-15}$
Al-26	$1.7\times10^{-14}\pm3\times10^{-16}$	Bi-210	$4.7\times10^{-13}\pm4\times10^{-15}$	Ba-133	$1.4\times10^{-13}\pm3\times10^{-15}$
Ni-59	$4.8\times10^{-15}\pm6\times10^{-18}$	Bi-212	$1.4\times10^{-13}\pm2\times10^{-15}$	Ti-44	$1.3\times10^{-13}\pm4\times10^{-15}$
Mn-54	$3.5\times10^{-15}\pm7\times10^{-18}$	Pb-212	$1.3\times10^{-13}\pm2\times10^{-15}$	Bi-212	$1.1\times10^{-13}\pm3\times10^{-15}$
SUM:	$1.9\times10^{-10}\pm9\times10^{-13}$		$3.0\times10^{-11}\pm4\times10^{-14}$		$4.3\times10^{-12}\pm6\times10^{-14}$

* Work supported by HGS-HIRe. #p.katrik@gsi.de
This report is also submitted to the GSI Scientific Report 2015

Status of the F8SR Project

M. Droba[1], A. Ates[1], H. Niebuhr[1], D. Noll[1], O. Meusel[1], U. Ratzinger[1] and J.F. Wagner[1,2]
[1]Goethe University Frankfurt, Frankfurt am Main, Germany, [2]CERN, Geneva, Switzerland.

The present investigation on the design of the **F**igure-**8** high current **s**torage **r**ing (F8SR) [1] focus on the beam injection part and diagnostics. The research and development include particle tracking simulations as well as an experimental investigation of the beam dynamics and beam manipulation in a scaled down version of the injection channel.

An optimized adiabatic magnetic channel, starting from a moderate magnetic field up to a maximum of 6 Tesla (main field level in a storage ring), with a realistic field model of the toroidal coils was proposed and investigated for the superconducting F8SR under full space charge condition (Fig. 1).

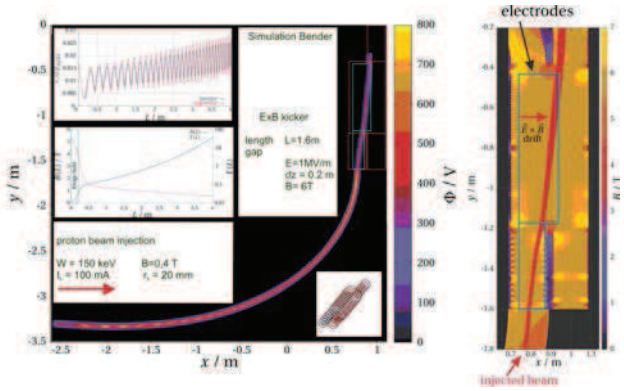

Figure 1: Beam tracking simulation through the proposed adiabatic injection channel and ExB kicker [2].

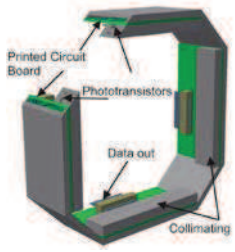

Figure 2: Further development of the non-destructive optical beam diagnostics.

An optical detector (Fig. 2) with photodiodes and phototransistors was developed and successfully tested in-situ with beam and at magnetic field levels up to 0.6T.

In parallel, a scaled down experimental set-up (Fig. 3) was built and first investigations with beam are planned this year. The upcoming tasks are the evaluation of the diagnostics system, the ion species filtering, beam injection and the comparison between beam dynamic simulations and experiments.

References

[1] J. Wagner et al., GSI-Report-2015-2, p.11.
[2] J. Wagner et al., "Status of injection studies into the Figure-8 storage ring", MOPWA036, Proc. of IPAC´15, Richmond, VA, USA, http://www. jacow.org.

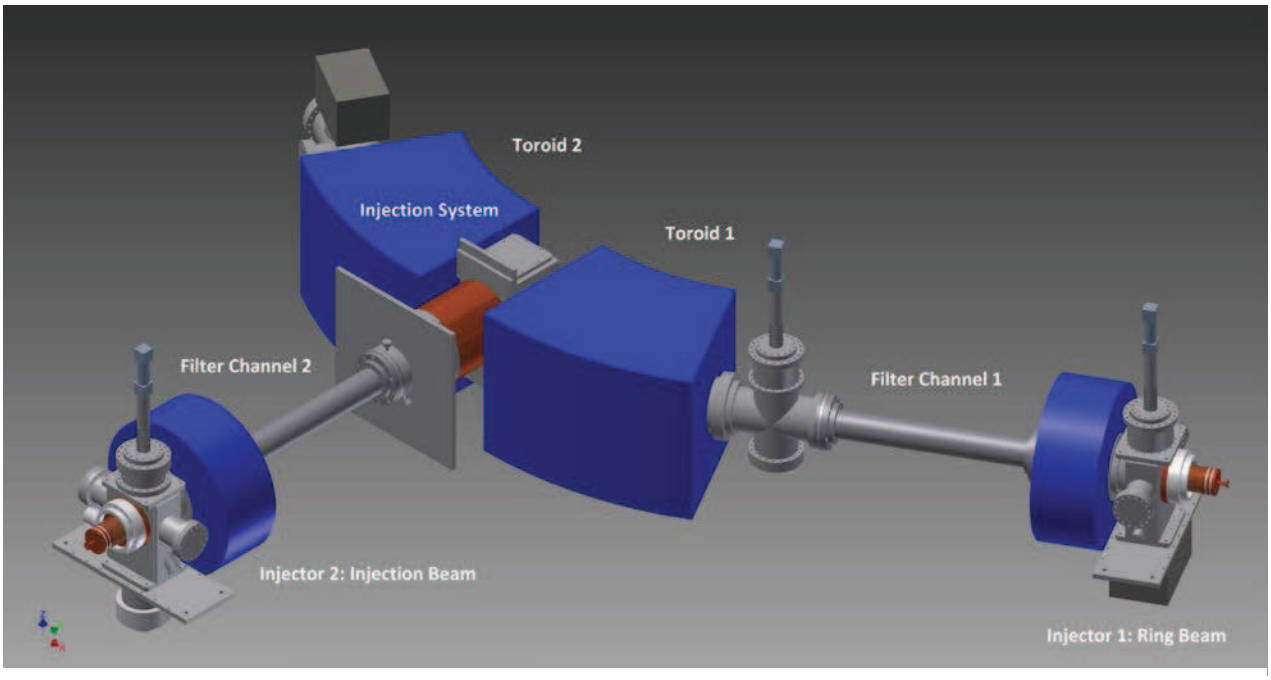

Figure 3: Design of the scaled down, room temperature (B ~ 0.6T) experimental set-up at IAP (Goethe University Frankfurt) for low energy ion beam injection and beam dynamics investigation related to F8SR.

5 Theory for HEDP/WDM in Plasma-, Laser- and Atomic Physics

Heat capacity of warm dense matter at constant volume *

C.-V. Meister[1,2] *and D.H.H. Hoffmann*[1,2]

[1]Institut für Kernphysik, Schlossgartenstr. 9, 64289 - Darmstadt; [2]Graduate School of Excellence Energy Science and Engineering, Jovanka-Bontschits-Str. 2, 64287 - Darmstadt, Germany

Abstract

To calculate the heat transport in the target material hitten by heavy ion beams, one may apply the inelastic thermal spike model. In this model, the heat capacity of the electrons and ions occurs. But, for the heat capacities of the electrons, up to now, only some rough approximations are available, and for the ions of the target materials, experimental data have to be used. Therefore, here a method is presented which may help to calculate the heat capacity at constant volume up to the density order $5/2$.

Heat capacity at constant volume

Expressions for the density of the free energy f and the pressure p of charged particles in warm dense matter, as function of volume and particle densities, are available as virial expansions in density order up to 5/2 [1-6]. From there, the heat capacity at constant volume V and constant particle densities n_a may be calculated using the formula

$$c_v = -TV\frac{\partial^2 f}{\partial T^2} = -TV\left(\frac{2\beta}{T^2}\frac{\partial f}{\partial \beta} + \frac{\beta^2}{T^2}\frac{\partial^2 f}{\partial \beta^2}\right),$$

where

$$\frac{\partial f}{\partial \beta} = -\frac{\kappa^3}{24\pi\beta^2} - 2\pi\sum_{ab} n_a n_b \Big\{ \frac{1}{6}\left(\frac{q_a q_b}{4\pi\varepsilon_o}\right)^3 \cdot \left(\beta + \frac{\beta^2 q_q q_b \kappa}{4\pi\varepsilon_o} + \ln(\kappa\lambda_{ab})\left[2\beta + \frac{7\beta^2 q_a q_b \kappa}{8\pi\varepsilon_o}\right]\right) + \left(\frac{\lambda_{ab}^3}{2\beta^2} + \frac{q_a q_b}{4\pi\varepsilon_o}\frac{2\kappa\lambda_{ab}^3}{\beta}\right) K_o(\xi_{ab}, s_a) + \frac{\lambda_{ab}^3 \xi_{ab}}{2\beta}\left(\frac{1}{\beta} + \frac{q_a q_b \kappa}{4\pi\varepsilon_o}\right)\frac{\partial K_o(\xi_{ab}, s_a)}{\partial \xi_{ab}} - \frac{7}{12}\left(1 - \ln\frac{4}{3}\right)\left(\frac{q_a q_b}{4\pi\varepsilon_o}\right)^4 \kappa\beta^2 \Big\} + \frac{7}{2}a_1 \sum_{abc} \frac{n_a n_b n_c}{\kappa\beta^2}\left(\frac{\beta}{4\pi\varepsilon_o}\right)^5 q_a^4 q_b^3 q_c^3 - \frac{7}{2}a_2 \sum_{abcd} \frac{n_a n_b n_c n_d}{2\kappa^3\beta^2}\left(\frac{\beta}{4\pi\varepsilon_o}\right)^6 (q_a q_b q_c q_d)^3 + \frac{1}{8}\sum_a \frac{q_a^2}{4\pi\varepsilon_o}\frac{\kappa^3\lambda_{aa}^3 n_a}{\beta} + O\left(\frac{n^3 \ln n}{\beta^2}\right).$$

$$\frac{\partial^2 f}{\partial \beta^2} = \frac{1\kappa^3}{48\pi\beta^3} - 2\pi\sum_{ab} n_a n_b \Big\{ \frac{1}{6}\left(\frac{q_a q_b}{4\pi\varepsilon_o}\right)^3 \left(1 + \frac{5}{2}\frac{\beta q_q q_b \kappa}{4\pi\varepsilon_o}\left[2\beta + \frac{7\beta^2 q_a q_b \kappa}{8\pi\varepsilon_o}\right] + \ln(\kappa\lambda_{ab})\left[2 + \frac{35\beta q_a q_b \kappa}{16\pi\varepsilon_o}\right]\right) + \left(\frac{-\lambda_{ab}^3}{4\beta^3} + \frac{q_a q_b}{4\pi\varepsilon_o}\frac{2\kappa\lambda_{ab}^3}{\beta^2}\right) K_o(\xi_{ab}, s_a) + \left(\frac{\lambda_{ab}^3}{2\beta^2} + \frac{7}{4}\frac{q_a q_b}{4\pi\varepsilon_o}\frac{\kappa\lambda_{ab}^3}{\beta^2}\right)\xi_{ab}\frac{\partial K_o(\xi_{ab}, s_a)}{\partial \xi_{ab}} - \frac{35}{24}\left(1 - \ln\frac{4}{3}\right)\left(\frac{q_a q_b}{4\pi\varepsilon_o}\right)^4 \kappa\beta \Big\} + \frac{35}{4}a_1 \sum_{abc} \frac{n_a n_b n_c}{\kappa\beta^3}\left(\frac{\beta}{4\pi\varepsilon_o}\right)^5 q_a^4 q_b^3 q_c^3 - \frac{35}{4}a_2 \sum_{abcd} \frac{n_a n_b n_c n_d}{2\kappa^3\beta^3}\left(\frac{\beta}{4\pi\varepsilon_o}\right)^6 (q_a q_b q_c q_d)^3 + \frac{1}{4}\sum_a \frac{q_a^2}{4\pi\varepsilon_o}\frac{\kappa^3\lambda_{aa}^3 n_a}{\beta^2} + O\left(\frac{n^3 \ln n}{\beta^3}\right).$$

K_o is the quantum virial function [3-5]. κ describes the inverse Debye radius, and $\beta = 1/(k_B T)$. k_B is the Boltzmann constant. q_a is the charge of the particle of type a, λ_{ab} - the de Broglie wavelength of a particle with reduced mass $m_{ab} = m_a m_b/(m_a + m_b)$. ξ_{ab} describes the Born interaction parameter. $a_1 = 10.134$ and $a_2 = 9.8227$ [6].

* Work financially supported by the BMBF project 05K13RDB "PRIOR"

References

[1] W.-D. Kraeft, D. Kremp, W. Ebeling, G. Röpke, "Quantum statistics of charged particle systems", Akademie-Verlag, Berlin 1986.

[2] C.-V. Meister, J. Staude, A.V. Pregla, An attempt to estimate nonideal effects on the electron partial pressure in the solar interior up to density order 5/2, Astron. Nachr. 320 (1) (1999) 43-52.

[3] A. Alastuey, V. Ballenegger, W. Ebeling, Comment on "Direct linear term in the equation of state of plasmas", Phys. Rev. E92, 047101, 2015.

[4] W.-D. Kraeft, D. Kremp, G. Röpke, Direct linear term in the equation of state of plasmas, Phys. Rev. E91, 013108, 2015.

[5] W.-D. Kraeft, D. Kremp, G. Röpke, Reply on "Comment on 'Direct linear term in the equation of state of plasmas"', Phys. Rev. E92, 047102, 2015.

[6] A. Alastuey, F. Cornu, A. Perez, Virial expansion for quantum plasmas; Maxwell-Boltzmann statistics, Phys. Rev. E51, 1725-1744, 1995.

Dynamical properties of dense plasma in inertial confinement fusion*

M.K. Issanova[1#], T.S. Ramazanov[1], S.K. Kodanova[1], D.H.H. Hoffmann[2]
[1]IETP, Al-Farabi Kazakh University, Almaty, Kazakhstan; [2]INP, TUD, Darmstadt, Germany

Recently, considerable attention of researchers has been paid to the study of matter with high energy densities and, as a consequence, with high pressures and temperatures. The research in the field of inertial confinement fusion (ICF) on heavy ion beams takes a special place among the works on various aspects of this problem [1-3]. One of the most important parameters used to describe the interaction of ions with matter is the energy of projectiles. The stopping power is a parameter characterizing the rate of loss of the average energy of fast electrons or ions in plasma [4-5]. The Coulomb logarithm based on the effective interaction potential of the particles is determined by the scattering angle of the pair Coulomb collisions [6-8]. In this work the dense plasma is considered for which quantum effects must be taken into account at short distances. Further, the effective interaction potential including both charge screening at large distances and quantum effects at short distances will be used [9-10].

In the present work the stopping time, the mean deflection angle, the depth of penetration and the effective range of particles with different energies generated in the DT plasma have been studied.

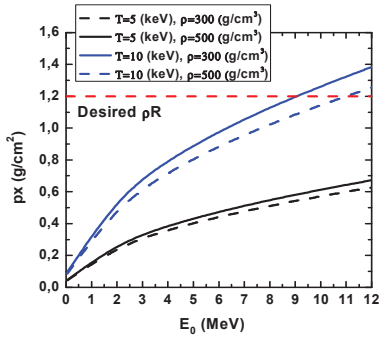

Figure 1: The penetration depth of the proton in DT plasma at different values of density and temperature.

Fig. 1 illustrates the dependence of the range and the penetration depth ρx [11] of protons with different energies on the density and temperature of the target. The results show that at a lower target temperature of $T = 5\ \kappa eV$, the target protons may conserve their energy inside the target if $\rho R < 1.2\ g/cm^2$. However, when the target is hotter $T = 10\ \kappa eV$, the required initial energy of the proton is reduced to $E \le 2\ MeV$, in order to meet the required optimal deposition depth.

The relaxation time of the temperature in the plasma were calculated for different density values on the basis of the Coulomb logarithm using the effective potential. Fig. 2 shows the comparison of the temperature relaxation time obtained on the basis of the effective potential with the results of MD at $r_S = 1$, $T_i = 10eV$. It is seen that the relaxation time increases with increasing temperature.

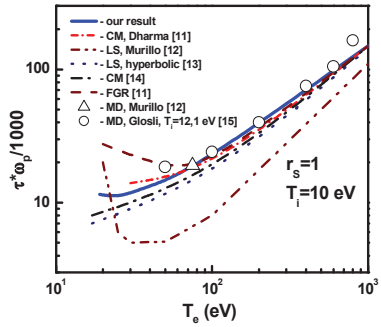

Figure 2:The relaxation time in units of plasma frequency.

The stopping time depends on the values of initial energy, density and temperature of the fuel. The results obtained for the Coulomb logarithm and temperature relaxation times for different plasma parameters are consistent with the results of other authors.

References

[1] D.H.H. Hoffmann, A. Blazevic, P. Ni et al. Laser and Particle beams 23, 47 (2005).
[2] D.H.H. Hoffmann et al. Phys.Rev. A 42, 2313 (1990).
[3] D.H.H. Hoffmann, J. Jacoby, W. Laux et al. Phys. Rev. Lett. 74, 1550 (1995).
[4] C.A. Ordonez, M.I. Molina. Phys. Plasmas. 1, 2515 (1994)
[5] T.S. Ramazanov, S.K. Kodanova. Phys. Plasmas 8, 5049 (2001)
[6] G. Belyaev, et al. Phys. Rev. E 53, 2701 (1996)
[7] A. Golubev, et al. Phys. Rev E. 53, 2701-2707 (1996)
[8] S.K. Kodanova, T.S. Ramazanov, et al. Contrib. Plasma Phys. 55, No. 2-3, 271 – 276 (2015)
[9] T. S. Ramazanov, Zh.A. Moldabekov, M.T. Gabdullin. Phys. Rev. E 92, 023104 (2015)
[10] M. Mahdavi and T. Koohrokhi. Physical Review E 85, 016405 (2012)
[11] M.W.C. Dharma-wardana, Phys. Rev. Lett. 101 035002 (2008)
[12] M.S. Murillo, M.W.C. Dharma-wardana, Phys. Rev. Lett. 100 205005 (2008)
[13] L. S. Brown, et al. Phys. Rep.410, 237 (2005)
[14] J. Vorberger, D.O. Gericke, Phys. Plasma 16 082702 (2009)
[15] J.N. Glosli, et al., Phys. Rev. E 78 025401(R) (2008)

* Work supported by MES RK, Grants No. 3083/GF4, 3086/GF4, 2016.
#isanova_moldir@mail.ru

Upgrade of the hydrodynamic code MULTI*

R. Ramis[1] *and F.Y. Wu*†[2]

[1]E. T. S. I. Aeronáutica y del Espacio, Universidad Politécnica de Madrid, Spain; [2]Institute of Nuclear Physics and Chemistry, CAEP, Mianyang, China

The radiation hydrodynamics code MULTI [1] has been extensively used in the analysis and design of experiments and in studies of Inertial Confinement Fusion (ICF). The 2D version [2] has been applied to the study of heavy ion irradiated ICF targets [3, 4]. In general, ion beam irradiated configurations are geometrically complex. For example, the target proposed in [5] and displayed in Fig. 1, involves four different materials submitted to three ion pulses with different cross sections and timming. Looking to the figure, it becomes apparent that the hydrodynamics of such targets is extremely complex. To resolve and understand the details, a fine grid is required (722×1200 for the simulation in Fig. 1). The code MULTI is based on Lagrangian hydrodynamics (numerical grid fixed to the fluid). This description is appropriate only in absence of large distortions. To solve complex flows, frequent remapping of fluid variables from a distorted grid into a regular one is required. If this process is performed after each time step ("continuous remapping"), the code operates in Arbitrary Eulerian-Lagrangian (ALE) mode. The first order remapping algorithm, included in the standard version of MULTI-2D [2], proves to be too diffusive, smoothing artificially the flow structure, resulting in a substantial degradation of the spacial resolution. By this reason, a new second order conservative algorithm for unstructured (an arbitrary arrangement of triangular and quadrangular cells) and staggered (some variables defined at nodes and others defined at cell centers) is being developed. Some preliminary results are displayed in Fig. 1. Several hydrodynamic phenomena can be observed: shock wave fronts (SW), interaction between shock waves (SI), Kelvin-Helmholtz instabilities at interfaces with a jump in tangential velocity (KH), Rayleigh-Taylor instability at places with opposed pressure and density gradients (RT). Eventually all these structures mix together losing their identity and giving place to turbulence. Another improvement in course is the implementation of a magnetohydrodynamics package. A 1D version will be presented at [6]. A 2D version including either B_θ magnetic field component (typical of Z-pinch configurations) or B_r and B_z components (typical of magnetized targets) are now under development.

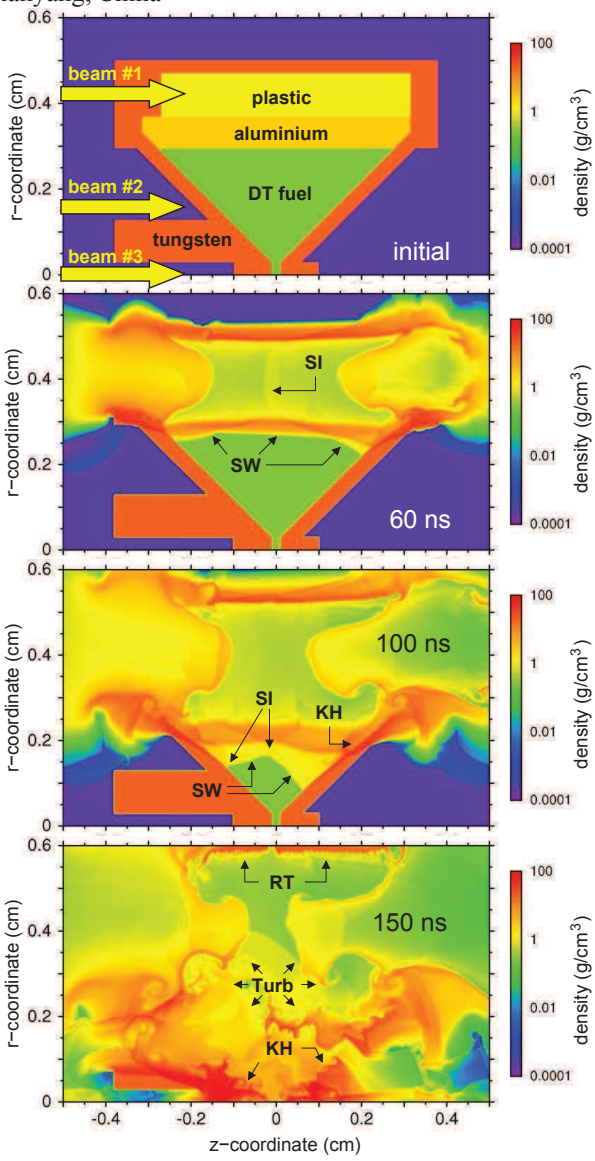

Figure 1: Hydrodynamic simulation. Density distribution at different times.

References

[1] R. Ramis, R. J. Schmalz, and J. Meyer-ter-Vehn, Comp. Phys. Comm. **49** (1988) 475-505.

[2] R. Ramis, J. Meyer-ter-Vehn, and J. Ramírez, Comp. Phys. Comm. **180** (2009) 977-994.

[3] R. Ramis and J. Ramírez, Nuclear Fusion **44** (2004) 720-730.

[4] R. Ramis and J. Meyer-ter-Vehn, Laser and Particle Beams **32** (2014) 41-47.

[5] E. Henestroza and B. G. Logan, Phys. Plasmas **18** (2011) 032702.

[6] F.Y. Wu, R. Ramis, and Z.H. Li, *Numerical simulation of the interaction between Z pinch plasma and foam converter using MULTI code*, to be presented at TOFE2016, Philadelphia, Aug. 22-25, 2016

* Work supported by Spanish MINECO project No. ENE2014-54960-R6065.

† Supported by the National Natural Science Foundation of China (Grant No. 11475153, 11305155)

Force-force correlations in warm dense plasmas. Influence of the ion-structure *

C.-V. Meister[1], *D.H.H. Hoffmann*[1], *T.S. Ramazanov*[2], *S.K. Kodanova*[2], *M.T. Gabdullin*[3], *and M.K. Issanova*[2]

[1]Institute for Nuclear Physics and Graduate School of Excellence Energy Science and Engineering, University of Technology Darmstadt, Germany; [2]IETP, Al-Farabi Kazakh National University, Almaty, Kasakhstan; [3]NNLOT, Al-Farabi Kazakh National University, Almaty, Kazakhstan

In warm dense matter, the transport coefficients of plasmas are strongly influenced by the ion distributions, i.e. by the ion-ion structure factor S [1-4]. The larger the ratio of the ion-ion potential energy to the ion kinetic energy Γ, the stronger the effect. On the other hand, it is believed that the hypernetted chain (HNC) approximation and the mean spherical (MS) approximation for S are applicable for systems with large Γ. Thus, in the present work, force-force correlation functions of ions and electrons in warm dense matter are calculated within Born approximation neglecting the ion-ion structure factor and considering it. In doing so, for S values are taken into account, which were observed in experiments or are calculated using HNC or MS approximations. It is found that the values of the correlation functions vary up to 20 percent in the special region of wave numbers $1 \leq qa \leq 4.5$, where a is the mean ion distance (see Fig. 1). The here obtained correlation functions may be used to calculate transport coefficients.

Numerical calculation

In Born approximation, i.e. in second order with respect to the interaction potential of the charged particles, one finds for the electron-ion force-force correlation functions

$$[M_{ei}^{(m)}; M_{ei}^{(n)}] = \frac{N m_e^2}{12\pi^3\hbar^3} \int_o^\infty I^{mn}(q)\, dq,$$

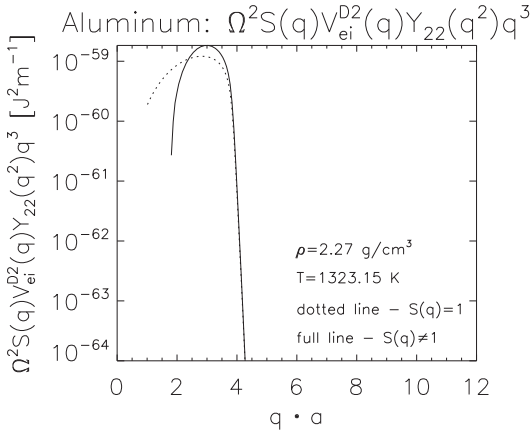

$$I^{mn}(q) = q^3 S(q) |V_{ei}(q)|^2 Y^{mn}(q^2),$$

where $V_{ei}(q)$ is the Fourier transform of the Debye potential screened by the electrons [4]. M_{ei}^0 are forces due to the particle current, and M_{ei}^2 - forces because of the heat current. The function $Y^{mn}(q^2)$ is given in [3] (Y^{02} has an additional summand $-2z$).

Figures 1 shows the function $I^{22}(q)$ in dependence on the normalized wave number aq. The calculations are performed for aluminum at 1323.15 K and electron densities of $5.07 \cdot 10^{28}$ m^{-3}. For the ion-ion structure factor $S(q)$, experimental data are used [5]. The chemical potential is estimated using the interpolation formula derived by Zimmermann [6]. In the work [7], the applicability of the Zimmermann formula was shown for electron gases at 12000 K and densities of 10^{24}-10^{30} m^{-3}. The full line in Figure 1 represent results taking the ion-ion structure factor into account and the dotted line shows results neglecting the structure factor.

* Work financially supported by the BMBF project 05K13RDB "PRIOR"

References

[1] C.-V. Meister, "Zur Theorie der Leitfähigkeit und Thermodynamik nichtidealer Plasmen", PhD, University Rostock, 1981.

[2] C.-V. Meister, G. Röpke, Electrical conductivity of non-ideal plasmas and the ion distribution function, Annalen der Physik 39 (2), 133-148 (1982).

[3] C.-V. Meister, D.H.H. Hoffmann, Transport coefficients of FAIR-S-FRS targets in Born approximation, Annual Report "News and Reports from High Energy Density Generated by Heavy Ion and Laser Beams", Vol. 1, 57-56 (2015).

[4] C.-V. Meister, D.H.H. Hoffmann, T.S. Ramazanov, S.K. Kodanova. M.T. Gabdullin, M.K. Issanova, Investigation of ion structure factors and transport coefficients in warm dense matter, Verhandlungen der DPG 1, 189 (2016).

[5] Structural Characterization of Materials Liquid Database, Institute of Advanced Materials Processing, Tohoku University, Japan, 1979, http://res.tagen.tohoku.ac.jp/waseda/scm/index.html.

[6] R. Zimmermann, "Many particle theory of highly excited semiconductors", Teubner, Leipzig, 1988.

[7] D. Kremp, M. Schlanges, W.-D. Kraeft, "Quantum statistics of nonideal plasmas", Springer, Berlin-Heidelberg-New York, 2005.

MSA ion structure factors in warm dense matter. Improved values *

C.-V. Meister

Institut für Kernphysik, Schlossgartenstr. 9, 64289 - Darmstadt and Graduate School of Excellence Energy Science and Engineering, Jovanka-Bontschits-Str. 2, 64287 - Darmstadt, Germany

Transport properties in solids and fluids, that will be considered in the present and future FAIR experiments, are strongly determined by the spatial distribution of the atoms, molecules, ions and electrons in the material. The distribution of the charged particles may be theoretically expressed by their structure factors. Indeed, in the expressions for the transport coefficients, squares of the absolute values of the Fourier transform of the interaction potential of an electron with all ions $|V_{ei}(\vec{q})|^2$ occur. Having N ions in the plasma, $|V_{ei}(\vec{q})|^2$ can be decomposed into the single ion scattering part $|v_{ei}(\vec{q})|^2$ and an ion distribution factor $\hat{S}(\vec{q})$, so that

$$|V_{ei}(\vec{q})|^2 = N\hat{S}(\vec{q})|v_{ei}(\vec{q})|^2,\ \ \hat{S}(\vec{q}) = \frac{1}{N}\sum_{ij}\exp^{i\vec{q}(\vec{R}_i-\vec{R}_j)}.$$

Averaging $\hat{S}(\vec{q})$ over the ion positions $\vec{R}_i$ and $\vec{R}_j$, one obtains the structure factor $S_{ii}(q) = \langle\hat{S}(\vec{q})\rangle$ which is related to the pair distribution function of the ions $f_{ii}(r)$ (r is the ion distance). In the thermodynamic limit of a classical plasma with an ion number $N \to \infty$, one has

$$S_{ii}(q) = 1 + n_i\int d\vec{r}\, f_{ii}(r)\exp(i\vec{q}\vec{r}),$$

$$\text{or}\quad S_{ii}(q) = \tilde{S}_{ii}(q) + (2\pi)^3 n_i\delta(\vec{q}),$$

$$\tilde{S}_{ii}(q) = 1 + n_i\int d\vec{r}\,[f_{ii}(r)-1]\exp(i\vec{q}\vec{r}).$$

n_i designates the ion particle density. As in mathematical expressions for transport coefficients, the ion structure factor is always multiplied by a power function of the transfer momentum $h\vec{q}$ (h - Planck constant), the term with the delta function $\delta(\vec{q})$ may be neglected.

A two-particle distribution function $f_{ab}(r)$ of particles of kind a and b, as it occurs in the structure factor, may be found from the Ornstein-Zernicke equation [1,2]

$$f_{ab}(r) - 1 = c_{ab}(r) + n_c\int_0^\infty c_{ac}(|\vec{r}-\vec{r}_1|)h_{cb}(\vec{r}_1)\,d\vec{r}_1.$$

Here the total correlation function $h_{ab}(r) = f_{ab}(r) - 1$ is the sum of the direct correlation function c_{ab} describing the interaction between the two particles a and b, and an indirect contribution caused by the interaction with all other particles of kind c. In mean spherical approximation (MSA) $f_{ab} = 0$ at $r = |\vec{r}_a - \vec{r}_b| < R_a + R_b$, and $c_{ab}(r) = -v_{ab}(r)/(k_BT)$ (k_B - Boltzmann constant, R_a and R_b - hard core radius of the ions of kind a and b, respectively).

material	crystal R_i [pm]	effective R_i [pm]
Al^{3+}	67.5	53.5
Fe^{2+} (ls)	75	61
Fe^{3+} (ls)	69	55
Fe^{2+} (hs)	92	78
Fe^{3+} (hs)	78.5	64.5
Cs^{+}	181	167

Calculating the ion structure factor $S_{ii}(q)$ in MSA, in this work expressions by Palmer and Weeks (assuming that the electrons form a neutralizing background) [2], given using complex numbers, are rewritten in the following form using real numbers (**function A of [3] corrected**)

$$S_{ii}(q) = 1 - \frac{2A+C}{A+B+C},$$

$$A = 144\eta^2(M^2u^4 + P^2u^2 + \tau^2 + 2\tau Mu^2),$$

$$B = u^8 + u^4(\frac{R^4}{4} - 24\eta\tau - 24\eta R(\tau - P))$$

$$+u^2(12\eta\tau R^2 + 144\eta^2(\tau-P)^2) + 144\eta^2\tau^2,$$

$$C = 24\eta\cos u\Big[Pu(-Ru^3 + 12\eta(\tau-P)u)$$

$$+(Mu^2+\tau)(u^4 - \frac{R^2u^2}{2} - 12\eta\tau)\Big]$$

$$+24\eta\sin u\Big[Pu(u^4 - \frac{R^2u^2}{2} - 12\eta\tau)$$

$$-(Mu^2+\tau)(-Ru^3 + 12\eta(\tau-P)u)\Big],$$

$$M = \frac{Q^2}{24\eta} - \frac{1+\eta/2}{(1-\eta)^2},\quad R = \frac{6\eta}{1-\eta} - Q,$$

$$P = \frac{1+2\eta}{(1-\eta)^2} - \frac{Q}{2(1-\eta)} + \frac{\tau}{2},$$

$$Q = \frac{1+2\eta}{1-\eta}\left[1 - \left(1 + \frac{2(1-\eta)^3\tau}{(1+2\eta)^2}\right)^{1/2}\right],$$

$$u = 2R_iq,\ \ \tau = 2R_i\kappa_i,\ \ \eta = \frac{4}{3}\pi n_iR_i^3,\ \ \kappa_i^2 = \frac{q_i^2n_i}{\varepsilon_ok_BT}.$$

Numerical results for the structure factor $S(q)$ in MSA are presented in Figs. (1-4) for cesium, aluminum and ferrum. The crystallographic and effective ion radii used are shown in Table 1 (ls - low spin, hs - high spin). The results are compared with data of numerical calculations presented in the Tohoku University database [4]. The MSA

* Work financially supported by the BMBF projects 05P12RDFN6 and 05K13RDB.

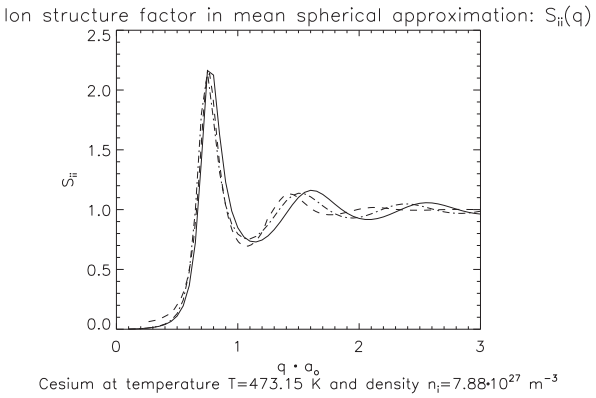

Figure 1: Structure factor of onefold ionized cesium at $T = 473.15$ K, $n = 7.88 \cdot 10^{27}$ m^{-3}. Full line - effective ion radius, dash-dot line - crystallographic radius, dashed line - [4].

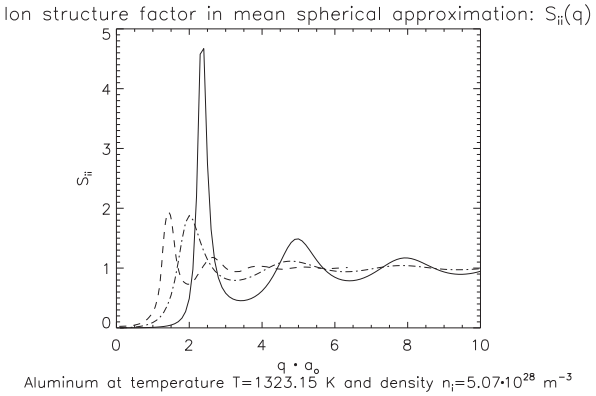

Figure 2: Structure factor of aluminum at $T = 1323,15$ K and $n = 5.07 \cdot 10^{28}$ m^{-3}. Full line - threefold ionized aluminum, dash-dot line - onefold ionized aluminum, dashed line - [4]. Calculations performed using the effective ion radius.

results presented in [3] are now improved taking into account a corrected A-function. Besides, the calculations in the limit of $q \to 0$ are improved on the basis of an additional analytical analysis. It is found that, $S_{ii}(q) = 1-(2A+C)/(A+B+C) \to \infty$ at $q \to 0$ and finite values of $\eta\tau$, i.e. in nonideal plasmas with finite inverse ion screening lengths κ_i.

The calculated structure factor values of onefold ionized cesium agree very well with the data presented in the Tohoku database [4]. But the values for threefold ionized aluminum and twofold as well as threefold ionized ferrum are much larger than the data given in [4]. Assuming onefold ionized aluminum and ferrum ions (and using the effective ion radii of the threefold ionized atoms), the amplitudes of the first maxima of the structure factor almost agree with the data of [4]. Taking into account the dependence of the effective ion radius on the spin in case of ferrum, it may be concluded that with increasing value of the spin the first maximum of the structure factor is shifted to lower values of the transfer momentum hq.

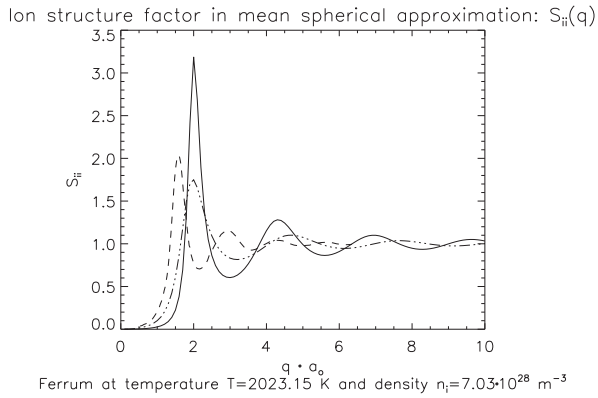

Figure 3: Structure factor of ferrum at $T = 2023,15$ K and $n = 7.03 \cdot 10^{28}$ m^{-3}. Full line - twofold ionized ferrum with low spin, dash-dot-dot line - onefold ionized ferrum, dashed line - [4]. Calculations performed using the effective ion radius.

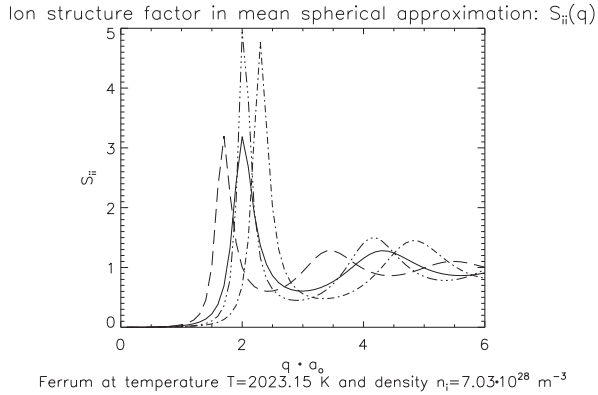

Figure 4: Structure factor of ferrum at $T = 2023,1$ K and $n = 7.03 \cdot 10^{28}$ m^{-3}. Full line - twofold ionized ferrum with low spin, dashed line - twofold ionized ferrum with high spin, dash-dot line - threefold ionized ferrum with low spin, dash-dot-dot line - threefold ionized ferrum with high spin. Calculations performed using the effective ion radius.

References

[1] R. Balescu, Equilibrium and nonequilibrium statistical mechanics, John Wiley and Sons, Chichester, New York, Sydney, Toronto (1975).

[2] R.G. Palmer, J.D. Weeks, Exact solution of the mean spherical model for charged hard spheres in a uniform neutralizing background, J. Chem. Phys., 58 (1973) 4171.

[3] C.-V. Meister, B. Jiang, D.H.H. Hoffmann, Calculation of ion structure factors in warm dense matter, Annual Report "News and reports from high-energy density generated by heavy ion and laser beams 2013-2014", GSI-2015-2 REPORT, 2015, 55.

[4] Structural Characterization of Materials Liquid Database, Institute of Advanced Materials Processing, Tohoku University, Japan, 1979, http://res.tagen.tohoku.ac.jp/∼waseda/scm/index.html (download August 2015, values for Cs at $q < 1\AA$ downloaded 13.05.16).

Magnetohydrodynamic formulae to estimate density, pressure, velocity, and magnetic field jumps in a perpendicular shock wave of an ideal plasma *

C.-V. Meister[1,2]

[1]Institut für Kernphysik, Schlossgartenstr. 9, 64289 - Darmstadt; [2]Graduate School of Excellence Energy Science and Engineering, Jovanka-Bontschits-Str. 2, 64287 - Darmstadt, Germany

To produce warm dense matter in laboratories, it is very important to predict the maximum plasma densities and pressures which might occur. Within the frame of the future FAIR experiment, a plasma production by shock waves is planned. In this connection, also the action of shock waves under the influence of external magnetic fields has to be known.

It is already well known that a magnetic field reduces the strength of a perpendicular shock. This is the consequence of the fact, that, besides of the heating of the plasma, part of the kinetic energy of the up-stream plasma flow of a shock may be converted into the energy of the magnetic field. Moreover, mathematical formulae exist, which describe the change of the magnetic field during the shock [1, 2]. But, unfortunately, the derivation of these formulae is unknown. So, it is unpossible to realize, which approximations were introduced deriving these formulae. Thus, here a rather short derivation of formulae describing the variations of the density, pressure, velocity, and magnetic field by a perpendicular shock is given. The expressions derived coincide with formulae contained in [1].

To derive the formula for the density variation $X = \rho_2/\rho_1$ of an ideal plasma during a perpendicular collisionless shock, let us start with the Hogoniot jump conditions for the magnetohydrodynamic parameters of an ideal plasma [1, 3]

$$\{\rho u\} = 0, \tag{1}$$

$$\left\{\rho u^2 + p + \frac{B^2}{4\mu_o}\right\} = 0, \tag{2}$$

$$\left\{\frac{1}{2}u^2 + \frac{\gamma}{(\gamma-1)}\frac{p}{\rho} + \frac{B^2}{2\mu_o\rho}\right\} = 0, \tag{3}$$

$$\left\{\frac{B}{\rho}\right\} = 0. \tag{4}$$

Here ρ, $\vec{u}$, p, $\vec{B}$, and γ describe mass density, fluid velocity, pressure, magnetic field and polytropic index of the plasma, respectively. The sign $\{A\}$ shows the jump of the plasma-parameter A, $\{A\} = A_2 - A_1$ from the up-stream region of the shock (index 1, A_1) to its downstream region (index 2, A_2). Equation eq. (1) results from the fluid continuity condition. Equation eq. (2) considers the momentum balance and eq. (3) describes the energy conservation of the plasma. The freezing of the magnetic field into the plasma is taken into account in eq. (4). $\vec{u}$ and $\vec{B}$ are directed perpendicularly.

To solve the system of equations eqs. (1-4), it is useful to introduce the Mach number M,

$$M^2 = \frac{u_1^2\rho_1}{\gamma p_1}, \tag{5}$$

and the plasma-β,

$$\beta = \frac{p_1}{B_t^2/(4\mu_o)}. \tag{6}$$

Then, from eqs. (1, 4) follows

$$\frac{B_2}{B_1} = \frac{\rho_2}{\rho_1} = \frac{u_1}{u_2} = X. \tag{7}$$

Equation (2) gives

$$p_1 - p_2 = \rho_2 u_2^2 - \rho_1 u_1^2 + \frac{B_2^2}{4\mu_o} - \frac{B_1^2}{4\mu_o}.$$

Using eq. 4, one may write

$$p_1 - p_2 = \rho_2 u_2^2 - \rho_1 u_1^2 + \frac{(\rho_1^2 - \rho_2^2)}{\rho_1^2}\frac{B_1^2}{4\mu_o}.$$

Dividing by p_1 and using the definitions of X and β (eq. 6), the expression may be transformed into

$$\frac{p_2}{p_1} = 1 + \frac{\rho_1 u_1^2 - \rho_2 u_2^2}{p_1} + \frac{1-X}{\beta}. \tag{8}$$

Further, applying the result of the transformations

$$\rho_1 u_1^2 - \rho_2 u_2^2 = \rho_1 u_1^2 - \frac{\rho_2^2 u_2^2}{\rho_2} = \rho_1 u_1^2 - \frac{\rho_1^2 u_1^2}{\rho_2} \tag{9}$$

$$= \frac{u_1^2\rho_1}{\rho_2}(\rho_2 - \rho_1) = \frac{\gamma p_1 M^2(\rho_2 - \rho_1)}{\rho_2},$$

one obtains finally from eq. (2)

$$\frac{p_2}{p_1} = 1 + \frac{\gamma M^2(X-1)}{X} - \frac{X^2-1}{\beta}. \tag{10}$$

Equation eq. (10) is rather useful to estimate the pressure variations in a perpendicular shock. But, to do this, in accordance with eq. (7), one has to know the density, velocity or magnetic field modifications. Thus, next, a relation will be found for X taking also eq. (3) into account.

* Work financially supported by the BMBF project 05K13RDB "PRIOR"

Considering eq. (3) one has

$$\frac{u_1^2}{2}-\frac{u_2^2}{2}+\frac{\gamma}{\gamma-1}\left[\frac{p_1}{\rho_1}-\frac{p_2}{\rho_2}\right]+\frac{B_1^2}{2\mu_o\rho_1}-\frac{B_2^2}{2\mu_o\rho_2}=0. \quad (11)$$

With $B_1\rho_2 = B_2\rho_1$ follows

$$\frac{u_1^2-u_2^2}{2p_1}+\frac{\gamma}{(\gamma-1)}\left[\frac{1}{\rho_1}-\frac{p_2}{\rho_2 p_1}\right]+\frac{B_1^2}{2\mu_o}\frac{(\rho_1-\rho_2)}{\rho_1^2 p_1}=0$$

or

$$\frac{u_1^2-u_2^2}{2p_1}+\frac{\gamma}{\gamma-1}\left[\frac{1}{\rho_1}-\frac{p_2}{\rho_2 p_1}\right]+\frac{2(\rho_1-\rho_2)}{\beta\rho_1^2}=0.$$

Substituting for p_2/p_1 the formula eq. (10) and using eq. (5) as well as

$$\frac{u_1^2-u_2^2}{2p_1}=\frac{u_1^2\rho_2^2-u_2^2\rho_2^2}{2p_1\rho_2^2}=\frac{u_1^2\rho_2^2-u_1^2\rho_1^2}{2p_1\rho_2^2} \quad (11)$$

$$=\frac{\gamma}{2}M^2\left(\frac{1}{\rho_1}-\frac{1}{\rho_2 X}\right),$$

one obtains

$$\frac{\gamma}{2}M^2\left(\frac{1}{\rho_1}-\frac{1}{\rho_2 X}\right)+\frac{\gamma}{(\gamma-1)}\Big[\frac{1}{\rho_1}-\frac{1}{\rho_2}$$

$$-\frac{\gamma M^2(X-1)}{X\rho_2}+\frac{X^2-1}{\beta\rho_2}\Big]+\frac{2}{\beta}\left(\frac{1-X}{\rho_1}\right)=0.$$

After multiplication with $\rho_1 X^2$, the expression may be written in the form ($X=\rho_2/\rho_1$)

$$\frac{\gamma}{2}M^2(X^2-1)+\frac{\gamma}{(\gamma-1)}\Big[X^2-X-\gamma M^2(X-1)$$

$$+\frac{X}{\beta}(X^2-1)\Big]+\frac{2}{\beta}(X^2-X^3)=0.$$

This is equal to

$$(X-1)\Big(\frac{\gamma}{2}M^2(X+1) \quad (12)$$

$$+\frac{\gamma}{(\gamma-1)}\left[X-\gamma M^2+\frac{X}{\beta}(X+1)\right]-\frac{2}{\beta}X^2\Big)=0.$$

Equation eq. (12) has two solutions. One is determined by the first factor $(X-1)$. It corresponds to a lack of a density jump across the perpendicular shock. The second solution is defined by the expression in the brackets $(...)$ of the second factor. This expression may be presented in the form

$$\left(\frac{\gamma}{(\gamma-1)\beta}-\frac{2}{\beta}\right)X^2+\Big(\frac{M^2\gamma}{2}+\frac{\gamma}{(\gamma-1)} \quad (13)$$

$$+\frac{\gamma}{(\gamma-1)\beta}\Big)X+\frac{\gamma}{2}M^2-\frac{\gamma}{(\gamma-1)}M^2=0.$$

Bringing the sums in the brackets $(...)$ on the main denominator and multiplying the whole equation with $2\beta(1-\gamma)$, one has finally

$$(\gamma-2)2X^2-(M^2\gamma(\gamma-1)\beta+2\beta\gamma+2\gamma)X \quad (14)$$

$$+\gamma(1+\gamma)M^2\beta=0.$$

Equation eq. (14) is equivalent to the expression

$$aX^2+bX-c=0, \quad (15)$$

with

$$a=2(2-\gamma), \quad b=\gamma(2\beta+(\gamma-1)\beta M^2+2), \quad (16)$$

$$c=\gamma(\gamma+1)\beta M^2,$$

given in [1]. Under the condition $1<\gamma\leq 2$, the only positive root of eqs. (14, 15) is

$$X=\frac{1}{2a}\left[-b+\sqrt{b^2+4ac}\right]. \quad (17)$$

In case of vanishing magnetic field, $\beta\to\infty$, one obtains the well-known relation [1]

$$X\approx\frac{c}{b}-\frac{ac^2}{b^3}=\frac{(\gamma+1)M^2}{2+(\gamma-1)M^2}-O(1/\beta). \quad (18)$$

presented already in [4] for nonmagnetized plasmas and large Mach numbers M.

In future, the here presented mathematical formulae will be extended for nonideal plasmas with particle collisions.

References

[1] C. Chiuderi, M. Velli, "Basics of plasma astrophysics", UNITEXT for Physics, Springer, Milan-Heidelberg-New York-Dordrecht-London (2015).

[2] U. Motschmann, Plasmaphysik. Skriptum zur Vorlesung, Kapitel V: Stoßwellen und Diskontinuitäten, Technische Universität Braunschweig, 2015.

[3] C.-V. Meister, Theoretical plasma physics, chapter 8: Magnetohydrodynamics, Lecture notes, summer semester 2015 and winter semester 2015/2016, University of Technology Darmstadt.

[4] L.D. Landau, E.M. Lifshitz, "Theoretical physics. Fluid mechanics", Vol. 6 (2nd ed.), Butterworth-Heinemann, Oxford (1987).

Simple model for calculation of optical properties of shock compressed gases*

M. E. Veysman[†1], *G. Röpke*[2], *and H. Reinholz*[2,3]

[1]Joint Institute for High Temperatures RAS, Moscow, 125412, Russia; [2]Universität Rostock, Institut für Physik, 18051 Rostock, Germany; [3]The University of Western Australia, School of Physics, Crawley, WA 6009, Australia

Experiments on measurements of reflectivity of shock compressed noble gases [1] had attracted much attention in view of their theoretical explanations. Previous studies attempted to explain experimentally measured reflectivities by final width of the shock wave front, but this width in those works [2–5] was considerably higher than theoretical estimates [6]. Subsequent study by means of Ab initio calculations using Kubo-Greenwood formalism and density functional theory (DFT) approach had revealed the importance of taking into account the contribution of transitions of electrons from bound shells [7] for explanation of experimental data.

In our work we had shown, that in wide range of frequencies of laser radiation experimental data on shock compressed noble gases reflectivity can be explained by means of much more simple, than Ab initio calculations, approach, using theoretical model for plasma permittivity [6], based on quantum statistical approach to linear response theory (LRT) for *intraband* part of permittivity $\varepsilon_{\mathrm{Dr}}$ and modified Drude-Lorentz model for *interband* contribution $\delta\varepsilon_{\mathrm{b}}$ to permittivity, see Fig. 1.

It can be shown, that at laser frequencies less than characteristic frequencies of interband transitions, than the imaginary part of $\delta\varepsilon_{\mathrm{b}}$ is close to zero, the real part can be treated as independent of laser frequency ω, and moreover, using arguments of the papers [8,9], it can be approximated as independent of density.

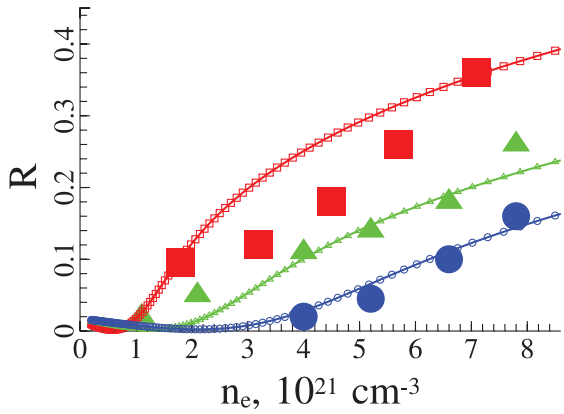

Figure 1: Reflection coefficient R of shock compressed Xenon plasmas with average ions charge $Z = 1$ and equal ion and electron temperatures, $T = T_{\mathrm{i}} \approx 30$ kK, as function of the electrons density n_{e}. Experimental data [1] are shown by large separate markers: red squares for wavelength $\lambda = 1.06$ μm, green triangles for $\lambda = 0.694$ μm, blue circles for $\lambda = 0.532$ μm. Marked lines (with the same colors and marks for the same λ) show the LRT two-moment screened Born calculations with account for: ion correlations, the restriction of the screening radius from below by inter-atomic distance [6], with the use of a pseudopotential according to Gericke *et al.* [10] model with pseudopotential cut off at $r_{\mathrm{cut}} = 0.5$ Å, and with the account for nonzero constant value of $\Re\delta\varepsilon_{\mathrm{b}}(\omega)$, $\Re\delta\varepsilon_{\mathrm{b}}(\omega) = 0.7$

References

[1] Y. Zaporoghets, V. Mintsev, V. Gryaznov, V. Fortov, H. Reinholz, T. Raitza, and G. Röpke, *J. Phys. A: Math. Gen.* **39**, 4329 (2006).

[2] H. Reinholz, G. Röpke, I. Morozov, V. Mintsev, Y. Zaparoghets, V. Fortov, and A. Wierling, *J. Phys. A: Math. Gen.* **36**, 5991 (2003).

[3] H. Reinholz, Y. Zaporoghets, V. Mintsev, V. Fortov, I. Morozov, and G. Röpke, *Phys. Rev. E* **68**, 036403 (2003).

[4] T. Raitza, H. Reinholz, G. Röpke, V. Mintsev, and A. Wierling, *J. Phys. A: Math. Gen.* **39**, 4393 (2006).

* The work of M. Veysman in JIHT was partly supported by the Presidium of RAS program "Thermo-physics of High Energy Density", No I.13P. The authors acknowledge financial support by DFG for collaborative projects funded jointly with RAS. H.R., G.R. have also been supported by the DFG within the CRC-SFB 652. M. Veysman thanks his German colleagues for hospitality and financial support during his visits to Rostock University and Johannes Kepler University in Linz.

† bme@ihed.ras.ru

[5] M. Winkel, H. Reinholz, A. Wierling, G. Röpke, Y. Zaporozhets, and V. Mintsev, *Contrib. Plasma Phys.* **49**, 687 (2009).

[6] M. W. H. R. M. Veysman, G. Röpke, *Phys. Rev. E* (2016, submitted).

[7] G. Norman, I. Saitov, V. Stegailov, and P. Zhilyaev, *Phys. Rev. E* **91**, 023105 (2015).

[8] A. Lankin and G. Norman, *Contrib. Plasma Phys.* **49**, 723 (2009).

[9] A. V. Lankin and G. E. Norman, *J. Phys. A: Math. Theor.* **42**, 214032 (2009).

[10] D. O. Gericke, J. Vorberger, K. Wünsch, and G. Gregori, *Phys. Rev. E* **81**, 065401 (2010).

The Stopping Power and Wakefield of an Ion Beam Pulse Moving in Magnetized Plasmas

X. Qi[1#], X. Y. Zhao[1], L. Yang[1] and Y. T. Zhao[2#]

1. IMP, Lanzhou, China; 2. XJTU, Xi'an, China

Understanding the interactions of charged particles with magnetized plasmas has been an interesting topic for electron cooling of ion beams, inertial confinement fusion (ICF) driven by ion beams and neutral beam injection (NBI) in magnetically confined fusion plasmas. In the presence of the magnetic field, electrons in plasmas are restricted in the direction perpendicular to the magnetic field, which strongly affects the wake field as well as energy loss of the ion-beam.

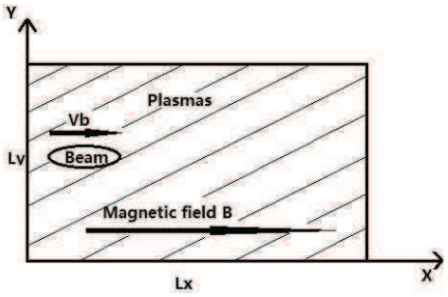

Fig. 1. A two-dimensional plasma slab model.

We used 2D3V Particle-In-Cell simulations to investigate the process of an ion-beam pulse moving longitudinal through hydrogen magnetized two-component plasmas. As shown in Fig. 1, the plasmas are composed of electrons and H ions with uniform plasma density $N_{e0} = N_{i0} = 2.0d17\ m^{-3}$ and an initial plasma temperature $T_{e0} = T_{i0} = 10eV$ for electrons and ions, respectively. The beam ions are chosen to be protons with different velocities and densities in the simulations.

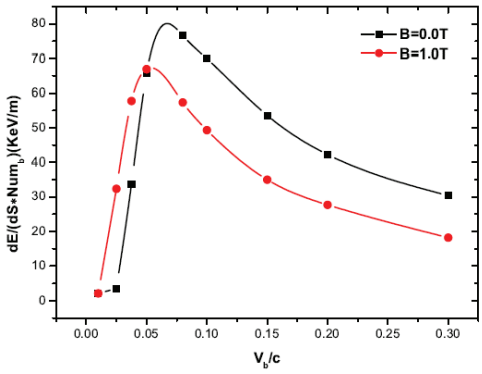

Fig. 2. Stopping power per ion as a function of beam velocity V_b when beam density B_0=$1.0d17\ m^{-3}$ with different magnetic fields. c is the light speed.

In the previous work [1], we showed that for a beam pulse moving in the plasma with initial energy 3MeV, the wakes spread and lose the typical V-shaped structures in the presence of the magnetic field. At a sufficiently strong magnetic field, the wakes exhibit conversed V-shaped structures.

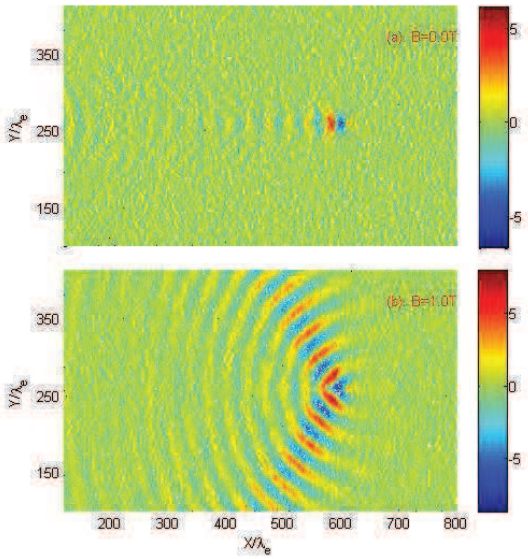

Fig. 3. Contour plot of the electric field E ($d4\ V/m$) in the wake-field region induced by the charged particles moving in the plasmas at the beam velocity $V_b = 0.025c$, beam density $B_0 = 1.0d17\ m^{-3}$. λ_e is Debye length of the plasma.

For ion beams with different energies [2], the stopping power are shown in Fig. 2. For high-energy ion beams, the stopping powers are inhibited compared with these in isotropic plasmas. However, for low-velocity conditions, the stopping power is greatly increased. Especially when $V_{b0} = 0.025c$, the stopping power increases by one order of magnitude. Fig. 3 gives the contour plot of the electric field E in the wake-field region induced by the ion beams moving in the plasmas at the beam velocity $V_{b0} = 0.025c$. In the presence of the magnetic field, it can be seen in Fig. 3(b) that beside the conversed V-shape structures of the wakes, the strong whistler waves are observed on both sides of the beam trajectory. The corresponding stopping power is enhanced due to the drag of these whistler waves.

References

[1] X. Y. Zhao, X. Qi, et al. (2015), Phys. Plasmas, 22, 093114

[2] X. Y. Zhao, X. Qi, Y. T. Zhao, et al. *Effects of beam velocity and density on an ion-beam pulse moving in magnetized plasmas,* to be submitted.

#qixin2002@impcas.ac.cn, zhaoyt@impcas.ac.cn

Ion potential in stationary nonequilibrium dense plasmas

Zh.A. Moldabekov[1,2], *P. Ludwig*[2], *M. Bonitz*[2], *and T.S. Ramazanov*[1]

[1]IETP, Al-Farabi Kazakh National University, Almaty, Kazakhstany; [2]ITAP, Christian-Albrechts-Universität zu Kiel, Germany

The modeling of the dynamics of an electron-ion plasma is hampered by the large mass difference. We, therefeore, apply a multi-scale approach. It is based on a previously developed dynamical screening model that is extended to quantum systems at any degeneracy [1]. The scheme allows to accurately study the dynamics of strongly correlated classical ions in the presence of quantum degenerate, streaming electrons. In particular, this includes thermal and non-equilibrium electronic effects such as quantum wake effects, Friedel oscillations [2] and also electron magnetization. In the recent contributions [3, 4] we presented first results for the dynamically screened ion potential in linear response approximation in the presence of streaming electrons on the basis of (i) RPA [5], and (ii) the Mermin dielectric function where electronic collisions are included self-consistently [6].

The dependence of the characteristic oscillatory wake structure on the electron streaming velocity, electron degeneracy (temperature), and density is investigated. In particular, the transition from high temperature regime to low temperature regime is discussed. Strong deviations from the static Yukawa potential [9] as well as the possibility of an attraction between like-charged ions are shown. It was shown under which conditions streaming of the plasma background is giving rise to a dynamically screened charge field with a negative trailing potential minimum behind the ion, which may lead to the attraction between like-charged, positive ions. This effect is similar to wakes behind an object in a moving fluid, wakes in laser plasmas or in dusty plasmas which all are able to accelerate particles – in this case, a second ion. The physical mechanisms are similar in all cases – it is the attraction between a heavy test particle and the streaming light particles giving rise to a deflection of the latter and, eventually, to an excess density behind the test particle. This interpretation was directly confirmed by computing the electron density perturbation which reveals a clear enhancement behind the ion.

The depth of the first (main) potential minimum reaches values of more than one Hartree, which may have a profound effect on the structure of strongly correlated ions in dense low-temperature plasmas. At the same time the minimum is separated from the ion significantly more than the mean interparticle distance. This will prevent a large scale ordering of ions at such distances. Only at small length scales and/or during nonequilibrium processes where charge neutrality is violated and the electron density exceeds the ion density this attraction may, eventually, play a role in the plasma dynamics.

Additionally, we presented the results of a detailed study of the anomalous behavior of the field distribution around an ion with respect to the change in the degeneracy parameter and the electron collision frequency [7]. In particular, this detailed study of the ion potential in the presence of quantum electrons revealed two remarkable effects which have not been studied so far. The first anomaly concerns the amplification of the trailing potential minimum of the wake field with increase of the electron collision frequency, which is notably counterintuitive as collisions should have an damping effect on the wake field. The second anomaly is the observed increase of the wake field's oscillation amplitude and that of the trailing potential minimum with increase of temperature.

The cases of moderately and strongly coupled electrons are beyond the relaxation time approximation and requests construction of the improved dielectric function for electrons. Such dielectric function can be obtained, for instance, on the basis of the method of moments [10]. However, the collision frequency should be determined via numerical simulation like molecular dynamics [11]. For self consistent simulation of the many-component plasma with large difference in the characteristic time scales of the components, the formalism of the effective interaction potentials can be used within a multi-scale approach [1].

References

[1] P. Ludwig, M. Bonitz, and H. Kählert, *J. Phys.: Conf. Series* **220**, 012003 (2010).

[2] D. Else, R. Kompaneets, and S. V. Vladimirov, *Phys. Rev. E* **82**, 026410 (2010).

[3] Zh. A. Moldabekov, P. Ludwig, M. Bonitz, and T. S. Ramazanov, Phys. Rev. E **91**, 023102 (2015).

[4] Zh. A. Moldabekov, P. Ludwig, J.P. Joost, M. Bonitz, and T. Ramazanov, Contrib. Plasma Phys. **55**, 186 (2015).

[5] Nestro R. Arista, Werner Brandt, *Phys. Rev. A* **29**, 3, 1471 (1984).

[6] N. D. Mermin, *Phys. Rev. B* **1**, 5, 2362 (1970).

[7] Zh. A. Moldabekov, P. Ludwig, M. Bonitz, and T. Ramazanov, Contrib. Plasma Phys. accepted for publication.

[8] Sergey V. Vladimirov, *Plasma Phys. Control. Fusion* **53**, 074005 (2011).

[9] Zh. Moldabekov, T. Schoof, P. Ludwig, M. Bonitz, and T. Ramazanov 2015, *Phys. Plasmas* **22**, 102104.

[10] V. M. Adamyan and I. M. Tkachenko 2003, *Contrib. Plasma Phys.* **43**, 252

[11] H. Reinholz, I. Morozov, G. Röpke, and T. Millat 2004, *Phys. Rev. E* **69**, 066412.

Generalized ponderomotive potential of the electron plasma wave

Ph. Bischoff[1], *P. Mulser*[1], *and G. Alber*[2]

[1]TQE: Theoretical Quantum Electronics, Inst. Applied Physics, TU Darmstadt, Germany; [2]Theoretical Quantum Physics, Inst. Applied Physics, TU Darmstadt, Germany

A general expression for the ponderomotive potential of the longitudinal electron plasma wave is found which is valid for arbitrary electron velocities and time-dependent wave amplitudes.

By definition the ponderomotive potential Φ_p and force f_p are the secular, i.e., zero frequency components, resulting from the high-frequency motion of the single electron in an electromagnetic wave. With the wave amplitude $\hat{E}$ the two quantities in their standard form are given by the well-known expressions

$$\phi_p = e^2 \hat{E}\hat{E}^*/(4m_e\omega^2)\ , f_p = -\nabla\phi_p \qquad (1)$$

for both, the transverse electromagnetic and the longitudinal electron plasma wave of frequency ω. Φ_p is the cycle-averaged oscillation energy W of the electron in the wave, $W = \Phi_p$. Closer inspection shows that the validity of (1) is restricted (i) to electron translational velocities v_0 much less than the phase velocity of the wave v_φ and (ii) to wave amplitudes $\hat{E}$ depending on space only, $\hat{E} = \hat{E}(x)$. A relativistic generalization of Φ_p and f_p under these restrictions has been given in [1]. There is a broad field of applications of ϕ_p: Parametric instabilities, radiation pressure acceleration, etc. Secular forces cause particle trapping and the "mystery" of Landau damping [2]. It is therefore highly desirable to generalize ϕ_p to all translation velocities v_0 and to wave amplitudes depending on space and time, $\hat{E} = \hat{E}(x,t)$.

Consider in a first step a longitudinal wave of the potential $V(x,t) = \hat{V}(x)\cos(kx - \omega t)$. In a reference system moving with phase velocity $v_\varphi = \omega/k$ (wave frame) the potential becomes static, $V = \hat{V}\cos kx', x' = x - v_\varphi t$.

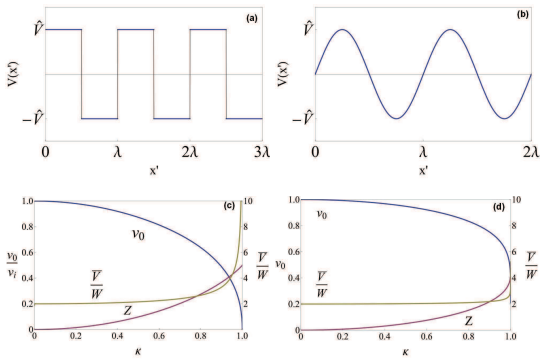

Figure 1: Square wave and sinusoidal wave. $\kappa = 2\hat{V}/v_i^2$

Energy conservation applies to the cycle average, of a square and a sinusoidal wave Fig.1(a),(b). In both cases the cycle-averaged energy conservation in the wave frame reads as follows:

$$v_i^2 = v_0^2 + 2W + 2\overline{V};\ \ v_i \text{ injection velocity}, m_e = e = 1 \qquad (2)$$

Hence, the ponderomotive potential Φ_p is the sum of two terms and f_p is their negative gradient,

$$\Phi_p(x') = W(x') + \overline{V}(x') = Z(x')\ ,\ f_p = \mathrm{d}v_0/\mathrm{d}t = -\nabla Z(x') \qquad (3)$$

In Fig.1(c), (d) the effect of the cycle averaged potential $\overline{V}$ plays the dominant role over W at low injection velocities v_i. It is responsible for particle trapping in the wave and leads to a qualitatively different behaviour of f_p (see Fig.2): (i) f_p becomes direction-dependent, thus producing a hysteresis in momentum space, and (ii) changes from repulsion of the standard formula to attraction (uphill acceleration). At injection velocities differing much from v_φ, i.e. in the lab frame $|v_{\text{lab}}| = |v_0 + v_\varphi| << v_\varphi$, $\overline{V}$ shrinks to zero and Φ_p reduces to formula (1).

In the wave with explicitly time dependent amplitude $\hat{V} = \hat{V}(x,t)$ energy conservation (2) no longer holds, it is to be replaced by an adiabatic invariant coupling together translational, quiver and averaged potential energies,

$$(v_0^2 + 2W + \overline{V} - E_{tot})T = \text{const}_a \qquad (4)$$

const_a stands for const if the explicit dependence on time of $\hat{V}(x,t)$ undergoes slow (adiabatic) changes with respect to $1/\omega$ only. Fig.2 shows that the hysteresis is reproduced by eq.(4) in a stupendous manner (dotted green line).

Sumarizing, the ponderomotive force in a longitudinal wave of time-dependent amplitude is governed by the adiabatic invariant eq. (4) for arbitrary injection velocity v_i. Particle trapping is a produced by the ponderomotive action of $\overline{V}$.

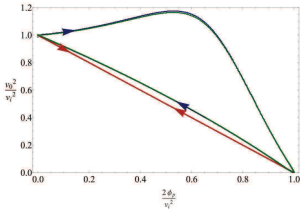

Figure 2: Dotted lines after eq.(4) coincide with exact numerical result (green). f_p is attractive for $2\Phi_p/v_i^2 < 0.6$

References

[1] D. Bauer, P. Mulser, W.-H. Steeb, PRL**75**, 4622 (1995)

[2] C. Mouhot and C. Villani, Acta Mathematica **207**, 29 (2011).

Mitigation of Rayleigh-Taylor Instability Growth in Heavy Ion Fusion

T. Karino[1], S. Kawata[1], and A. I. Ogoyski[2]
[1] Utsunomiya University, Utsunomiya, Japan, [2] Varna Technical University, Varna, Bulgaria

The dynamic stabilization for the Rayleigh-Taylor instability (RTI) has been studied for a uniform compression of a fusion fuel target in inertial confinement fusion [1]: the oscillation amplitude of the driving acceleration should be sufficiently large to stabilize RTI. In inertial fusion, the fusion fuel compression is essentially important to reduce an input driver energy, and the implosion uniformity is one of critical issues to release the fusion energy stably.

The heavy ion accelerator could provide a beam axis wobbling with a high frequency. The wobbling heavy ion beams also define the perturbation phase. This means that the perturbation phase is known, and so the perturbations successively imposed are superposed in the plasma. The heavy ion beams accelerate the fusion target fuel with a large acceleration in inertial fusion. The wobbling heavy ion beams would provide a small oscillating acceleration perturbation in an inertial fusion fuel target during the target implosion. So the RTI growth would be reduced by the phase-controlled superposition of perturbations in heavy ion inertial fusion [2].

Figure 1 shows an example simulation for RTI. In this example, two stratified fluids are superposed under an acceleration such as:

$$g = g_0 + \delta g\,,\ \delta g = g_1 e^{ikx} e^{i\Omega t} \qquad (1)$$

In this example case the wobbling frequency Ω is γ, the amplitude of δg is $0.1\,g_0$, and the results shown in Figs. 1 are at $t = 5\gamma$. The density jump ratio between the two fluids is 10/3. The growth rate of the instability is γ. In Fig. 1(a) δg is constant and drives the RTI as usual, and in Fig. 1(b) the phase of δg is shifted or oscillated with the frequency of Ω as stated above for the dynamic mitigation. The RTI growth mitigation ratio is 72.9% in Fig. 1 The growth mitigation ratio is defined by $(H_0\text{-}H_{\text{mitigate}})/H_0$. Here H is defined as shown in Fig. 1(a), H_0 shows the in Fig. 1(a) without the oscillation ($\Omega=0$), and H_{mitigate} presents the deviation for the other cases with the oscillation ($\Omega\neq0$). The example simulation results support well the effect of the dynamic mitigation mechanism.

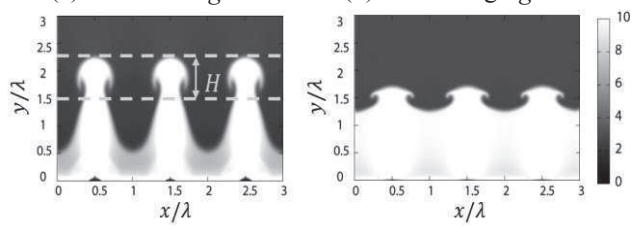

Figure 1: Example simulation results for the Rayleigh-Taylor instability (RTI) mitigation.

In the case of Fig. 1(b), the amplitude g_1 and the wave number k of δg are constant. In realistic situations the parameter of g_1, k and Ω would change in time and space.

In Fig. 2(a) the wobbling amplitude g_1 varies in time: $g_1(t) = g_1(1+\Delta\sin\Omega' t)$ in Eq. (1). In the simulations we employ $\Omega'=3\Omega$, Ω and $\Omega/3$. For Δ=0.1 and 0.3, and for $\Omega'=3\Omega$, Ω and $\Omega/3$, the RTI growth reduction ratio is 54.9~72.9% at t=5/γ. In Fig. 2(b) the wobbling wave number k varies in time: $k(t) = k(1+\Delta\sin\Omega' t)$ in Eq. (1). In the simulations we employ $\Omega'=3\Omega$, Ω and $\Omega/3$. For Δ=0.1 and 0.3, and for $\Omega'=3\Omega$, Ω and $\Omega/3$, the RTI growth reduction ratio is 68.8~93.3% at t=5/γ. Figure 2 shows an example simulation for RTI in Δ=0.3 and $\Omega'=\Omega$[3].

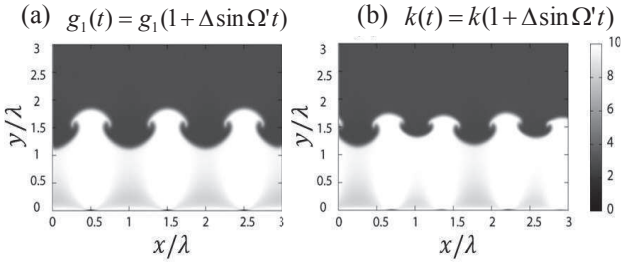

Figure 2: Fluid simulation results for the RTI mitigation for the time-dependent amplitude and wave number.

The wobbling or the modulation defines the imposed perturbation phase and amplitude at each time. Consequently the overall superposition of all the perturbations mitigates its growth through the control of the wobbling or modulating motion. The dynamic mitigation would work for the mitigation of instabilities in which the imposed perturbation phase is controlled actively.

References

[1] G. H. Wolf, *Phys. Rev. Lett.* **24**, 444 (1970)
[2] S. Kawata, *et al*, *Physica Scripta* **89**, 088001 (2014)
[3] S. Kawata and T. Karino, *Phys.* of Plasmas **22**, 042106 (2015)

Acknowledgements

This work was partly supported by MEXT, JSPS, ILE/Osaka University, ASHOLA, CORE/Utsunomiya University, CDI/Utsunomiya University, Collaboration Center for Research and Development of Utsunomiya University, and Japan/U.S. Fusion Research Collaboration Program conducted by MEXT, Japan.

Contact E-mail: mt146615@cc.utsunomiya-u.ac.jp, kwt@cc.utsunomiya-u.ac.jp

Two-body and three-body mesonic bound states in ultradense plasmas of fusion catalysis concern

Claude Deutsch
LPGP, CNRS, Univ. Paris-Sud, Université Paris-Saclay, 91405 Orsay, France

Atomic and molecular recombination of negatively charged mesons in warm dense matter (WDM) and fast ignition (FIS) ultradense plasmas, on low lying bound states is demonstrated, as well as a former conjecture about the negligibility of meson sticking on fusion produced α particles.

Mesonic catalysis of DT fusion reactions is then shown possible in short lived FIS and WDM plasma targets.

For several decades, since its inception in the 50's [1] the field of muon catalyzed fusion has featured impressive achievements in basic theoretical understanding and experimental vindication, as well [2]. Let us notice the detailed investigation of catalysing μDT molecules [3], as well as the production of about 150 fusions per muon. This tremendous effort has nevertheless been kept to a rest, essentially because of the negative muon getting stuck to the He^{2+} ion (α particle) resulting from the fusion process. To circumvent this infortunate occurence, several authors [4] proposed to replace the usual cold and liquid deuterium target by a fully ionized and low temperature plasma, in order to secure an efficient μ-desticking from the α_s' through collisions with plasma particles [5].

However, this challenging proposal has not yet been granted the attention it is deserving, presumably because of difficulties encountered in matching a low energy meson beam with a target plasma.

In the mean time, novel and ultra dense experimental facilities of useful relevance have appeared.

Let us first mention, an high energy extension [6] of the fast ignitor scenario (FIS) [7, 8] in inertial confinement fusion (ICF), highlighting in situ production of negative pions out of DT fuel electroproduction with ultra relativistic electron beams in the 100's MeV range originating from PW-lasers, and interacting with an ultra dense ($N_e = 10^{26} cm^{-3}$) plasma with a few hundreds eV temperature. When the pion is produced with only a few MeV above threshold, its stopping time in this target is then shorter than 1 psec [9], typical FIS time scale. Another promising option is afforded by meson stopping in a warm dense matter (WDM) target plasma featuring $N_e = 5.64 \times 10^{23}/cm^3$ and $T = 1.75eV$, deployed on the Linac Coherent Light Source (LCLS) at Stanford with an interaction time between 1 psec and 0.5 nsec.

Both approaches highlight strong collisions with classical ions embedded in partially (FIS) a strongly (WDM) degenerate electron fluid. Therefore a few MeV meson will be mostly stopped on target ions, within target dimensions ($\sim 100\mu m$ for FIS and $\sim 1mm$ for WDM).

To avoid unnecessary algebra, we shall qualify in the sequel the DT target component as D/T with ion mass $(m_D + m_T)/2 = 4583.70 m_e$.

The very existence of mesonic exoatoms can be probed through plasma Stark broadening of $Ly\alpha$ and $Ly\beta$ lines evaluated within the standard impact formalism applied to the usual electron-ion plasma surrounding them, in the FIS option.

The binding process of concern for achieving μ-catalyzed fusion highlights a further D/T capture by exoatom $D/T - \mu$. This can be obtained with a Langevin-like superposition of the exoatom polarizability α with its asymmetric dipole contribution μ_D, so that the D/T capture rate constant (in cm^3/sec and per exoatom) reads as (μ, relative mass)

$$\overline{K} = (2\pi q/\mu^{1/2})[\alpha^{1/2} + c\mu_D(2/\pi k_B T)^{1/2}] \quad (1)$$

with [9]

$$\alpha = \frac{1}{n}\sum_{\ell=0}^{n-1}\left[a_0^{n\ell} + 2\sum_{m=0}^{\ell} a_2^{n\ell}\frac{3m^2-\ell(\ell+1)}{\ell(2\ell-1)}\right] cm^3 \tag{2}$$

where

$$a_0^{n\ell} = \frac{n^4}{4}[4n^2+14+7\ell(\ell+1)]$$
$$a_2^{n\ell} = \frac{-n^4\ell}{4(2\ell+3)}[3n^2-9+11\ell+\ell(\ell+1)]$$

and dipole moment $\mu_D = \frac{ea_0^\mu}{2n}\sum_{\ell=0}^{n-1}(3n^2-\ell(\ell+1)$ averaged over (n,ℓ) levels through Holtsmark Stark-mixing, with tuning parameter c featuring either a locked dipole ($c=1$) or a rotating one ($c=0.1$).

Table 1: Three-body capture rates $N_{D/T}\bar{K}$ (psec^{-1}) in terms of exoatom main quantum number n and amount of dipole contribution c.

a) WDM target
($T = 1.75eV, N_{D/T} = 5.64\times10^{23}/cc$)

n	1	2	3	4	5	6
c=0.1	1.34	5.71	14.45	29	50.2	64.4
c=1	10.55	39.5	189.2	161	256	375.5

b) FIS target ($T = 1keV, N_{D/T} = 10^{26}/cc$)

n	1	2	3	4
c=0.1	64.32	374.45	115.3	2622.03
c=1	132.64	624.95	1795.4	3601.25

Corresponding capture rates $N_{D/T}\overline{K}(psec^{-1})$ are tabuled in Table 1 for $1\leq n\leq 6$ (WDM) and $1\leq n\leq 4$ (FIS). One witnesses a non negligible contribution down to $n=1$ with $c=0.1$ on 1 psec time scale, FIS targets show up as the most effective ones. However, including the fact that WDM targets could keep their parameters up to 0.5 nsec, these latter appear as most promising for an experimental vindication. These capture rates can easily induce the production of hydrogenic molecular ions μDT^+ on low lying bound levels, thus triggering a significant DT thermonuclear reaction.

To conclude, a nearly instantaneous ionization of the muon stuck on the α particle, through D/T collisions, has been documented, altogether with collisional stability of exoatom D/T-μ in similar conditions.

The two-body Oppenheimer recombination mechanism has then been adapted to feature a very swift exoatom production, which when applied to a negative pion may easily supersede its hadronic capture on low lying S levels.

Moreover, the Langevin procedure has been used to demonstrate D/T ion attachment on exoatom D/T-μ.

Then, the present analysis is expected to underlie a plasma path to meson catalysis which is very different from the usual one making use of cold fuel target. In lieu of having the meson replacing highly excited but bound electron (Auger process), the present approach highlights Coulomb interactions involving the lowest bound levels through a dynamic process involving ionic collisions.

The very dense plasma targets herein envisaged could lead to a fruitful meson catalysis on a time scale much shorter than pion decay time ($\sim$ 28 nsec), so its direct electroproduction out of the D/T nuclear fuel can very significantly lower the initial cost of the catalyzing meson production.

References

[1] J.D. Jackson, Phys. Rev. **106**, 330 (1957).

[2] H.E. Rafelski, D. Harley, G.R. Shin and J. Rafelski, J. Phys. B **24**, 1469 (1991).

[3] L. Bracci and G. Fiorentini, Phys. Rep. **56**, 169 (1982).

[4] For instance, L.I. Menshikov and L.I. Ponomarev, JETP Lett. **46**, 312 (1987).

[5] J. Rafelski and D. Harley, Part. Accel. **37-38**, 409 (1992).

[6] C. Deutsch and J.P. Didelez, Laser Part. Beams **29**, 39 (2011).

[7] M. Tabak, I. Hammer, M.E. Glinsky, W.L. Kruer, S.C. Wilks, J. Woodworth, E.M. Cambell, M.D. Perry, and R.J. Mason, Phys. Plamas **1**, 1626 (1994).

[8] T.S. Su and M.T. Bowers, J. Chem. Phys. **58**, 3027 (1973).

[9] D. Baye, Phys. Rev. **A86**, 062514 (2012).

The corrected Bethe-Larkin formula applied*

Yu.V. Arkhipov[1], A.B. Ashikbaeva[1], and I.M. Tkachenko[2,#]
[1]Al -Farabi Kazakh National University, Almaty, Kazakhstan; [2]Universidad Politécnica de Valencia, Valencia, Spain.

Abstract: The corrected Bethe-Larkin formula for the non-ideal plasma stopping power asymptotic form is successfully applied to recent experimental data.

In 1930, Bethe derived his seminal formula for the fast projectile energy losses assuming that the atoms of the medium behave as quantum-mechanical oscillators [1]. Thirty years later, Larkin [2] showed that when fast ions transpire an electron gas, the same formula is applicable, but with the mean atomic ionization potential I replaced by the plasma frequency ω_p:

$$S(v \to \infty) \cong \left(\frac{Z_p e \omega_p}{v}\right)^2 \beta a \, ln \frac{2mv^2}{\hbar \omega_p}, \qquad (1)$$

where $Z_p e$, and v stand for the charge and velocity of a projectile, β^{-1}, a and m are the plasma temperature in energy units, the electronic Wigner-Seitz radius and mass, $\hbar$ is the Planck constant, and $S(v)$ is the dimensionless plasma stopping power. This formula is often employed to determine experimentally the number density of electrons, n_e, in a charged particle system [3].

Leaving the ionization losses and other effects like the Barkas [4] one aside, for calculating the stopping power of a fast projectile passing through a Coulomb fluid we adopted the polarizational picture [5]. Then the expression for the stopping power can be simplified by applying the Fermi golden rule [6]:

$$S(v) = \left(\frac{Z_p e}{v}\right)^2 \frac{2\beta a}{\pi} \int_0^\infty \frac{dk}{k} \int_0^{kv} \omega^2 L(k,\omega) d\omega \,, \qquad (2)$$

where $L(k,\omega) = -\epsilon^{-1}(k,\omega)/\omega$ and $\epsilon(k,\omega)$ are the plasma loss and dielectric functions. Usually, the interaction of target electrons with the plasma ions is neglected in the stopping power. Nevertheless, the target plasma electron-ion static structure factor $S_{ei}(k)$ influences the plasma polarizational stopping power. This effect was taken into account in [7] using the canonical solution of the Hamburger moment problem in the corrected Bethe-Larkin formula:

$$S_{TCP}(v \to \infty) \cong \left(\frac{Z_p e \omega_p}{v}\right)^2 \beta a \, ln \frac{2mv^2}{I_{eff}}. \qquad (3)$$

Here $I_{eff} = \hbar\omega_p\sqrt{1+H}$, $H = \int_0^\infty \frac{p^2 S_{ei}(p) dp}{6\pi^2 \sqrt{n_e n_i}}$ and $n_i = Z n_e$ is the number density of ions of charge Ze in the system. The previous result (3) contrasts with the case of energy losses in one-component plasmas (OCPs), where the Bethe-Larkin formula (1) is not modified by the electron-electron correlations [8]. The electron-ion correlations should be accounted for along other effects like the influence of core electrons [9] on the stopping power of complex plasmas.

We have carried out some calculations based on the results of the recent work [9] and a reasonable agreement has been found between the precalculated values of the mean ionization potential in warm dense matter [9]:

$$\bar{I} \in [38.9, 48.8] \; eV$$

and our effective ionization potential. We have determined the effective number density of electrons corresponding to the plasmon energy $\hbar\omega_p$ of about 27 eV (see Fig. 5b from [9], see below): $n_e \approx 5.3 \cdot 10^{23} \; cm^{-3}$ ($Z = 1.82$), the temperature was assumed to belong to the error interval [9], $\beta^{-1} \in (17, 47) \; eV$ and calculated the coupling parameter H. The values of the latter turned out to be $H \in [0.92, 1.515]$ so that the effective potential determined by the target ions, $I_{eff} = \hbar\omega_p\sqrt{1+H} \in [37.4\,,\ 42.8]\; eV$, overlaps with the data provided in Fig. 5b of [9]. The H parameter was computed in the hypernetted chain approximation for the Deutsch potential.
More experimental studies are needed for further verification of the presented results.

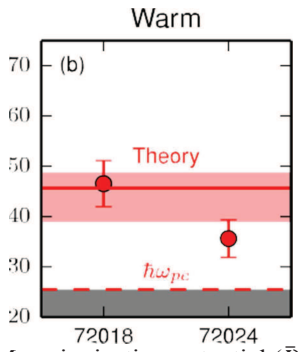

Fig. 5(b) [9]. Mean ionization potential ($\bar{I}$) inferred from the stopping power data obtained for two different experimental shots in the warm case compared to the ideal plasma theory ($\hbar\omega_{pe}$) and electronic structure theory.

References

[1] H. Bethe, Ann. Phys. (Lpz.) 5 (1930) 325.
[2] A. I. Larkin, Sov. Phys. JETP 37 (1960) 186.
[3] G. Belyaev et al., Phys. Rev. E 53 (1996) 2701; A. Golubev et al., Phys. Rev. E 57 (1998) 3363.
[4] W. H. Barkas, J. N. Dyer, and H. H. Heckman, Phys. Rev. Lett. 11 (1963) 26.
[5] J. Lindhard, Mat. Fys. Medd. K. Dan. Vidensk. Selsk. 28 (1954) 8.
[6] K. Morawetz and G. Röpke, Phys. Rev. E 54 (1996) 4134.
[7] D. Ballester, I. M. Tkachenko, Phys. Rev. Lett., 101 (2008) 075002.
[8] J. Ortner and I. M. Tkachenko, Rev. E 63 (2001) 026403.
[9] A.B. Zylstra et al., Phys. Rev. Lett., 114 (2015) 215002.

* Work supported by the Republic of Kazakhstan Ministry of Education and Science grant No. 3120/GF4 and by the Spanish Ministerio de Economía, Ciencia e Innovación Project ESP2013-41078-R.
#imtk@mat.upv.es

Influence of the Diagnostic Pulse Temporal Asymmetry on a Precision of the Phase Shift Reconstruction using a Complex Interferometry Approach*

M. Kalal

Faculty of Nuclear Sciences and Physical Engineering, CTU in Prague, Czech Republic

Overview of the Principles

Interferometry belongs to the key *active* diagnostics of optically transparent objects (e.g., laser produced plasma). In its *classical* form by analyzing *interferograms* one can obtain information about the *phase shift* between the *signal* and the *reference* part of the *diagnostic* beam. There are various methods how to perform this analysis. The most *precise* of all is based on the fast Fourier transform (FFT). This particular method paved the way to a more advanced interferogram usability, which allows *recording* (intentional or even unintentional) and subsequent *reconstruction* of up to *three* sets of *independent* data from just *one* data object - a *complex interferogram*. Using this approach, not only the usual *phase shift*, but also the *amplitude* and the *fringe contrast* can be recorded *simultaneously* and subsequently analyzed. This technique became known as the *complex interferometry*.

In its latest development it was shown that this advanced *CI* approach provides even the way of characterizing an influence of the diagnostic beam temporal profile *asymmetry* on the *phase shift* reconstruction, thus even further increasing its *accuracy*. An algorithm for *evaluation* and *removal* of this *systematic error* related to this effect was proposed [1] and its basics will be summarized in this contribution.

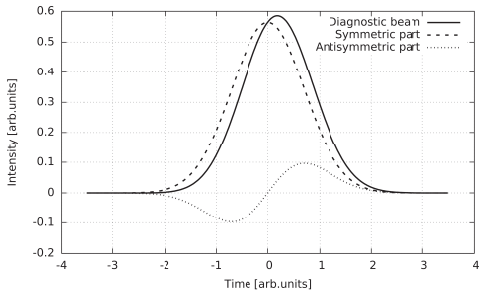

Figure 1: Example of a typical diagnostic beam *temporal profile* featuring a hard-to-notice *asymmetry* (continuous) and the same profile *split* into its *symmetric* (dashed) and *anti-symmetric* (dotted) parts.

In case of using a typical FFT based approach (for both the *classical* as well as the *complex* interferograms), the resulting *total* reconstructed *phase shift* value $\varphi_{total}(y,z)$ consists of *three* contributions:

$$\varphi_{total}(y,z) = \varphi_p(y,z) + \varphi_{derr}(y,z) + \varphi_{serr}(y,z)\,. \quad (1)$$

* Work supported by the Ministry of Education, Youth and Sports of the Czech Republic project LD14089

Here $\varphi_p(y,z)$ stands for the *pure* phase shift caused by the *object itself* (this is the quantity we are looking for !!!); $\varphi_{derr}(y,z)$ stands for the *error* caused by the *diagnostic system* itself (interferometer setup and the diagnostic beam wave front quality); $\varphi_{serr}(y,z)$ stands for the *systematic error* caused by the *degree of asymmetry* of the diagnostic pulse $f(t)$ and goes to *zero* in case of its *symmetry*.

The *second* contribution, $\varphi_{derr}(y,z)$, can be completely *corrected* when a *reference* interferogram would become available (and the diagnostic system is reasonably *stable* between shots). As by its analysis exactly this contribution would be reconstructed. In this case one can still safely remain in the *classical* interferometry area.

However, in order to deal with the *third* contribution, $\varphi_{serr}(y,z)$, a full *CI* approach needs to be employed, as for this purpose the following quantity, the so called *q-function*, would be required (for full details see Ref. [1]):

$$q(y,z) = \int_{-\infty}^{+\infty} f(t)\exp[i\varphi'(y,z)t]dt\,. \quad (2)$$

Here $\varphi'(y,z)$ stands for the *phase shift time derivative* in the time $t = 0$. This time needs to be determined from the *temporal profile* of the diagnostic pulse $f(t)$ such a way that both the *symmetric* $f_s(t)$ as well as the *anti-symmetric* $f_a(t)$ part would have it in common (while *minimizing* the *anti-symmetric* part area). In fact, only the function $|q(y,z)|$ can be reconstructed from complex interferograms and not the full $q(y,z)$. Due to the following inequalities:

$$0 \le |q_i(y,z)| \ll q_r(y,z) \le 1\,, \quad (3)$$

where $q_r(y,z)$ and $q_i(y,z)$ represents the *real* and the *imaginary* part of $q(y,z)$, respectively, the absolute value of this function, i.e., $|q(y,z)|$, can be regarded as a very good approximation of its real part $q_r(y,z)$. From $|q(y,z)|$ the $\varphi'(y,z)$ can be reconstructed (based on the obtained $f_s(t)$ profile) and subsequently $q_i(y,z)$ can be determined:

$$q_i(y,z) = \int_{-\infty}^{+\infty} f_a(t)\sin[\varphi'(y,z)t]dt\,. \quad (4)$$

Finally, the $\varphi_{serr}(y,z)$ itself can be evaluated:

$$\varphi_{serr}(y,z) = \arcsin\left(\frac{q_i(y,z)}{|q(y,z)|}\right)\,. \quad (5)$$

References

[1] M. Kalal, M. Krupka, J. Dostal, R. Dudzak, and J. Ullschmied, Proceedings of Science (ECPD2015) 014 (2015).

Bright X-Ray Source from a Laser-Driven Microplasma Waveguide*

L. Yi[1,2,#], A. Pukhov[1], Ph. Luu-Thanh[1], and B. Shen[2,3]
[1]Institut für Theoretische Physik I, Heinrich-Heine-Universität Düsseldorf, Düsseldorf 40225, Germany;
[2]State Key Laboratory of High Field Laser Physics, Shanghai Institute of Optics and Fine Mechanics, Chinese Academy of Sciences, Shanghai 201800, China;
[3]Collaborative Innovation Center of IFSA, Shanghai Jiao Tong University, Shanghai 200240, China.

We have demonstrated, via 3D particle-in-cell (PIC) simulations, when coupled with a readily available 1.8 J laser, a microplasma waveguide (MPW) may serve as a novel compact x-ray source [1]. Electrons are extracted from the walls and form a dense helical bunch inside the channel. These electrons are efficiently accelerated and wiggled by the superluminal optical modes in the MPW, results in a bright, well-collimated emission of synchrotron x rays in the range of 1 ~ 100 keV.

The sketch of our simulation setup is shown in Fig. 1(a). A circularly polarized laser enters the MPW from the left side, extracting the electrons from the skin layer. Electrons with proper phase can be accelerated with a peak acceleration gradient of 4 TV/m. The map of longitudinal fields in the MPW [Figs. 1(b)–1(d)] shows an interference between different optical modes excited in the MPW, which overtake the accelerating electron bunches and wiggle them efficiently. As a result, bright synchrotron radiation is generated in forward direction [Fig. 1(e)]. The waveguide modes slowly separate from each other owing to the different group velocities, some pure high order mode patterns are observed in the rear of the simulation box behind the main laser pulse as shown in Fig. 1(d).

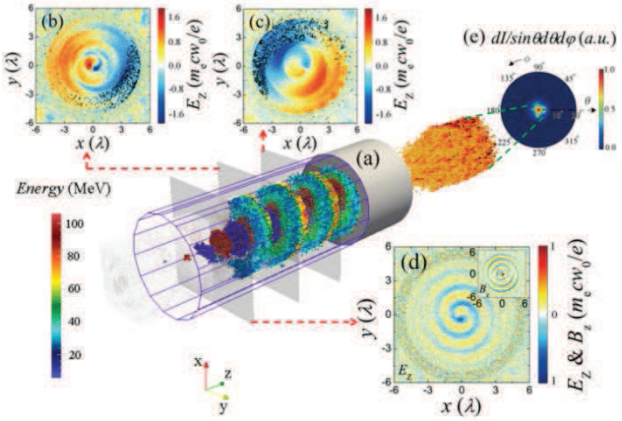

Figure 1: (a) Sketch of x-ray production by laser interacting with a MPW. (b-d) Longitudinal electric & magnetic fields at different cross-sections, black dots in (b-c) denotes the position of electrons. (e) Typical radiation pattern and divergence.

In general, the features of synchrotron radiation are governed by (i) the gamma factor (γ) of electrons and (ii) transverse wiggling force. In the proposed scheme, the acceleration (i) is due to the transverse magnetic (TM) modes in the channel, the maximum electron energy can be reached before dephasing [2] is 300 MeV and the total charge attained is 2.4 nC as shown in Fig. 2.

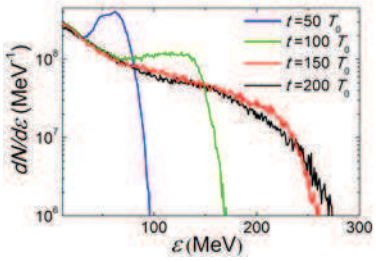

Figure 2: The electron spectrum at different times.

Meanwhile, since part of the laser energy is coupled into the longitudinal field, the transverse electric and magnetic fields become asymmetric. As a result, a net transverse Lorentz force (ii) exerts on the ultra-relativistic electrons, which can be estimated [3] to be one percent of the laser electric force. X-rays are generated (Fig.3) by synchrotron motion of the electrons with small divergence owing to this relatively-small transverse force. Hence a high brilliance can be achieved.

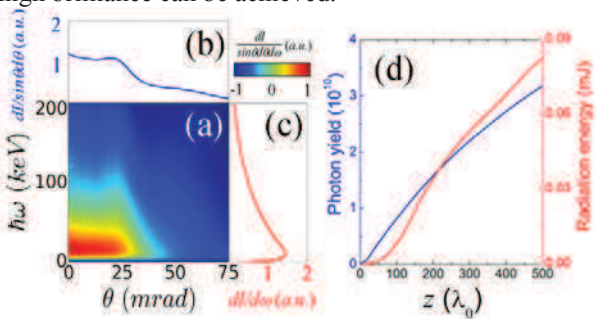

Figure 3: (a) Angular dependence of the emitted photon energy, and dependence of radiation intensity on (b) angle and (c) photon energy. (d) Total photon yield and radiation energy.

References

[1] L. Yi, A. Pukhov, Ph. Luu-Thanh, and B. Shen, "Bright X-ray Source from a Laser-Driven Microplasma Waveguide", Phys. Rev. Lett. **116**, 115001 (2016).
[2] L. Yi, A. Pukhov, and B. Shen, "Direct Acceleration of electrons by a CO_2 laser in a curved plasma waveguide", 2016 (http://arxiv.org/abs/1603.02983).
[3] H. Shen, "Plasma waveguide: A concept to transfer electromagnetic energy in space", J. Appl. Phys. 68, 6827 (1991).

* Work supported byEUCARD-2, Deutsche Forschungsgemeinschaft SFB TR 18 and National Natural Science Foundation of China (No. 11505262, No. 11125526, and No. 11335013).
# yi@uni-duesseldorf.de

Strong Ionization in carbon Nanowires*

Vural Kaymak† [1], *Alexander Pukhov*[1], *Vyacheslav N. Shlyaptsev*[2], *and Jorge J. Rocca*[2,3]

[1]Institut für Theoretische Physik, Heinrich-Heine-Universität Düsseldorf, 40225 Düsseldorf, Germany; [2]Department of Electrical Computer Engineering, Colorado State University, Fort Collins, Colorado 80523, USA; [3]Department of Physics, Colorado State University, Fort Collins, Colorado 80513, USA

In this article [1] we investigate the ionization dynamics of carbon nanowires by using full three dimensional PIC simulations [2]. The wires have a diameter of $400nm$, a length of $5\mu m$ and are irradiated by a $\lambda_0 = 400nm$ laser pulse of $60fs$ duration at FWHM and a vector potential of $a_0 = 18$. We analyze the influence of the polarization of the laser beam on strength and structure of the ionization. It turns out that the nanowires are fully ionized after about 30 laser cycles. Circular polarized light proves to cause a slightly faster ionization of the nanorods than linear polarized light.

Figures 1a and 1b present the averaged ionization state Z of the carbon ions along the whole nanowire for a linear and circular polarized laser pulse. Comparing both polarizations, it can be seen that the circular polarization ionizes the material faster. This becomes obvious in the intervals $2\lambda_0 < x < 9\lambda_0$ at $t = -41T_0$, $7\lambda_0 < x < 12\lambda_0$ at $t = -33.5T_0$ and $12\lambda_0 < x < 14.5\lambda_0$ at $t = -26T_0$. In both cases, the nanowire is almost fully ionized 26 lacercycles before the peak of the laser pulse hits the tip of the wire.

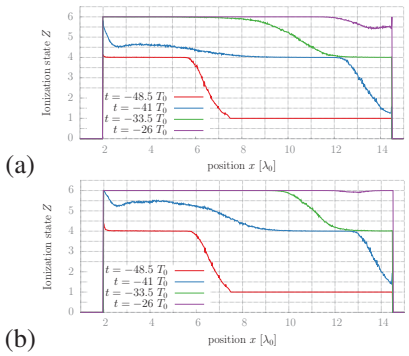

Figure 1: Averaged ionization state Z for a (a) linearly polarized and (b) circularly polarized laser pulse at four different times (measured with respect to the peak of the pulse reaching the wire tip) [1].

Figures 2 and 3 show the averaged ionization state in the y-z plane for linear polarization (in y-direction) and circular polarization, respectively. First field ionization takes place at the surface of the nanowire. For linear polarization (Fig. 2a), this is along the $z = 0$ line whereas for circular polarization the whole surface is involved (Fig. 3a). The electrons that are ionized this way then carry out collisional ionization within the wire core. The preferred direction for linear polarization becomes apparent in the wire along the $z = 0$ line through the wire center with values up to $Z \sim 5.6$ (Fig. 2b) and $Z \sim 6$ (Fig. 2c).

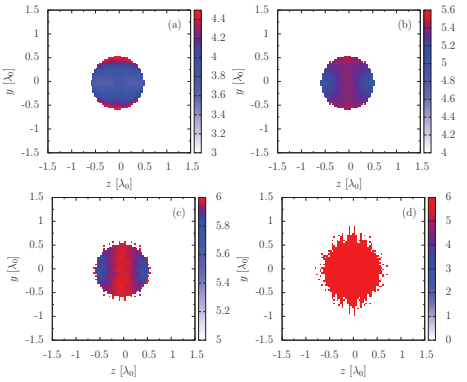

Figure 2: Averaged ionization state Z at (a) $t = -41\ T_0$, (b) $t = -33.5\ T_0$, (c) $t = -26\ T_0$ and (d) $t = -18.5\ T_0$ (linear polarization) [1].

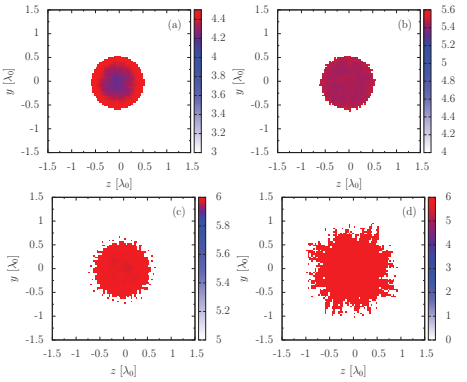

Figure 3: Averaged ionization state Z at (a) $t = -41\ T_0$, (b) $t = -33.5\ T_0$, (c) $t = -26\ T_0$ and (d) $t = -18.5\ T_0$ (circular polarization) [1].

On the other hand, the circular polarization causes the ionization distribution to be homogeneous along the whole crosssection (Fig. 3b). Eventually, the nanowire expands (Fig. 2d and 3d).

References

[1] V. Kaymak et al., Quantum Electron, 2016, 46

[2] A. Pukhov, J. Plasma Phys. 61, 425 (1999)

*This work was funded by DFG TR18, EU FP7 EUCARD-2 and by AFOSR award FA9560-14-10232.

† vural.kaymak@tp1.uni-duesseldorf.de

Electron Acceleration in Periodic Structures*

Phuc Thanh Luu† [1] *and Alexander Pukhov*[1]

[1]Institut für Theoretische Physik I, Heinrich Heine Universität Düsseldorf, Germany

Introduction

In this report, we present a new scheme of electron acceleration in periodic structures. The design of the scheme is shown in Fig. 1. Each period (1) consists of a shielding structure (2) and two pairs of lasers (3) focused at the centre of the gap. The other laser pairs at later time (4) are delayed in time. The parameter detail of the shielding structure is shown in Fig. 2. After being injected into the structure, the momentum of an electron will remain constant in the shielded region (5), but increase in the open region (6). Since the acceleration is based on the direct interaction between the particle and laser, it is also known as direct laser acceleration [1].

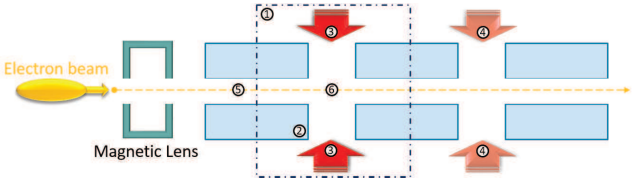

Figure 1: The schematic layout of the electron acceleration in periodic structures.

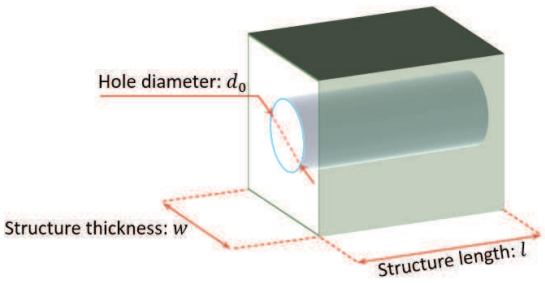

Figure 2: The parameter detail of the shielding structure.

Simulation

We have performed simulations in which an electron beam is injected into the structure and will propagate through twelve structure periods of silicon. The initial Lorentz factor of the beam is assumed to be $\gamma_0 = 1000$, the laser normalised intensity $a_0 = 2.5$ with pulse duration $\tau_0 = 30$ (fs) and wavelength $\lambda_0 = 800$ (nm). For each period, the structure has thickness $w = 4\lambda_0$, length $l = 7.5\lambda_0$, and hole diameter $d_0 = 0.2\lambda_0$. The ionisation process and the dielectric response are included in the simulation.

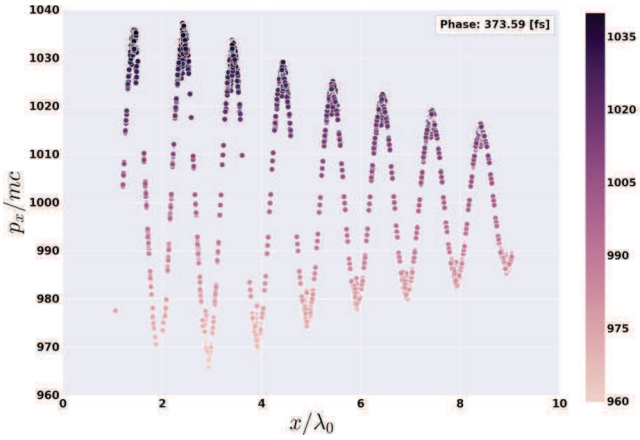

Figure 3: The phase space x/p_x of the electron beam at the end of the simulation, after propagating through twelve structure periods.

Fig. 3 shows the phase space x/p_x of the electron beam at the end of the simulation. We observe that the phase space distribution of the beam has evolved into resembling the oscillation of the laser beam in gap in which the particles are concentrating around the extreme points. Moreover, the magnitude of each extreme point is different. Indeed, the average energy of the second acceleration window (from left) is approximately 525.3 (MeV) (acceleration gradient 167.85 (GeV/m)) and at the same time the eighth window obtains 517.1 (MeV) average energy (acceleration gradient 68.87 (GeV/m)). We also notice that the first acceleration window achieves a lower average energy, compared to the second window and are losing particles. This indicates that the laser field in the gap for this window and later on has become unstable and thus not suited for acceleration.

Summary

We have presented the new scheme of electron acceleration in periodic structures. The simulation result shows that the scheme provides a high acceleration gradient. Future efforts will revolve around how to improve the number of trapped particles in the acceleration phases.

References

[1] R. J. England, "Dielectric Laser Accelerators", Rev. Mod. Phys., Vol. 86, No. 4, 2014.

* Work supported by GSI Darmstadt.

† luu@tp1.uni-duesseldorf.de

Bright attosecond high harmonic source with controllable polarization*

Zi-Yu Chen† [1,2] *and Alexander Pukhov*[1]

[1]Heinrich-Heine-Universität Düsseldorf, Germany; [2]Institute of Fluid Physics, China Academy of Engineering Physics

Ultrafast radiation sources in the extreme ultraviolet (XUV) range have become a major tool to study electronic structures and dynamics of atoms, molecules and condensed matter. It is particularly important to have such a light source with tunable polarization, as polarization is a fundamental property of light and controls its interaction with matter. The polarization control opens a wider range of applications in investigate chiral molecules magnetic materials. However, such light sources are still limited to a few free electron laser facilities and very recently to high-order harmonic generation (HHG) from noble gases. Here we propose and numerically demonstrate a new laser-plasma scheme to generate bright XUV pulses with fully controlled polarization[1].

It was commonly assumed up to now that relativistically oscillating mirror (ROM) mechanism fails for harmonic generation from plasma surfaces with a circularly polarized (CP) driving laser. However, this is true just for normal incidence. For oblique incidence interactions, harmonics can be efficiently generated even by CP laser pulses.

To verify this scheme, particle-in-cell simulations have been carried out using the code VLPL[2]. In the 2D simulations, we choose the laser and plasma parameters matching the realistic experiments. The CP laser pulse has a duration of 30 fs and a pulse energy of 1 J. The incidence angle is 40°. The plasma has a density of $200n_c$ and an initial density scale length of $0.2\lambda_L$. Figure 1 shows the 3D reconstructed waveform of the harmonics after spectral filtering of selecting the 10^{th}-20^{th} harmonic orders. It can be seen that a train of attosecond helical XUV pulses with high ellipticity has been generated. The peak amplitude reaches 2×10^{13}V/m. We also checked the intensity scaling of the harmonic spectrum, which is in excellent agreement with the predicted $I(n) \propto n^{-8/3}$ from the ROM theory with n the harmonic number. This suggests the radiation mechanism here is within the ROM regime.

A series of 1D simulation results show the polarization state of the harmonics can be well controlled, as can be seen from Fig. 2, where laser normalized amplitude $a_L = 5$ and plasma density $n_e = 200n_c$. With the increase of the incidence angle, the harmonic polarization state changes continuously from quasi-circular, through elliptical and linear, to elliptical of opposite helicity. This provides a practical and straightforward way to control over the ellipticity of the HHG pulses by simply adjusting the incidence angle of the laser pulse.

Besides, CP harmonics can also be generated using elliptically polarized laser pulses at oblique incidence. We also demonstrate that one single isolated attosecond helical XUV pulse can be generated using few cycle laser pulses with pulse duration of 5 fs (FWHM). In addition, by switching the helicity of the incidence laser, the handedness of the harmonics can be easily reversed. Moreover, parametric studies show that the present scheme works for a wide range of laser and plasma parameters. The efficiency is comparable to that using LP laser pulses.

In summary, we numerically demonstrate a promising new procedure, which provides a straightforward and efficient way to obtain bright attosecond XUV source with desirable ellipticities, and holds the potential of enabling a very large avenue of research more accessible within a number of laser laboratories worldwide.

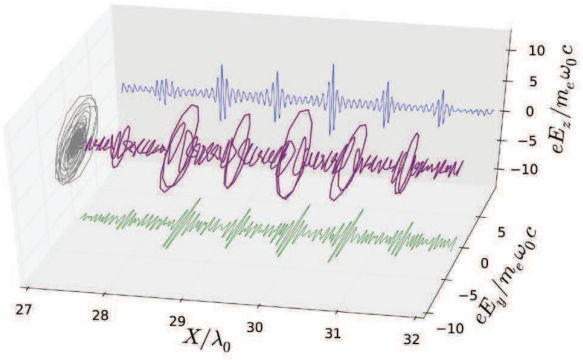

Figure 1: 2D simulation results of the attosecond helical XUV pulses.

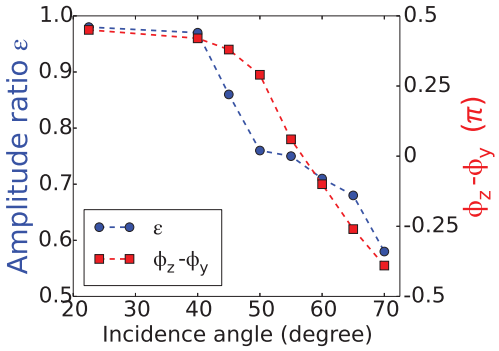

Figure 2: The harmonic polarization state as a function of the laser incidence angle.

References

[1] Z.-Y. Chen and A. Pukhov, arXiv:1601.05923 (2016).

[2] A. Pukhov, J. Plasma Phys. 61 (1999) 425.

* Work supported by CSC, DFG TR18, and by EU FP7 EUCARD2.

† ziyu.chen@uni-duesseldorf.de

Analytical description of attosecond pulse generation on plasma surface irradiated by high-intense lasers

M. Cherednychek and A. Pukhov

Institut für theoretische Physik, Heinrich-Heine-Universität Düsseldorf

We investigate the interaction between a few cycle ($T = 10\lambda/c$) high-intensity ($a_0 = 10$) laser pulse and an over dense plasma with exponential density ramp using one dimensional version of PIC code VLPL [1]. Assuming that the ions are at rest during the whole interaction process we consider only the interaction between the electrons and the incident wave.

We derive an analytic expression, which roughly describe the electron density profile at the intervals where the sharp spikes appear. Describing the local phase space distribution as

$$f_a(x,p) = \mathcal{C}\delta_a\left(x - \alpha p^2\right), \qquad (1)$$

where $\mathcal{C}$ is a normalization constant and δ_a is defined as

$$g_a(x) \equiv \frac{3}{4a}\left(1 - \frac{x^2}{a^2}\right)$$

$$\delta_a(x) \equiv \begin{cases} g_a(x) & \text{for} \quad x \in [-a,a] \\ 0 & \text{otherwise} \end{cases},$$

with the property $\lim_{a\to 0}\delta_a(x) = \delta(x)$, we obtain the expression for local electron density profile

$$n_a(x) = \begin{cases} \dfrac{N_{a,\Delta x}}{5a^3\sqrt{\Delta x}}\left(3a^2 - 2x^2 + ax\right)\sqrt{x+a} & \text{for} \quad x \in [-a,a] \\ \dfrac{N_{a,\Delta x}}{5a^3\sqrt{\Delta x}}\Big(\left(3a^2 - 2x^2\right)\left(\sqrt{x+a} - \sqrt{x-a}\right) & \\ \qquad + ax\left(\sqrt{x+a} + \sqrt{x-a}\right)\Big) & \text{for} \quad x > a \\ 0 & \text{for} \quad x < -a, \end{cases} \qquad (2)$$

which fits the simulated density quite well (Fig.1). Here is Δx the interval where the assumption (1) makes sense and $N_{a,\Delta x}$ the number of electrons within this interval.

We are interested in high frequency spectrum of the reflected pulse mostly determined by the behavior of the electron nanobunch when it moves away from plasma with maximal velocity. This moment corresponds to a stationary phase point (SPP) (see [2]). The gamma factor of the bunch exhibits a sharp spike in this time, it is called γ-spike [3]. Doing some simple assumption and using (2) we was able to obtain an analytical expression of the transverse current distribution in vicinity of SPP at the time where an attosecond pulse is generated, as well as the radiated electric field and its spectrum [2]. The corresponding results are shown in Fig. 2. See [4] for more details.

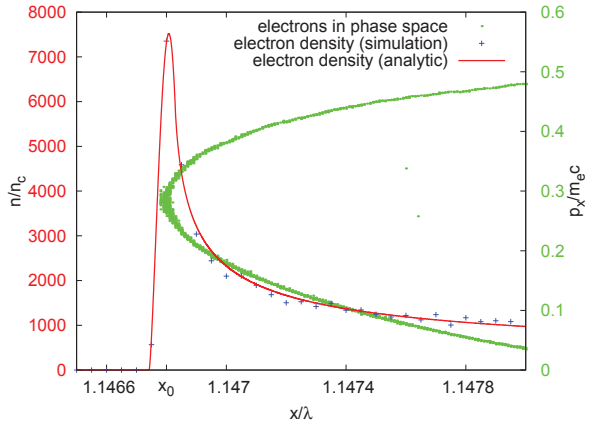

Figure 1: Electron density taken from the simulation (blue) and calculated analytically via (2) (red). Simulation parameters: initial density $n_0 = 38.9n_c$ (Laboratory frame), Pulse amplitude $a_0 = 10$, p-polarized oblique incidence at 57° angle, $\lambda = 820$nm. $\Delta x = 0.0012\lambda$; $a = 4.4 \cdot 10^{-5}$ (simulation frame).

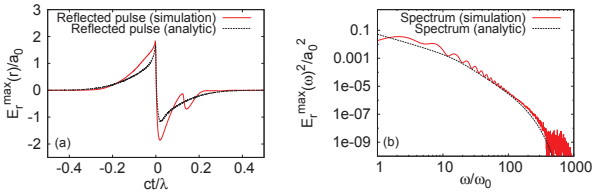

Figure 2: Reflected radiation obtained from the simulation ((a) red) and from analytical current distribution ((a) black), as well as the corresponding spectra in (b). Simulation parameters: initial density $n_0 = 100n_c$ (laboratory frame), Pulse amplitude $a_0 = 10$, p-polarized oblique incidence at 60° angle.

References

[1] A. Pukhov, "Three-dimensional electromagnetic relativistic particle-in-cell", J. Plasma Phys. **61**(1999) 425.

[2] D. an der Brügge and A. Pukhov, "Enhanced relativistic harmonics by electron nanobunching", Phys. Plasmas **17**(2010) 033110.

[3] T. Baeva, S. Gordienko and A. Pukhov "Theory of high-order harmonic generation in relativistic laser interaction with overdense plasma", Phys. Rev. E **74**(2006) 046404.

[4] M Cherednychek, A Pukhov, "Analytical description of attosecond pulse generation on plasma surface irradiated by high-intense lasers ", Quantum Electron, **46**(2016).

Modeling excitation and relaxation of laser-excited semiconductors *

Anika Rämer[1] *and Bärbel Rethfeld*[1]

[1]Department of Physics and State Research Center OPTIMAS, University of Kaiserslautern, Germany

Introduction

For many years now, the interaction of laser pulses with solid matter has been subject of both experimental as well as theoretical research. Particularly ultrashort laser pulses causing minimal collateral damage to the surrounding material are of high interest for applications.

Modeling and Results

Here, we present results obtained with the density-dependent two-temperature model (nTTM), a flexible and comprehensive theoretical approach accounting for the highly transient free carrier density in laser-excited semiconductors that is introduced in detail in Refs. [1, 2].

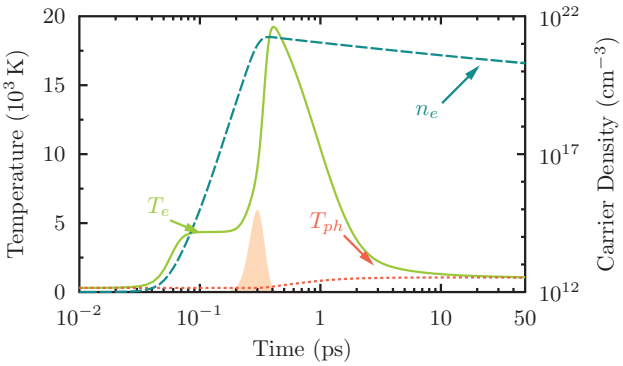

Figure 1: Characteristic temperature and density evolution at the surface of laser-irradiated silicon.

Figure 1 shows the evolution of both, free carrier density and temperature, at the surface of a silicon sample irradiated with an 800 nm Gaussian laser pulse of 100 fs duration and a fluence of 130 mJ cm^{-2}. It clearly demonstrates the highly transient nature of the free carrier density that increases over several orders of magnitude during pulse duration. This has a huge influence on several modeling parameters and processes like reflectivity, free carrier absorption, transport and carrier-phonon coupling. As is shown in Fig. 2, the carrier-phonon coupling parameter strongly depends on the free carrier density and also increases by several orders of magnitude during pulse duration.

With the nTTM, we estimated damage thresholds. Note that for the fluences applied here, thermal melting is predominant. Thus, we assumed that the material is damaged once lattice temperature exceeds melting temperature.

Figure 3 shows that the simulated damage thresholds are in very good agreement with experimental data obtained by Allenspacher *et al.* [3] and Pronko *et al.* [4] over a wide range of pulse durations ranging from 50 fs to 6 ps. We have shown that the density-dependence of the optical parameters plays a crucial role in our simulations [2].

* Financial support by the Deutsche Forschungsgemeinschaft through the Heisenberg Program (Grant No. 1141/15) is gratefully acknowledged.

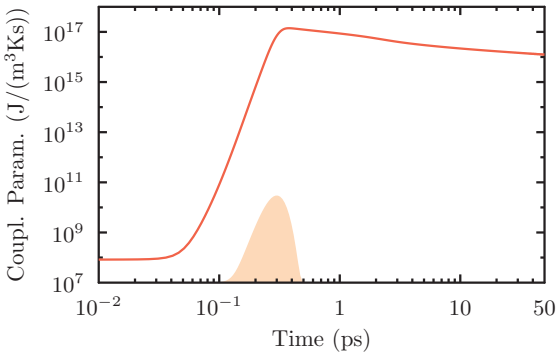

Figure 2: Evolution of the carrier-phonon coupling parameter at the surface of laser-irradiated silicon.

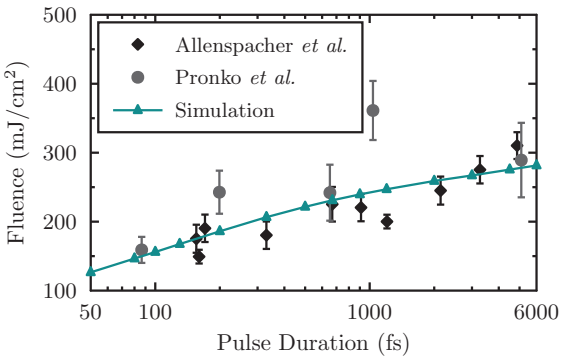

Figure 3: Damage thresholds calculated with the nTTM in comparison to experimental data obtained in Refs. [3, 4].

Conclusion

We demonstrated that the highly transient free carrier density in laser-excited semiconductors has to be taken into account in theoretical models as it strongly influences several processes like carrier-phonon coupling and optical absorption.

References

[1] H. M. van Driel, Phys. Rev. B **35**, 8166 (1987).

[2] A. Rämer *et al.*, J. Appl. Phys. **116**, 053508 (2014).

[3] P. Allenspacher *et al.*, Proc. SPIE **4923**, 358 (2003).

[4] P. P. Pronko *et al.*, Phys. Rev. B **58**, 2387 (1998).

Relaxation of a nonequilibrium phonon distribution

I. Klett and B. Rethfeld

Department of Physics and OPTIMAS Research Center, Erwin Schroedinger Str. 46, 67663 Kaiserslautern, Germany

The irradiation of solids with an ultrashort laser pulse leads to a hot electron system, while the lattice temperature stays nearly unaffected. After laser excitation, the energy absorbed by the electrons is distributed within the electron system and transferred to the phonons due to electron-phonon collisions. Both processes have been described by assuming a thermalized phonon distribution [1], however, mainly one phonon mode is able to absorb the energy of the electrons [2]. This leads to a thermodynamic nonequilibrium within the phonon system. Such a nonequilibrium can also be achieved by exciting different phonon modes directly with an ultrashort terahertz laser pulse. We describe the evolution of the phonon distribution function with Boltzmann collision integrals

$$\frac{\partial g}{\partial t} = \Gamma_{\mathrm{ph-ph}} + \Gamma_{\mathrm{ph-el}} + \Gamma_{\mathrm{absorb}} \ . \qquad (1)$$

The left side of the Boltzmann equation contains the temporal derivative of the distribution function, changes due to the different scattering processes can be found on the right side. The term $\Gamma_{\mathrm{ph-ph}}$ describes the thermalization within the phononic system. In the following calculations, only these phonon-phonon collisions are considered. In contrast to other collision integrals in our Boltzmann approach, the phonon-phonon collision term is direction-dependent, in order to distinguish between different phonon modes. Phonon frequencies and polarization vectors follow from the interatomic potential and the stucture of the unit cell of the chosen material. These quantities are material-specific and enter the phonon-phonon matrix element. To calculate the matrix element, which is included in the phonon-phonon collision term, a suitable interatomic potential needs to be chosen. This has to be at least a three-body potential, because a Taylor expansion up to the third order is required. We apply a Stillinger-Weber [3] potential, which is a well known analytical three-body potential with a small cutoff, so for most materials only nearest neighbors have to be considered. The Stillinger-Weber potential was developed for silicon, however, we use a copper-like testing system, because of its easier crystal structure. The unit cell of copper contains only one atom, so only acoustic phonons have to be considered. We assume a nonequilibrium distribution function, shown in figure 1, which is a Bose function with an additional peak at $5 \times 10^9 \frac{1}{m}$. We consider the phonon wave vectors and atomic movements in different crystal directions, namely, (100), (110) and (111) and calculate the temporal derivative of the distribution function for each direction. The results are shown in figure 2. A trend of the distribution function towards a Bose distribution can be noticed for all three calculations. We observe considerable differences for the rate of change of the phonon distribution function (1) depending on the direction of the phonon wave vector. We attribute these differences to different atomic forces for these crystal directions. Note that these different forces generally lead also to different dispersion relations [4].

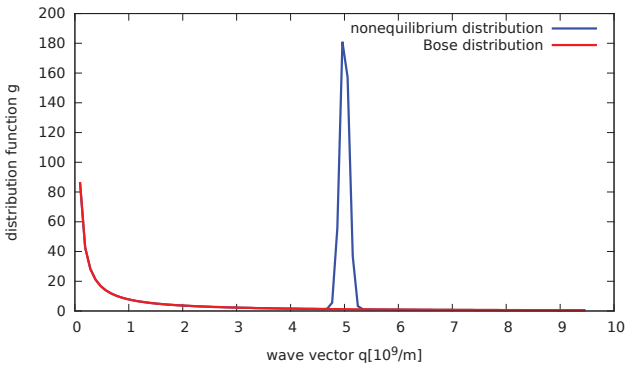

Figure 1: Nonequilibrium phonon distribution function in comparison to a Bose distribution

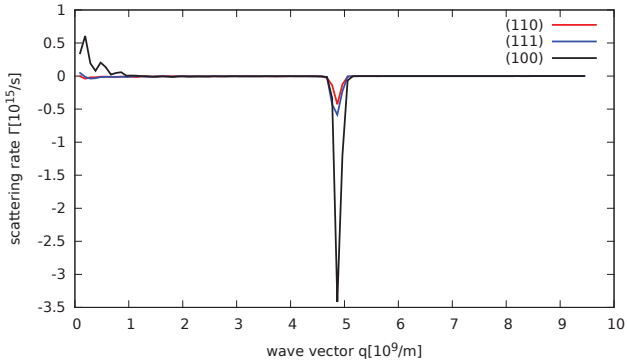

Figure 2: Temporal derivative of the phonon distribution function (1) for wavevectors in different crystal directions

References

[1] B. Rethfeld, A. Kaiser, M. Vicanek and G. Simon, Phys. Rev. B 65, 214303 (2002)

[2] L. Waldecker, R. Bertoni, J. Vorberger and R. Ernstorfer, Phys. Rev. X, accepted 2016

[3] F. H. Stillinger and T. A. Weber, Phys. Rev. B 31, 8:5262 (1985)

[4] I. Klett, T. Zier, B. Rethfeld, M. E. Garcia and E. S. Zijlstra, Phys. Rev. B 91, 144303 (2015)

Generation of high energy electron and positron beams in solid-plasma-nanolayers under relativistic laser pulses *

H.K. Avetissian† [1], *A.K. Avetissian*[1], *H.H. Matevosyan*[2], *G.F. Mkrtchian*[1], *and Kh.V. Sedrakian*[1]

[1]Centre of Strong Fields Physics, Yerevan State University, Yerevan 0025, Armenia; [2]Plasma Theory Group, Institute of Radiophysics and Electronics, 0203 Ashtarak, Armenia

Acceleration of electrons by relativistic laser pulses and their interaction with the matter in ultrashort space-time scales have attracted broad interest over the last two decades due to the continued progress in laser technology. Laser-charged particle interaction is characterized by relativistic invariant dimensionless parameter ξ - the work of the wave electric field on a wavelength λ in the units of electron rest energy. Thus, available optical lasers provide ξ up to 100, meanwhile with the next generation of laser systems [1] the exploitation of photon beams at $\xi > 10^3$ will be available. At the laser acceleration of electrons to obtain ultrarelativistic net energies for the field-free electrons one should bypass the limitations imposed by the Lawson-Woodward theorem. The latter can be reached by terminating the field, either by reflection, absorption, or diffraction.

In the work [2] we propose an efficient mechanism for creation of ultrarelativistic field-free electron bunches, γ-ray and positron beams of high fluxes by a single laser pulse of ultrarelativistic intensities. The scheme is as follows: a laser beam of ultrarelativistic intensities is focused onto the nanoscale-solid plasma-target with relatively low $\mathcal{Z}$. For concreteness we take a carbon target ($\mathcal{Z} = 6$). From this target under the action of ultrashort laser pulse a superdense electron bunch is formed and accelerated up to ultrarelativistic energies. Then we place a high-$\mathcal{Z}$ target (tungsten or gold) at the distances where the electron bunch gains maximum energy from the laser pulse. The purpose of the second target is twofold. First, it acts as a reflector for laser pulse. As a consequence we get field-free ultrarelativistic electron bunch. Second, within this target with sufficiently large thickness the generation of hard γ-quanta and positron fluxes take place due to the electron-ion collisions.

The typical energy distribution in accelerated electron layer at various $\mathcal{Z}$ is shown in Fig. 1 for linearly polarized wave with waist 10λ and $\xi = 30$. The reflector-target is located at 100λ.

In the high-Z target due to the electron bunch–ion collisions along with primary bunch one will have substantial amounts of produced high energy photons and positrons. In Fig. 2. in the logarithmic scale it is shown the energy distribution functions for primary accelerated electrons, produced γ-quanta, and positrons for the target of thickness $L_t \approx 0.2\mathcal{L}_{\rm rad}$ ($\mathcal{L}_{\rm rad}$ is the target radiation length).

As is seen from these figures, through two-target scheme

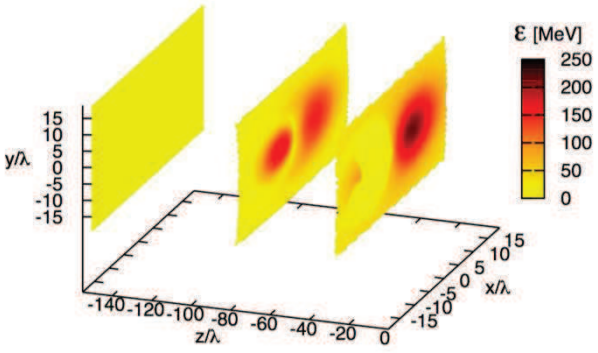

Figure 1: Energy distribution in accelerated electron layer at various z for linearly polarized wave with $w_0 = 10\lambda$ and $\xi = 30$.

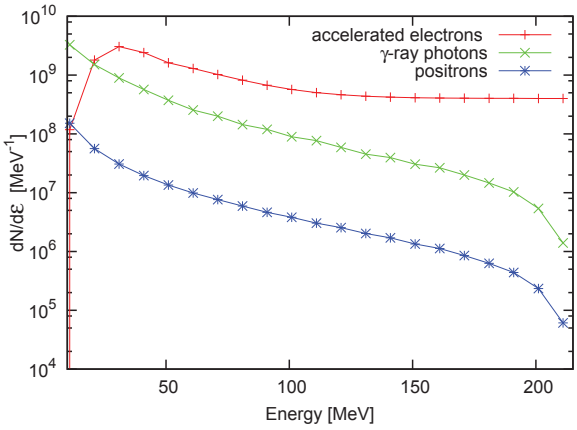

Figure 2: In the logarithmic scale it is shown the energy distribution functions for primary accelerated electrons, produced γ-quanta and positrons for the setup of Fig. 1

one can produce dense electron/positron bunches and substantial amounts of γ-quanta of energies up to 200 Mev that may have applications in material science, medicine, and nuclear physics.

References

[1] The Extreme Light Infrastructure (ELI) project: http://www.extreme-light-infrastructure.eu/eli-home.php.

[2] H.K. Avetissian, H.H. Matevosyan, G.F. Mkrtchian, Kh.V. Sedrakian, Phys. Rev. ST Accel. Beams 18 (2015) 121301.

* Work supported by SCS of RA.

† avetissian@ysu.am

Nonlinear absorption of high-intensity x-ray radiation in ultradense plasma*

H.K. Avetissian† [1], *A.K. Avetissian*[1], *A.G. Ghazaryan*[1], *H.H. Matevosyan*[2], *and G.F. Mkrtchian*[1]

[1]Centre of Strong Fields Physics, Yerevan State University, Yerevan 0025, Armenia; [2]Plasma Theory Group, Institute of Radiophysics and Electronics, 0203 Ashtarak, Armenia

The recent remarkable progress in x-ray free electron laser technology allows production of wave pulses with intensity 10^{20} W/cm^2 [1] exceeding the peak brilliance of conventional synchrotron sources by many orders of magnitude. For such intensities the electron-radiation field energy exchange over a x-ray wavelength is larger than the photon energy, and the laser-matter interaction proceeds via essentially multiphoton channels. Thus, in recent decade the wide research field is opened up where common nonlinear effects are extended to high energy transitions for various systems - from atoms, through molecules, to plasma and solid samples. Among the fundamental processes of laser-plasma interaction the inverse bremsstrahlung absorption (IBA) of an intense laser field in plasma is one of the contemporary mechanisms that have applications ranging from plasma diagnostics to thermonuclear reactions and generation of intense x-ray radiation. Note that in the field of an intense x-ray laser, an electron may gain considerable energies absorbing even of a few quanta which makes it as an effective mechanism for laser heating of plasma.

In the paper [2], we have presented the microscopic relativistic quantum theory of multiphoton IBA of an intense shortwave laser radiation in the classical and quantum plasma. The Liouville-von Neumann equation for the density matrix has been solved analytically considering a laser field exactly, while a scattering potential of the plasma ions as a perturbation. With the help of this solution we derived a relatively compact expression for the nonlinear IBA rate when electrons are represented by the grand canonical ensemble. Numerical investigation of the obtained results for Maxwellian, as well as degenerate quantum plasmas at x-ray frequencies and large values of laser fields has been performed. As a reference sample we take fully ionized Aluminum and consider plasma of solid densities $n_e = 10^{23}\mathrm{cm}^{-3}$. In Fig. 1 and Fig. 2 the total x-ray IBA rates are shown for Maxwellian and degenerate quantum plasmas versus the interaction parameter χ_0 - the ratio of the amplitude of the momentum transferred by the laser field to the momentum at one-photon absorption. As is seen from these figures, for the pulse durations 0.1 fs one can achieve 100 eV absorbed energy by a per electron.

The obtained results demonstrate that for the shortwave radiation the IBA rate, being practically independent of the plasma temperature, is saturated with the increase of the wave intensity and in the x-ray domain of frequencies

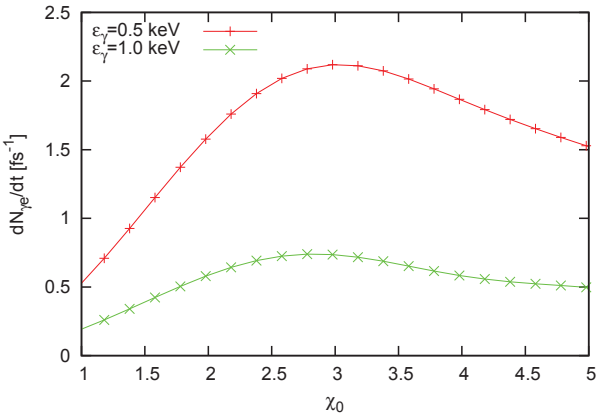

Figure 1: Total rate of IBA for circularly polarized wave in Maxwellian plasma versus the dimensionless parameter χ_0 for various photon energies at $T_e = 100$ eV.

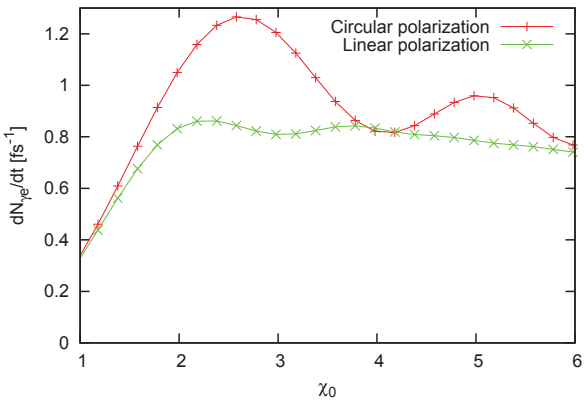

Figure 2: Total rate of IBA for circularly and linearly polarized waves in degenerate plasma versus the parameter χ_0 at $\varepsilon_F = 11.7$ eV, $Z_a = 13$, and $T_e = 0.1\varepsilon_F$.

one can achieve an efficient absorption of powerful radiation, specifically, in plasma of solid densities and reach the plasma heating in excess of 10^6 kelvin by x-ray lasers with the intensity 10^{22} W/cm^2.

References

[1] H. Mimura *et al.*, Nat. Commun. 5 (2014) 3539.

[2] H.K. Avetissian, A.G. Ghazaryan, H.H. Matevosyan, G.F. Mkrtchian, Phys. Rev. E 92 (2015) 043103.

* Work supported by SCS of RA.

† avetissian@ysu.am

Simulation study of terahertz radiation generation by propagation of intense laser pulses in plasma

Nirmal Kumar Verma*# and Pallavi Jha
Department of Physics, University of Lucknow, Lucknow-226007, India

Abstract: A simulation study for the generation of THz radiation by the propagation of intense, linearly polarized laser pulses in magnetized plasma, in the relativistic regime has been presented using XOOPIC code [1]. The presence of external magnetic field leads to the generation of slow transverse currents. These slow currents further lead to the generation of transverse electric and magnetic wakefields of equal amplitudes. It is found that these transverse component of wakefields can transmit into vacuum without energy loss, leading to the generation of THz radiation that can propagate out of plasma while the longitudinal electrostatic wakefield tends to zero in vacuum.

INTRODUCTION

Interaction of intense short laser pulses with plasma is an active area of research due to its potential applications such as laser wakefield accelerators [2], high harmonic generation [3], advanced laser fusion schemes [4] and terahertz (THz) radiation generation [5]. THz radiation finds a number of applications including ultrafast spectroscopy, terahertz imaging, health monitoring and explosive detection [6,7]. Due to non-ionising nature and the ability to penetrate several millimetres, terahertz radiation is suitable for material characterization and diagnosis of cancerous cells

FORMULATION

Consider a linearly polarized laser pulse, represented by $\vec{A}_L = \hat{y}A(x,t)\cos(kx-\omega t)$, propagating through plasma along the positive z-direction. The plasma, assumed to be cold, homogeneous and underdense is embedded in a static external magnetic field $B_0\hat{z}$. The fluid equations governing the interaction of the laser pulse with plasma are the Lorentz force, continuity and Poisson's equations respectively given by,

$$\frac{\partial(\gamma\vec{v})}{\partial t}+(\vec{v}.\vec{\nabla})(\gamma\vec{v})=-\frac{e}{m}\left(\vec{E}+\frac{\vec{v}}{c}(\vec{B}+\vec{B}_0)\right), \quad (1)$$

$$\frac{\partial n_e}{\partial t}+\vec{\nabla}(n_e\vec{v})=0, \quad (2)$$

$$\nabla^2\varphi=-4\pi e(n_0-n_e) \quad (3)$$

where γ is the relativistic factor, $\vec{E}$ and $\vec{B}$ represent the fast (oscillating at laser frequency) as well as the slow (oscillating at plasma frequency) electric and magnetic fields.

The plasma electron velocities may be considered to be a superposition of slow and fast components. The fast components of the transverse and longitudinal, relativistic plasma electron velocities are respectively obtained from Eq. (1) as,

$$v_{yf}=\frac{ac\gamma\omega^2}{(\gamma^2\omega^2-\omega_c^2)}\cos(kx-\omega t) \quad (4a),$$

$$v_{xf}=\frac{ac\omega\omega_c}{(\gamma^2\omega^2-\omega_c^2)}\sin(kx-\omega t) \quad (4b)$$

where $a\left(=eA/mc^2\right)$ is the amplitude of the normalized vector potential of the laser pulse. The equations governing the evolution of the transverse and longitudinal slow plasma electron velocities may be obtained from Eq. (1) as,

$$\frac{\partial(\gamma v_{ys})}{\partial t}+v_{xs}\frac{\partial(\gamma v_{ys})}{\partial x}+v_{xf}\frac{\partial(\gamma v_{yf})}{\partial x}=c\left(\frac{\partial a_{ys}}{\partial t}+v_{xs}\frac{\partial a_{ys}}{\partial y}+v_{xf}\frac{\partial a_{yf}}{\partial x}\right)+\omega_c v_{xs}, \quad (5a)$$

$$\frac{\partial(\gamma v_{xs})}{\partial t}+v_{xs}\frac{\partial(\gamma v_{xs})}{\partial x}+v_{xf}\frac{\partial(\gamma v_{xf})}{\partial x}=\frac{e}{m}\frac{\partial\varphi}{\partial x}-c\left(v_{ys}\frac{\partial a_{xs}}{\partial x}+v_{yf}\frac{\partial a_{yf}}{\partial x}\right)-\omega_c v_{ys}. \quad (5b)$$

It may be seen from Eqs. (5a) and (5b), that force arises due to the external magnetic field leads to the coupling between axial and transverse slow velocities, pointing towards the possibility of generating a slow transverse vortex current .

The slow field generated behind the laser pulse is given by the wave equation

$$\left(\frac{\partial^2}{\partial x^2}-\frac{1}{c^2}\frac{\partial^2}{\partial t^2}\right)e_{ys}=-\frac{\omega_p}{c^2}\frac{\partial(nv_{ys}/c)}{\partial t} \quad (6)$$

where $e_{ys}(=eE/m\omega_p c)$ is the normalized amplitude of the generated field behind the laser pulses.

SIMULATION STUDY THz GENERATION

In order to analyze the generation of the slow transverse electromagnetic waves, we consider a laser pulse having a sinusoidal profile of the form $a = a_0 \sin(\pi\xi/L)$, where a_0 and L are the normalized peak amplitude and length of the laser pulse respectively. The laser frequency is considered to be $\omega = 2.355x10^{15}$ *Hz*, $(\lambda = 800$ *nm)*. The study has been performed in the relativistic regime, with $a_0 = 1$,

* Work supported by UGC, Govt. of India under the Basic Science Research Scheme.

#nirmal87lu@gmail.com

which corresponds to a laser intensity of $I_0 = 2.4\times10^{18} W/cm^2$. The ambient plasma electron density (n_0) and hence the plasma frequency are $1.09\text{x}10^{19}/cm^2$ and $5.887\text{x}10^{13}$ *Hz* respectively. Since sinusoidal pulses propagating in plasma generate maximum amplitude wakes when $L \approx \lambda_p$ the laser pulse length is assumed to be 31 μm .

For the simulation process, a linearly polarized (along the *y*-direction) laser pulse having sinusoidal profile was launched (along the x-direction) in a homogeneous magnetized plasma. The simulations were performed for a spot size of 80 μm. The size of the simulation domain was taken to be 400 µm in the transverse direction and 160 μm in the laser propagation direction. The longitudinal domain comprised of 80 μm plasma length while the remaining was considered to be vacuum. The domain was divided into 4096 x 512 meshes. The time step (satisfying the courant condition) was 0.127 *fs*.

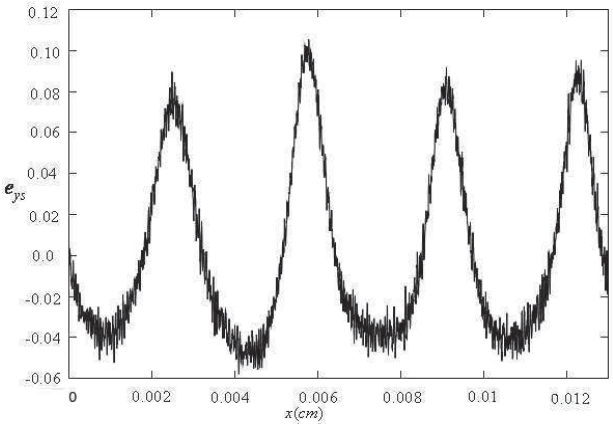

Fig.1: Transverse electric field generated behind the laser pulse obtained from XOOPIC code

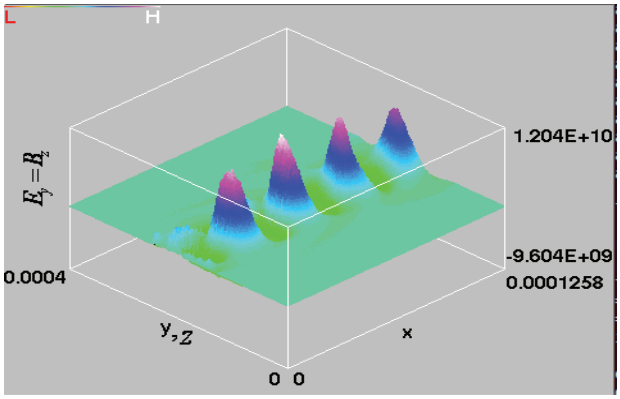

Fig. 2: 2-D plot of electric and magnetic field generated behind the laser pulse obtained from XOOPIC code

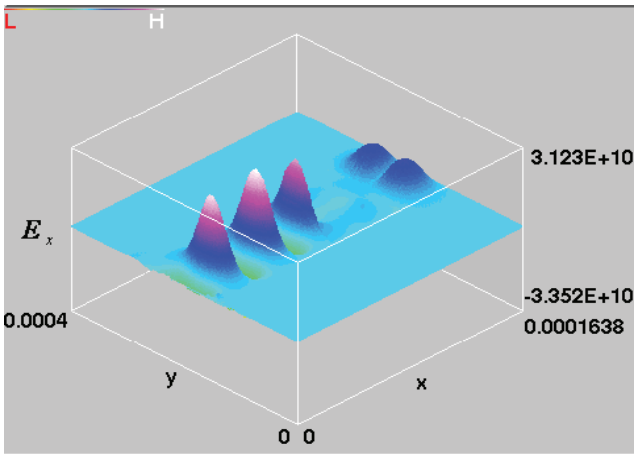

Fig. 3: Longitudinal electrostatic wakefield generated behind the laser pulse

SUMMARY AND DISCUSSION

A simulation study for the generation of THz radiation by the propagation of an intense, linearly polarized laser pulse in magnetized plasma has been presented. Due to the presence of external magnetic field the slow axial velocities couples with the transverse slow velocities. This coupling set up a slow non zero transverse vortex current in the wake of laser pulses. The occurrence of slow vortex current leads to the generation of a transverse electromagnetic wave behind the laser pulse. These transverse fields are observed to be oscillating at the plasma frequency, thereby leading to the generation of THz radiation in the wake of laser pulses. It is seen that the transverse electric and magnetic fields generated inside the plasma can transmit into vacuum leading to the THz radiation generation, while the longitudinal field being electrostatic in nature tends to zero in vacuum.

References

[1] P. Verboncoeur, A. B. Langdon, and N. T. Gladd, Comput. Phys. Commun. 87, (1995) 199.
[2] T. Tajima, and J. M. Dawson, Phys. Rev. Lett. 43 (1979) 267.
[3] S. Y. Chen, A. Maksimchuk, E. Esarey, and D. Umstadter, Phys. Rev. Lett. 84 (2000) 5528.
[4] M. Tabak, J. Hammer, M. E. Glinsky, W. L. Kruer, S. C. Wilks, J. Woodsworth, E. M. Campbell and M. D. Perry, Phys. Plasmas 1 (1994) 1626.
[5] H. Hamster, A. Sullivan, S. Gordon, W. White, and R. W. Falcome, Phys. Rev. Lett. 71 (1993) 2725.
[6] Q. Wu, T. D. Hewitt, and X.-C. Zhang, Appl. Phys. Lett. 69 (1996) 1026
[7] K. Yamaguchi, M. Nakajima, and T. Sunemoto, Phys. Rev. Lett. 105 (2010) 237201.

Analytical study of Wakefield generation via propagating of laser pulses in homogeneous plasma

Pooja Sharma and Pallavi Jha
Department of Physics, University of Lucknow, Lucknow-226007, India

Abstract: The present work includes an analytical study of the electrostatic wakefield generation due to the propagation of a circularly polarized laser pulse in homogeneous plasma. Under appropriate conditions, an enhancement in the peak amplitude of the wakes generated by circularly polarized laser pulse, as compared to the linearly polarized case, has been observed.

INTRODUCTION

The propagation of intense laser pulses in underdense plasma is relevant to a wide range of physical mechanisms. This includes relativistic optical guiding [1], harmonic generation [2], and excitation of large amplitude plasma waves for particle acceleration [3]. The motion of plasma electrons is largely influenced by the ponderomotive force of a short laser pulse, which is responsible for generating large amplitude electrostatic wakefields.

In this paper, analytical study of electrostatic wakefield generation due to the propagation of circularly polarized laser pulses through homogeneous, plasma has been presented . A perturbative technique is used to obtain the electric and magnetic wakefields generated behind the laser pulse, in the mildly relativistic regime. Under appropriate conditions, an enhancement in the peak amplitude of the wakes generated by circularly polarized laser pulse, as compared to the linearly polarized case, has been observed.

FORMULATION

Consider a circularly polarized laser beam having electric field vetor

$$\vec{E} = \hat{e}_x E_0(r,z,t)\cos(k_0 z - \omega_0 t) + \hat{e}_y E_0(r,z,t)\sin(k_0 z - \omega_0 t)$$

where $E_0(r,z,t)$, k_0, ω_0 are the amplitude, wave number, and frequency of the laser pulse respectively, propagateing along z direction through the homogeneous plasma. Plasma electrons obey the fluid equations,

$$\frac{\partial \vec{v}}{\partial t} = -\frac{e}{m\gamma}\left\{\vec{E} + \frac{\vec{v}\times\vec{B}}{c}\right\} + \vec{v}\times(\vec{\nabla}\times\vec{v}) - \frac{1}{2}\vec{\nabla}(\vec{v}.\vec{v}) \quad (1)$$

and $$\frac{\partial n}{\partial t} + \vec{\nabla}(n\vec{v}) = 0. \quad (2)$$

where $\gamma(=(1-v^2/c^2)^{-1/2})$ is the relativistic factor. In the mildly relativistic regime, a perturbative technique is used to expand various parameters in orders of the laser strength parameter $a_o(=eE_0/mc\omega_0 << 1)$.

The zeroth order describes the equilibrium plasma state, prior to the passage of the laser pulse, such that $\vec{v}^{(0)} = 0$, $n = n_0$ and $\gamma^{(0)} = 1$. The first order quiver velocity of the plasma electrons in the mildly relativistic regime can be obtained from Eq. (1) and (2) as $v_x^1 = \hat{x}ca_0\sin(k_0 z - \omega_0 t)$, $v_y^1 = \hat{y}ca_0\cos(k_0 z - \omega_0 t)$ and $v_z^1 = 0$ also, $n^{(1)} = \gamma^{(1)} = 0$.

In order to study the generation of wakefields in homogenious plasma, we use the quasi-static approximation (QSA) i.e. it is assumed that the laser pulse amplitude does not evolve significantly as it transits a plasma electron . The plasma fluid equations are written in terms of independent variables $\xi = z - ct$ and $\tau = t$. Under QSA, the plasma electrons experience a static (independent of τ) laser field and therefore the field variations with respect to τ are neglected in the plasma fluid equations. In order to obtain the generated electric and magnetic wakefields, the time dependent Maxwell's equations,

$$\vec{\nabla}\times\vec{E} = -\frac{1}{c}\frac{\partial \vec{B}}{\partial t} \quad (3)$$

$$\vec{\nabla}\times\vec{B} = \frac{4\pi}{c}\vec{J} + \frac{1}{c}\frac{\partial \vec{E}}{\partial t} \quad (4)$$

written in the transformed frame are given by,

$$\frac{\partial E_z}{\partial y} - \frac{\partial E_y}{\partial \xi} = \frac{\partial B_x}{\partial \xi} \quad (3a)$$

$$\frac{\partial E_x}{\partial \xi} - \frac{\partial E_z}{\partial x} = \frac{\partial B_y}{\partial \xi} \quad (3b)$$

$$\frac{\partial E_y}{\partial x} - \frac{\partial E_x}{\partial y} = \frac{\partial B_z}{\partial \xi} \quad (3c)$$

and

$$\frac{\partial B_z}{\partial y} - \frac{\partial B_y}{\partial \xi} = \frac{4\pi}{c}J_x - \frac{\partial E_x}{\partial \xi} \quad (4a)$$

$$\frac{\partial B_x}{\partial \xi} - \frac{\partial B_z}{\partial x} = \frac{4\pi}{c}J_y - \frac{\partial E_y}{\partial \xi} \quad (4b)$$

$$\frac{\partial B_y}{\partial x} - \frac{\partial B_x}{\partial y} = \frac{4\pi}{c}J_z - \frac{\partial E_z}{\partial \xi} \quad (4c)$$

where, $J_{x,y}$ and J_z are the transverse and axial current densities respectively. . The slow current densities driving the wakefields are obtained with the help of the Lorentz force equation (1) and continuity equation (2). The equa similar (opposite) polarization directions. The peak values

tions governing the lowest (second) order slow components of velocities are obtained with the help of Eq. (1) as

$$\frac{\partial v_x^{(2)}}{\partial \xi} = \frac{e}{mc} E_x^{(2)} + \frac{c}{2}\frac{\partial a_0^2}{\partial x} \quad (5a)$$

$$\frac{\partial v_y^{(2)}}{\partial \xi} = \frac{e}{mc} E_y^{(2)} + \frac{c}{2}\frac{\partial a_0^2}{\partial x} \quad (5b)$$

$$\frac{\partial v_z^{(2)}}{\partial \xi} = \frac{e}{mc} E_z^{(2)} + \frac{c}{2}\frac{\partial a_0^2}{\partial \xi} \quad (5c)$$

While deriving Eqs. (5), the first order velocity componentshave been used.

For a sinusoidal laser pulse profile of the form $a^2 = a_r^2 \sin^2 \pi\xi / L$ where $a_r^2 (= a_0^2 \exp(-2r^2/r_0^2))$, represents a Gaussian beam, the respective wakefields behind ($\xi < 0$) the laser pulse are given by,

$$E_{x,y}^{(0)} = -\frac{(x,y)\varepsilon f}{r_0^2}[f(\cos k_p(L-\xi) - f\cos k_p\xi - 1 + \cos(\frac{2\pi\xi}{L})] \quad (6)$$

$$E_z^{(0)} = \frac{\varepsilon k_p f}{4}(\sin k_p(L-\xi) + \sin k_p\xi) \quad (7)$$

$$B_{x,y}^{(0)} = \frac{\varepsilon(x,y)}{r_0^2}\cos\frac{2\pi\xi}{L} \quad (8)$$

$$B_z^{(0)} = 0 \quad (9)$$

While the equation governing the longitudinal wakefield for a linearly polarized laser pulse is given by

$$E_z^{(0)} = \frac{\varepsilon k_p f}{8}(\sin k_p(L-\xi) + \sin k_p\xi) \quad (10)$$

where $\varepsilon = mc^2 a_r^2 / e$ and $f = (1 - k_p^2 L^2 / 4\pi^2)^{-1}$.

It may be noted that the on-axis transverse wakefields as well as plasma electron velocities, behind the laser pulse, are zero.

In Fig. 1, dotted and solid curves represent respectively the variation of normalized, longitudinal electric wakefields $E_{nz} (= eE_z / mc\omega_p)$ with respect to ξ / L, generated behind (ξ / L = 0 to -4) the linearly and circularly polarized laser pulse respectively, in homogeneous plasma. The laser and plasma parameters used are $a_0^2 = 0.1$ (which corresponds to laser intensity $I = 2.13\times10^{17} W/cm^2$), $L = \lambda_p = 15.0\mu m$, $n_0 = 4.958\times10^{18} cm^{-3}$ and $\omega_c / \omega_p = 0.1$. It is seen that the peak amplitude of the net electric wakefield generated behind the circularly polarized laser pulse in homogeneous plasma is enhanced by 49.98 % in comparison to that generated by linearly polarized laser pulse .

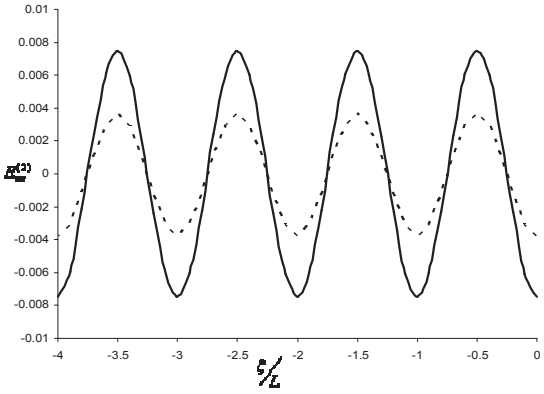

Fig. 1: dotted and solid curves represent respectively the variation of normalized, longitudinal electric wakefields $E_{nz} (= eE_z / mc\omega_p)$ with respect to ξ / L.

SUMMARY AND CONCLUSION

Generation of electric and magnetic wakefields in homogeneous and underdense plasma, in the mildly relativistic regime has been analyzed in detail. This study will be significant for the enhancement of the generated wakefield through laser- plasma interaction. The electric and magnetic wakefields are derived for laser -plasma with the help of time dependent Maxwell's equations. The source driving these equations is obtained with the help of the Lorentz force and continuity equations. The quasi-static approximation is used to study the evolution of the slow plasma electron velocities and wakefields.

Comparing the amplitudes of the generated wakes, it is seen that the amplitude of wakefield generated by the propagation of a circularly polarized laser pulse is about 49.8% more in comparison to the amplitude of the wakes generated by a linearly polarized laser pulse of same intensity. This study will be useful for the generation of wakefields with enhanced amplitudes and hence particle acceleration due to the propagation of circularly polarised laser pulse through homogeneous plasma.

References

[1] E. Esarey, P. Sprangle, J. Krall, and A. Ting, IEEE J. Quantum Electronics, **33** (1997) 1879.

[2] P.Jha, R.K.Mishra, G.Raj and A.K. Upadhyay Physics of Plasmas, **14** (2007) 053107.

[3] P.Jha, A.Saroch, R.K.Mishra Laser and Particle Beams, **31** (2013) 583-588.

Group velocity dispersion and self phase modulation induced chirping of short laser pulses in a plasma channel

Amita Malviya, Department of Physics, University of Lucknow, Lucknow-226007

Abstract- In this paper, nonlinear, nonparaxial propagation of intense, short, Gaussian laser pulses in a pre-formed plasma channel having a parabolic radial density profile has been set up. Taking into account the effect of group velocity dispersion, the wave equation describing the evolution of the laser field amplitude driven by relativistic nonlinearity has been set up. Chirping of the laser pulse induced due propagation in plasma is analyzed and a comparison of group velocity dispersion and self phase modulation induced chirp is presented. Variation technique is used to obtain describing the simultaneous evolution of the laser spot-size and pulse length in the plasma channel. It is seen that, an initially unchirped laser pulse becomes chirped as it propagates in a plasma channel, due to group velocity dispersion (GVD) as well as self- phase modulation (SPM) .

INTRODUCTION

Nonlinear interaction of an intense laser pulse with plasma is relevant to a wide range of applications including laser driven acceleration [1], inertial confinement fusion [2], and harmonic generation [3]. For all these applications the laser pulse is required to propagate beyond the Rayleigh length without diffraction. A plasma channel having a parabolic radial density variation [4] prevents diffraction of the laser pulse. While propagating in a plasma channel the laser spot undergoes betatron oscillations, which allow the pulse to remain confined close to the channel axis. When the laser pulse length becomes sufficiently short, finite pulse length can play an important role. Therefore it is important to study the simultaneous evolution of the laser spot size and pulse length for most laser-plasma applications. The nonlinear effects such as relativistic

EVOLUTION OF SPOT-SIZE AND PULSE LENGTH

Consider the propagation of a linearly polarized laser pulse in a pre-formed plasma channel having a parabolic density profile of the form $n(r) = n_0 + (\Delta n r^2 / r_{ch}^2)$ where n_0 the ambient plasma density and Δn and r_{ch} are the channel depth and radius respectively. The vector potential of the radiation field is given by,

$$\vec{A} = \hat{x}\frac{A}{2}(r,z,t)\exp(ik_0 z - i\omega_0 t) + c.c \qquad (1)$$

where $A(r,z,t)$, k_0 and ω_0 are the amplitude, wave number and frequency of the laser field respectively. The transformed wave equation z, t to z, ξ ($= z - \beta_g ct$ where $\beta_g = v_g / c$ governing the evolution of the vector potential of the radiation field is given ,

$$(\nabla_\perp^2 + 2ik_0\frac{\partial}{\partial z} + (1-\beta_g^2)\frac{\partial^2}{\partial \xi^2} + \left(\frac{\omega_0^2}{c^2} - k_0^2 - k_P^2\right))a(r,z,\xi)$$
$$= -k_P^2\left\{\frac{|a|^2}{4} + \frac{\Delta n r^2}{n_0 r_{ch}^2}\left(\frac{|a|^2}{4} - 1\right)\right\}a(r,z,\xi). \qquad (2)$$

In order solve the wave equation (2), a trial function is assumed as,

$$a = f(z)\exp\left[i\theta(z) - \frac{i\beta(z)\xi^2}{L^2(z)} - \frac{\xi^2}{L^2(z)} + \frac{i\alpha(z)r^2}{r_s^2(z)} - \frac{r^2}{r_s^2(z)}\right] \qquad (3)$$

where f, r_s, L, θ, β and α $\left(= k_0 r_s^2 / 2R(z)\right)$ represent the laser amplitude , spot-size, pulse length, phase, chirp and curvature respectively.The action integral $\left(\int_0^\infty r\left(\int_{-\infty}^{+\infty} l d\xi\right)dr\right)$ yields the reduced Lagrangian density,

$$\hat{l} = \frac{\sqrt{\pi} f^2(z) L(1+\alpha^2)}{2\sqrt{2}}$$
$$-\frac{\sqrt{\pi}k_0 f^2(z) L r_s^2}{2\sqrt{2}}\left[-\frac{\partial\theta}{\partial z} + \frac{1}{4}\left(\frac{\partial\beta}{\partial z} - \frac{2\beta}{L}\frac{\partial L}{\partial z}\right) + \frac{1}{2}\left(\frac{2\alpha}{r_s}\frac{\partial r_s}{\partial z} - \frac{\partial\alpha}{\partial z}\right)\right]$$
$$+\frac{\sqrt{\pi}f^2(z)r_s^2(1-\beta_g^2)(1+\beta^2)}{4\sqrt{2}L} + \frac{\sqrt{\pi}f^2(z)r_s^2(1-\beta_g^2)(1+\beta^2)}{4\sqrt{2}L}$$
$$(4) - k_P^2\left[\frac{\sqrt{\pi}f^4(z)r_s^2 L}{128} + \frac{\sqrt{\pi}f^4(z)r_s^4 L\Delta n}{512 n_0 r_{ch}^2} - \frac{\sqrt{\pi}f^2(z)r_s^4 L\Delta n}{8\sqrt{2}n_0 r_{ch}^2}\right]$$

The variation of reduced Lagrangian density θ, α, r_s, β, and L gives respectively, the conservation of energy of the laser pulse. Therefore,

$$f^2 r_s^2 L = f_0^2 r_0^2 L_0 = \text{constant} = M \qquad (5)$$

$$\alpha = \frac{k_0 r_s}{2}\frac{\partial r_s}{\partial z} \qquad (6)$$

$$\frac{\partial^2 r_s}{\partial z^2} = \frac{4}{k_0^2 r_s^3}\left[1 - \frac{P}{P_c} - \frac{r_s^4}{r_M^4}\right] \qquad (7)$$

Where P/P_c $\left(= \sqrt{2} f_0^2 r_0^2 L_0 k_P^2 / 64 L\right)$ represents the laser power normalized by critical power for self- focusing. Now evolution of the chirp parameters and pulse length as,

$$\beta = -\frac{k_0 L}{2\left(1-\beta_g^2\right)}\frac{\partial L}{\partial z} \tag{8}$$

$$\frac{\partial^2 L}{\partial z^2} = \frac{4(1-\beta_g^2)^2}{k_0^2}\frac{1}{L^3} - \frac{\sqrt{2}(1-\beta_g^2)k_P^2 M}{16k_0^2 r_s^2}\left(1+\frac{\Delta n r_s^2}{4n_0 r_{ch}^2}\right)\frac{1}{L^2} \tag{9}$$

GROUP VELOCITY DISPERSION AND SELF-PHASE MODULATION INDUCED CHIRPING OF SHORT LASER PULSES IN A PLASMA CHANNEL

Consider a matched $(\Delta n = \Delta n_c)$ laser beam propagating in the plasma channel. The variation of frequency across the laser pulse may be obtained by writing the resultant phase of the laser pulse as,

$$\phi = \left(\theta - \frac{\xi^2}{L^2}\beta\right) \tag{10}$$

Frequency shift across the laser pulse (chirp) is given by

$$\delta\omega = \left(-\frac{\partial\phi}{\partial t}\right) = \left(-\frac{\partial\phi}{\partial\xi}\frac{\partial\xi}{\partial t}\right) \tag{11}$$

Combining Eqs. (10) and (11) and substituting $\partial\xi/\partial t = -v_g$ gives,

$$\delta\omega = -\frac{2\beta\xi v_g}{L^2} \tag{12}$$

Eq. (12) indicates that if $\beta > 0\,(<0)$ the laser pulse will be positively (negatively) chirped i.e. the frequency increases (decreases) from the front to the back of the pulse. Further, substituting the value of β (Eq. (9)) into Eq. (12) leads to

$$\delta\omega = \frac{\xi v_g k_0}{L\left(1-\beta_g^2\right)}\frac{\partial L}{\partial z} \tag{13}$$

Eq. (13) shows that the frequency chirp is a function of propagation distance and varies with the laser pulse length evolution. Since the pulse length evolves Eq. (9) primarily on account of GVD and SPM, therefore GVD as well as SPM are also responsible for inducing chirp of the laser pulse. In fig. 1, solid curves (dotted curves) a, b and c $(d, e$ and $f)$ show the variation of frequency induced chirp due to SPM, GVD and combined effect of both, respectively at the front (back) of the laser pulse. Curve *a* (*d*) shows that due self-phase modulation the frequency at the front (back) of the pulse decreases (increases). Group velocity dispersion leads to a converse frequency variation as seen in curves *b* and *e*. It may be noted that when both effects are taken into account SPM dominates over GVD since curve *c* (*f*) follows curve *a* (*d*) with a lesser magnitude. Therefore GVD effects tend to reduce the chirp generated by self-phase modulation of the laser pulse.

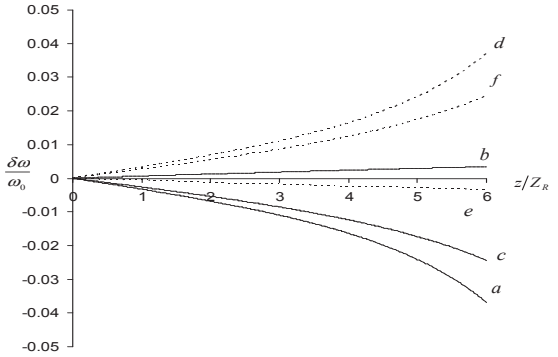

Fig.1 Variation of normalized frequency $(\delta\omega/\omega_0)$ with propagation distance Solid (dotted) curve *a* (curve *e*) , curve *b* curve *c* (curve*d*) are due to SPM, GVD and combined effectof SPM and GVD at front (back) $\xi = 0.5$ (-0.5) of the pulse for $f_0^2 = 0.03$, $\lambda = 1\mu m$, $\lambda_P = 10\ \mu m$, $r_0 = 33\ \mu m$, $r_{ch} = 50\mu m$, $\Delta n = \Delta n_c = 1.7 \times 10^{17}$ cm^{-3}.

SUMMARY AND DISCUSSION

The present paper is a significant contribution toward understanding the evolution dynamics of short laser pulse in a plasma channel. The study shows that the evolution characteristics of the laser pulses are affected by group velocity dispersion as well as relativistic nonlinearity. It is shown that, an initially unchirped laser pulse becomes chirped as it propagates in a plasma channel, due to group velocity dispersion (GVD) as well as self-phase modulation (SPM). For a matched $(r_s = r_0, \Delta n = \Delta n_c)$ laser pulse the frequency at the front (back) of the pulse decreases (increases) due to SPM effect whereas it increases (decreases) due to GVD effect. However, when both effects are taken into account SPM dominates over GVD leading to an increase in frequency from front to back of the pulse (positive chirping). Since SPM depends upon the intensity of the laser pulse, a reduction in intensity causes the GVD and SPM induced chirp to approximately cancel each other so that the initially unchirped laser pulse remains nearly unchirped.

References

[1]. E. Esarey, P. Sprangle, J. Krall and A. Ting IEEE Trans. Plasma Sci. **24**, 252 (1996).

[2]. H. Hora Am. Jr. Appl. Sci. **2(6),** 1085 (2005).

[3]. W.B. Mori , C.D. Deeker and W.P. Leemans IEEE Trans. Plasmas **21,** 110 (1993).

[4]. P. Jha, A. Malviya and A.K. Upadhyay Lasers and Particle Beams **28,** 245 (2010).

Third harmonic radiation generation via interaction of circularly polarized laser beam with plasma

Ekta Agrawal*,#, and Pallavi Jha

Department of Physics, University of Lucknow, Lucknow-226007, India.

ABSTRACT

In the current study, generation of third harmonic radiation due to propagation of an obliquely incident circularly polarized laser beam through homogeneous plasma, in the mildly relativistic regime, has been presented. The amplitude of third harmonic radiation as well as its detuning distance has been obtained and their variation with the angle of incidence is analyzed. It is observed that the generated third harmonic radiation is elliptically polarized. The ellipticity of the third harmonic radiation increases as the angle of incidence is increased. The harmonic radation vanishes at normal incidence of the circularly polarized laser beam.

INTRODUCTION

Interaction of intense laser pulses with plasma is relevant to many nonlinear phenomenon including laser fusion schemes, charged particle accelerators , and coherent harmonic radiation sources [1]. The excitation of coherent radiation at harmonics of the fundamental frequency of the laser is of much practical importance due to its potential for producing x-ray lasers and coherent radiation sources. Interaction of intense laser pulses with homogeneous plasma leads to the generation of odd harmonics of the laser frequency [2]. Even harmonics of the laser frequency can be generated by interaction of linearly polarized laser pulses with inhomogeneous plasma [3] and also in the presence of external fields [4]. Recently, generation of second harmonic radiation via interaction of an obliquely incident p-polarized laser beam with homogeneous plasma has been reported [5].

FORMULATION

Consider a circularly polarized laser beam obliquely incident on a vacuum- plasma interface, at an angle θ with respect to the z axis. The plane of incidence is assumed to be the $y-z$ plane. The vacuum electric fields of the incident laser oscillating at the fundamental as well as its harmonic frequencies are given by

$$\vec{E}_0 = \frac{1}{2}\sum_{j=1}^{2}\left(-i\hat{x} + \hat{y}\cos\theta - \hat{z}\sin\theta\right)E_{0j} \exp\left[i\left(k_{jy}y + k_{jz0}z - j\omega t\right)\right] + c.c \quad (1)$$

where ω is the frequency while $k_{jy} = (j\omega\sin\theta)/c$ and $k_{jz0} = (j\omega\cos\theta)/c$ are the propagation constants along the $\hat{y}$ and $\hat{z}$ directions, respectively. E_{0j} represents the amplitude of the fundamental and the harmonic frequencies such that $E_{0j} << E_{01}$ where j>1. The beam refracts inside the homogeneous plasma, having ambient density n_0, at angle $\alpha_j = \tan^{-1}\left(\sin\theta/\sqrt{\varepsilon_j - \sin^2\theta}\right)$, where $\varepsilon_j = 1 - \omega_p^2/\left(j^2\omega^2\right)$ is the dielectric constant and $\omega_p = \left(4\pi e^2 n_0/m\right)^{1/2}$ is the plasma frequency. Hence the electric field transmitted inside the plasma are evaluated to be

$$\vec{E}_L = \frac{1}{2}\sum_{j=1}^{2}\left[-\hat{x}iE_{j\perp} + \left\{\hat{y}\left(\sqrt{\varepsilon_j - \sin^2\theta}/\sqrt{\varepsilon_j}\right) - \hat{z}\left(\sin\theta/\sqrt{\varepsilon_j}\right)\right\}E_{j\|}\right] \exp\left[i\left(k_{jy}y + k_{jz}z - j\omega t\right)\right] + c.c \quad (2)$$

where $k_{jz} = \left(j^2\omega^2\varepsilon_j/c^2 - k_{jy}^2\right)^{1/2}$ is the propagation constant of the laser inside the plasma, along the $\hat{z}$ direction while k_{jy} remains unchanged. The electric field amplitudes along directions perpendicular and parallel to the plane of incidence are respectively given by $E_{j\perp} = 2\cos\theta E_{0j}/\left(\cos\theta + \sqrt{\varepsilon_j - \sin^2\theta}\right)$ and $E_{j\|} = 2\cos\theta\sqrt{\varepsilon_j}E_{0j}/\left(\varepsilon_j\cos\theta + \sqrt{\varepsilon_j - \sin^2\theta}\right)$. It is seen that the electric field of the obliquely incident circularly polarized laser field inside the plasma is a superposition of *s* and *p* polarized fields of unequal amplitude and a phase difference of $\pi/2$. Hence $E_{j\perp} = E_{js}$ and $E_{j\|} = E_{jp}$.

The wave equation governing the interaction of the laser pulse with plasma is given by

$$\left(\nabla^2 - \frac{1}{c^2}\frac{\partial^2}{\partial t^2}\right)\vec{E}_L = \frac{4\pi}{c^2}\frac{\partial\vec{J}}{\partial t} \quad (3)$$

where $\vec{E} = \vec{E}_L + \vec{E}_S$, $\vec{E}_S$ represents the space charge field and the plasma current density $\vec{J} = -n_e e\vec{v}$.

With the help of Lorentz force and electric field equation (2), the plasma electron velocities along the $\hat{x}$, $\hat{y}$ and $\hat{z}$ directions, upto the third order of the radiation field, are obtained. Hence, by using Continuity and Poisson's equations alongwith plasma electron velocities, the plasma electron density upto the second order of the laser frequency can be obtained.

* Work supported by Unversity Grants Commission, Government of India, under the Basic Science Research Fellowship Scheme.

#ektaagrawal555@gmail.com

THIRD HARMONIC RADIATION GENERATION

The electric field components of the transmitted third harmonic radiation along directions lying in, as well as perpendicular to, the plane of incidence, are respectively given as

$$a_{3s}(z) = \frac{9\omega_p^4 a_{1s}\left(a_{1p}^2 - a_{1s}^2\right)}{32\omega^2 c^2 k_{3z}\Delta k\varepsilon_2}\exp i(\Delta k.z/2)\sin(\Delta k.z/2)$$

$$a_{3p}(z) = \frac{9i\omega_p^4\sqrt{\varepsilon_1}a_{1p}\left(a_{1p}^2 - a_{1s}^2\right)}{32\omega^2 c^2 k_{3z}\Delta k\varepsilon_2\sqrt{\varepsilon_1}}\exp i(\Delta k.z/2)\sin(\Delta k.z/2)$$

where $\Delta k = 3k_{1z} - k_{3z}$ and the dispersion relation $c^2\left(k_{3y}^2 + k_{3z}^2\right) = 9\omega^2 - \omega_p^2$ has been used Since the value of the field amplitude lying in the plane of incidence is not equal to the field amplitude lying in the perpendicular plane, it may be concluded that the third harmonic radiation is elliptically polarized. The eccentricity and the resultant amplitude of the third harmonic are respectively given by

$$\psi = \sqrt{1 - \frac{a_{1s}^2}{a_{1p}^2}}$$

$$a_3(z) = \frac{9\omega_p^4\left(a_{1p}^2 - a_{1s}^2\right)\sqrt{a_{1s}^2 + a_{1p}^2}}{32\sqrt{2}\omega^2 c^2 k_{3z}\Delta k_3\varepsilon_2}\exp i(\Delta k.z/2)\sin(\Delta k.z/2)$$

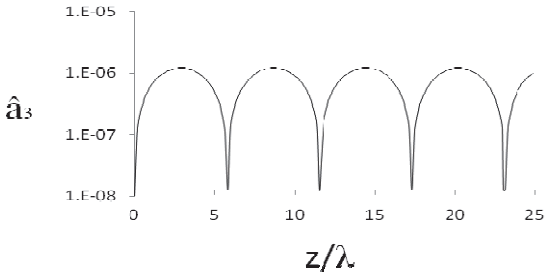

Figure 1: Variation of normalized third harmonic amplitude with normalized propagation distance for $\lambda = 1.0\mu m$, $\omega_p/\omega = 0.2$, $\theta = 70^o$, $a_o = 0.3$

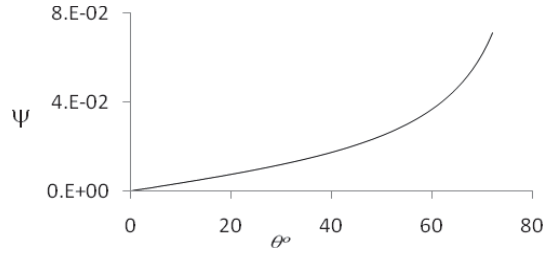

Figure 2: Variation of eccentricity for third harmonic with angle of incidence for $\lambda = 1.0\mu m$, $\omega_p/\omega = 0.2$ and $a_o = 0.3$.

The maximum normalized third harmonic amplitude obtained after traversing a detuning distance $l_c = \pi/\Delta k$ is

$$\hat{a}_{3(\max)} = \frac{9\omega_p^4\left(a_{1p}^2 - a_{1s}^2\right)\sqrt{a_{1s}^2 + a_{1p}^2}}{32\sqrt{2}a_0\omega^2 c^2 k_{3z}|\Delta k|\varepsilon_2}$$

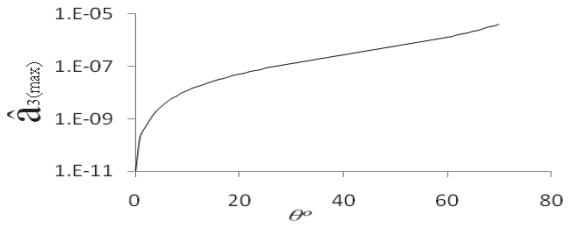

Figure 3: Variation of maximum third harmonic normalized amplitude with angle of incidence for $\lambda = 1.0\mu m$, $\omega_p/\omega = 0.2$ and $a_o = 0.3$.

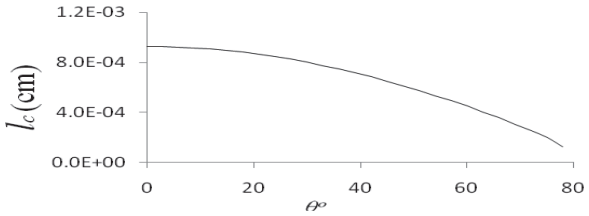

Figure 4: Variation of detuning distance for third harmonic with angle of incidence for $\lambda = 1.0\mu m$, $\omega_p/\omega = 0.2$ and $a_o = 0.3$.

CONCLUSIONS

It is observed that the third harmonic amplitude oscillates with normalized propagation distance. The maximum amplitude and ellipticity of the harmonic increases as the angle of incidence is increased, upto an angle $\theta_{\max}$ (for which the propagation constant k_1 of the fundamental frequency is real). However, the detuning length considerably decreases as the angle of incidence is increased. Hence an optimum value of incidence angle can be chosen for which a reasonable third harmonic is obtained without significant reduction in detuning length. The generated third harmonic radiation is elliptically polarized. At $\theta = 0^0$ the eccentricity is zero, implying that the radiation is circularly polarized and the third harmonic amplitude vanishes.

References

[1] P. Amendt D. C. E,der and S. C. Wilks, Phys. Rev. Lett. 66 (1991) 2589.

[2] W. B. Mori, C. D. Decker, and W. P. Leemans, IEEE Trans. Plasma Sci. 21 (1993) 110.

[3] E. Esarey, A.Ting, P. Sprangle, D. Umstadter and X. Liu, IEEE Trans. Plasma Sci. 21 (1993) 95.

[4] P. Jha, R. K. Mishra, G. Raj, and A. K. Upadhyay, Phys. Plasmas 14 (2007) 053107.

[5] P. Jha, and E. Agrawal, Phys. Plasmas 21, (2014) 053107.

Simulation study of electron acceleration by wakes driven by super-Gaussian laser pulses propagating in homogeneous plasma

Akanksha Saroch*# and Pallavi Jha
Department of Physics, University of Lucknow, Lucknow-226007, India

Abstract: Evolution of longitudinal electrostatic wakefields, due to the propagation of a linearly polarized super-Gaussian laser pulse through homogeneous plasma has been presented via 2-D VORPAL simulations. The wakes generated are compared with those generated by a Gaussian laser pulse in the relativistic regime. Further, one-dimensional numerical model has been used to plot the separatrix curves to study the trapping and energy gain of an externally injected test electron, due to the generated electrostatic wakefields. An enhancement in the peak energy of an externally injected electron accelerated by wakes generated by super-Gaussian pulse as compared to Gaussian pulse case has been observed.

INTRODUCTION

The amplitude of the generated wakefields depends on the shape of an ultrashort, intense laser pulse. Interaction of highly relativistic short laser pulses with plasma and nonlinear wakefield generation by the laser pulses with realistic shapes has been studied by Berezhiani *et al* [1]. Zeng *et al.* [2] have theoretically predicted the dependence of relativistic harmonic radiation on the pulse shape of pumping laser. Considering super-Gaussian beam profile, THz radiation generation [3] has also been shown.

In the present analysis, the excitation of longitudinal, electrostatic wakefields produced by a linearly polarized super-Gaussian laser pulse propagating through uniform plasma has been studied using two-dimensional PIC simulations. The study proceeds by considering plasma to be cold as well as underdense. In order to validate the results obtained via simulations, we have studied the generation of wakefields by one-dimensional numerical model. Further the trapping and acceleration of an externally injected test electron, by the generated wakefields, has been studied.

2-D VORPAL SIMULATION STUDY

In order to study the generation of longitudinal electrostatic wakefields via passage of super-Gaussian laser pulse through cold, homogeneous and underdense plasma, we have performed 2-D simulations using VORPAL code. The temporal profile of the laser pulse is considered to be of the form $a = a_0 \exp(-(\xi - \xi_0)^{2m} / L^{2m})$ (where $m = 2$, 3, 4… for super-Gaussian while $m = 1$ represents a Gaussian profile). Here, L and ξ_0 are respectively the pulse length and arbitrary pulse center of the laser pulse. The full width at half maximum (FWHM) pulse length L_{FWHM} $(= \sqrt{2 \ln 2} L)$ was considered to be 14.2 μm, corresponding to $L = 12.0 \mu m$. The minimum laser spot size of the two laser pulses (assumed to be equal) is 50 μm. The size of the simulation domain is 78.9 μm (this includes 10 μm vacuum distance) in the laser propagation direction (x) and 366 μm in the transverse directions (y and z), respectively. The simulation uses one particle per cell along x as well as y direction to represent the plasma electrons. The time step satisfying the Courant condition is considered to be 177.14×10^{-18} seconds. In the present simulation study the plasma wavelength is taken to be $\lambda_p = 32\ \mu m$ $(= 2\pi c / \omega_p$, $n_0 = 1.09 \times 10^{18}\ / cm^3$ is the plasma electron density). We have performed the simulations in the relativistic regime of the laser pulse intensity $2.14 \times 10^{18}\ W/cm^2$ which corresponds to $a_0 = 1.0$.

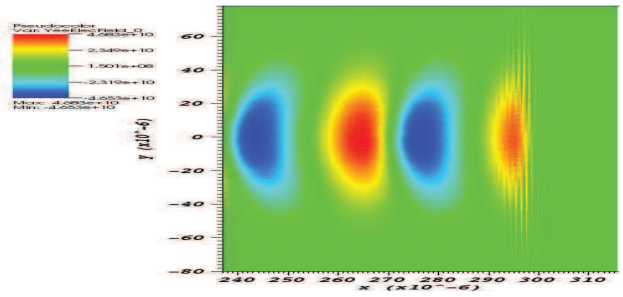

Figure 1: Surface plot of the longitudinal electric wakefield (E_x) generated by super-Gaussian laser pulses.

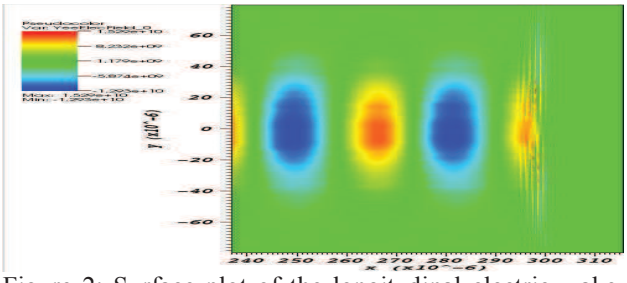

Figure 2: Surface plot of the longitudinal electric wakefield (E_x) generated by Gaussian laser pulses.

* Work supported by CSIR, Govt. of India vide Project file No.09/107(0372)/2015-EMR-I.

#akshusaroch@gmail.com

Fig. 1 (2) represents the surface plot of the longitudinal electric wakefield generated by super-Gaussian (Gaussian) laser pulses. The peak values of the generated wakes are respectively $4.6 \times 10^{10}\ V/m$ and $1.255 \times 10^{10}\ V/m$ forsuper-Gaussian and Gaussian laser pulses. Comparing the amplitudes of the generated wakes, it is seen that the amplitude of wakefield generated by super-Gaussian laser is more in comparison to the amplitude of the wakes generated by Gaussian laser pulse.

1-D NUMERICAL MODEL FOR TEST ELECTRON ACCELERATION

Consider a linearly polarized laser pulse represented by the vector potential $\vec{A}_{L0} = \hat{x}A_0(z,t)\cos(k_0 z - \omega_0 t)$ propagating through uniformly pre-ionized plasma having ambient density n_0 along the positive z-direction. Wakefield generation due to the interaction of laser pulses with cold and relativistic plasma is governed by basic nonlinear fluid equations: Lorentz force, continuity and Poisson's equations.

In order to study the generation of wakefields, transverse quiver velocity the longitudinal velocity of the plasma electrons is obtained to be,

$$\frac{\partial(\gamma v_z)}{\partial t} + v_z \frac{\partial(\gamma v_z)}{\partial z} = \frac{e}{m}\frac{\partial \Phi}{\partial z} - \frac{e^2}{m^2 c^2 \gamma}\left(\frac{\partial A_0^2}{\partial z}\right) \quad (1)$$

While writing Eq. (1), we have retained the terms which oscillate at the plasma frequency and neglected the terms comprising of oscillations at the second harmonics of the laser field. Using quasistatic approximation the transformed, normalized fluid equations governing the evolution of the longitudinal electrostatic wakefield are given by,

$$\frac{\partial u_z}{\partial(k_p\xi)} = \frac{1}{\gamma(u_z - \beta_g)}\left[\frac{\partial \phi}{\partial(k_p\xi)} - \frac{a_0}{2\gamma}\frac{\partial a_0}{\partial(k_p\xi)}\right] - \frac{u_z}{\gamma}\frac{\partial \gamma}{\partial(k_p\xi)} \quad (2)$$

$$\frac{\partial^2 \phi}{\partial(k_p\xi)^2} = n - 1 \quad (3)$$

$$\frac{\partial n}{\partial(k_p\xi)} = -\frac{n}{(u_z - \beta_g)}\frac{\partial u_z}{\partial(k_p\xi)} \quad (4)$$

Eqs. (2-4) can be solved simultaneously using the fourth order Runge-Kutta numerical technique. Using the same parameters as used in the simulation study, the normalized wake potential and hence the electrostatic longitudinal wakefield ($E_{nz} = -\vec{\nabla}\phi$) may be obtained.

Further, the acceleration mechanism of a test electron injected behind the laser pulse is studied. With the help of Hamiltonian dynamics the peak energy (γ_e) of the test electron as

$$\gamma_e = \gamma_p(1 + \gamma_p \Delta\phi) \pm \gamma_p \beta_p [(1 + \gamma_p \Delta\phi)^2 - 1]^{1/2}. \quad (5)$$

Since, the external test electron is assumed to be driven by the generated plasma wave, so the initial velocity of the injected test electron is taken to be equal to the phase velocity (v_p) of the plasma wave. The separatrix plots for the test electron being accelerated by the super-Gaussian as well as Gaussian laser pulses are plotted by simultaneously solving Eq.(5) along with transformed plasma fluid equations using fourth order Runge-Kutta algorithm.

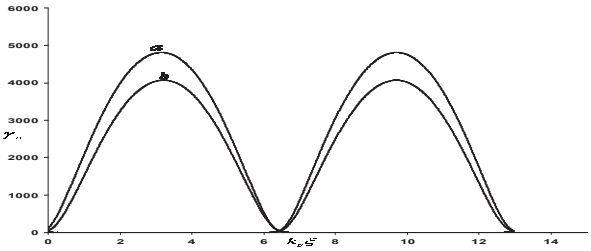

Figure 3: Separatrices plots for the test electro driven bywakes generated by super-Gaussian (curve *a*) and Gaussian (curve *b*).

Plots *a* & *b* in Fig.3, depict the separatrix curves traced by an externally injected test electron being driven by the wakes generated by the super-Gaussian and Gaussian laser pulses, respectively. The injection energies necessary for trapping the test electron excited by the wakes generated by super-Gaussian and Gaussian laser pulses is same (=20.47 MeV), while the maximum energies attained after acceleration are 2.46 GeV, and 2.08 GeV for curves a and b respectively. Hence, a gain of 15.4% in the maximum energy of the accelerated test electron is seen for super-Gaussian pulse as compared to Gaussian pulse case.

SUMMARY AND DISCUSSION

Generation of longitudinal electrostatic wakefields by the interaction of super-Gaussian laser pulse with homogeneous plasma has been presented via two-dimensional VORPAL simulations in the relativistic regime. It is observed that the generated wake amplitude for super-Gaussian driving laser pulse show a remarkable increase as compared to the wakefield amplitude for a Gaussian laser pulse. Further, the trapping and acceleration of an externally injected test electron has been studied. The peak energy attained by the test electron being accelerated by the wakes generated by a super-Gaussian laser pulse is evaluated and compared with the Gaussian pulse case. Comparing the difference between the peak energies attained by the test electron and injection energies for two different pulse shapes, we see that the energy gain is appreciably enhanced for test electron accelerated by wakes generated by super-Gaussian pulse as compared to energy gain for Gaussian pulse case of same intensity.

References

[1] V. I Berezhiani,. & I. G. Murusidze, Phys. Scripta 45, (1992) 87

[2] G.Zeng, B Shen, W. Yu, & J. Xu, Phys. Plasmas 3, (1996) 4220

[3] H. K. Malik, & A. K. Malik, Europhys. Lett. 100, (2012) 45001

Spot-size evolution of two-color laser pulses in homogeneous plasma

Hemlata and Pallavi Jha
Department of Physics, University of Lucknow, Lucknow-226007, India

Abstract: The evolution of two-color, sinusoidal laser pulses in cold, underdense and homogeneous plasma has been presented. The wave equations governing the evolution of the radiation fields are set up and a variational technique is used to obtain the simultaneous equations describing the evolution of the laser spot-size. Numerical methods are used to graphically analyze the simultaneous evolution of spot-size due to the combined effect of the two-color laser pulses. Further, the spot-size is compared with those obtained for a single laser pulse.

INTRODUCTION

The propagation of intense laser beams through homogeneous plasma finds application in harmonic generation , X-ray laser sources , laser-plasma acceleration and inertial confinement fusion. Recently, Jha et al have shown the evolution of chirped laser pulses in a magnetized plasma channel [1]. High order harmonic generation via two color laser pulses has been reported [2]. Feng *et al* have studied the generation of isolated attosecond pulses due to two color chirped laser pulses [3].

FORMULATION

Consider the propagation of two linearly polarized laser pulses of frequency ω_1 and ω_2 copropagating along the positive *z*-direction in plasma. Both the laser pulses are polarized along the *x*-direction. The vector potential of the first and second laser pulse is given by

$$\vec{A}_{1,2} = \hat{x}\frac{A_{1,2}(r,z,t)}{2}\exp\, i(k_{1,2}z - \omega_{1,2}t) + c.c. \tag{1}$$

The subscripts 1 and 2 correspond to the parameters associated with the first and second laser pulse respectively. $A_{1,2}(r,z,t)$, $k_{1,2}$ and $\omega_{1,2}$ represent the amplitude, wave number and angular frequency of the two laser pulses. Transforming independent variables z, t to $z, \xi\left(= z - \beta_{g1,2}ct\right.$ where $\beta_{g1,2}\left(= ck_{1,2}/\omega_{1,2}\right)$ is the normalized group velocity of the two laser pulses). The transformed wave equations describing the evolution of the vector potential of two-color laser pulses propagating in a plasma channel are given by

$$\left[\nabla_{\perp}^2 + 2ik_{1,2}\frac{\partial}{\partial z} + 2\frac{\partial^2}{\partial\xi\partial z} + (1-\beta_{g1,2}^2)\frac{\partial^2}{\partial\xi^2} + \frac{\partial^2}{\partial z^2} + \left(\frac{\omega_{1,2}^2}{c^2} - k_{1,2}^2 - k_p^2\right)\right]a_{1,2}(r,z,\xi) = -k_p^2\left[\frac{|a_{1,2}|^2}{4} + \frac{|a_{2,1}|^2}{4}Q\right]a_{1,2}(r,z,\xi). \tag{2}$$

where

$Q\left[= \left\{3 - \frac{c^2(k_1+k_2)^2}{(\omega_1+\omega_2)^2} - \frac{c^2(k_1-k_2)^2}{(\omega_1-\omega_2)^2}\right\}\right]$ quantifies the nonlinear effects, $k_p\left[= \left(4\pi n_0 e^2/mc^2\right)^{1/2}\right]$ is the plasma wave number and $\vec{a}_{1,2}(r,z,t)\left\{= (e\vec{A}_{1,2}/mc^2) << 1\right\}$ is the normalized vector potential. Considering the limits $k_p r_{01,2} > 1, k_p L_{01,2} > 1$ (where $r_{01,2}$ and $L_{01,2}$ are respectively the initial spot size and pulse length of the two laser beams), the ponderomotive nonlinearity has been neglected while deriving Eq.(2). Coulomb gauge $\left(\vec{\nabla}.\vec{A} = 0\right)$ has been used.

Assuming that the laser pulses have a sinusoidal profile, the trial function for the laser amplitude may be represented by

$$a_{1,2} = f_{1,2}(z)\exp\left(i\theta_{1,2}(z) + \frac{i\alpha_{1,2}(z)r^2}{r_{s1,2}^2(z)} - \frac{r^2}{r_{s1,2}^2(z)}\right)\sin\left(\frac{\pi\xi}{L_{01,2}(z)}\right) \tag{3}$$

where $f_{1,2}(z)$, $\theta_{1,2}(z)$, $\alpha_{1,2}(z)$ and $r_{s1,2}(z)$ are respectively the amplitude, phase shift, curvature and spot size of the two pulses. Using $\hat{l} = \int_0^\infty rdr\int_0^{L_{01,2}} ld\xi$ yields the reduced Lagrangian density

$$\hat{I}_{1,2} = \frac{(\alpha_{1,2}^2+1) f_{1,2}^2 L_{01,2}}{4} + \frac{f_{1,2}^2 r_{s1,2}^2 L_{01,2} k_{1,2}}{4}\left[\frac{\partial \theta_{1,2}}{\partial z} + \left\{\frac{1}{2}\frac{\partial \alpha_{1,2}}{\partial z} - \frac{\alpha_{1,2}}{r_{s1,2}}\frac{\partial r_{s1,2}}{\partial z}\right\}\right] + \frac{(1-\beta_{g1,2}^2)\pi^2 f_{1,2}^2 r_{s1,2}^2}{8L_{01,2}} - \left(\frac{\omega_{1,2}^2}{c^2} - k_{1,2}^2 - k_p^2\right)\frac{f_{1,2}^2 r_{s1,2}^2 L_{01,2}}{8} - \frac{3k_p^2 f_{1,2}^4 r_{s1,2}^2 L_{01,2}}{512} - \frac{k_p^2 f_{1,2}^2 f_{2,1}^2 r_{s1,2}^2 r_{s2,1}^2 Q}{64\left(r_{s1,2}^2 + r_{s2,1}^2\right)}\left\{L_{01,2} - \frac{L_{02,1}^3}{2\pi\left(L_{02,1}^2 - L_{1,2}^2\right)}\sin\left(\frac{2\pi L_{01,2}}{L_{02,1}}\right)\right\} \tag{4}$$

The variation of the reduced Lagrangian density with respect to $\theta_{1,2}$, $\alpha_{1,2}(z)$ and $r_{s1,2}(z)$ give , $f_{1,2}^2 r_{s1,2}^2 = f_{01,2}^2 r_{01,2}^2 = U_{1,2}$, where $f_{01,2}$ is the initial amplitude of the two pulses.

$$\alpha_{1,2} = \frac{k_{1,2} r_{s1,2}}{2}\frac{\partial r_{s1,2}}{\partial z} \tag{5}$$

$$\frac{\partial^2 r_{s1,2}}{\partial z^2} = \frac{4}{r_{s1,2}^3 k_{1,2}^2}\left[1 - \frac{3k_p^2 U_{1,2}}{128 L_{01,2}} - \frac{U_{2,1} r_{s1,2}^4 k_p^2 Q}{16 L_{02,1}\left(r_{s1,2}^2 + r_{s2,1}^2\right)^2}\left\{1 + \frac{L_{02,1}^3 \sin\left(\frac{2\pi L_{01,2}}{L_{02,1}}\right)}{2\pi L_{01,2}\left(L_{01,2}^2 - L_{02,1}^2\right)}\right\}\right] \tag{6}$$

NUMERICAL SOLUTIONS

The simultaneous evolution of the laser spot size of the two color pulse system, can be obtained by numerically solving Eqs. (6) using the fourth order Runge Kutta method. In the present study we have assumed that at $z = 0$, $\partial r_{s1,2}/\partial z = 0$, $r_{s1,2} = r_{01,2} = 45\mu m$, , $L_{01} = 19\mu m$ and $L_{02} = 20\mu m$. The other laser and plasma parameters are $f_{01}^2 = 0.02$, $f_{02}^2 = 0.04$, $\omega_1 = 1.88\times10^{15}\,Hz$, $\omega_2 = 1.253\times10^{15}\,Hz$ and $n_0 = 1.1\times10^{19}\,cm^{-3}$. The figure shows the simultaneous evolution of the normalized (by $r_{01,2}$) spot-size with respect to the propagation distance for the two color laser pulse system. The solid curves *a* and *b* respectively depict the evolution of the first $(L_{01} = 19\mu m)$ and second $(L_{02} = 20\mu m)$ laser pulses when the two pulses are considered to be co-propagating, while the dashed curves (*a* and *b*) represent the independent propagation of the two laser pulses. It is observed that the spot sizes focus for the two color system while they defocus when the two pulses propagate individually. The focusing of the spot size of the two color laser pulse system occurs due to a significant decrease in critical power required for focusing of the laser pulses. It may be noted that the critical power of the laser pulses is reduced due to copropagation of the second pulse.

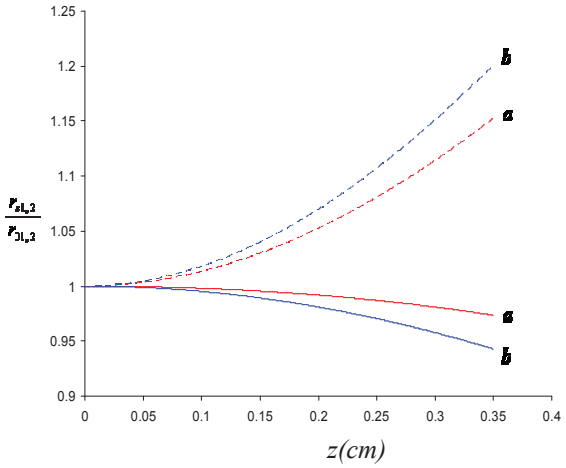

SUMMARY AND DISCUSSION

In the present paper, nonlinear propagation of intense, short, two-color laser pulses in homogeneous plasma has been studied. The two-color laser pulses are polarized along the *x*-direction. Using the variational technique, the simultaneous equations describing the evolution of laser spot size have been obtained for the two-color pulsed laser system and compared with the results obtained for a single pulse case. The initial spot size for the two-color pulses is considered to be the same, while pulse length is considered approximately the same. It is seen that the spot size focuses significantly for the two-color system as compared to individually propagating pulses.

References

[1] P. Jha, Hemlata, and R. K. Mishra, Phys. Plasmas 21, 123106 (2014).
[2] P. Jha, N. K. Verma and A. Saroch, J. Plasma Phys. 79, (2013).
[3] L. Feng and T. Chu, Phys. Rev. A 84, 053853 (2011).

List of Contributing Institutes

Al-Farabi Kazakh University
Almaty, Kazakhstan

Beijing National Laboratory for
Condensed Matter Physics
Beijing, China

CERN
Geneva, Switzerland

Christian-Albrechts-Universität
Kiel, Germany

Commissariat à l'énergie atomique et aux
énergies alternatives (CEA)
France

Czech Technical University
Prague, Czech Republic

Ecole Polytechnique, LULI
Université Paris-Saclay
Palaiseau Cedex, France

ELI-ALPS
Szeged H-6720, Hungary

European XFEL
Hamburg, Germany

Facility for Ion and Antiproton
Research (FAIR)
Darmstadt, Germany

FEI STU
Bratislava, Slovakia

GSI Helmholtzzentrum für
Schwerionenforschung GmbH
Darmstadt, Germany

Johann-Wolfang-Goethe-Universität
Institut für Angewandte Physik
Frankfurt, Germany

Handong Global University
Pohang, Republic of Korea

Heinrich-Heine-Universität Düsseldorf
Institut für Theoretische Physik I
Düsseldorf, Germany

Helmholtz-Zentrum Dresden – Rossendorf
Dresden, Germany

Helmholtz-Institut Jena
Jena, Germany

Institute of Modern Physics (IMP)
Lanzhou, China

Institute of Nuclear Physics and
Chemistry (CAEP)
Mianyang, China

Institute of Problems of Chemical
Physics (IPCP)
Chernogolovka, Russia

Institute of Radiophysics and Electronics
Ashtarak, Armenia

Institute of Theoretical and
Experimental Physics (ITEP)
Moscow, Russia

Joint Institute for High Temperatures,
RAS
Moscow, Russia

Joint Institute of Nuclear Research
Dubna, Russia

Korea Advanced Institute of Science and
Technology (KAIST)
Daejeon, Republic of Korea

Lawrence Berkeley National Laboratory
Berkeley, CA, USA

Lawrence Livermore National Laboratory
Livermore, CA, USA

Lebedev Physical Institute, RAS
Moscow, Russia

Los Alamos National Laboratory
Los Alamos, NM, USA

LPGP, CNRS,
Université Paris-Sud
Orsay, France

Max Born Institute
Max-Born-Str. 2a
Berlin, Germany

Moscow Engineering Physics Institute (MEPhI)
Moscow, Russia

Naval Research Laboratory
Washington, DC, USA

Osaka University, Institute for Academic Initiatives
Suita, Osaka, 565-0871, Japan

Princeton Plasma Physics Laboratory
Princeton, NJ, U.S.A.

Rutherford Appleton Laboratory
Central Laser Facility
Didcot OX11, United Kindom

Shanghai Insitute of Optics and Fine Mechanics, CASciences
Shanghai, China

Technion
Haifa, Israel

Technische Universität Darmstadt
IKP, TQE
Darmstadt, Germany

Technische Universität Dresden
Dresden, Germany

Technische Universität Kaiserslautern, Fachbereich Physik und Landesforschungszentrum OPTIMAS
Kaiserslautern, Germany

Technische Universität München,
München, Germany

TPU
Tomsk, Russia

Universidad Politcnica Madrid
ETSI Aeronauticos
Madrid, Spain

Universidad Politécnica de Valencia
Valencia, Spain

Universität Rostock, Institut für Physik
Rostock, Germany

Université Bordeaux, CELIA
Bordeaux, France

University of California Berkeley
Berkeley, CA, USA

University of California Los Angeles (UCLA)
Los Angeles, CA, U.S.A

University of Chinese Academy of Sciences (UCAS)
Beijing, China

University of Lucknow
Department of Physics
Lucknow, India

University of Strathclyde, SUPA
Glasgow, G 0NG, United Kingdom

University of York
Plasma,Institute, Department of Physics
York YO10 5DD, United Kingdom

Utsunomiya University
Utsunomiya, Japan

Varna Technical University
Varna, Bulgaria

Xianyang Normal University
Xianyang, China

Xi'an Jiaotong University (XJTU)
Xi'an, China

Yerevan State University, Centre of Strong Fields Physics
Yerevan Armenia

HEDgeHOB Institute | **First Author Institute** | Contributing Institute

Author Index